Alahmade, Walaa, Ph.D., MAY 2021 NUCLEAR PHYSICS

EXPERIMENTAL INVESTIGATION AND MONTE CARLO SIMULATION OF QUASIELASTIC ELECTRON SCATTERING FROM HELIUM-3 CLUSTERS IN HELIUM-4 (179 pp.)

Director of Dissertation: Dr. A. Mina T. Katramatou

Experiment E04-018 was conducted in Hall A of the Jefferson National Laboratory (JLab) from November 2006 through July 2007. The experiment used the two superconducting, high-resolution magnetic spectrometers of Hall A to detect scattered electrons and recoil nuclei. One goal of this experiment was to provide accurate data on the elastic charge form factor of ^{4}He to high momentum transfers (up to $Q^2 = 77$ fm^{-2}). The purpose of this thesis is to analyze and simulate a very unique and unexpected class of data from this experiment. The work performed involved the analysis of electron scattering data with the ^{4}He target of the JLab E04-018 experiment and Monte Carlo simulation studies of elastic and quasielastic electron scattering from the ^{4}He and ^{3}He few-body nuclear systems. The results of this experiment and the simulations provide insights into the existence of $A =$ 3 clustering in ^{4}He, and possibly in heavier nuclei.

EXPERIMENTAL INVESTIGATION AND MONTE CARLO SIMULATION OF QUASIELASTIC ELECTRON SCATTERING FROM HELIUM-3 CLUSTERS IN HELIUM-4

A dissertation submitted to
Kent State University in partial
fulfillment of the requirements for the
degree of Doctor of Philosophy

by

Walaa M Alahmade

May, 2021

Dissertation written by

Walaa M Alahmade

B.S., Umm Al-Qura University, 2008

M.S., Kent State University, 2015

Ph.D., Kent State University, 2021

Approved by

______________________________, Chair, Doctoral Dissertation Committee
Dr. A. Mina T. Katramatou

______________________________, Member, Doctoral Dissertation Committee
Dr. Gerassimos G. Petratos

______________________________,
Dr. Spyridon Margetis

______________________________,
Dr. Michael N. Olson

______________________________,
Dr. Edgar Kooijman

______________________________, Member, Graduate Faculty Representative
Dr. Diane Stroup

Accepted by

______________________________, Chair, Department of Physics
Dr. James T. Gleeson

______________________________, Interim Dean, College of Arts and Sciences
Dr. Mandy Munro-Stasiuk

Table of Contents

List of Figures

List of Tables

Acknowledgments

At the beginning of my dissertation, it is a pleasure to thank everyone who gave me support, helped and made this dissertation possible.

Firstly, I'm sincerely and heartily thankful for my Ph.D advisor, Dr. Mina Katramatou, for her guidance and support throughout my time at Kent, whether research, writing, or life. I honestly cannot imagine a better advisor. Also, I would like to express my gratitude to Dr. Gerassimos Petratos, who was as co-advisor for my research. They both have provided me with time, assistance, valuable feedback, persistent encouragement and knowledge. I couldn't reach this point without their help and guidance. They worked hard with me to make this dissertation clear and understandable. I deeply feel grateful to work with them and have them in my life.

I would like to thank my dissertation committee members, Dr. Spyridon Margetis, Dr. Michael N. Olson, and Dr. Edgar Kooijman, and the graduate faculty representative, Dr. Diane Stroup, for their time, comments, and advices.

To my precious family, I would like to thank them for their endless support. My unlimited thank for my beloved husband, Ar. Ammar Alahmadi who walked with me each step of the way during this long journey to reach for our dreams and success. I would like to express my love and thank to my wonderful daughter Eyatt, who always sent me many notes and texts with a lot of hearts and emojis about how much she misses me and want to spend more time together, but she understands that I have work to do. Thank you, my little angel, for your motivation, patience, and understanding.

I would like to thank my mom, Hanan, and my father, Saleh, for being role models for me and my siblings. Thank you for your unconditional love and support. I would like also to thank my siblings: Rehab, Saffanah and Mohammed for being close to me despite the distances. Thank you to my grandmas, my parents and my siblings for their emotional support and prayers. To my big family, I thank you all.

Chapter 1

Electron Scattering

1.1 Introduction

Nuclear physics is the study of the fundamental structure that comprises the nucleus. Scattering experiments are considered a powerful tool of studies of nuclear and particle physics as they provide important information about the internal structure of the atomic nuclei and their nucleon constituents.

Initially, it was found that atoms have internal structure, composed of a positively charged nucleus surrounded by electron clouds, which interact through the electromagnetic force. As nuclear physics developed, in addition to the electromagnetic force, new short-range forces appeared to play a role in understanding the nuclear structure, the nuclear and weak forces. The weak force was primarily manifested in the nuclear β-decay. The nuclear force is a manifestation of what holds the nucleus together, and ultimately, as we understand it today, results from the strong force acting among quarks and gluons. Since nuclear physics was established, the main research goals have been to fully describe the nuclear structure, which requires understanding the interaction between nucleons and nuclei and how these interactions determine the nuclear properties.

In a typical scattering experiment, a beam of particles with well-known momentum or energy and angle, is directed towards a nuclear target under investigation. From the scattering process, we can learn about the properties and structure of the target and study the interaction force mediating the scattering by measuring the kinematical parameters of the final products of the scattering process [1].

1.2 A Short History Overview

The history of scattering experiments dates back to the early years of the twentieth century. In 1910, Rutherford's team performed what is often considered the first scattering experiment by aiming alpha particles at a thin gold foil. The team observed that a few particles were scattered at large angles, even entirely backward in some cases [2]. This remarkable result of the experiment indicated that the atom had a localized positive charge, which was not evenly distributed throughout the volume of the atom. This indication came a decade after J. J. Thomson discovered the electron in 1897 through the deflection of cathode rays [3]. In 1932, the neutron was discovered by James Chadwick. Over time, the discoveries boundary was pushed more as experiments probed deeper inside the atom using higher energy beams and building more powerful accelerators. These developments led to the findings of more clues on the nature and the structure of the nucleus.

In particular, lepton scattering by nuclei is considered pivotal in the uncovering of nuclear structure. In the 1950s, Hofstadter and his colleagues [4] at Stanford performed several elastic electron-nucleus scattering experiments to investigate the substructure of the nuclei, including hydrogen, and determine the nuclear radii. The Stanford experiments indicated that the proton and the neutron are not point-like particles but may have a sub-structure. These pioneering elastic scattering experiments led to the proposal to build the two-mile linear accelerator, the Stanford Linear Accelerator Center (SLAC). The early SLAC deep inelastic electron-nucleon scattering experiments were able to investigate the substructure of the nucleon (proton and neutron) using high-energy electron beams (up to 20 GeV) for elastic and inelastic scattering experiments. In the late 1960s, a series of experiments on deep inelastic scattering was performed [5] which led to the discovery of the presence of quarks inside the nucleon and validated the quark model of the nucleon as proposed by Gell-Mann [6] and Zweig [7] in the early 1960s. The leaders of the SLAC experiments were recognized with the 1990 Nobel award in Physics (J. Friedman, H. Kendall and R. Taylor).

1.3 Electron Scattering

Charged leptons, such as electrons and muons, provide a powerful tool for studying the internal structure and dynamics of nuclei and the nucleons that comprise them. They are well suited due to their point-like nature. Electron scattering became one of the most important tools to explore the nucleon and nuclear structure for many reasons. First, the electron-nucleus interaction is well described by quantum electrodynamics (QED). Moreover, the structureless nature of electrons allows them to probe the entire nucleus. The wavelength of the virtual photon exchanged in the scattering defines the electron probe's resolution; a smaller wavelength (larger momentum transfer to the nucleus) corresponds to higher resolution. In a simple way, the scattering process can be considered as the process of taking a photograph. To create a picture with high spatial resolution, a structureless and fast projectile such as an electron must be used instead of low energy particles with structure. The only disadvantage of electron scattering is the small cross section involved, which requires a high-intensity electron beam and thick targets. Fortunately, advancements in accelerator technologies have provided for electrons with much higher beam energy and for beams of high intensity (high current).

The electron scattering processes can be described in terms of Lorentz invariant quantities. At the Born one-photon exchange approximation level, which is shown in Figure 1.2, an electron scatters from a nucleus of mass M by exchanging a virtual photon. The invariant mass squared of the final hadronic system of the interaction is given by:

$$W^2 = (p+q)^2 = M^2 + q^2 + 2p \cdot q = M^2 + q^2 + 2M\nu \tag{1.1}$$

where ν is the energy transfer from the electron to the nucleus, q is the square of the four-momentum transfer carried by the virtual photon, and p is the four-momentum of the initial nuclear target. The spectrum of inclusive (where only scattered electrons are detected) electron-nucleus cross section is shown as a function of transferred energy ν in Figure 1.1. Different kinematic regions of electron scattering can be explored, which are sensitive to different electron-nuclear physics mechanisms.

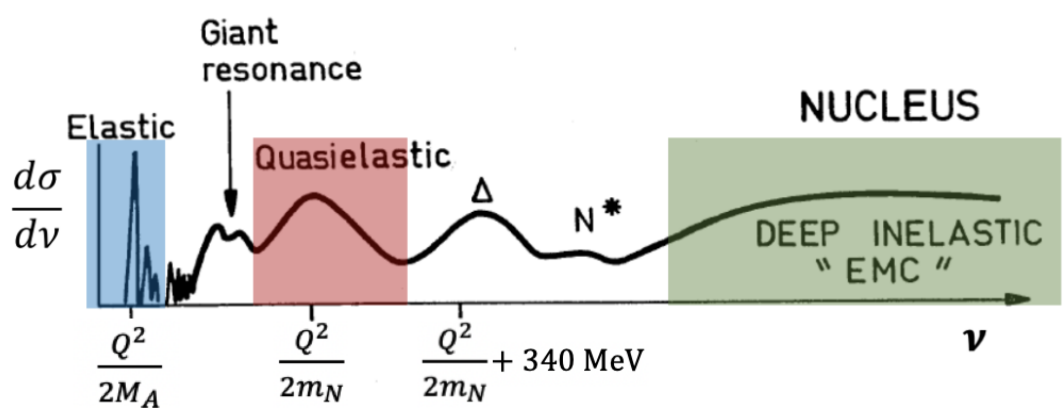

Figure 1.1: Schematic shape of electron-nucleus cross sections as a function of the energy transfer ν showing the regions of scattering.

Elastic scattering (ES) occurs when the incoming electron scatters off of the nucleus with a minimal energy transfer. The interaction takes place with the entire nucleus, leaving it intact and in its ground state (lowest energy state) after the interaction. In ES, the wavelength of the exchanged photon is typically greater than the radius of the nucleus, which appears as a point, and the electron is sensitive to the size of the nucleus. The final hadronic state for elastic scattering is defined by $W^2 = M^2$. Elastic scattering is used to study the nucleus via the extraction of form factors, from measured cross sections. Form factors determine the charge and magnetization distributions of the nucleus, as well as, the associated root-mean-square (rms) radii.

In the Quasielastic scattering (QES) regime, the electron interacts with the nucleus by transferring to it a larger energy as compared to elastic scattering. The exchanged photon accesses more of the internal structure of the nucleus as its wavelength decreases. A single nucleon is knocked free from the nucleus after absorbing the virtual photon. Quasielastic scattering can be considered as an elastic scattering from an individual nucleon in motion inside the nucleus, and the scattering is sensitive to the form factors of the nucleon. QES is used to study such things as the momentum distribution of the nucleons inside the nucleus.

As the wavelength of the photon decreases and momentum and energy transfer increase more, resonance scattering occurs. In this case, the knocked off nucleon is excited to a higher energy state and quickly decays back into a lower state by emitting the excess energy as an additional particle such as a pion.

At even higher momentum and energy transfer, we enter the Deep Inelastic Scattering (DIS) region. The electron can interact directly with the internal constituents of the nucleon by scattering from a single quark in a nucleon, in a process where the nucleon breaks apart. In the DIS regime kinematic, the electron provides the opportunity to study the quark momentum distribution functions and their modification inside the nucleus [1, 8, 9].

Experiment E04-018 aim was to measure and study the charge and magnetic form factors of ^{3}He and the charge form factor of ^{4}He at large squared four-momentum transfers, $Q^2 \equiv -q^2$, values up of 3.2 (GeV/c)^2. The experiment preformed elastic electron scattering for this study. The remainder of this chapter will be focused on the ES kinematics and cross section and what we can learn from this type of scattering.

1.4 Elastic Scattering Kinematics

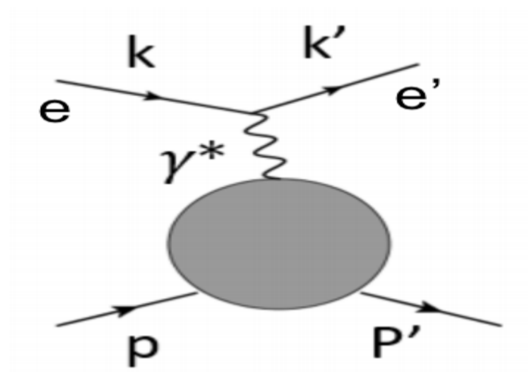

Figure 1.2: Feynman Diagram for elastic electron-nucleus process in the one-photon-exchange approximation. The symbols k and P denote particle four-momenta.

The Feynman diagram for elastic electron-nucleus scattering, in the one-photon-exchange approximation, is shown in Figure 1.2, where $k = (E, \vec{k})$ and $k' = (E', \vec{k})$ are the four-momenta of the incident and scattered electron respectively, with E and E' the incident and scattered electron energy, respectively. The virtual photon, γ^*, has a four-momentum of $q = (\nu, \vec{q})$. The four momenta of the target and recoil nucleus are $P = (E_t, \vec{P_t})$ and $P' = (E_r, \vec{P_r})$, respectively. Using Lorentz-invariant quantities, the squared four momentum transfer and squared invariant mass of the final hadronic state are given by:

$$q^2 = -Q^2 = (k - k')^2 \ , \ W^2 = (P + \nu)^2 \tag{1.2}$$

In the laboratory reference frame, where the target is at rest $P = (M, 0)$, and neglecting the mass of the electron, we obtain:

$$Q^2 = 4EE^{'} \sin^2 \frac{\Theta_e}{2} = 2M\nu \tag{1.3}$$

$$W^2 = M^2 - Q^2 + 2M\nu \tag{1.4}$$

Here, Θ_e is the electron scattering angle, M is the mass of the target nucleus, and ν is the energy transferred of the virtual photon, $\nu = E - E'$. The energy E' of the scattered electron is given in terms of E and Θ_e as:

$$E^{'} = \frac{E}{1 + \frac{E}{M}(1 - \cos\Theta_e)} \tag{1.5}$$

The momentum of the recoil nucleus P_r equals to:

$$P_r = \sqrt{2M(E - E^{'}) + (E - E^{'})^2} \tag{1.6}$$

The recoil nucleus angle Θ_r is given by:

$$\Theta_r = \cos^{-1}\left(\frac{EE_r - E^{'}M}{EP_r}\right) \tag{1.7}$$

where E_r is the energy of the recoil nucleus.

Similarly, for a non stationary target ($\vec{P}_t \neq 0$) with $P = (E_t, \vec{P}_t)$, the above physical quantities can be expressed as:

$$E' = \frac{E(E_t - P_t \cos\Theta_t)}{E_t - P_t \cos(\Theta_t - \Theta_e) + E(1 - \cos\Theta_e)} \tag{1.8}$$

$$P_r^2 = (E - E')^2 + E_t^2 - M^2 + 2E_t(E - E') \tag{1.9}$$

$$\cos\Theta_r = \frac{EE_r - E'(E_t - P_t\cos(\Theta_t - \Theta_e))}{EP_r} \tag{1.10}$$

where E_t, P_t and Θ_t are the energy, momentum and angle of the moving target nucleus.

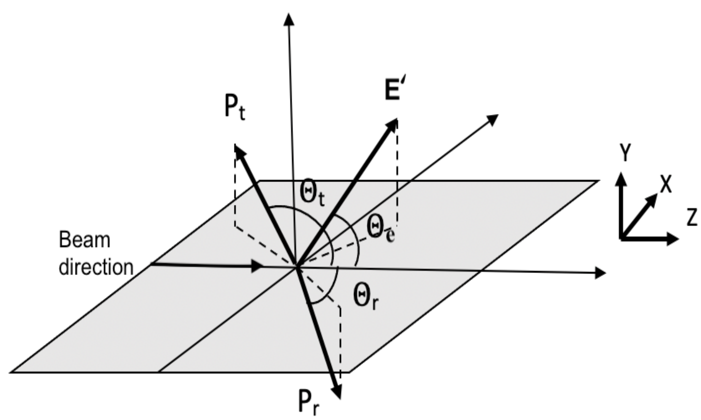

Figure 1.3: Electron-nucleus elastic scattering diagram for a moving nucleus. Shown are the momenta and angles for the target, the scattered electron, and the recoil nucleus.

1.5 Elastic Scattering Cross Section and Form Factors

The cross section formula for Rutherford scattering is given for the relativistic case as:

$$\frac{d\sigma}{d\Omega} = \frac{(Z\alpha)^2}{4E^2\sin^4\left(\frac{\Theta_e}{2}\right)} \tag{1.11}$$

For elastic scattering, as shown in Figure 1.2, the cross section for a relativistic electron and a point-like (structureless) target is, as computed by Mott [1]:

$$\left(\frac{d\sigma}{d\Omega}\right)_{NS} = \frac{(Z\alpha)^2 E' \cos^2\left(\frac{\Theta_e}{2}\right)}{4E^3 \sin^4\left(\frac{\Theta_e}{2}\right)} \tag{1.12}$$

with Z being the nuclear charge and $\alpha = 1/137$ the fine-structure constant (NS stands for "No Structure").

The cross section for elastic scattering of an (unpolarized) electron from the spin 1/2 ^{3}He nucleus is given, in the one-photon exchange approximation, by the Rosenbluth formula [11]:

$$\frac{d\sigma}{d\Omega}(E, \Theta_e) = \left(\frac{d\sigma}{d\Omega}\right)_{NS} \left[A(Q^2) + B(Q^2)\tan^2\left(\frac{\Theta_e}{2}\right)\right] \tag{1.13}$$

where the elastic structure function $A(Q^2)$ and $B(Q^2)$ quantities can be expressed in terms of the charge $F_C(Q^2)$ and magnetic $F_M(Q^2)$ form factors of ^{3}He as:

$$A(Q^2) = \frac{F_C^2(Q^2) + \mu^2 \tau F_M^2(Q^2)}{1+\tau} \tag{1.14}$$

$$B(Q^2) = 2\tau\mu^2 F_M^2(Q^2) \tag{1.15}$$

with μ being the magnetic moment of the target nucleus, and $\tau = Q^2/4M^2$.

For the spinless ^{4}He nucleus, the cross section for elastic scattering of a relativistic electron, has a contribution only from the charge form factor, and is given by [10]:

$$\frac{d\sigma}{d\Omega}(E, \Theta_e) = \left(\frac{d\sigma}{d\Omega}\right)_{NS} F_C^2(Q^2) \tag{1.16}$$

Figures 1.4, 1.5 and 1.6 show the $F_C(Q^2)$ and $F_M(Q^2)$ of ^{3}He and $F_C(Q^2)$ of ^{4}He from JLab experiment, E04-018, with selected previous world data.

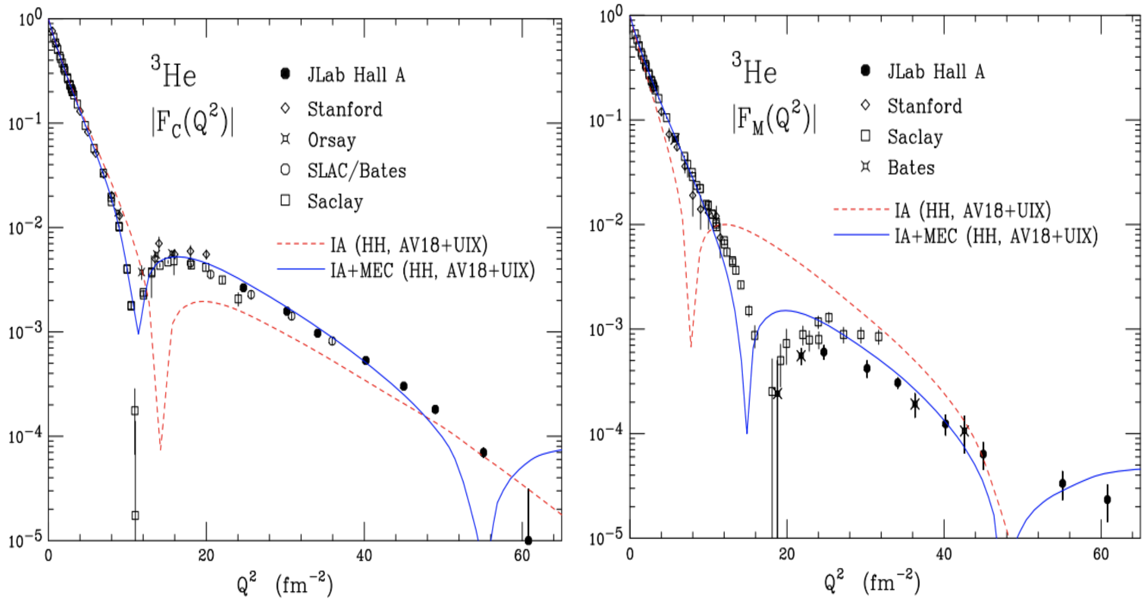

Figure 1.4: Absolute values of the ^{3}He charge F_C and magnetic F_M form factors, as determined from JLab Experiment E04-018. Also shown are selected previous world data and various theoretical calculations [11].

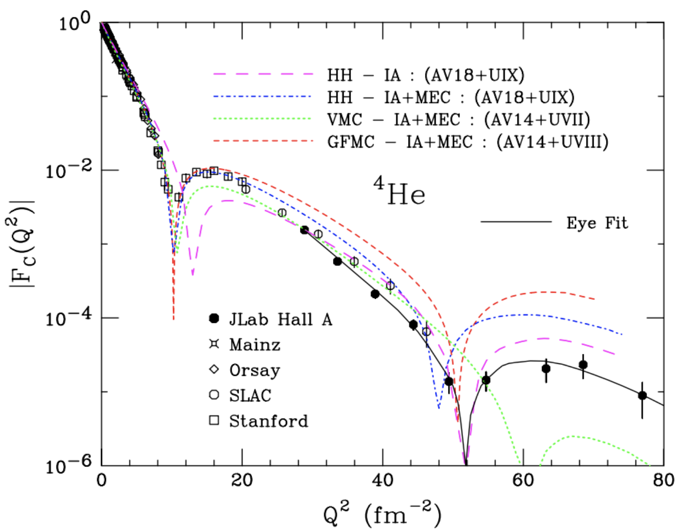

Figure 1.5: Absolute values of the ^{4}He charge F_C form factor, as determined from JLab Experiment E04-018. Also shown are selected previous world data and various theoretical calculations [10].

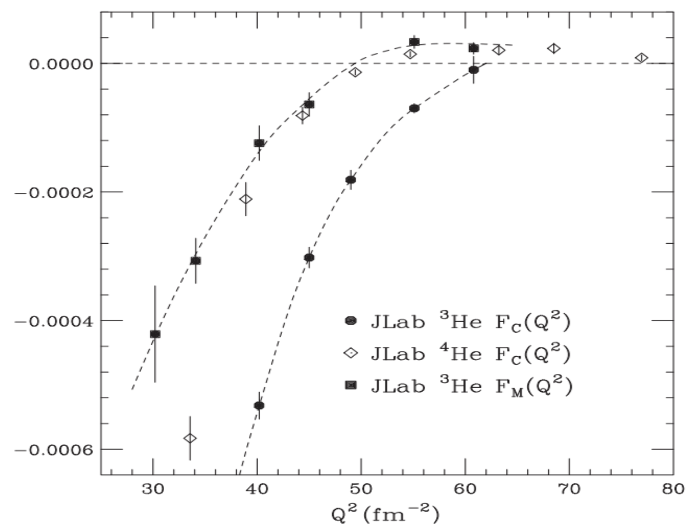

Figure 1.6: Algebraic values of ^{3}He and ^{4}He elastic form factors over a selected Q^2 range [11].

Chapter 2

Theoretical Overview

2.1 Introduction

The subject of Clustering is an interesting phenomenon of many-body dynamics that appears in many areas of science. The nature of clustering on different scales and subjects is very intriguing. On a macroscopic scale, galaxy clusters are formed by mutual gravitational bonds between hundreds or thousands of galaxies, which are several millions of light-years across, creating a splendid collective motion in the universe. In Biology, on a microscopic scale, the cluster of a micro-organism "colony" is the formation of visible micro-organisms on a surface composed of conspecific individuals. In Chemistry, clusters are formed by aggregating atomic or molecular units into atomic or molecular clusters [12].

In nuclear physics, clusters are formed from protons and neutrons. A nucleus can be considered as an assembly of clusters or subunits. The formation of clustering enhances the binding energy of the system. However, clusters are more challenging in nuclear physics due to the complicated nuclear binding effects of the particles (nucleons) involved. The cluster structure emerges from a delicate balance among the nucleon-nucleon forces (repulsive short-range, and attractive medium-range and long-range), Coulomb repulsion among protons, and the Pauli exclusion principle fulfillment.

2.2 Overview

Clustering is one of the most intriguing phenomena in nuclear interaction processes as well as in nuclear structure. This phenomenon has been observed not only in stable light and heavy nuclei, but also in short-lived, radioactive nuclei. The study of nuclear clustering began with Rutherford's discovery of alpha radiation in 1899 [23] and continued with many observations of the emission of α particles (^{4}He nuclei) from heavy nuclei, and many other nuclear reactions, which have supported the notion of the cluster nature of nuclei. About a century later, heavier cluster radioactivity like in ^{14}C, ^{24}Ne, etc. was predicted by Sandulescu *et al.* [13] in their pioneering work in 1980, which has been observed experimentally by Rose and Jones (1984) in ^{14}C radioactivity of ^{223}Ra [14]. Other clusters with the character of tritons (^{3}H) and helions (^{3}He) have also been considered and will be further discussed.

2.3 Cluster Models

The concept of cluster models has a history of more than 50 years in the progress of understanding the physical mechanisms behind various cluster phenomena. It is actually one of the oldest models of the nucleus which was developed even before the discovery of the neutron in 1932 [15]. In general, the cluster models are based on the assumption that nuclei can be thought of as aggregates of small "clusters" of nucleons besides protons and neutrons. The most well known and understood cluster example is composed of two protons and two neutrons (the α-particle). Clustering and, in particular, α-particle clustering has already been studied for quite a long time, but the mechanism of cluster formation has not yet been fully understood. However, despite various cluster models' successes, not one of them can be considered as a general model. To cover all these models is beyond the scope of this thesis; however, a short summary of some of these different models will be discussed next.

Alpha-particle models

The alpha-particle model, one of the oldest cluster models of the nucleus, was developed by G. Gamow (1928) [16, 24] before the discovery of the neutron. The model was based on the assumption that nuclei were composed of α-particles, protons and electrons. Models of this kind have been popular since Gamow's original studies. In 1938, after the discovery of the neutron, Hafstad and Teller [17] proposed a cluster model describing the possible structures of $Z = N$ nuclei as constructed from α-particles. The α-particles are arranged in a $4n$ nucleus (n integer number), like ^{8}Be and ^{12}C, in a close-packed structure interacting with nearest neighbors [21]. Following along the same lines, Dennison (1940) proposed [18] a model of ^{16}C as a team of 4 alphas arranged at the corners of a regular tetrahedron. In this structure, energy levels were due to the rotation-vibration interactions of the 4 alphas.

Later on, Ikeda *et al.* (1968) suggested [19] possible subunit clusters that can appear within $N = Z$ nuclei. By increasing the excitation energies, different cluster structures can be formed around threshold energies. The $n\alpha$ structure models (for example in ^{16}O) are typically not found in ground states, but are observed as excited states close to the decay thresholds, with an exception for ^{8}B which can decay into two α particles in the ground state. The Ikeda diagram, which is shown in Figure 2.1, proved to be powerful in identifying situations where cluster structure can be observed [12].

By the 1960s, Ali and Bodmer [21] made a detailed study and obtained many good interaction potentials which fitted well experimental data on alpha-alpha scattering.

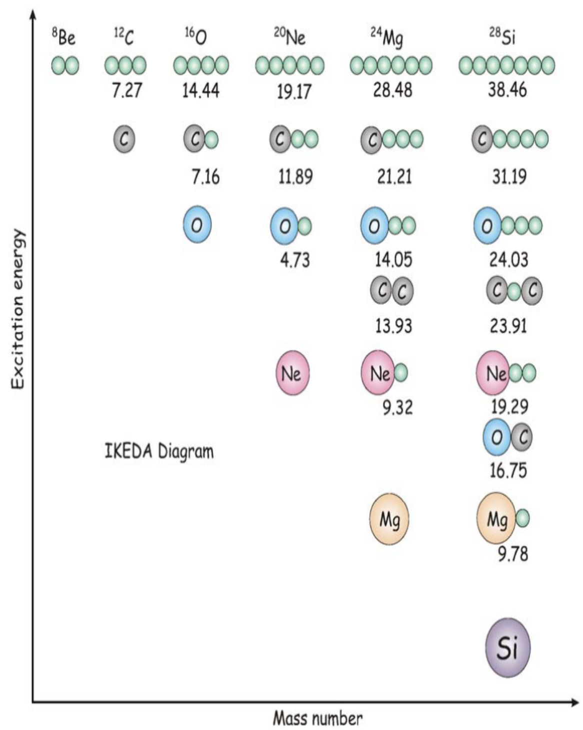

Figure 2.1: The Ikeda threshold diagram for nuclei with α-clustering. Cluster structures are predicted to appear close to the associated decay thresholds. The threshold energies for the breakup of clusters in MeV are also shown [12].

The potentials had a repulsive part V_{0l}, which depends on the angular momentum l, and an attractive part with a constant strength V_l [20]:

$$V(r) = V_{0l}\ exp(r^2/a^2)\ - V_l\ exp(r^2/a^2) \tag{2.1}$$

where r is the distance between the alpha particles, and a is constant.

Resonating Group Model

The Resonating Group Method (RGM) is one of most powerful traditional microscopic cluster models and the first for dealing with the relative motion of clusters in nuclei. It was introduced by Wheeler (1937) [22] after the discovery of the neutron to describe α-clusters and other cluster groupings within nuclei while maintaining fermionic quantum statistics for the nucleons [23]. In RGM, neutrons and protons are divided into various clusters (such as alpha particles), which are continually being broken up and reformed in various ways due to the anti-symmetrization effect. As for N nucleons divided into a two-cluster system, the RGM wave function can be written as [21]:

$$\Psi = A[\phi_1(r_1, ..., r_m)\phi_2(r_{m+1}, ..., r_N)\ \chi(R_1 - R_2)] \tag{2.2}$$

Here, the vectors R_1 and R_2 are the centre of mass of the nucleons in the first and second clusters and $\chi(R_1 - R_2)$ is the relative wave function of two clusters. A is the anti-symmetrization operator that exchanges the nucleons of two clusters, and $\phi_1(r_1, ..., r_m)$ and $\phi_2(r_{m+1}, ..., r_N)$ are the wave functions of the nucleons in the first and second cluster, respectively. In 1977, RGM was successfully used by Kamimura *et al.* in their seminal work to explain the cluster structure of ^{12}C [24].

Generator Coordinate Model

The Generator Coordinate Model (GCM) is another general and more popular microscopic cluster model (Brink cluster model) [12] for constructing wave functions for cluster nuclei. As in RGM, the anti-symmetrization of all nucleons composing clusters are fully taken into account. The GCM wave function is based on the Brink wave function of n-cluster (called the Bloch-Brink cluster wave function) and takes the form [12]:

$$\Phi^B(R_1, ..., R_n) = n_0 A[\psi_{c1}(R_1)\psi_{c2}(R_2).....\psi_{cn}(R_n)] \tag{2.3}$$

Here, $\psi_{ci}(R_i)$ represents the i^{th} cluster wave function with the generator coordinate R_i where the i^{th} cluster is located, n_0 is a normalization constant, and A is the anti-symmetrization operator that exchanges the nucleons of different clusters. The Brink wave function is a perfect Slater determinant [12], which uses a certain developed matrix technique. This is the reason why the Brink wave function can be widely used in nuclear cluster physics. In fact, the GCM wave function is much richer than the single Brink one, and can be written as a linear combination of Brink wave functions. The general GCM-Brink wave function can be written as [12]:

$$\Phi^B_{GCM} = \int dR \; f(R) \; \Phi^B(R) \tag{2.4}$$

where R is the generator coordinate, and $f(R)$ is the weight function which can be determined from a variational Monte Carlo calculation [24]. The GCM was used by Uegaki *et al.* [24] for the calculation of cluster states in ^{12}C about the same time as Kamimura *et al.* with great success.

In general, in recent years, there has been considerable transition and renewed interest in the structure of α-cluster nuclei applying different models. A review of cluster models up to 2006 can be found in Reference [15]. The most recent advances in cluster models can be investigated further in References [24, 23].

2.4 Direct Possible Experimental Evidence of ^{3}He Clustering in Light Nuclei

Clusters in nuclei have been studied for quite a long time. Evidence for nucleon clustering deep inside the nucleus comes from the many observations of α-particle emission or knockout from nuclei. As mentioned before, a large number of experimental and theoretical papers have been published on the subject of α-cluster phenomena in atomic nuclei. On the other hand, ^{3}He and ^{3}H cluster formation in light nuclei are still puzzling due to the conflict with the requirement of the Pauli Exclusion principle.

But still, one of the most direct ways to confirm the presence of clustering within atomic nuclei is via the direct knockout of particle clusters using high energy projectiles. A clear existence of helion (h) and triton (t) clusters can be shown through experimental studies similar to those that undoubtedly show α-clustering. In simple words, if ^{3}He or ^{3}H have been removed by knockout, this process leaves the residual nucleus in a state of low excitation or even in the ground state. This situation is impossible if the initial nucleus is composed of single particle orbitals of shell model. However, this can be possible if these clusters have been already preexisting in the nucleus. Moreover, over the past 40 plus years, several experimental results point to evidence of ^{3}He and ^{3}H clustering occurring throughout the interior of the nucleus [27, 26].

Artun *et al.* [28] bombarded several targets of light and medium-mass nuclei (N, O, P, S, V, Al, Si, Ca, and Fe) with protons of beam energy ranging from 150 to 960 MeV. A prompt spectrum of γ rays was measured which provided information of multi-nucleon, t, h and α removal from these nuclei while the residual nucleus was left in low excited states. Their conclusion, *"Qualitatively these results suggest a breaking of an excited system via the weakest bonds between groups of strongly bound nucleons"*, provided strong support to the notion that t, h, and α do exist as single entities in nuclei, and that a direct interaction process knocked them out. The probability for this assumption to be valid would be extremely low in the shell model. It is puzzling as to how a low binding energy ($\sim$ 8 MeV) ^{3}He and ^{3}H could have been knocked out as a single block. Their only conclusion was to accept the fact that these clusters were already preexisting inside the nuclei.

Poskanzer *et al.* [29] bombarded Ag and U targets with 2.7 GeV protons, 1.05 GeV/nucleon α particles and ^{16}O ions, and measured the energy spectra and angular distributions of ^{3}He and ^{4}He emitted fragments. They observed a clear separation of ^{3}He and ^{4}He branches in their plots, and they discerned that all cross sections increase dramatically with projectile mass. In the last paragraph of their paper they summarized *" Our data present evidence for the non-evaporative emission of* ^{3}He *and, to a somewhat lesser extent,* ^{4}He *products in collisions between relativistic heavy ions. The cross sections for these high-energy products are two to three orders of magnitude higher than those found for proton-induced reactions at comparable incident velocity"*, meaning that their data provide a clear evidence of preexisting of ^{3}He clusters inside these nuclei.

Recently, H. Akimune *et al.* [30] investigated the tri-nucleon cluster structure at high-excitation energies in $A = 6$ Nuclei, ^{6}He and ^{6}Be, by using ^{6}Li(^{7}Li, ^{7}Be)^{6}He and ^{6}Li(^{3}He, ^{3}H)^{6}B reaction at 455 and 450 MeV, respectively. Binary decays into ^{3}He in ^{6}Be and ^{3}H in ^{6}He were observed from a broad state at excitation energy $E_x = 18.0$ MeV, by measuring tri-nucleon cluster decays in coincidence with other reaction particles. The branching ratios for tri-nucleon decay from the experiment were estimated to be 0.7 for both ^{6}He and ^{6}Be. They concluded that the explanation of this large branching ratio was that a tri-nucleon cluster state existed as an isobaric partner in ^{6}He and ^{6}Be, and that was a clear evidence of ^{3}He clustered inside nuclei.

Another important experiment and first of its kind [26] by S. Ohkubo and Y. Hirabayashi [31] has provided evidence of the existence of an excitation mode of intercluster relative motion, higher nodal band state, with ^{3}He cluster structure in ^{19}Ne by studying ^{3}He $+^{16}$O scattering with a wide range of incident energies which enhances the importance of the concept of ^{3}He clustering in nuclei. In their conclusion, they state *"The present findings about the higher nodal band states with the* ^{3}He *cluster* *in* ^{19}Ne *in addition to the higher nodal states with the* α *cluster structure in the* ^{20}Ne, ^{40}Ca, *and* ^{44}Ti *nuclei and the higher nodal states with the* ^{16}O *cluster structure in the* ^{32}S *nucleus reinforce the importance of the concept of the higher nodal state and the* ^{3}He *cluster in nuclei"*, which also support the concept that ^{3}He clusters are well-formed in nuclei.

Cunsolo *et al.* [33] measured the energy spectra and angular distributions of tritons from the ^{14}C(^{6}Li, t)^{17}O reaction. The observed selectivity in the tritons spectra and the forward peaked angular distribution suggested a predominantly direct reaction mechanism. Also, they demonstrated ^{3}He+^{14}C clustering in the ^{17}O nucleus and confirmed a dominant direct ^{3}He transfer in this reaction.

The cluster quasielastic knockout reaction from light nuclei by various projectiles remains an active area of experimental and theoretical research to study the structure of clusters and nuclei, especially in electron-nucleon quasielastic scattering. The ^{6}Li nucleus has long been considered to be an ideal target to study the cluster model of light nuclei, as theoretical investigation have shown that $\alpha + d$ cluster configuration in ^{6}Li has a high probability via one-step reaction. Also, an additional cluster configuration of (^{3}He+^{3}H) has been suggested because the total photoneutron plus photoproton cross section for ^{6}Li appeared to be strikingly like the photodisintegration cross sections for ^{3}He and ^{3}H [32].

J. P. Connelly *et al.* [32] measured the momentum-transfer dependence of trinucleon cluster knockout reactions from ^{6}Li via the mirror ^{6}Li(e,e$'$ ^{3}He)^{3}H and ^{6}Li(e,e$'$ ^{3}H)^{3}He reactions. This well known experiment was performed at the NIKHEF electron accelerator in the Netherlands. The experimenters noticed that the momentum-transfer dependence of the measured ^{3}He knockout cross section is in good agreement with a simple tri-nucleon knockout mechanism. This was good evidence of the existence of tri-nucleon cluster in ^{6}Li. Furthermore, they compared their data with ^{4}He(e,e$'$ ^{3}He)n and ^{4}He(e,e$'$ ^{3}H)p data as seen in Figure 2.2. The general similarity suggested the existence of ^{3}He and ^{3}H as clusters in ^{4}He .

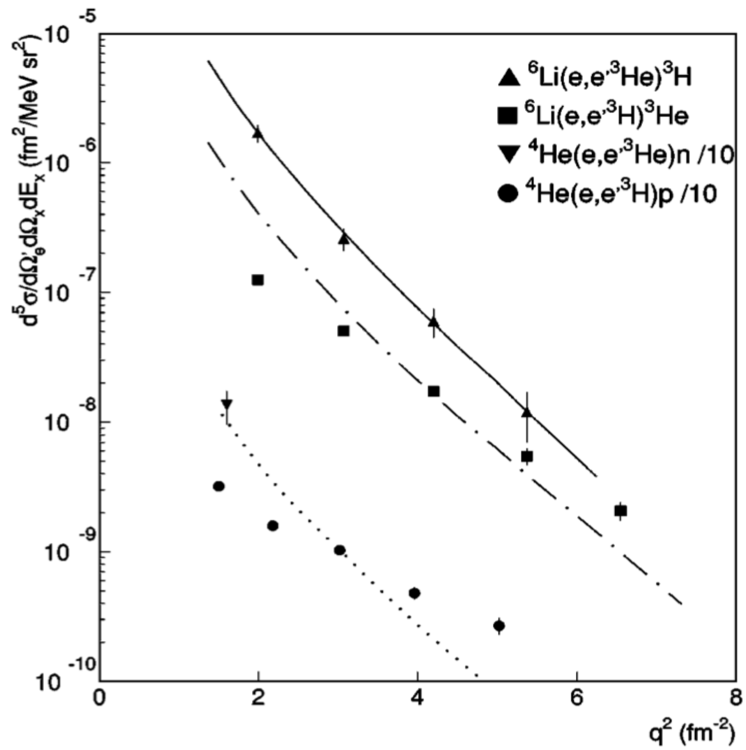

Figure 2.2: Momentum-transfer dependence of the fivefold cross sections for the ^{6}Li(e,e$'$ ^{3}He) ^{3}H, ^{6}Li(e,e$'$ ^{3}H) ^{3}He, ^{4}He(e,e$'$ ^{3}H)p and ^{4}He(e,e$'$ ^{3}He)n reactions. The curves are calculations assuming a direct cluster knockout mechanism, normalized to a data point at intermediate momentum transfer. Note that the data for the latter two reactions have been rescaled by a factor of 1/10. Curves are calculations assuming a direct cluster-knockout mechanism, normalized to a data point at intermediate momentum transfer. Since only one data point is available for the ^{4}He(e,e$'$ ^{3}He)n reaction, no curve has been added for this case [32].

The aforesaid suggests that the only way to understand the above results is to consider that the ^{3}He cluster possibles preexist inside these nuclei. Both Mac Gregor [27] and S. Abbas and S. Ahmad [26] have referred to experiments that provide substantial evidence of preexisting tri-nucleon clusters besides α-clusters in nuclei.

One can also consider ^{3}He clusters as basic as ^{4}He clusters, assuming that ^{4}He itself has a sub-cluster structure $^4\text{He} = {}^3\text{He} + n$, as strongly argued by the authors of Reference [26].

2.5 Nusospin Symmetry Group in Nuclei - $SU(2)_A$

Proton and neutron are fermions with spin 1/2, have nearly equal masses, and play similar roles in nuclear interactions. This can be seen in the study of Mirror nuclei, where the number of protons in one nuclide is equal to the number of neutrons in the other or vice versa. Because of their similarity, the proton and neutron are considered as two states of the same particle, the Nucleon N. In analogy to a particle with spin 1/2 and projection $S_3 = \pm 1/2$, a new quantum number is assigned to the nucleon in order to describe the symmetry between protons and neutrons. The new quantum number is called Isospin I with projection $I_3 = \pm 1/2$. The two basic states of nucleon can be written as [34]:

$$|1/2, +1/2\rangle = \begin{pmatrix} 1 \\ 0 \end{pmatrix} \equiv |p\rangle \quad \text{proton} \tag{2.5}$$

$$|1/2, -1/2\rangle = \begin{pmatrix} 0 \\ 1 \end{pmatrix} \equiv |p\rangle \quad \text{neutron} \tag{2.6}$$

Hence, the symmetry of the (p,n) pair can be described as a fundamental representation of $SU(2)_I$ (spin, isospin). The treatment of the NN configuration analog of the spin's singlet and triplet states is leading to the following [34]:

$$\begin{aligned}
|I=0, I_3=0\rangle &\equiv 1/\sqrt{2}\ (|pn\rangle - |np\rangle) \\
|I=1, I_3=-1\rangle &\equiv |nn\rangle \\
|I=1, I_3=0\rangle &\equiv 1/\sqrt{2}\ (|pn\rangle + |np\rangle) \\
|I=1, I_3=1\rangle &\equiv |pp\rangle
\end{aligned} \tag{2.7}$$

In a similar fashion to the (p, n) pair providing fundamental representation of the isospin group $SU(2)_I$, a new symmetry group, proposed by Abbas [35], hypothesized that ^{3}He and ^{3}H as a pair of (h, t) provide a fundamental representation of $SU(2)$. To avoid confusion, the new symmetry group was named nusospin group $SU(2)_A$. Abbas argues that the nusospin group is supported by a large number of empirical evidences favoring $A = 3$ clustering in nuclei [27, 26], a few of which were mentioned earlier.

Moreover, the idea of treating the tri-nucleon systems as elementary entities is not new. The Elementary Particle Model (EPM) [36], first developed by Kim and Primakoff for muon capture mechanism in 1965, treated ^{3}He and ^{3}H nuclei as elementary particles (as for p and n). The EPM is a phenomenological approach using empirical information based on experimental data from electron scattering and beta decay to evaluate and describe the capture process [37]. The EPM became an Effective Field Theory which successfully explained the weak charge-changing processes in nuclei and was as successful as those models obtained from nuclear microscopic models using two and three body forces [38]. Both, the empirical evidences favoring $A = 3$ clustering in nuclei and the EPM model in particle physics provide a justification for the treatment of the (h,t) pair as a fundamental entity, and support the $SU(2)_A$ nusospin group.

In analogy to the isospin symmetry between p and n, the h and t are treated as elementary isospin 1/2 entities. Hence [39]:

$$
\begin{aligned}
(S=1, T=0) &\equiv (p-n) &&\equiv (h-t)\\
(S=0, T=0) &\equiv (p-n) &&\equiv (h-t)\\
(S=0, T=1) &\equiv (p-p) &&\equiv (h-h)\\
(S=0, T=1) &\equiv (n-n) &&\equiv (t-t)
\end{aligned}
$$

2.6 ^{3}He and ^{4}He Clustering

Tri-nucleon clusters, such as ^{3}He, are fermions with a neutron and two protons with spin 1/2 and binding energy of $\sim$ 8 MeV. On the other hand, ^{4}He clusters are formed by two protons and two neutrons, being bosons with total spin 0 and large binding energy of 28 MeV. Therefore, nuclei with tri-nucleon clusters have a very different structure than those with α-clusters. The high probability of creating α-clusters in nuclei is due to its high symmetry and binding energy [40]. Considering only such requirements in the formation of clusters limits the creation of tri-nucleon in the nuclei. However, it appears that results of early experiments support the notion of preexistence of tri-nucleon clusters inside some nuclei and favor $A = 3$ clustering in others. Thus, one may conclude that the cluster formation is due to not only the symmetry and binding energy but also to other characteristics [26], as will be discussed below.

In order to understand the formation of an $A = 3$ cluster in ^{4}He, some critical features must be considered in comparisons among the three nuclei. Both ^{3}He, ^{3}H are compact nuclei with a unique density distribution, as is the case for ^{4}He. It can be seen from Figure 2.3 that the central charge densities of ^{4}He and ^{3}He are extraordinarily high as compared that of other medium-size nuclei [43]. Also, ^{3}He and ^{3}H have similar binding energy and charge densities [45]. This similarity in the

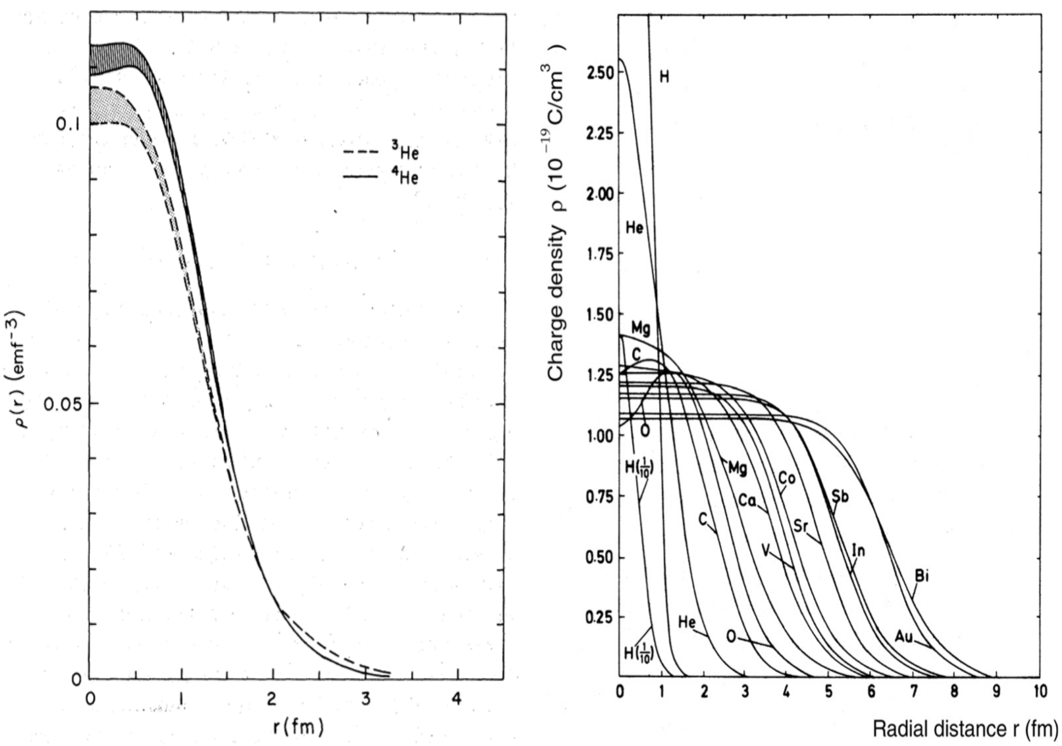

Figure 2.3: Charge density distributions of ^{4}He and other medium and heavier nuclei: (left plot) The density distributions of ^{3}He and ^{4}He [42]. (right plot) The density distributions of ^{4}He, ^{3}H and other nuclei by electron-scattering methods, redrawn for clarity in Reference [41] from Hofstadter's seminal paper [43].

density between t, h and α and their differences with other nuclei indicate that these nuclei must be treated on the same footing as ^{4}He and differently from other nuclei.

Another remarkable property of ^{4}He is the pronounced depression in the central charge density, called "hole". Both t and h appear to have a hole at the center too and can be explained using the quark model [45]. In QCD, when two nucleons approach each other, the two 3-quark systems start to significantly overlap as the relative distance between them goes to zero, and then the so called hidden colour configuration manifests itself [44]. The NN system must work against colour forces at short relative distances, which induce colour repulsion, creating a hole at the center. The ^{3}H and ^{3}He nuclei with nine-quark configurations and ^{4}He with 12-quark configurations, have sizes of 1.70 fm, 1.88 fm and 1.67 fm, respectively. In the same manner as for the NN system, where the nucleon has a size of approximately of $\leq$1 fm, a hidden colour mechanism dominates. The center of ^{3}He and ^{4}He nuclei, $3N$ and $4N$ systems, would strongly overlap. The calculation of the hidden colour components for 9- and 12-quark systems were determined to be 97.6% and 99.8%, respectively [45]. As a result of the predominantly hidden colour, an effective repulsion at the center keeps the three or four nucleons away from the center and creates a hole.

The above consideration enhances the notion that t, h and α are very different from all other nuclei, and this led Abbas and Ahmad to conclude that *"The primary reason for the formations of clusters of $A = 3$ and $A = 4$ nuclei is due to their unique and identical density distributions. It also shows why no other nucleus may form good cluster substructures in nuclei. None have such high and hole-like density profiles"* [26].

2.7 A Model for the ^{4}He System

As mentioned above, ^{4}He consists of 4 nucleons $(4N) = (2p + 2n)$ with unique properties (high binding energy, degree of symmetry and density). The ^{4}He system can have several cluster configurations, such as:

- $N + N + N + N$ configuration in form of $n + n + p + p$
- $2N + 2N$ configuration in the form of $d + d$
- $3N + 1N$ configuration in the form of $n + h$ or $p + t$

plus the possible pseudo-inelastic configurations involving pseudo-excitations of the deuteron d^* in the form of ($d^* + d$, $d^* + d^*$, $d^{**} + d$, $d^{**} + d^*$, and $d^{**} + d^{**}$) to take into account the specific distortion effect of the deuteron. This arises from the attractive forces in NN system interaction [48] due to the overlap of wave functions of two NN systems. Using the microscopic cluster model in terms of RGM [46], as briefly described in Section 2.3, the binding energy of the ground state 0_1^+ and the first excited state 0_2^+ of the ^{4}He nucleus have been examined using different cluster configurations [46]. The Table in Figure 2.4 shows the results calculated for theses states with the above basis configurations. (For more configurations see Reference [46]). Looking at

Configuration	0_1^+ state (MeV)	0_2^+ state (MeV)
$p+{}^3$H, $n+{}^3$He	−25.17	−5.10
$p+{}^3$H, $n+{}^3$He, $d+d$	−26.03	−5.98
$p+{}^3$H, $n+{}^3$He, $d+d$ d^*+d, d^*+d^*	−26.28	−6.10
$d+d$	−19.21	−3.22
$d+d$, d^*+d, d^*+d^*	−21.90	−3.68
Full calculation	−26.50	−6.43
Experiment	−28.3	−8.3

Figure 2.4: Comparison of the calculated binding energies for the ground 0_1^+ and first excited 0_2^+ states in ^{4}He as obtained in different cluster model spaces [47].

the Table of Figure 2.4 one can observe several interesting facts. Contrary to a widely used picture, the ground state and the excited state of ^{4}He cannot be described as a $d + d$ cluster configuration. However, including $d^* + d$ and $d^* + d^*$ configurations somewhat improve the results [47] which indicates that the specific distortion effect of the deuteron plays a role. On the other hand, the $p+t$ and $n+h$ cluster configurations, as the $1N+3N$ configuration, are the most favored and dominant in both the ground and the first excited states of ^{4}He for making the binding energy to be close to the experimental value. Including $2N+2N$ configuration seems to play a role in lowering the binding energy of the states by nearly 0.85 MeV. However, the distortion effect of the deuteron cluster is greatly weakened in the $1N$+$3N$ configuration, indicating that it is indeed the energetically most favored one [46].

From the above considerations, one can conclude that, contrary to expectations, the dominant structure of the 4 nucleons system (^{4}He) may be $3N + 1N$, not $2N + 2N$ or $N + N + N + N$. The nucleus ^{4}He could be made up of $n + h$ and $p + t$ clusters [26] with very little of $d + d$ configuration in the ground state. Thus, the wave function of the ground 0_1^+ and first excited 0_2^+ states of ^{4}He may be written through the product group $(SU(2)_I \otimes SU(2)_A)$, the product of the isospin group and the nusospin group, as [26]:

$$\Psi_{0_1^+} = \frac{1}{\sqrt{2}}(\psi_h \otimes \psi_n - \psi_t \otimes \psi_p) \tag{2.8}$$

$$\Psi_{0_2^+} = \frac{1}{\sqrt{2}}(\psi_h \otimes \psi_n + \psi_t \otimes \psi_p) \tag{2.9}$$

where ψ_h and ψ_t are the ground state wave functions of ^{3}He and ^{3}H, respectively. The ψ_n and ψ_p are the wave functions of n and p, respectively.

2.8 Models Including ^{3}He Clusters

Over the last few decades, significant progress has been made to adequately understand the structure of nuclei and the formation of clusters within. Historically, two authors (L. Pauling and M. H. Mac Gregor) were the first to consider helion and triton as clusters and led other authors [26] in the last decade to adopt this concept in the development of their models. A brief description of these unconventional models is presented in the following sections.

2.8.1 The Close Packed Spheron Model - Pauling's Model

The close-packed-spheron model consolidates some of the features of the shell model, the alpha-particle model, and the liquid-drop model [51]. The model was presented by Linus Pauling [49, 52] in the 1960s by assuming that nucleons in nuclei aggregate into spherical 2, 3, and 4 nucleon clusters, called spherons. A spheron can be arranged geometrically into close-packed symmetrical structures that correspond to the nuclear magic numbers. The spherons are dineutron, deuteron, triton, helion, and alpha particles, where the largest spheron is the alpha, arranged in spherical or ellipsoidal layers, which are called the mantle, the outer core, and the inner core to avoid confusion with the shells of the shell model. The idea of considering spherons as building blocks in the Pauling's model was interesting based on common sense but a theoretical dilemma arising from an uncertainty in the magic numbers of the nuclear shells, which are not as unique and unambiguous as those of electron shells [25].

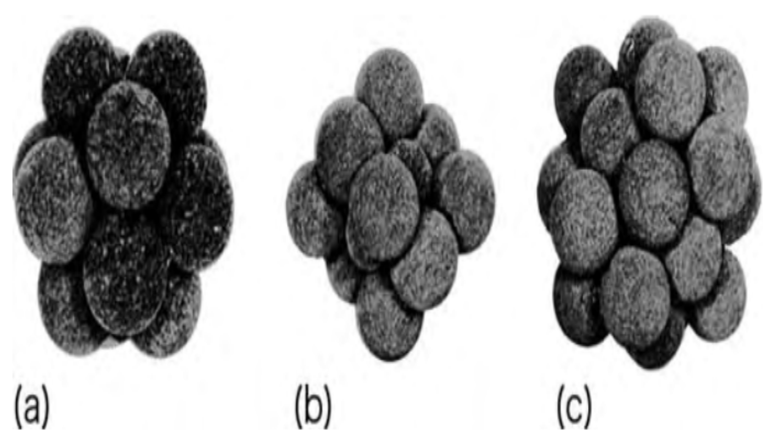

Figure 2.5: Spheron model structures giving approximately spherical nuclear shapes. Figure (a) shows an icosahedral spheron structure containing 12 outer spherons and one at the center. Figure (b) shows a 14 spherons structure obtained by using spheres of two different diameters (used to explain the magic number 28). Figure (c) shows a 22 spherons structure used to explain the partially-magic character of number 40 (from Pauling, 1965) [25].

2.8.2 2D-Ising Cluster Model - MacGregor's Model

In the Ising Cluster Model, MacGregor [27] attempted to explain the inner structure of all nuclei as an aggregation of small building blocks of 1, 2, 3, and 4 nucleon clusters. Protons and neutrons inside atomic nuclei combine into clusters of alpha-particles, tritons, helions, and deuterons. Then, these clusters together with unclustered protons or neutrons are arranged into two-dimensional Ising layers. The basic idea of the Ising model, developed in detail by Ising in 1925 but first suggested earlier (1920) by Wilhelm Lenz, is a physical system that can be represented by a lattice arrangement of molecules with nearest-neighbor interactions [53]. The model specifies the number of clusters within each layer; however, the actual configuration within each layer is left unspecified among several possible geometries for a given number of clusters. The Ising cluster model explained the observed nuclear properties (binding energies, spins, parities, magnetic moments, and RMS radii) of nuclei by the summations of the properties of the smallest nuclei clusters. Unlike the standard alpha-particle model, MacGregor's model was well applied to all nuclei, even those with an odd number of Z or N [25].

2.8.3 Abbas & Ahmad's Model

The most recent model was developed in the last decade by Abbas & Ahmad [26]. The model was supported by some experimental evidence, indicates possible nucleon clustering in the nuclear interior [27], and explains some nuclear properties. Their model was built on past ideas and on the recent observation of unique properties for the $A = 3$ nuclei, after introducing a new symmetry group.

As is evident from Figure 2.3, h, t, and α particles have a unique density distribution and holes at the center of their distribution. This allows classifying nuclei into three blocks. The first block has n and p only due to the similarity of their masses and the absence of the hole at the center. The second block includes h, t, and α due to the reasons pointed in Section 2.6. The last block is for all other nuclei due to the similarity pattern in their density distribution and no holes found within as in the first block. Noting this categorization, provides a first view of the model.

Another important observation from the symmetry groups $SU(2)$, discussed in Section 2.5, induces more classification. Both n and p particles are considered elementary entities and manifest as a fundamental representation of the isospin group $SU(2)_I$. Therefore, (n, p) form a building block as mentioned above. In the same analog, h and t particles are considered elementary entities and manifest as a fundamental representation of the new symmetry group $SU(2)_A$, the nusospin group. Consequently, h and t are different from α, and form a separate block.

As a result of the above classifications and by comparison to the other mentioned models, Abbas and Ahmad considered only four particles as the basic building blocks of all nuclei, namely n, p, t, and h. The basic idea of their model is that the building blocks must be elementary particles and not an aggregate of other basic building entities. Therefore, in their model, the deuteron is not considered a building block since it consists of the elementary particles p and n. In the same manner, the α-particle is not considered as a fundamental building block since it is made up of the elementary particles t or h plus one p or n, respectively [26]. Thus, the α-particle may be treated as the first and most basic structured nucleus since its binding energy per nucleon is 7 MeV/A, which is very close to heavy nuclei 8 MeV/A. The authors concluded that "*Alpha keeps popping up as a cluster in the build up of heavier nuclei - but not as a basic building block but as a good cluster which nuclear dynamics prefers to create*" [26].

Abbas and Ahmad argued that both n and p are made up of three quarks and only at relatively high energies, the compositeness of n and p manifest itself. Despite that, they still are considered elementary particles. In the same manner, both h and t with binding energy around 8 MeV are unique entities. It is also stressed that besides the deuteron, these two are the only nuclei known to have no excited states [26]. Hence, they can be considered as elementary entities and basic building blocks as long as the relative excitation energies are low.

Chapter 3

Experimental Setup

3.1 Overview

Experiment E04-018 was conducted in the Hall A Facility of the Thomas Jefferson National Laboratory (JLab). The data taking phase took place in the period November 2006 to July 2007, with two interruptions to run other experiments. The main goal of E04-018 was to improve the quality of the existing data of the ^{3}He and ^{4}He form factors and to extend the existing measurements to the highest momentum transfers possible [54].

The electron beam was generated in the recirculating accelerator - the Continuous Electron Beam Accelerator Facility (CEBAF) of JLab. At the time of the experiment, in addition to Hall A, JLab had two other Halls, B and C. Since then, the accelerator was upgraded to increase the maximum beam energy up to 12 GeV, and a new experimental Hall, named Hall D, was constructed and became ready to use in 2015 [56]. Therefore, this chapter will describe the accelerator properties and Hall A apparatus in detail as they were during the time of the data taking of the E04-018 experiment. An overview of the upgrade of the accelerator will be discussed shortly. An areal view of the JLab can be seen in Figure 3.1.

3.2 Accelerator (CEBAF)

CEBAF is a Superconducting Radio Frequency (SRF) linear accelerator that could deliver a high-quality, continuous, and polarized electron beam with energies, at the

Figure 3.1: Aerial photo of JLab showing the racetrack shape accelerator that the electrons are accelerated around, the three existing Halls, A, B and C, and the Hall D under construction.

time of the experiment, up to 6 GeV, currents up to 200 μA and polarization approximately 80% [55]. The accelerator has a shape resembling a racetrack with two anti-parallel superconducting linacs, the North Linac and the South Linac, used to accelerate electrons, which are connected by two sets of recirculation arcs, as can be seen in Figure 3.2. Each superconducting linac consisted of 20 cryomodules, at the time of the experiment, adding 600 MeV to the energy of the electrons per superconducting linac.

The source of the electrons is the polarized photogun in the Injector via photoemission from a GaAs cathode that is illuminated by a circularly polarized laser beam. In the Injector, the ejected electrons are accelerated up to 45 Mev by passing through a superconducting accelerator, consisting of 2 1/4 cryomodules. The beam is then injected into the North Linac for further acceleration. The North Linac adds 600 MeV to the beam energy. At the end of the North Linac, the beam is steered by magnetic arcs through the East Arc to the South Linac and accelerated by the South Linac, which adds another 600 MeV. When the electron beam passes through each linac once, it completes one pass. Every pass increases the beam energy up to 1.2 GeV. The electron beam can be circulated up to five times, five "passes", through the Linacs, increasing the energy up to 6 GeV. When the beam reaches the requested energy (the number of pass multiples times the energy of a single pass), it is directed for delivery to the appropriate experimental Hall at the end of the South Linac. Each Hall can be controlled independently and receive the maximum energy beam simultaneously.

The original CEBAF was designed to accelerate the electrons up to 4 GeV by recirculating the beam up to 4 times. Each pass increased the energy by 800 MeV. In 2000, the accelerator was upgraded to reach maximum energy up to 6 GeV by recirculating the beam up to 5 times. The beam was raising up by 1.2 GeV per pass. In 2015, CEBAF was upgraded to generate beam energy up to 12 GeV by increasing the number of the cryomodules by 5, 25 in each linac. These additions allowed the accelerator to gain an energy of 2.2 GeV per pass. All Halls A, B, and C were able to receive energy up to 11 GeV through 5 passes. Furthermore, a new experimental Hall, named Hall D, was constructed at the end of the North Linac. An additional arc that was added at the west side of the accelerator allowed the electron beam to recirculate an extra pass through the north linac to reach the new Hall D. Hall D can receive energy up to 12 GeV through a 5.5-pass beam. The schematic of the 12 GeV

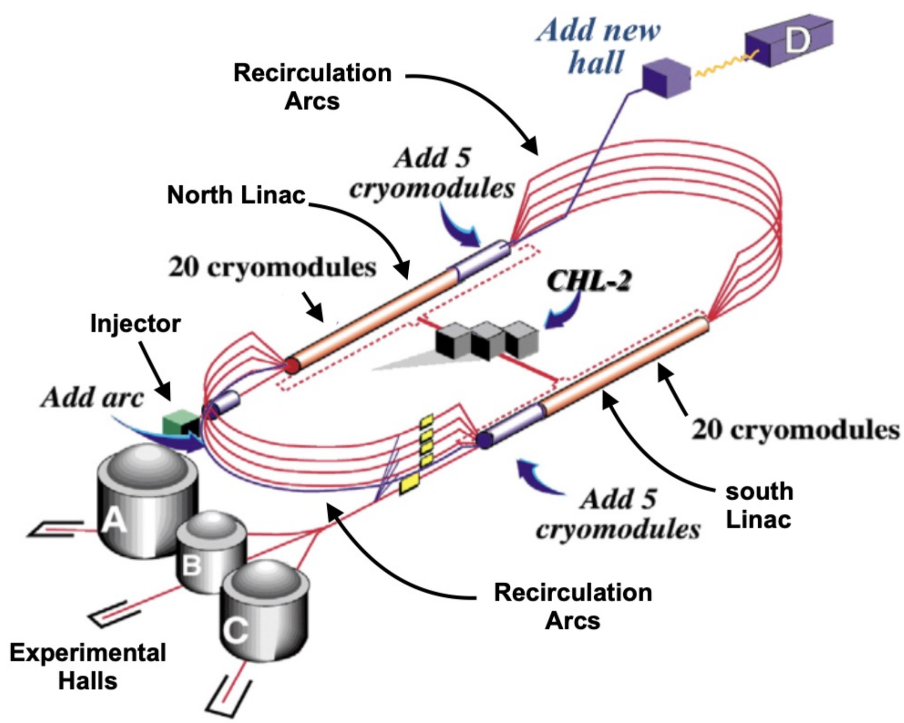

Figure 3.2: A schematic view of the originally 6-GeV Jefferson Lab Accelerator configuration is shown along with the upgrades that were made towards the current 12-GeV configuration. Also shown are the Halls A, B, C, and D.

CEBAF configuration is shown in Figure 3.2.

3.3 The Hall A Facility

The Hall A Facility is the largest among the three experimental halls. It is built underground in a circular shape with a 53 m diameter and 24.4 m height. The main components of Hall A are the beamline, which transports the beam, the scattering chamber, which shelters the target cells, and two identical High Resolution Spectrometers (HRS), which detect scattered and recoil particles. Each of these components will be discussed in detail in the following sections.

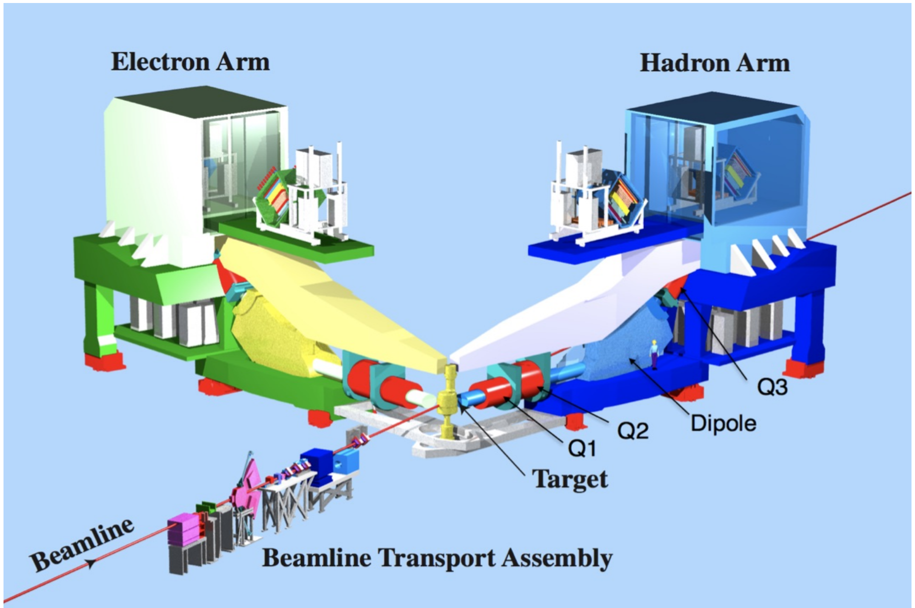

Figure 3.3: 3D Schematic of Hall A. Shown are the two High Resolution Spectrometers with their detector packages, the target chamber, and the beamline.

The HRSs are respectively known as the Left or Electron High Resolution Spectrometer (LHRS), which is normally used to detect scattered electrons, and the Right or Hadron High Resolution Spectrometer (RHRS) for detecting recoil particles. Both spectrometers can be rotated clockwise or counter-clockwise around the center of the Hall. The LHRS and RHRS can both reach a minimum angle of 12.5^o, and a maximum angle of 140.0^o, 100.0^o respectively, with respect to the beamline. The basic layout of the Hall A Facility is shown in Figure 3.3.

3.4 Beamline

In order to have a successful operation, after reaching the desired energy, the beam has to be transported to the target through the beamline. The Hall A beamline consists of various apparatuses to transport the electron beam to the target and then to the dump, where it is eventually deposited. The apparatuses simultaneously measure and monitor some of the beam characteristics such as its energy, current, position, direction, size, and stability of the beam at the Hall A target location. A schematic of Hall A with the beamline elements is shown in Figure 3.4. Some of the critical beamline elements that will be described in this section, are:

- Beam Arc Energy Measurement
- Beam Current Monitor
- Beam Rastering System
- Beam Position Monitor

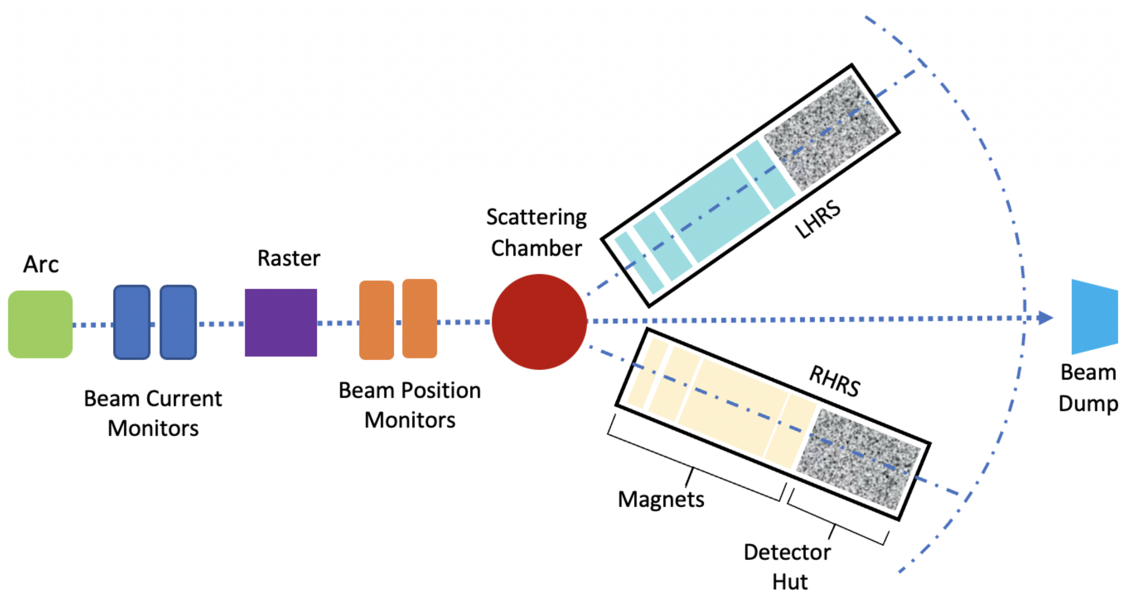

Figure 3.4: An overhead schematic of the Hall A Facility of JLab and the beamline from the entrance of the Hall up to the beam dump.

3.4.1 Beam Arc Energy Measurement

A precise knowledge of the incident beam energy in Hall A is required to extract and control the physics - related quantities for each scattering kinematics. The energy of the beam is measured by using the ARC method [58], which uses the measured deflection of the beam in the Arc. The Hall A Arc contains a series of eight identical dipoles that bend (deflect) the beam. The beam energy then is measured as a function of the field integral of the eight-dipole magnets and the Arc's bend angle. The eight dipoles are inaccessible. Therefore, their magnetic field integrals are determined by a ninth identical reference dipole. The ninth dipole is connected in series to the eight dipoles and placed outside the beam tunnel. A set of harps [58], which are wire scanners, is used to determine the bending angle of the beam in the Arc. The harps are located at the entrance and exit of the Arc, two harps at each location. Knowing the dipoles' magnetic field and the bending angle, the magnitude of the momentum of the transported electrons (in GeV/c) can be expressed as:

$$p = k\frac{\int \vec{B} \cdot \vec{dl}}{\theta} \tag{3.1}$$

where $k = 0.299792$ GeV·rad/(Tmc), $\int \vec{B} \cdot \vec{dl}$ is the field integral (in Tm), and θ is the bending angle of the Arc (in radians). The precision of the beam energy using this method is of the order of 10^{-4} [55]. A schematic of the Hall A Arc is shown in Figure 3.5.

3.4.2 Beam Current Monitors

A pair of Beam Current Monitors (BCM) located inside the experimental Hall are used to determine the beam current and subsequently, the amount of charge that is delivered to the target. The pair is designed for a stable, low-noise, and non-interfering beam current measurement, and consists of a Parametric Current Transformer (PCT), an Unser monitor, and two radio frequency (RF) cavities. The monitoring system is located 25 meters upstream of the target [55].

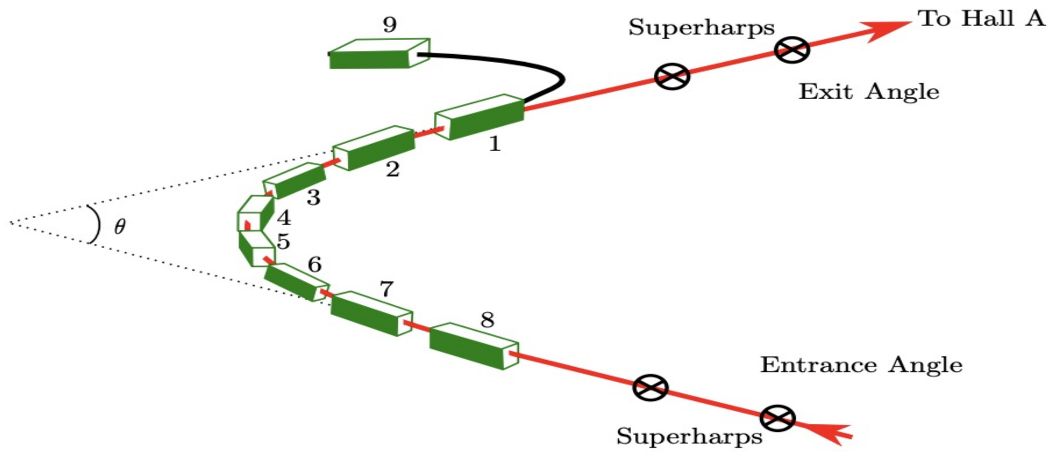

Figure 3.5: Schematic for the arc energy monitor in Hall A Arc, which consists of nine quadruple magnets (green) and four superharp wire scanners.

The Unser Monitor, which provides an absolute reference, is located along the beamline between the two RF cavities. The Unser can be calibrated by a wire placed remotely along the beamline carrying a known current. Due to drifts caused by having the beam running through the monitor in relatively short times of several minutes, the Unser cannot be used to continuously measure the beam current. In order to minimize the noise and reduce the drift to zero, the Unser monitor is equipped with temperature stabilization and extensive magnetic shielding. However, the Unser is mainly used to calibrate the gain of the BCM.

The two RF cavities, which are located one upstream and one downstream of the Unser monitor, are stainless steel cylindrical waveguides tuned to the frequency of the beam (1.497 GHz) resulting a voltage at their outputs that is proportional to the beam current. Each of the RF output signals is split into two parts to be either sampled or integrated. The RFs are used to continuously monitor the beam. The BCM can measure currents down to 1 μA with an accuracy of 0.5% [55].

3.4.3 Beam Rastering System

Since the high-current electron beam delivered to Hall A has a small transverse size (typically within 80-200 μm), it means that it will impinge on a small area of the target with very little spread. A beam with these characteristics can cause safety concerns for the material of the target used, by melting a solid target, "boil" a gas or liquid of a cryotarget, or rupture the cell of a target.

In order to minimize any possible damage to the target due to the intensity of the beam spot, the size of the beam is increased up to 4 mm full width, in both the vertical and horizontal directions before it impinges on the target by changing the magnetic fields through a raster system. The raster system consists of a set of four dipoles located 23 m upstream of the target, two in the horizontal direction and two in the vertical direction, which can deflect the beam with a frequency of 25 kHz and 17.7 kHz, respectively. In this experiment, the raster was set to expand the beam to a 2 x 2 mm^2 spot size [59].

3.4.4 Beam Position Monitors

The Beam Position Monitors (BPMs) are used to provide information on the position and direction of the beam at the target location. There are two BPMs located at a distance of 7.542 m and 1.286 m upstream of the target, respectively [55]. Each one of the BPMs consists of four antennae parallel to the beam direction, with two wires being used to measure the horizontal position and two more to measure the vertical position. The antenna wires are arranged at 90^o with respect to one other and oriented $\pm$ 45^o from the horizontal and vertical direction. The BPMs provide a method to determine the relative position of the beam within 100 μm for currents above 1 μA. To determine the absolute position of the beam, the BPMs are calibrated with the use of the superharp wire scanners located adjacent to each of the BPMs and known within 200 μm.

3.5 High Resolution Spectrometers

As mentioned before, Hall A has two 4 GeV/c high resolution spectrometers. The HRSs were designed to provide high resolution and large angular and momentum acceptance for the scattered particles, with ± 2 x10^{-4} momentum resolution and ± 0.1 mrad scattering angle resolution [55]. The entrance foil window of each spectrometer is separated from the scattering chamber exit windows by 54 cm of air. It is made of Kapton, of thickness 0.007 inch. The exit window is 0.004 inch thick, made of Titanium. Each spectrometer consists of two main parts: the magnetic particle transport system, and the detector package. The two spectrometers are identical in terms of their magnetic systems but different in their detector packages [61].

3.6 Optics Design

The magnetic transport system has four superconducting magnets: three $\cos(2\theta)$ quadrupoles and one 6.6 m long dipole. They are in the order of a QQDQ (quadrupole, quadrupole, dipole, quadrupole) configuration, named Q1, Q2, D, and Q3 as shown in Figure 3.6. The first quadrupole Q1 is designed to focus scattered particles in the vertical (dispersive) direction. The Q2 and Q3 quadrupoles are identical in the design and construction and provide focusing in the horizontal (transverse) direction. The D dipole magnet bends central ray-particles by 45^o in the vertical with respect to the horizontal axis [55, 61].

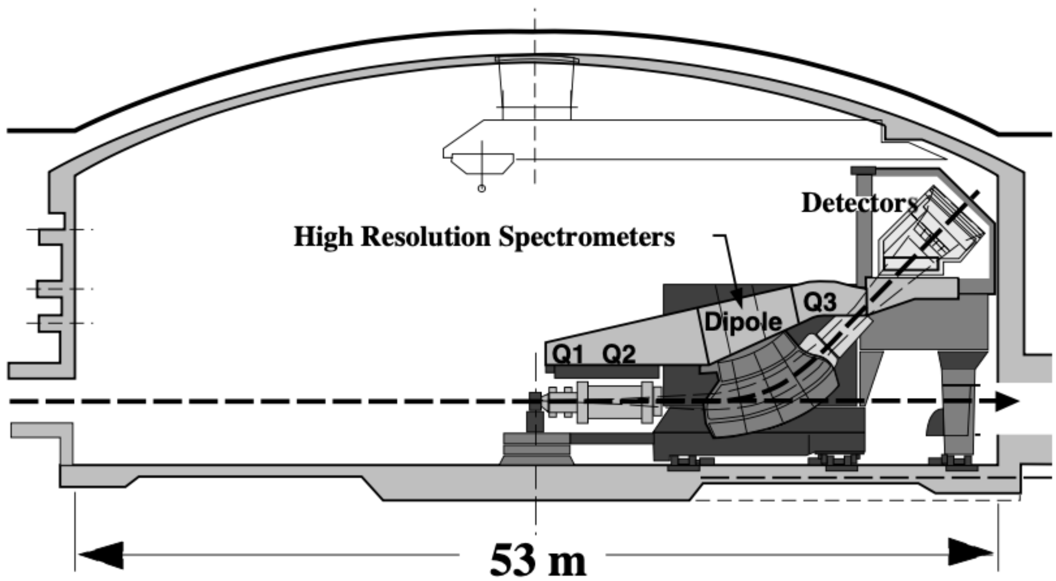

Figure 3.6: Side-view of the Hall A High Resolution Spectrometer. Shown are the spectrometer magnetic elements, and the detectors, which are inside the shield house at the top of the spectrometer.

3.7 Detector Package

The detector packages of the two spectrometers are equipped with a series of detectors designed to measure and identify scattered particles passing through the spectrometers, which originate from the target. The detector package for each spectrometer is located on top of the spectrometers and mounted on a steel frame. The frame with the detector package is placed inside a Shield Hut (SH) made of metal and concrete. The SH is intended to shield the detectors from room background radiation that could cause spurious events. The detector packages in both spectrometers are similar but not identical, as will be discussed later. Each spectrometer arm is equipped with the following:

• A pair of Vertical Drift Chambers, VDC1 and VDC2, for scattered or recoil particle

Figure 3.7: Side-view of the Hall A Left High Resolution Spectrometer. Shown are the spectrometer magnetic elements and and the shield house at the top of the spectrometer.

track reconstruction.

• A pair of (plane) scintillator hodoscopes, S1 and S2, for triggering and timing purposes.

In addition to these, the electron spectrometer detector package included one CO_2 gas threshold Cherenkov counter and a segmented lead-glass calorimeter for electron identification. Electron-nucleus coincidence events were identified by measuring the double-arm Time of Flight (TOF) between the electron and recoil triggers. The following sections will briefly discuss the functions and characteristics of each detector for the two detector packages, which are shown in Figures 3.8 and 3.9.

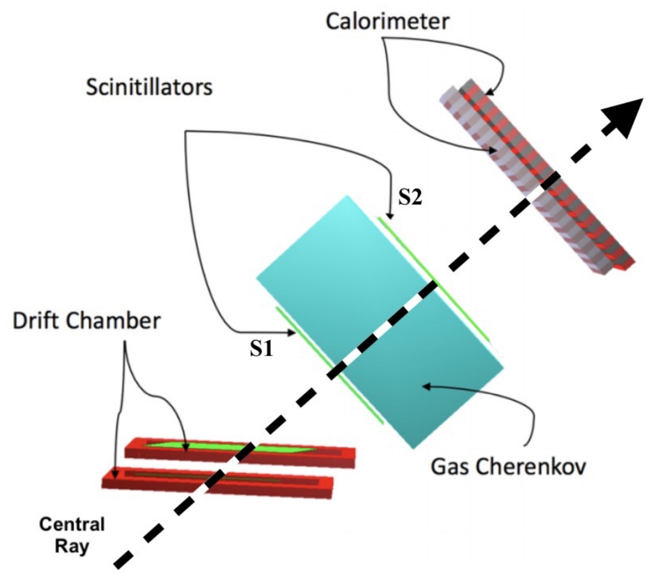

Figure 3.8: Schematic of the Electron Arm detector package as used in this experiment. Shown are the two VDCs, the S1 scintillator plane, the gas Cherenkov detector, the S2 scintillator plane, and the lead-glass calorimeter.

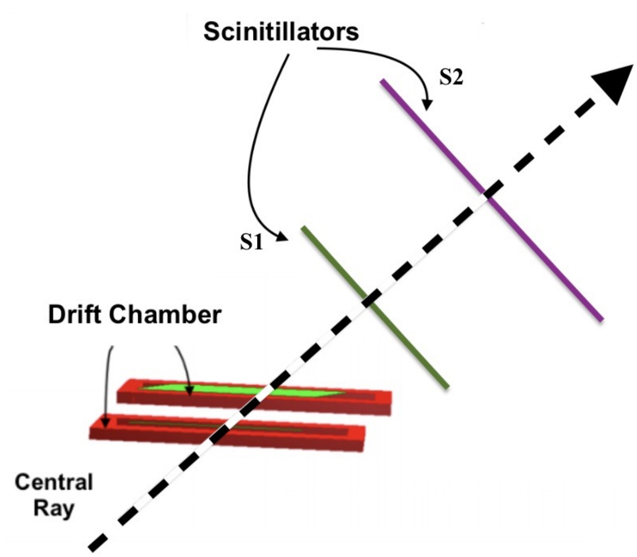

Figure 3.9: Schematic of the Hadron Arm detector package as used in this experiment. Shown are the two VDCs, and the two S1 and S2 scintillator planes.

3.7.1 Vertical Drift Chambers

The detector package of each spectrometer is equipped with a pair of identical Vertical Drift Chambers (VDC) separated by 33.5 cm, used to determine the position and angle of the particles passing through at the spectrometer Focal Plane (FP) position. The effective detection area of the VCD is 211.8 cm $\times$ 28.8 cm in the dispersive and transverse directions, respectively [61]. Each VDC has two wire planes consisting of 368 sense wires separated by 4.24 mm from each other. The sense wires of each plane are perpendicular to each other and form a 45^o angle with respect to the central ray, a standard UV configuration. The planes are filled with a gas mixture of argon (62%) and ethane (38%). A schematic of the two Vertical Drift Chambers is shown in Figure 3.10.

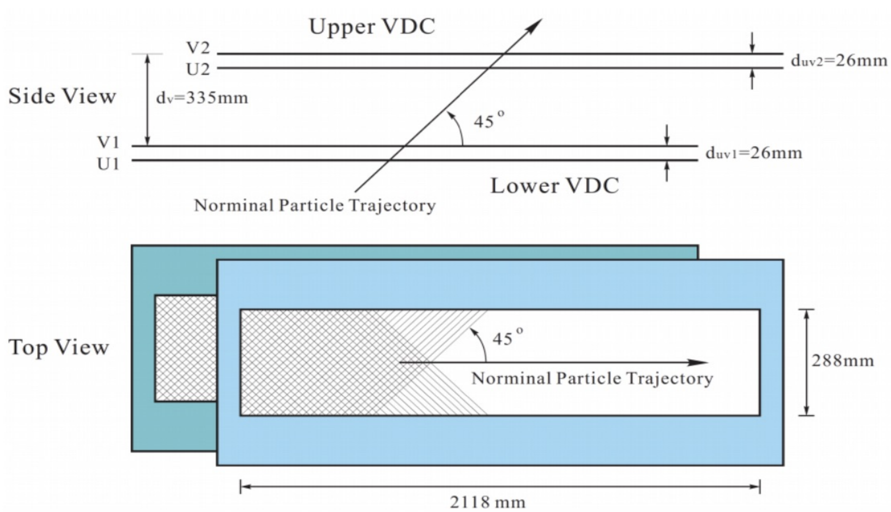

Figure 3.10: Schematic of the two Vertical Drift Chambers of the HRS system.

As a charged particle passes through a drift chamber, it ionizes the gas mixture and produces electrons and ions along its path. The electrons are accelerated by the electric field defined by the high voltage of the wire plane. The accelerated electrons drift towards the closest sense wire and produce additional ions and electrons. The signals from each sense wire are amplified and sent to Time-to-Digital Converters (TDCs), as will be discussed later in this chapter, located in the back of the detector hut. The corresponding drift time and velocity information are used to calculate the distance between the wires and then the particle position, which eventually provides a determination of the particle's momentum, scattering or recoil angle, and the reaction vertex along the target.

3.7.2 Scintillators

Each HRS contains a set of two trigger scintillator planes, referred to as S1 and S2 planes. The scintillator planes are made of plastic (polystyrene) separated by approximately 2 m, (1.933 m in the Electron arm and 1.854 m in the Hadron arm). The S1 plane in both arms consists of six identical thin (0.5 cm) paddles. To ensure complete coverage of the detector plane by avoiding any gap, the scintillator paddles overlap by 0.5 cm. The S2 plane in the electron arm is identical to the S1 plane. The S2 plane in the Hadron arm is composed of 16 paddles of a thick (5 cm) scintillator. The paddles are made of Bicron BC-408 plastic with a density of 1.1 g/cm^3 and have a time resolution of approximately 0.3 ns. Each scintillator paddle is attached to a 2-inch photomultiplier tube (PMT) at both ends. The S1 plane is placed just above the VDCs, and the S2 plane is located towards the back of the detector stack. Both planes are perpendicular to the spectrometer central ray. Figures 3.12 and 3.11 show the layout of the scintillators planes.

When charged particles pass through the scintillator paddles, the paddle atoms become excited by absorbing a small amount of energy. These excited atoms emit light in the form of fluorescence that travels through the light guide to the PMTs.

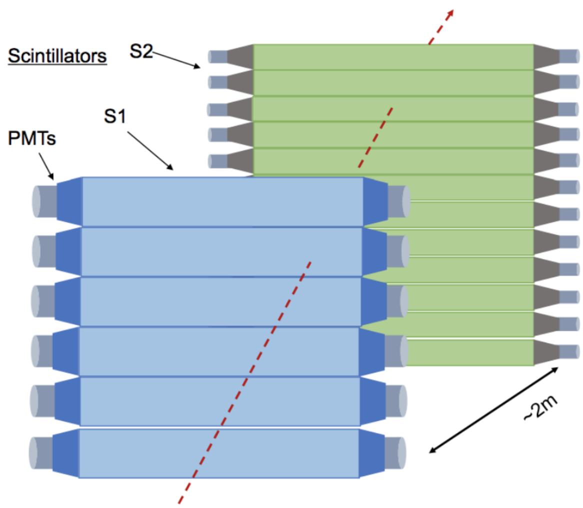

Figure 3.11: Schematic of the Right HRS S1 and S2 scintillator planes.

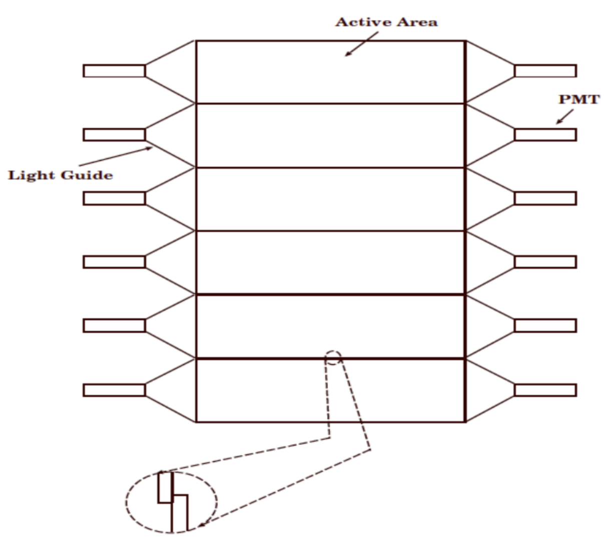

Figure 3.12: Schematic diagram of the S1 plane of the Left and Right HRS systems. Show also is a small overlap of different paddles.

Then, the signals from each PMT are sent to Analog-to-Digital Converters (ADC) and to TDCs to be recorded. The time difference between the signals of the left and right tubes of each scintillator is considered as the mean time of a paddle. The difference between the S1 and S2 mean times for each HRS provides the Time of Flight (TOF) for each particle and may be used to distinguish electrons from heavier particles.

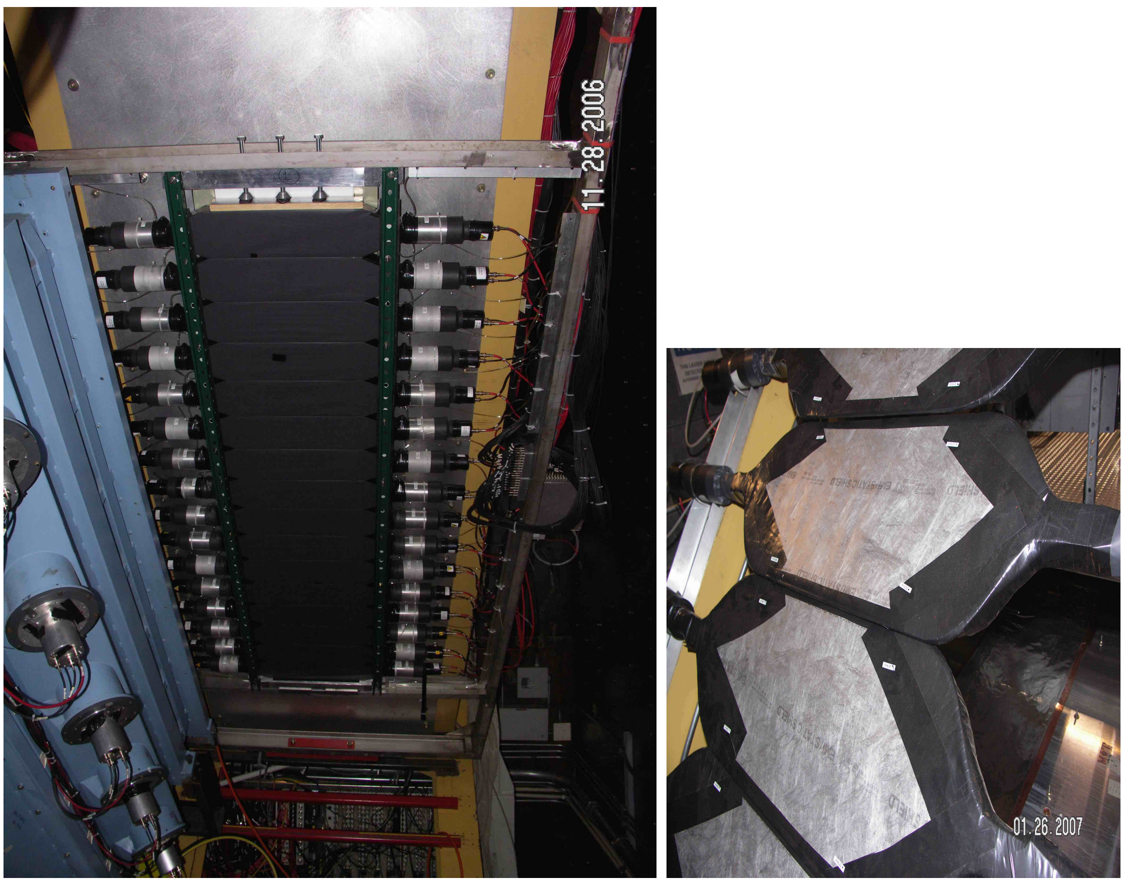

Figure 3.13: Left image: front view of the Right HRS S2 scintillator plane. Shown are the 16 paddles and the attached PMTs. Right image: partial front view of the Left RHS S1 scintillator plane. Shown are the paddles, the attached PMT and the small overlap between the paddles.

3.7.3 Gas Cherenkov Counter

The Gas Cherenkov Counter (GCC) is used for particle identification (PID), to separate pions from electrons. It is mounted between the S1 and S2 scintillator planes in the electron arm LHRS. The length of the particle path in the GCC is 120 cm. The detector is filled with CO_2 at atmospheric pressure, which has an index of refraction $n = 1.00041$. The heart of the GCC consists of 10 spherical partially overlapping mirrors with a radius of 90 cm, facing 10 5-inch PMTs. The PMTs are divided into two columns of five, placed at the detector's side as shown in Figure 3.14.

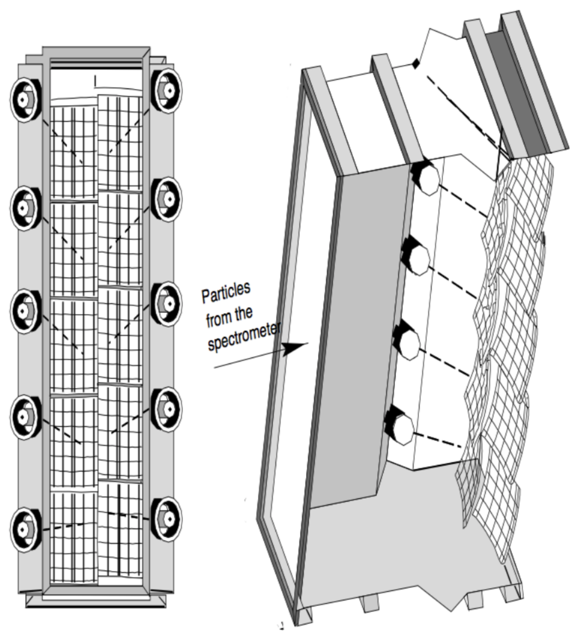

Figure 3.14: Gas Cherenkov detector in the electron arm with front mirror view, and 3-D view of the entire detector.

The working principle of the Gas Cherenkov is that when a charged particle passes through the gas faster than the speed of light, it emits electromagnetic radiation (Cherenkov radiation), ultimately directed to PMTs by the associated mirrors. The angle θ between the Cherenkov radiation and the incoming charged particle is given

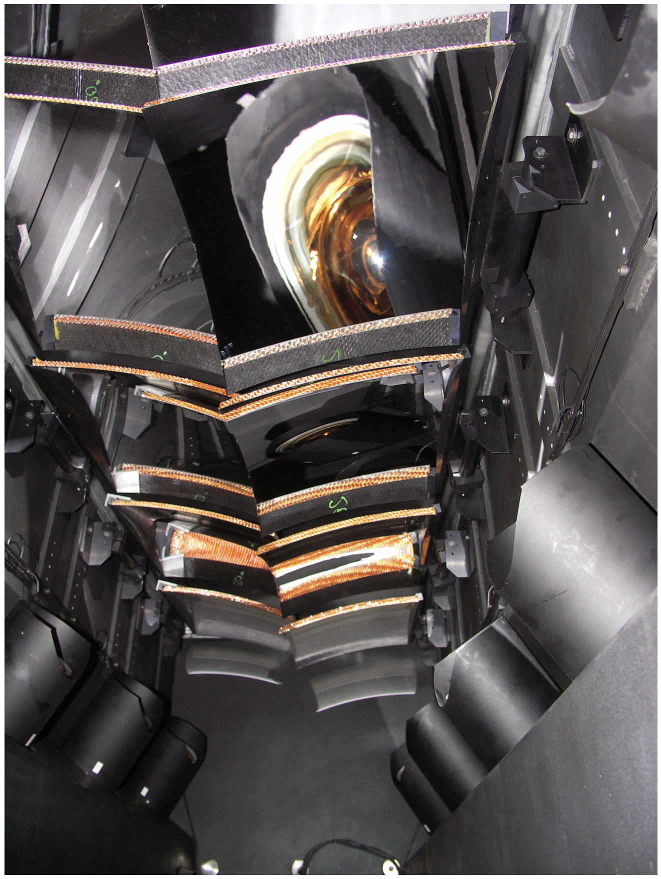

Figure 3.15: A top view of the Gas Cherenkov detector in the electron arm. Shown are the mirrors, the PMTs, and the reflection of one of the PMT in the mirror.

by $\cos\theta = \frac{1}{\beta n}$, where β is the velocity of the incoming particle relative to the speed of light, and n is the refractive index of the gas. The Gas Cherenkov Counter is a threshold-type detector, where the Cherenkov radiation is emitted only by particles having energy greater or equal to a threshold kinetic energy. For CO_2, the minimum particle momentum threshold is 17.0 MeV/c for electrons and 4.8 GeV/c for pions. Note that the threshold momentum for pions is above the maximum momentum for the HRS 4.0 GeV/c.

3.7.4 Lead-Glass Calorimeter

In addition to GCC, the LHRS is equipped with an electromagnetic calorimeter to provide further particle identification by measuring the energy deposited by the particles that pass through it. The calorimeter consists of two layers of segmented lead-glass blocks, the first one called Preshower and the second Shower detectors respectively, located after the S2 plane. Each layer contains 34 identical lead-glass blocks. Each block has a size of 15 cm x 15 cm x 35 cm and is attached to a 3-inch PMT at each end [55]. Both layers are oriented perpendicular to the path of the particle. The configuration of the LHRS calorimeter is shown in Figure 3.16.

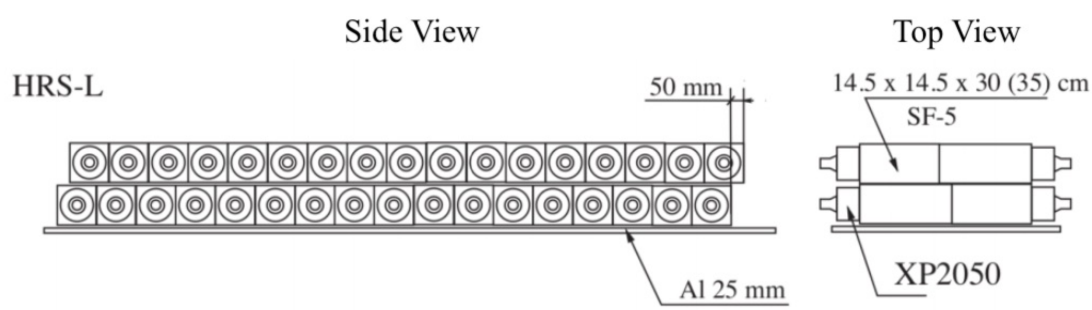

Figure 3.16: Schematic lay-out of the shower detector. Particles enter from the bottom of the figure.

As a charged particle passes through the calorimeter medium, it deposits different amount of energy depending on its bremsstrahlung radiation and ionization/excitation energy losses. When a high-energy electron enters the calorimeter, it loses energy primarily by interacting with the medium nuclei and radiates bremsstrahlung photons. These photons generate positron-electron pairs which, in turn, radiate photons, and so a shower of particles is produced: photons, electrons, and positrons. This process repeats until the electron deposits its entire energy in the calorimeter, unlike the pion

Figure 3.17: A top view of the shower from the back of the Hut. Shown are the lead-glass blocks and the attached PMTs.

which deposits only a few percent of its energy in most cases in the form of ionization energy loss or through hadronic interactions. Then, the energy ratio E'/P, which is the energy deposited in the calorimeter to the particle momentum as determined from the VDC tracking, is used to distinguish electrons from a mostly pion background. The electron peak should be at 1, while a higher-mass particle will result in a much lower ratio (around 0.1 for a pion). The combination of the gas Cherenkov Counter and the Leaded-Glass Calorimeter provides a good particle identification with high efficiency.

3.8 The Cryogenic Target

The cryogenic target system [55] which is located inside the scattering vacuum chamber at the center of the hall contains sub-systems of cooling, gas handling, temperature and pressure monitoring, a movement controller, and a solid target ladder. The scattering vacuum chamber consists of an aluminum cylinder with 103.7 cm in diameter and 1 cm thickness. Scattered particles exit the scattering chamber to enter the spectrometers through exit windows, made of an aluminum sheet with thickness of 0.0381 cm and 0.0305 cm, for the electron and the hadron spectrometer, respectively.

The Hall A target ladder consisted of three different types of targets. The first type

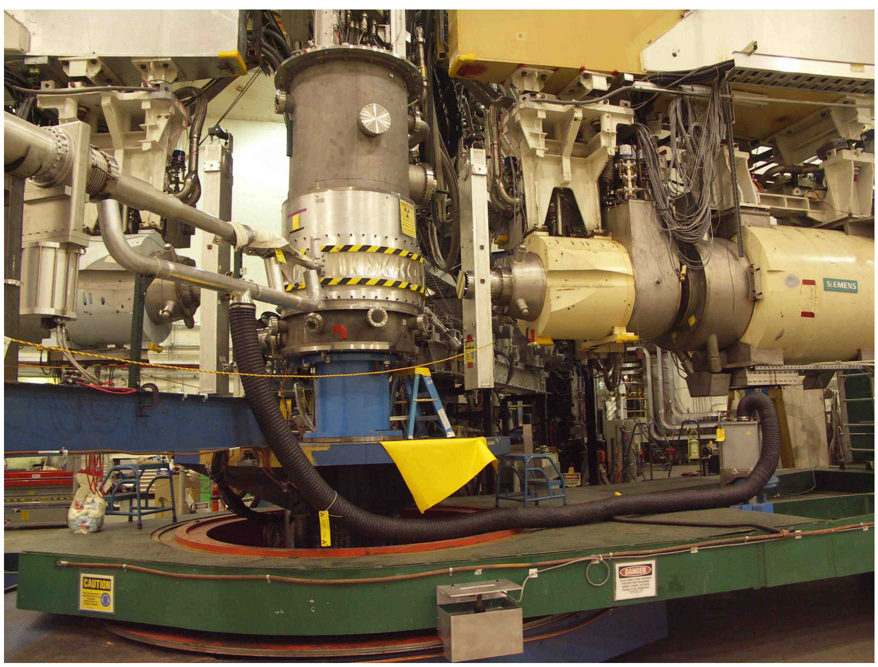

Figure 3.18: A front view of the center of the Hall A Facility. Shown are the scattering chamber, and the first magnetic element of the Left and Right HRSs Arms.

contained a liquid hydrogen or a gaseous helium loop. The gaseous helium target

Figure 3.19: Side view of the three types of targets inside the scattering chamber. Shown are from top to bottom the helium target cell, the optics target, and the dummy target.

cell can be filled with either ^{3}He or ^{4}He gas. The second type contained a series of seven thin Al foils for spectrometer optics studies. The third type, which is called the dummy target, was a replica of the two endcaps of the nominal target cell. The dummy target consisted of two thin aluminum foils, separated by 20 cm, and was used to measure possible contributions to the electron yields (counting rates) by effects originating from the nominal target cell endcaps. The target ladder as used in experiment E04-018 is shown in Figure 3.19.

For E04-018, the gaseous ^{4}He was put in a racetrack-shaped cell, which was made of Aluminum 20 cm long and 2 cm in diameter. The cell's sidewall was 0.0161 cm thick, whereas the endcap of the cell was 0.0137 cm thick. Some of the physical characteristics for the gaseous ^{4}He target are shown in Table 3.1. The target was cooled with helium fed by the End Station Refrigeration (ESR) [55].

Target	Pressure (atm)	Temperature (K)	Density (g/cm^3)
^{4}He	13.7-14.2	7.14-8.68	0.0994-0.1241

Table 3.1: The physical characteristics of ^{4}He gas target.

3.9 Trigger Setup

In this experiment, three detectors were used to build the trigger system. The hardon arm's main trigger was formed by a coincidence between its two scintillator planes S1 and S2. The electron main arm trigger consisted of the coincidence signal between the S1 and S2 planes. specifically, five types of triggers were generated:

- T1: RHRS arm S1 AND S2.
- T2: OR of RHRS S1 and S2.
- T3: LHRS S1 AND S2.
- T4: 2/3 (two out of three) of LHRS S1, S2, and Cherenkov.
- T5: T1 AND T3 in coincidence.
- T6: T3 AND T2 in coincidence.

Trigger T5 was a coincidence of T1 and T3, implying that two particles were detected by the two spectrometers in both scintillator planes of each HRS. The T2 Trigger was used to identify recoil particles that were absorbed in the S1 plane and did not reach the S2 plane. Trigger T6 was implying that both scintillators in LHRS were fired in coincidence with S1 in RHRS. A simplified diagram of the LHRS, RHRS and coincidence trigger circuits used for this experiment are shown in Figures 3.20, 3.21 and 3.22.

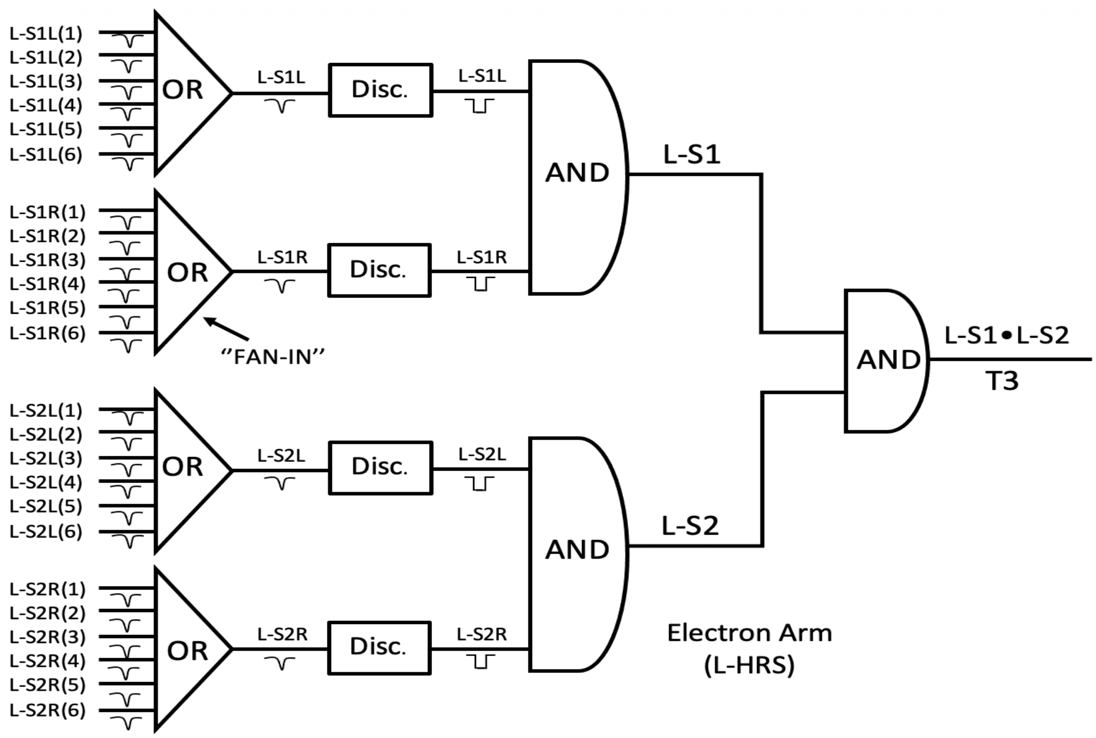

Figure 3.20: Schematic layout of the electron arm (LHRS) trigger circuit used for the JLab E04-018 experiment.

3.10 Data Acquisition

The data acquisition (DAQ) in Hall A uses CODA (CEBAF On-line Data Acquisition System) [55]. CODA was developed by the JLab data acquisition group. Data for each run were written directly to a local memory computer storage disk and contained the physics event data from the detectors ADC's and TDC's, scaler

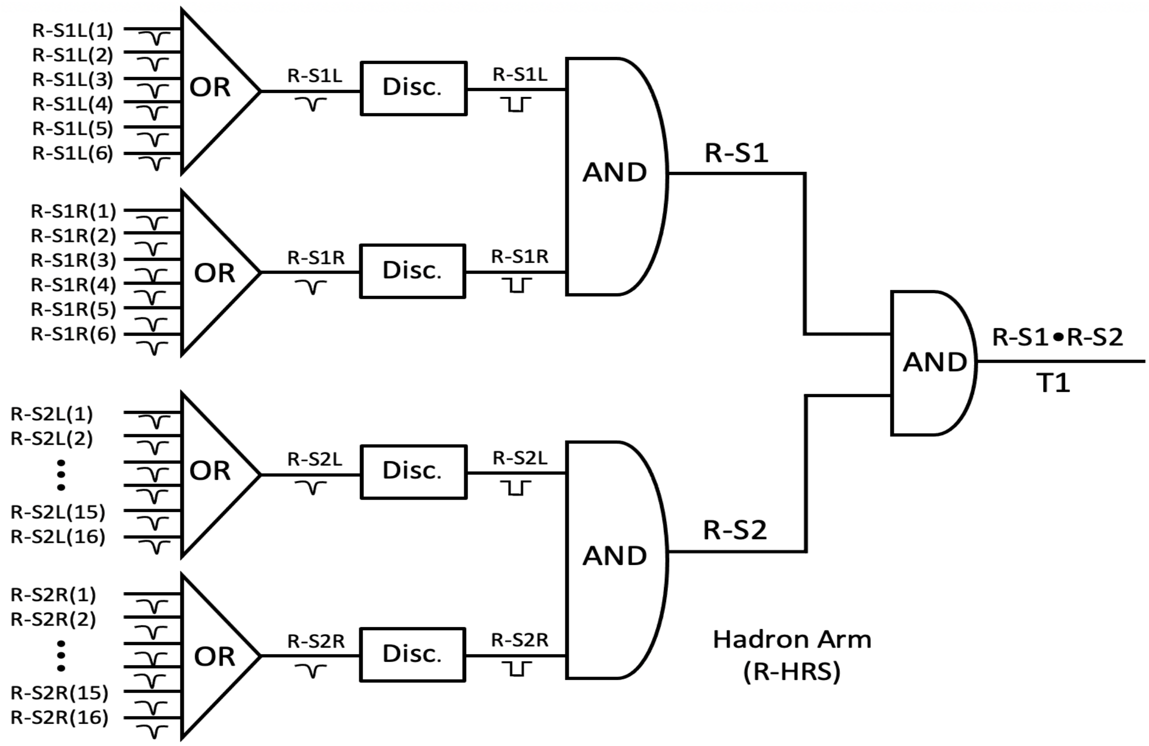

Figure 3.21: Schematic layout of the hadron arm (RHRS) trigger circuit used for the JLab E04-018 experiment.

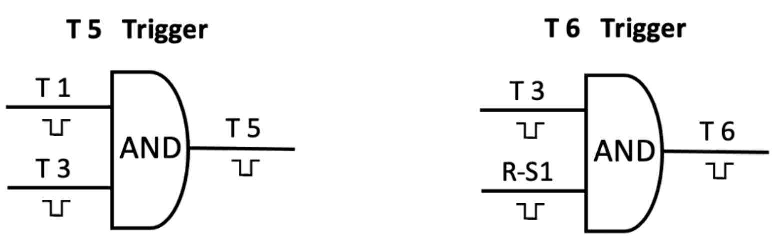

Figure 3.22: Schematic layout of the two coincidence trigger circuits used for the JLab E04-018 experiment. Shown are the triggers T5 and T6.

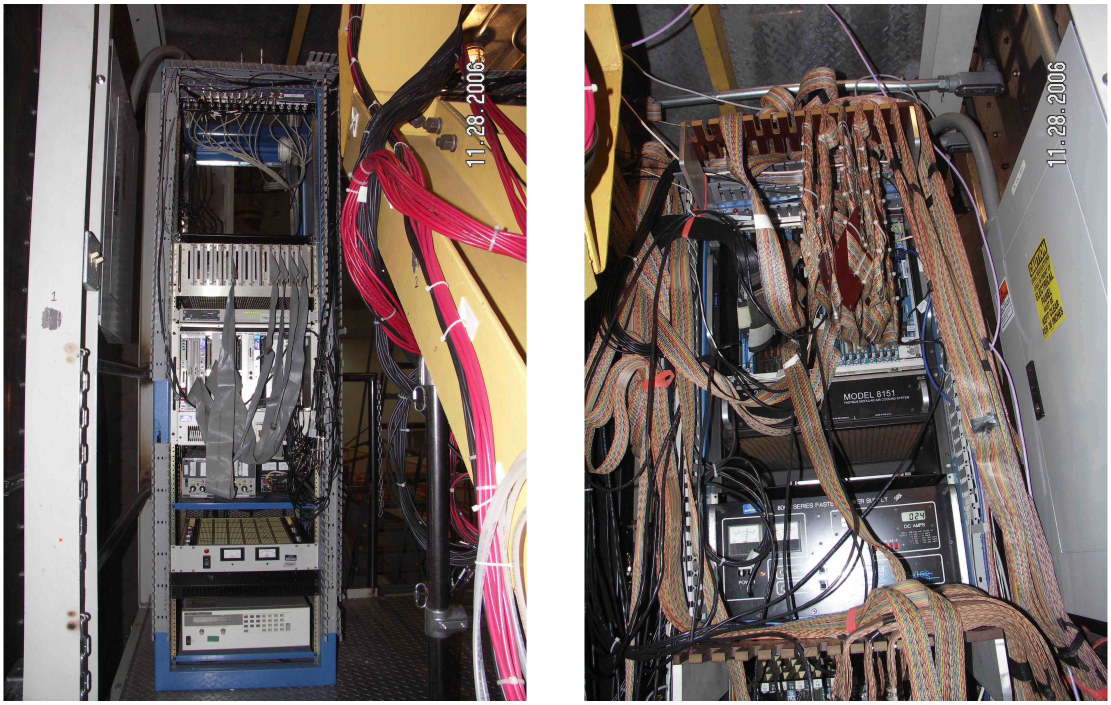

Figure 3.23: A front view of the Trigger electronics system in Hall A which is located in the LHRS Hut.

data, VDC data, and data from the hardware slow controls systems (EPICS). The Data were copied at specified times to the Mass Storage System (MSS) in the JLab Computer Center, where they were archived on data tapes [61].

Chapter 4

Monte Carlo Simulation and Analysis

In order to achieve a good understanding of the experimental data, a Monte Carlo (MC) simulation was performed by using a computer program designed to simulate a coincidence (e,e′X) experiment in Hall A. The program's name is MCSP. In this chapter details of the simulation method will be given. A comparison between simulation and experimental data will be presented in Chapter 6. The main goal of this study is to prove the existence of ^{3}He clusters within ^{4}He and to provide an excellent and reliable method to distinguish between the two distinct classes of coincidence events in the ^{4}He target elastic data of JLab experiment E04-018.

4.1 Some Background

The Monte Carlo (MC) method is a very powerful scientific tool used to study and explore the behavior of complex systems. It is a numerical method using a sequence of events that are generated randomly to study determinable problems [70]. Simulation methods have been used in both theoretical and experimental investigations of physical phenomena. In particular, in nuclear physics experiments, such a method has been essential for the design of their apparatuses, and data analysis and interpretation by allowing physicists to simulate stochastic interactions events in order to arrive upon the desired result [71]. However, using a Monte Carlo process requires extensive and detailed knowledge of the relevant physics concepts, probabilities, and models employed. Otherwise, Monte Carlo results can be incorrect or inaccurate without any indication.

The fundamental method of the Monte Carlo simulation was first employed by John Von Neumann, Stanislaw Ulam and Nicholas Metropolis in the 1940s [72] during the Manhattan Project, in World War II. The MC method was developed in order to investigate the properties of neutron travel through radiation shielding. The name of the method originally came from the Monte Carlo Casino in Monaco. Since then, large and extensive simulation codes with significant computational times were developed for solving complex problems. The development of fast computers and the subsequent evolution of computational modeling provided strong support for using the Monte Carlo method. As computers have gotten faster and input information or models have become more accurate, the Monte Carlo method can provide a very good estimate of the solution within a specified statistical accuracy as long as the number of attempts used in the simulation is high [69, 70].

4.2 Monte Carlo Simulation Overview

The present Monte Carlo simulation program MCSP was developed using the C language package and run in the MacOS system to study elastic electron-^{4}He scattering and quasielastic electron-^{3}He scattering within ^{4}He, in coincidence (detection of both scattered electron and recoil nuclei). The program employs a random distribution sampling method to populate the experiment's acceptance and setup. An event is defined as a combination of variables that completely specifies the reaction in the experiment. The MCSP reads input files containing various quantities such as incident energy, scattering angle, and running conditions that are representable of the actual experiment. The program starts by calculating the central experimental settings for the given conditions and then generating the Lab coordinates randomly for both scattered and recoil particles at the target. Then, transport matrices related to the spectrometer optics, transport the generated particles through the spectrometers to the detector packages. In this process, when either an electron or a recoil nucleus are stopped in the apertures of the vacuum pipe inside the spectrometer, the generated event has "failed". Successful events are those for which both electrons and recoil nuclei make it through the apertures and reach the detectors. All of the above will be discussed in detail later on in this chapter. The outputs of MCSP can be analyzed by the CERN ROOT software package [73] and produce the needed histograms and plots. A flowchart diagram of the MCSP simulation is shown in Figure 4.1. The working flow of this simulation program can be summarized in the following steps:

<u>For each kinematics, MCSP:</u>

• Calculates the experimental setup "central value kinematics" for the electron and recoil particle, corresponding to scattering at the center of the target coordinate system ($z = 0$).

• Generates uniformly the event target coordinates, including the position (x, y, z) and direction (in-plane θ, out-plane ϕ) angles. In addition, it generates the beam energy considering a Gaussian distribution to account for its finite resolution.

• Applies corrections for multiple scattering effects, ionization energy loss effects, and radiation effects (for electrons).

• Applies the spectrometer optics cuts after using a matrix or drift method to transport the events through every aperture, and checks whether a particle passed through or got stopped.

• Transports the surviving events from the target to the Focal Plane (FP) using transport matrices.

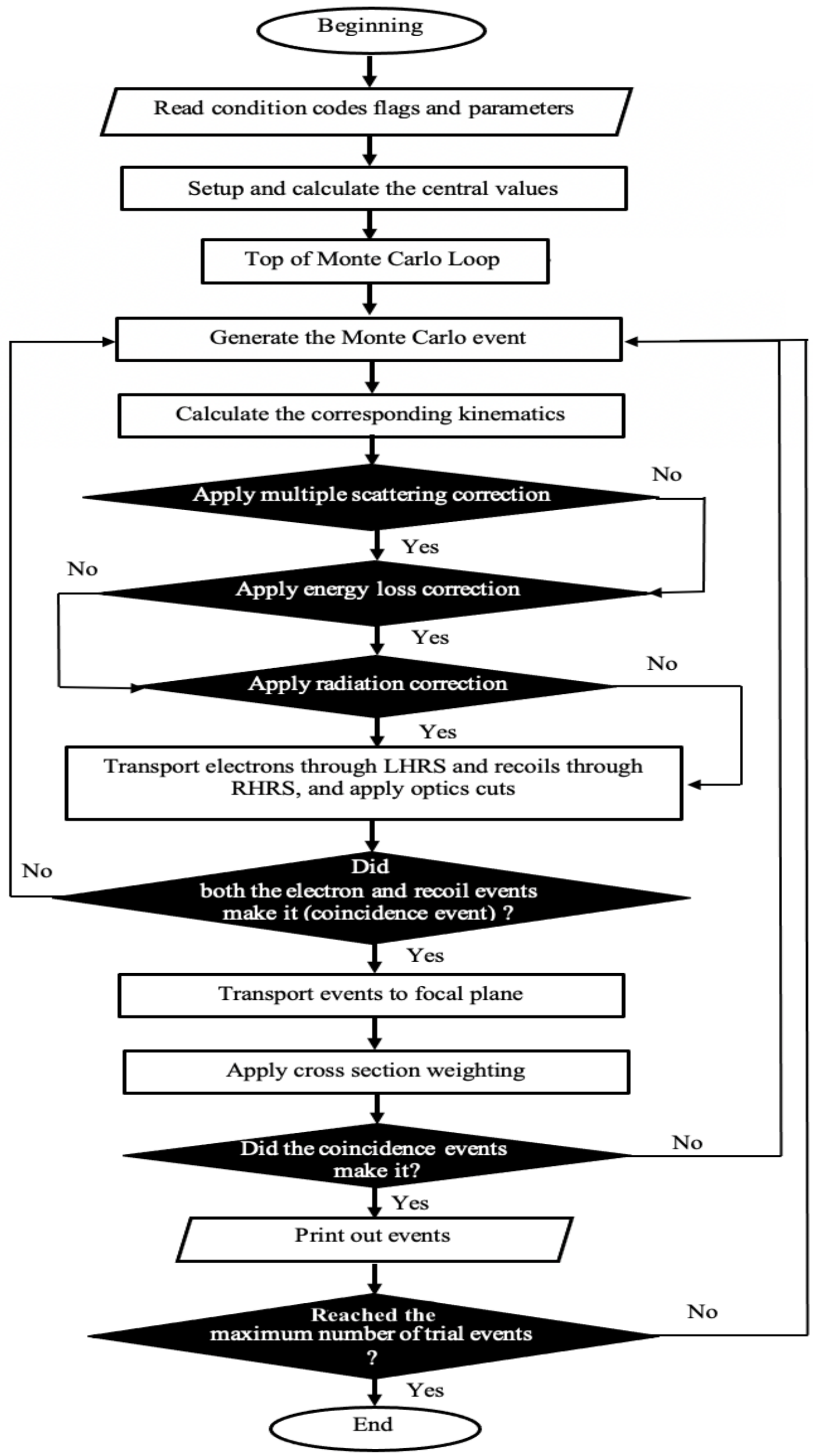

Figure 4.1: A flowchart diagram of the Monte Carlo simulation program (MCSP).

• Adds a cross section weighting factor to the surviving events.

For ^{3}He, in addition to all above:

• Generates the Fermi momentum of ^{3}He nuclei within ^{4}He in the target with the corresponding θ and ϕ angles.

• Applies the required energy to separate ^{3}He clusters (separation energy) from the ^{4}He nuclei.

Some analysis steps need to be followed in order to extract physics variables from the events to achieve the simulation goals. The following sections will go over each step in detail. Specifically examined will be corrections, optics cuts and fits that go into the calculation of the results.

4.3 MCSP Files

The main program reads all required physical quantities from two input files and prints out the results in several output files, which may be imported to ROOT for plotting and analysis. The input files include the following files:

• Setup_in: This is the main input file. The file contains the given experimental kinematics and apparatus settings, such as the beam energy, angles, and central momenta of the HRSs, as well as information about the target and other materials. It also contains the maximum number of trial events.

• Flag_in: This file contains a set of logical flags, that controls the flow of the program, choice of target type, and application of desired corrections.

The output files include:

• Setup_out: This file contains all calculated quantities corresponding to the given values in the Setup_in file, such as the scattered energy, the recoil energy, and angles.

• Kinm_out: This file contains all the generated events information for the incident, scattered, and recoil particles as well as their coordinates and pertinent kinematics.

• Corr_out: This file contains all pertinent information for the applied corrections, such as multiple scattering effects, ionization energy loss effects, and radiation effects.

• Optic_std: This file includes the positions and angles information of the events through the spectrometer.

• FP_out: This file contains all particle coordinates at the HRS Focal Plane, after applying all the required cuts and corrections.

In addition to the above files, there are other output files involving more details for investigating the effects of the different corrections and cuts. Figure 4.2 shows a schematic diagram of the program with the input and output files.

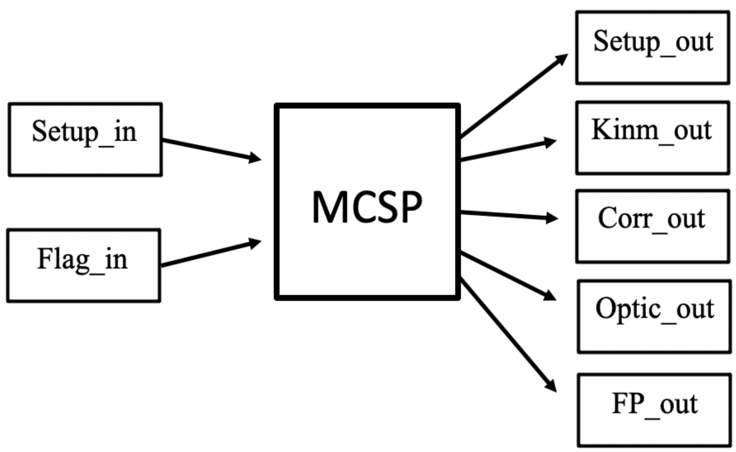

Figure 4.2: A schematic diagram of the program with the input and output files.

4.4 Selection of Running Conditions

The running conditions are given to the code by a set of parameters and logic flags. The parameters are given to the program either by the main input file Setup_in or calculated in the program. Examples of the main input file parameters are the target properties (length, density, etc.), the total number of tries, and the incident beam energy. Some of the calculated parameters are the energy and momentum of recoil and scattered particles at the scattering vertex. The logic flags are read from the Flag_in file. Examples of the flags in this file are the corrections flags, which turn on or off some applied corrections such as ionization and radiation energy loss, and one that sets the mass of the recoil particles.

4.5 MCSP Main Program Structure

The MCSP program simulation code's main part is the Monte Carlo loop. The loop will be executed numerous times, depending on the maximum number of trials in the MCSP Setup_in file. This part of the program consists of the sequence of operations for the simulation and sorting out of the events.

Before starting the main MCSP loop, the program calculates, for each kinematic setting, the central energy for the scattered electron. The corresponding energy, momentum, and angle for the recoil particle are calculated using the kinematic equations given in Section 1.4. The central values correspond to scattering happening at the center of the target which is at the center of the Hall. The coordinate system used is shown in Figure 4.3.

In the present work, data from five different kinematic settings were simulated and analyzed. Each kinematic setting was defined by the given central values of beam energy E and scattering angle Θ_e, and the calculated central values of the scattered electron energy E', recoil momentum P_r, and recoil angle Θ_r. Shown in Table 4.1 the central kinematic values for e-^{4}He elastic scattering.

At the start of the Monte Carlo event loop, the sequence of operations begins with the generation of elastic electron-nucleus scattering events in the target coordinate

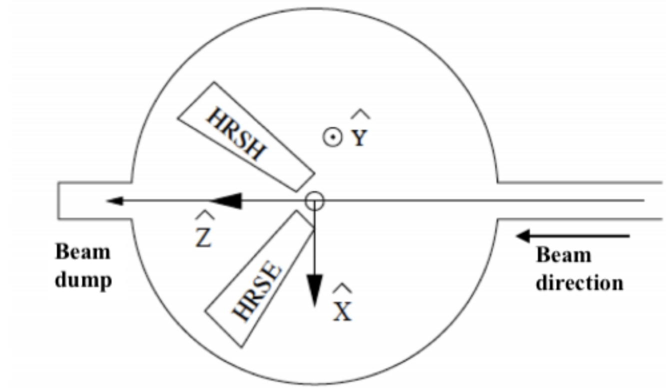

Figure 4.3: The Target Coordinate System (TCS) used in the Monte Carlo program (top view).

Kinematic	Kin34	Kin39	Kin45	Kin50	Kin55
Q^2 (fm^{-2})	33.6	38.9	44.4	49.9	54.7
E (GeV)	2.0941	2.0941	4.0506	4.0508	4.0512
Θ_e (^{o})	33.198	36.108	19.252	20.404	21.556
E' (GeV)	1.914	1.886	3.815	3.784	3.761
P_r (GeV/c)	1.091	1.194	1.295	1.377	1.458
Θ_r (^{o})	65.037	63.022	70.513	69.419	68.337

Table 4.1: The central kinematic variables for each kinematic setting (for an event with scattering vertex at the center of the target) for elastic e-^{4}He scattering.

system (TCS). The TCS is, in the Monte Carlo program, a right-handed coordinate system with the origin at the target center. The positive Z-axis is along the beam direction, the positive Y-axis is up vertical, and the positive X-axis points to the left of the beam direction as seen in Figure 4.3.

The interaction vertex position of the event is defined in the TCS as: $(x_{trg},\ y_{trg},\ z_{trg})$. The z_{trg} position of the event is generated using random numbers uniformly distributed over the target length L, in the interval $[-L/2,\ L/2]$. The x and y coordinates of the interaction vertex x_{trg}, y_{trg} are generated taking into account the dimensions of the beam spot size. The electron scattering angles ($\theta_e,\ \phi_e$) are generated with respect to the electron spectrometer axis using random numbers uniformly distributed between predefined limits $[-\theta_{lim},\ \theta_{lim}]$ and $[-\phi_{lim},\ \phi_{lim}]$, respectively. Here, θ_e is in non-dispersive direction (in-plane) and ϕ_e is in the dispersive direction (out-of plane). The interval limits of the electron angles are chosen to be larger than the nominal angular acceptance limits of the HRS ($\pm$30 mrad in the horizontal, $\pm$60 mrad in the vertical, approximately) to avoid any loss of good events. The energy of the incident electron is modeled using a Gaussian distribution of random numbers around the central beam energy with a width of $\Delta E/E = 10^{-4}$.

In the quasielastic e-^{3}He scattering scenario, the ^{3}He particle within ^{4}He nucleus is not stationary but has a momentum P_t and angular directions $\theta_t,\ \phi_t$. In addition to all of the above, to satisfy the elastic scattering criteria for non-stationary target, more quantities need to be generated. The ^{3}He cluster directions within the target nuclei are generated using random numbers uniformly distributed to cover all possible directions. Thus, θ_t (the in-plane angle relative to the beam direction) is generated within the range [-180^o, 180^o], and ϕ_t (the out-plane angle), is generated within [-90^o, 90^o]. Figure 4.5 shows an example of the direction of the movement of the ^{3}He cluster.

The momenta of the ^{3}He nuclei are determined from a Fermi momentum distribution. It is the same distribution that describes moving nucleons in a nucleus. This distribution is specified by a spectral function which can take a simple form as a Fermi gas spectral function or a more complicated one as a Benhar-Fantoni spectral function. In the present work, the recent effective spectral function (ESF) that reproduces the kinematics of the final state lepton predicted by ψ' superscaling function

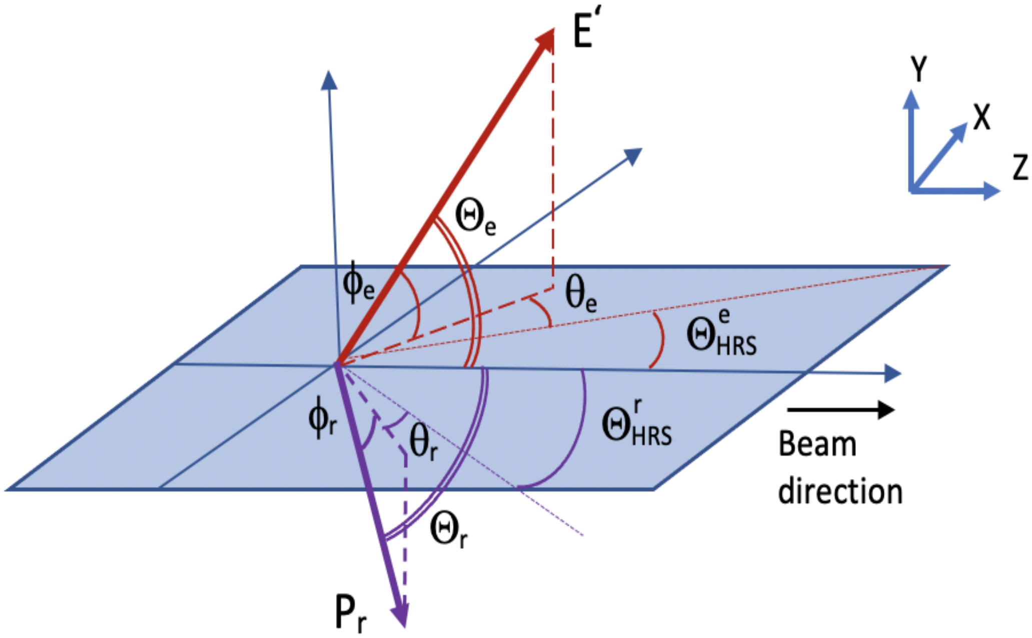

Figure 4.4: Angular coordinates of the scattered electron and recoil nucleus in the target. Θ^e_{HRS} and Θ^r_{HRS} are the central values where the spectrometers were set. The dotted lines are the axes of the LHRS and RHRS spectrometers. Θ_e and Θ_r are the physical angles for a particular scattered electron and corresponding recoil nucleus, respectively. $\theta_{e,r}$ and $\phi_{e,r}$ are the angles with respect to spectrometer axes.

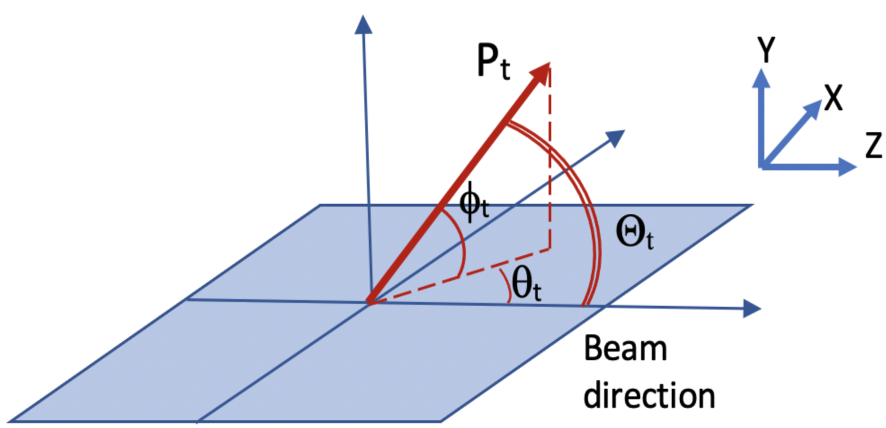

Figure 4.5: Angular coordinates of ^{3}He moving nuclei in the target.

for quasielastic scattering was used to simulate the momentum distribution of ^{3}He clusters within ^{4}He nuclei [74]. The probability distribution for a nucleon in a nucleus to have momentum k can be described as [75]:

$$P(k)dk = 4\pi k^2 |\phi(k)|^2 dk \tag{4.1}$$

where $P(k)$ is zero for $k > 0.7$ GeV, and for $k < 0.7$ GeV is given by:

$$P(k)dk = \frac{\pi}{4c_o}\frac{1}{N}(a_s + a_p + a_t)y^2 \tag{4.2}$$

Here:

$$\begin{aligned} y &= \frac{k}{c_o} \\ a_s &= c_1\ e^{(-b_s y)^2} \\ a_p &= c_2(b_p y)^2\ e^{(-b_p y)^2} \\ a_t &= c_3 y^\beta\ e^{-\alpha(y-2)} \end{aligned} \tag{4.3}$$

where $c_o = 0.197$ and the quantities $c_1,\ c_2,\ c_3,\ b_s,\ b_p,\ \alpha,\ \beta$ and N depend on the particular nucleus in question. The parameter k is in GeV and N is a normalization factor (it normalizes the integral of the momentum distribution from $k = 0$ to $k = 0.7$ to 1.0 GeV). The values of the above parameters are given for selected nuclei including ^{4}He in Reference [75]. Figure 4.6 shows the momentum distribution of the effective spectral function for the ^{4}He nucleus, as simulated in this thesis work.

The corresponding energy and momentum of scattered electrons and the recoil nuclei momentum, energy and angles are calculated from elastic kinematics at the interaction vertex. The directions ($\theta_r,\ \phi_r$) for the recoil nucleus at the TCS are calculated from conservation of momentum. However, this is done after the required corrections for ionization and radiation energy loss in the target material is taken into account for the incident energy beam.

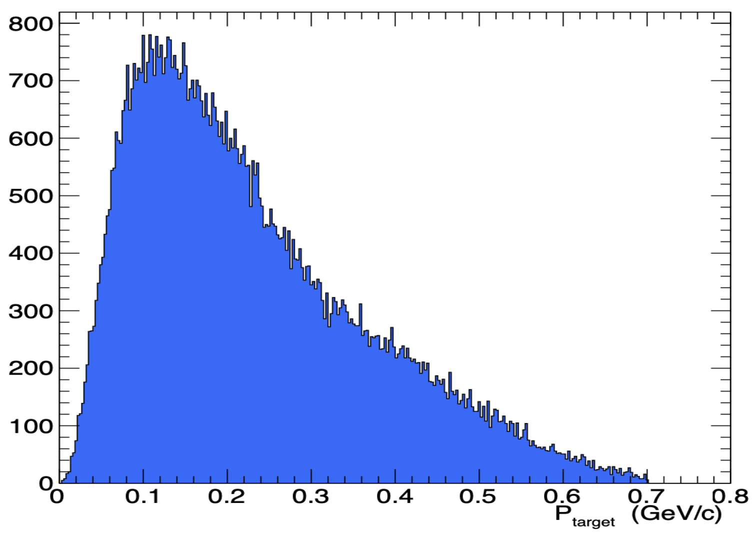

Figure 4.6: The momentum distribution of ^{3}He clusters within ^{4}He nuclei.

The scattered and recoil particles' coordinates are rotated from the target coordinate system to the spectrometer coordinate system by the central angle values Θ^e_{HRS} and Θ^r_{HRS} corresponding to the central beam ray around the Y-axis using a rotation matrix. The event's coordinates in the target are distributed over the target length, and depend on the beam dimensions [76]. Therefore, the particle coordinates are projected to the origin ($z = 0$) before applying the transport (discussed in detail in Section 4.9) or drift method.

4.6 Applied Corrections

As charged particles travel through a material, they interact with the nuclei and electrons of the material. The probability that a charged particle passes unscattered through a material without an interaction is very small. Two principles characterize each interaction: a loss in the energy and a deflection in the direction of the particle. These effects primarily occur through Coulomb forces as a result of elastic scattering from nuclei and inelastic collisions from atomic electrons of the materials. Losses and deflections occur many times per unit length in the material and add up statistically.

A charged particle may lose energy, in general, in one of the four possible following ways: 1) Coulomb interactions with atomic electrons, 2) Bremsstrahlung (emission of electromagnetic radiation) in the field of a nucleus, 3) Nuclear interactions, 4) Emission of Cherenkov radiation [77]. The energy loss due to nuclear interactions and Cherenkov radiation may be neglected since they constitute a tiny fraction of the energy loss [78].

An excellent understanding of the passage of particles through matter is crucial in experimental nuclear physics. It is an important part of the analysis and the Monte Carlo simulation performed in this work. The Coulomb multiple scattering and energy loss due to ionization and radiation must be accurately determined and associated corrections must be applied. In this experiment, the electron and recoil events passed through several layers of materials. The incident electron passed through some part of the gaseous target and the target upstream cell endcap before it got scattered by a nucleus. After scattering, the scattered electron and recoil nucleus passed through: 1) some part of the gaseous material and either the downstream endcap or the side wall of the target cell, 2) the scattering chamber exit window, 3) the air gap between the target chamber and the spectrometer entrance, and 4) the spectrometer entrance window. Table 4.2 provides a summary of the type and thickness of the above materials.

4.6.1 Multiple Scattering

A charged particle passing through a medium suffers many small-angle interactions due to elastic Coulomb scattering from nuclei as described by the Rutherford

Materials	Thickness (cm)
Target length (^{4}He)	20.0
Target radius (^{4}He)	1.0
Wall of target (^{27}Al)	0.0161
Endcap of the wall (^{27}Al)	0.0137
Scattering chamber exit window (^{27}Al)	0.0381 in LHRS
	0.0305 in RHRS
Air gap	54.0
Spectrometer entrance window (Kapton)	0.0178 in LHRS
	0.0179 in RHRS

Table 4.2: The materials and thickness that detected particles pass through. The numbers in the table are used for the simulation of different physical process in the materials.

cross section. The net effect of these many small-angle scatterings is the deflection of the particle from its original direction. The resulting angular distribution from these Coulomb scatterings is described in detail by Molière [79]. The probability distribution of these multiple scattering follows, for small deflection angle θ, a Gaussian distribution of the form:

$$P(\theta)d\theta \simeq \frac{1}{\pi\langle\theta^2\rangle}\ \exp\left(\frac{-\theta^2}{\langle\theta^2\rangle}\right)d\theta \tag{4.4}$$

The mean square root (rms) of the resultant θ is given by [80]:

$$\theta_{rms} = \langle\theta^2\rangle^{1/2} = \left[\frac{0.157\ Z(Z+1)z^2t}{A(pv)^2}\ln\left[1.13\times 10^4 Z^{\frac{4}{3}}z^2tA^{-1}\beta^{-2}\right]\right]^{1/2} \tag{4.5}$$

Here p, v and z are the momentum, velocity, and charge number of the incident particle, and A, Z and t are the mass number, atomic number, and length (in g/cm^2) of the scattering medium.

A convenient approximation formula to determine well the standard deviation

(θ_{rms} in radian) for all Z, especially for small Z, is obtained by Lynch and Dahl [81]:

$$\begin{aligned}\theta_{rms} &= 13.6\,\frac{z\,[\mathrm{MeV}/c]}{p\beta}\sqrt{\frac{x}{L_{rad}}}\left(1+0.088\log_{10}\frac{x}{L_{rad}}\right)\\ &= 13.6\,\frac{z\,[\mathrm{MeV}/c]}{p\beta}\sqrt{\frac{x}{L_{rad}}}\left(1+0.038\ln\frac{x}{L_{rad}}\right)\end{aligned}\tag{4.6}$$

where x and L_{rad} are the thickness and radiation length of the material in cm.

The multiple scattering effect for the incident and scattered electrons and recoil nuclei due to the Coulomb field of the target are incorporated and calculated for all target materials and the materials between the target and spectrometer window. The standard deviation θ_{rms} is calculated using Equation (4.6) and the angle θ is generated by means of a Gaussian distribution of random numbers of standard deviation equal to θ_{rms}. All angles (electron and recoil) are corrected for multiple scattering.

4.6.2 Energy Loss Due to Ionization and Excitation

When charged particles pass through materials, they lose energy by ionizing or exciting the materials' atoms due to collisions with atomic electrons. The liberated particles from the collision may in turn make a new collision if they acquire the energy needed, and contribute in the production of ionization and excitation. Each collision has a different probability to occur due to the statistical nature of these processes. Therefore, the energy loss is subject to appreciable fluctuation about the most probable energy loss ΔE_{prob}. The most probable energy loss can be obtained using the Landau formula [82]:

$$\Delta E_{prob} = \frac{2\pi n e^4 z^2 t}{m_e c^2 \beta^2 \rho}\left[\ln\frac{4\pi n e^4 z^2 t}{I^2(1-\beta^2)\rho} - \beta^2 + 0.198 - \delta - U\right]\tag{4.7}$$

where:

e is the electronic charge,

$m_e c^2$ is the rest energy of the electron (0.511 MeV),

z is the charge of the incident particles,

n is the electron density (number of atoms per cm^3 in the material),

$\beta = v/c$, where v is the velocity of the particles and c is the speed of light,

ρ is the density of the material in g/cm^3,

t is the path length of the particles in the material in g/cm^2,

I is the mean excitation potential of the absorbing material in eV, which is given by:

$$\begin{aligned} I &= 12Z + 7 && Z < 13 \\ I &= 9.76Z + 58.8Z^{-0.19} && Z \geq 13 \end{aligned} \tag{4.8}$$

with δ being the density effect correction due to the polarization of the atoms along the path of the incoming particles. The expression of δ is given by the Sternheimer parametrization as follows [83, 84]:

$$\delta = \begin{cases} 0 & (X < X_o) \\ 4.606X + C + a(X_1 - X)^m & (X_o < X < X_1) \\ 4.606X + C & (X > X_1) \end{cases} \tag{4.9}$$

where the quantities a, m, X_0 and X_1 are parameters depending on the absorbing material and can be found in tables in Reference [84]. The parameter X is given by:

$$X = \log_{10}\left(\frac{P}{m_o c}\right) \tag{4.10}$$

where P and m_o are the momentum and mass of the incident particles. The parameter C is given by:

$$C = -2\ln\frac{I}{h\nu_p} - 1 \tag{4.11}$$

where $h\nu_p$ in eV is the plasma frequency of the material and defined as:

$$h\nu_p = h\sqrt{\frac{ne^2}{\pi m_e}} = 28.8\sqrt{\rho\left\langle\frac{Z}{A_o}\right\rangle} \tag{4.12}$$

where Z and A_o are the atomic and mass number of the material.

U is the shell correction due to non-participation of the incident particles in the inner shells for very low incident energy and is very small. The factor U is given empirically by [77]:

$$\begin{aligned} U(I,\eta) = \;& (0.422377\ \eta^{-2} + 0.0304043\ \eta^{-4} + 0.00038106\ \eta^{-6}) \times 10^{-6} I^2 \\ & + (3.850190\ \eta^{-2} + 0.1667989\ \eta^{-4} + 0.00157955\ \eta^{-6}) \times 10^{-9} I^3 \end{aligned} \tag{4.13}$$

where $\eta = P/m_o c$.

To simplify the calculation, the Landau expression in Equation (4.7) can be written in terms of a parameter A and a parameter B as follows [82]:

$$\Delta E_{prob} = \frac{At}{\beta^2}\left(B + \ln\frac{At}{\beta^2} + 2\ln\frac{P}{m_o c} - \beta^2 + 0.198 - \delta - U\right) \tag{4.14}$$

where parameters A and B are defined as:

$$A = \frac{2\pi n e^4 z^2}{m_e c^2 \rho} = \frac{0.154 z^2 Z}{A_o} \tag{4.15}$$

$$B = \ln\frac{m_e c^2 10^6}{I^2} \tag{4.16}$$

The parameter A is given in MeVc^2/g and ΔE_{prob} in MeV. In the case where the particles pass through a compound or mixture of several elements, the effective atomic number and atomic weight should be used, and Z/A_o is replaced by [85]:

$$\left\langle \frac{Z}{A_o} \right\rangle = \sum_i w_i \frac{Z_i}{A_i} \tag{4.17}$$

where w_i is the weight fraction of the ith element, and Z_i and A_i are the atomic and mass numbers of ith element, respectively.

Energy Loss Distribution

The shape of the energy loss distribution is defined by a parameter $\mathcal{K}$, for a given particle type, and given by [86, 87]:

$$\mathcal{K} = \frac{\xi}{\epsilon_{max}} \tag{4.18}$$

where ξ is the mean energy loss in MeV as [87]:

$$\xi = \frac{2\pi n e^4 z^2 t}{m_e v^2}\frac{Z}{A_o} = \frac{0.154 z^2 Z t}{\beta^2 A_o} \tag{4.19}$$

and ϵ_{max} is the maximum energy transfer in a collision between an incident particle and an atomic electron, approximately given by:

$$\epsilon_{max} = \begin{cases} \dfrac{2m_e v^2}{1-\beta^2} & \text{for a heavy incident particle} \\ \dfrac{T_e}{2} & \text{for incident electrons} \end{cases} \tag{4.20}$$

where T_e is the electron's kinetic energy.

Based upon on the parameter $\mathcal{K}$, the ratio of the total energy loss to the maximum possible energy loss in a single collision, there are three basic cases to be considered: (a) $\mathcal{K} \geq 1.00$: here $\xi \geq \epsilon_{max}$. There are no large energy transfers and the effect of fluctuations is negligible. The energy loss distribution becomes Gaussian with a variance obtained in terms of the path length t by [86]:

$$\sigma^2 = 4\pi n e^4 z^2 t = \frac{0.307 z^2 Z t}{A_o m_e c^2} \tag{4.21}$$

(b) $\mathcal{K} \leq 0.01$: this case is the opposite of the previous one where $\xi \leq \epsilon_{max}$. The energy loss follows the Landau distribution which is asymmetric with a long high-energy loss tail and a broad peak. If ΔE is the observed energy loss, the Landau distribution is given by using a universal function $\phi(\lambda)$ defined by [88]:

$$\phi(\lambda) = \frac{1}{2i\pi}\int_{\sigma-i\infty}^{\sigma+i\infty} \exp(u \;\ln u + \lambda u)du \tag{4.22}$$

where parameter λ is given in the term of the mean energy loss and the most probable energy loss:

$$\lambda = \frac{\Delta E - \Delta E_{prob}}{\xi} \tag{4.23}$$

(c) $0.01 < \mathcal{K} < 1.00$: the energy loss has a Symon distribution shape [90]. Unfortunately, the application of Symon's distribution to specific case needs considerable manipulation and extrapolation of his results. His results are expressed in a graphic form which make them inconvenient for a practical application [90, 77].

Therefore, in the present work, the energy loss distribution is taken a Landau distribution for $\mathcal{K} \leq 0.1$, and a Gaussian distribution for $\mathcal{K} \geq 0.1$.

In order to ensure that the simulation simulates well the experiment, the energy loss subroutine in the code computes the probable energy loss as follows:

1- The energy that the incident electron loses due to passing through the upstream endcap and the gas target length are calculated for each event, and the energy loss, ΔE_{prob}, are subtracted from the measured beam energy, $E_{Cor} = E - \Delta E_{prob}$.

2- A scattered energy E'_{new} is calculated corresponding to E_{Cor}. Then, the energy loss of the scattered electrons $\Delta E'_{prob}$ due to passing through the remaining gas target length, the target cell wall or the downstream endcap, the scattered chamber exit window, and the spectrometer entrance window are calculated and subtracted from the new calculated scattered energy, $E'_{Cor} = E'_{new} - \Delta E'_{prob}$.

3- A new recoil energy $E_{rec,new}$ is calculated. The energy loss of the recoil particles $\Delta E_{rec,prob}$ due to passing through the remaining gas target length, the target cell wall or the downstream endcap, the scattered chamber exit window, and the spectrometer entrance window are calculated and subtracted from the new calculated energy, $E_{rec,Cor} = E_{rec,new} - \Delta E_{rec,prob}$.

The most probable energy loss is obtained, for all particles, from Equation (4.15). The energy loss distribution of the recoil particles, ^{3}He and ^{4}He, follows a Gaussian distribution with rms given by Equation (4.21). The energy loss of both incident and scattered electrons follows a Landau distribution around the most probable energy loss. The Landau distribution is created in the code using the formalism of Tabata and Ito [89] and Equation (4.23).

4.6.3 Radiative Corrections

It is well known that in any scattering process involving charged particles, such as an electron, photons are radiated [91]. The effect of these radiative-nature process results in important corrections in the analysis of electron scattering experiments and simulations. The Feynman diagram representing the process of electron scattering via a single-photon exchange, the Born approximation, in the lowest order of the fine structure function α is given in Figure 4.7. However, during an actual experiment, higher order processes in α beyond the Born approximation may have large contributions to the scattering process. These high order processes include vacuum polarization, vertex correction and Bremsstrahlung. Bremsstrahlung is referred to the radiation of real photons by incoming or outgoing electrons during the interaction due to deceleration in the field of the nucleus. Vacuum polarization is when the exchanged virtual photon annihilates into a particle-antiparticle pair, which in turn reannihilates back to a virtual photon. Vertex correction is the emission and reabsorption of a virtual photon by the incoming and outgoing electron during the interaction.

The radiative effects can be classified into two types: internal and external processes. The internal processes imply the emission of real or virtual photons at the vertex during the elastic scattering and include vacuum polarization, vertex processes and internal bremsstrahlung. On the other hand, the external processes occur when the incoming and outcoming electron pass through the materials of the target and emit real photons before and after the scattering. All of the higher order process mentioned above pictured in Figure 4.7 must be considered, calculated and accounted for, and are known as the Radiative Correction. In this section, we will describe the method to compute the radiative corrections in order to allow a comparison between the experiment and the simulation.

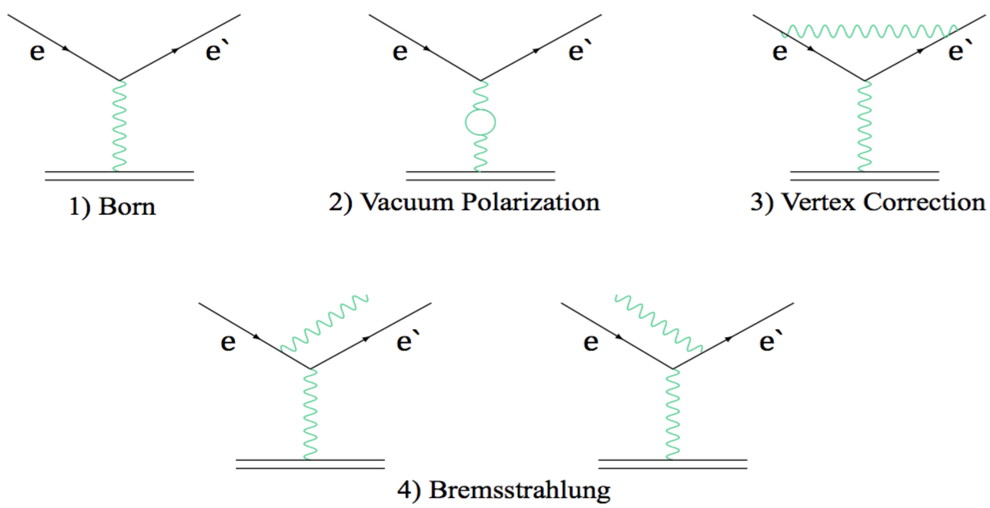

Figure 4.7: 1) Lowest order Feynman diagram with a single-photon exchange for electron-nucleon scattering (Born approximation). 2-4) Feynman diagrams for higher order radiative processes to the single-photon exchange approximation for electron nucleus scattering.

Including all radiation processes mentioned above, in the absence of other corrections, the differential cross section formulation for electron with incident energy E scattered at an angle Θ to a final energy E' from a target of radiation length T is given by Mo-Tsai as [92]:

$$\sigma_{exp}(E, E', \Theta) = \frac{d\sigma_{exp}}{d\Omega dE'} = \int_0^T \frac{dT}{T} \int_{E_{min}}^{E} dE_1 \int_{E'}^{E'_{max}} dE'_1 \; I_e(E, E_1, t)\; \sigma_{rad}(E_1, E'_1, \Theta)\; I'_e(E', E'_1, T-t) \tag{4.24}$$

where:

$I_e(E, E_1, t)$ is the probability of finding an electron starting at initial energy E and straggling down to E_1 after traveling a distance t radiation length in the target.

$I'_e(E', E'_1, T-t)$ is the probability of finding an electron after the scattering at initial energy E'_1 and straggling down to E' after passing through the rest of the target.

$\sigma_{rad}(E_1, E'_1, \Theta)$ is the basic elastic scattering cross section at incident energyE_1 to final energy E'_1 at an angle Θ including all internal radiation and vertex corrections.

Following the assumption by Mo and Tsai [93], in any practical application of the radiative corrections, the shape of internal bremsstrahlung is similar to that of external bremsstrahlung. The internal bremsstrahlung has roughly the same effect as that given by two external equivalent radiators with one placed before and one after the scattering, each of thickness:

$$t_{eq} = \frac{\alpha}{b\,\pi}\left[\ln\frac{Q^2}{m_e^2} - 1\right] \tag{4.25}$$

where the quantity b is a number very close to 4/3, and depends weakly on the atomic number of the target material Z and given by:

$$b = \frac{4}{3}\left\{1 + \frac{1}{9}\left[\frac{(Z+1)}{(Z+\xi)}\right]\left[\ln(183\; Z^{\frac{-1}{3}})\right]^{-1}\right\} \tag{4.26}$$

and

$$\xi = \frac{\ln(1440\; Z^{\frac{-2}{3}})}{\ln(183\; Z^{\frac{-1}{3}})} \tag{4.27}$$

The changes in the interaction vertex due to radiative effects are included in the factor:

$$F(Q^2, 0) = 1 + \delta' \tag{4.28}$$

Here the expression for δ' containing these effects is provided by Tsai [93].

The probability of external bremsstrahlung expression before and after the elastic scattering when $E > 100$ MeV and near the elastic peak is given by Tsai as:

$$\begin{aligned} I_e(E, E_1, t) &= \frac{bt}{\Gamma(1+bt)} \left(\frac{E-E_1}{E}\right)^{bt} \frac{1}{E-E_1} \qquad \text{(Before)} \\ I'_e(E'_1, E', t') &= \frac{bt'}{\Gamma(1+bt')} \left(\frac{E'_1-E'}{E'_1}\right)^{bt'} \frac{1}{E'_1-E'} \qquad \text{(After)} \end{aligned} \tag{4.29}$$

From Equations (4.28), (4.29) and (4.24) after applying the external equivalent radiators t_{eq} and removing the integral over the target thickness, the following expression for the radiative tail is obtained:

$$\begin{aligned} \frac{d\sigma_{exp}(E, E', \Theta, t)}{d\Omega dE'} &= \int_{E_{min}}^{E} dE_1 \, \frac{bT'_b}{\Gamma(1+bt_b)} \left(\frac{E-E_1}{E}\right)^{bT'_b} \frac{1}{E-E_1} \\ & \frac{d\sigma(E_1, \Theta)}{d\Omega}(1+\delta') \, \frac{bT'_a}{\Gamma(1+bt_a)} \left(\frac{E'_1-E'}{E'_1}\right)^{bT'_a} \frac{1}{E'_1-E'} \end{aligned} \tag{4.30}$$

where:

$$\begin{aligned} T'_b &= t_b + t_{eq} \\ T'_a &= t_a + t_{eq} \end{aligned} \tag{4.31}$$

with T'_b and T'_a being the effective radiator lengths before and after scattering, and t_b and t_a are the real radiation lengths before and after the scattering. The integral over dE_1 in Equation (4.31) is accomplished in the Monte Carlo following the formalism given by Miller [91, 90] as follows:

If R is a random number uniformly distributed in the interval [0,1], then the quantity

$$\Delta E = E \; R^{\frac{1}{bT'_b}} \tag{4.32}$$

will be distributed like:

$$\frac{bT_b'}{\Delta E}\left(\frac{\Delta E}{E}\right)^{bT_b'} \tag{4.33}$$

which is the distribution of soft photon energy losses before the scattering for an equivalent radiator T_b'. Similarly, the distribution of soft photon energy losses after the scattering is given by:

$$\Delta E' = E' \; R^{\frac{1}{bT_a'}} \tag{4.34}$$

In the simulation, the radiation correction was calculated based on the Mo and Tsai formalism described above. In the first step, a random number R is uniformly generated from [0,1] following the Miller formalism. Then, for each event uniformly distributed along the target length, the effective radiator before T_b and after T_a are calculated for all the materials the electron passes through. In the third step the radiative corrections ΔE are calculated.

In order to ensure that the simulation performed consistently, the radiative corrections are computed as follows:

1- For the incident electron, the energy loss ΔE due to passing though the materials (the target cell endcap and the gas up to interaction vertex) is calculated for each event using Equation (4.32). The incident energy E is corrected the by amount ΔE as $E_{rad} = E - \Delta E$ taken into consideration the ionization correction.

2- From the kinematics, the new scattered energy E' is calculated at the vertex. The energy loss of the scattered electrons $\Delta E'$ due to passing through the materials (the remaining of the target length, the target cell wall or downstream endcap, the scattering chamber exit window, air, the spectrometer entrance window) are obtained, i.e $E'_{rad} = E' - \Delta E'$.

3- The recoil events are affected by the radiation effects from the incident electrons before the scattering at the vertex, so there is a change in their energy E_{rec}.

Figures 4.8 to 4.12 show the applications of the different corrections on the incident beam, scattered and recoil particles for e-^{4}He and e-^{3}He scattering. The ionization energy loss of the incident and scattered electron shifts the centroid of the energy distribution by the amount ΔE_{prob}. The radiative energy loss of the incident and scattered electron causes a tail at the low energy side, but it does not shift the centroid of the energy. The ionization energy loss shifts the recoil centroid, the tail is an outcome mainly of the incident beam radiation tail. These effects can be seen clearly in the e-^{4}He elastic scattering process. However, in the e-^{3}He scattering process, the energy peak width is large due to the momentum P_t spread of ^{3}He nucleus within ^{4}He target. In the end, the radiative tail will be cut away as the events pass through the spectrometer, and only a very clean sample of events with a small tail will reach the Focal Plane.

The evolution of the incident beam energy distribution after application of corrections

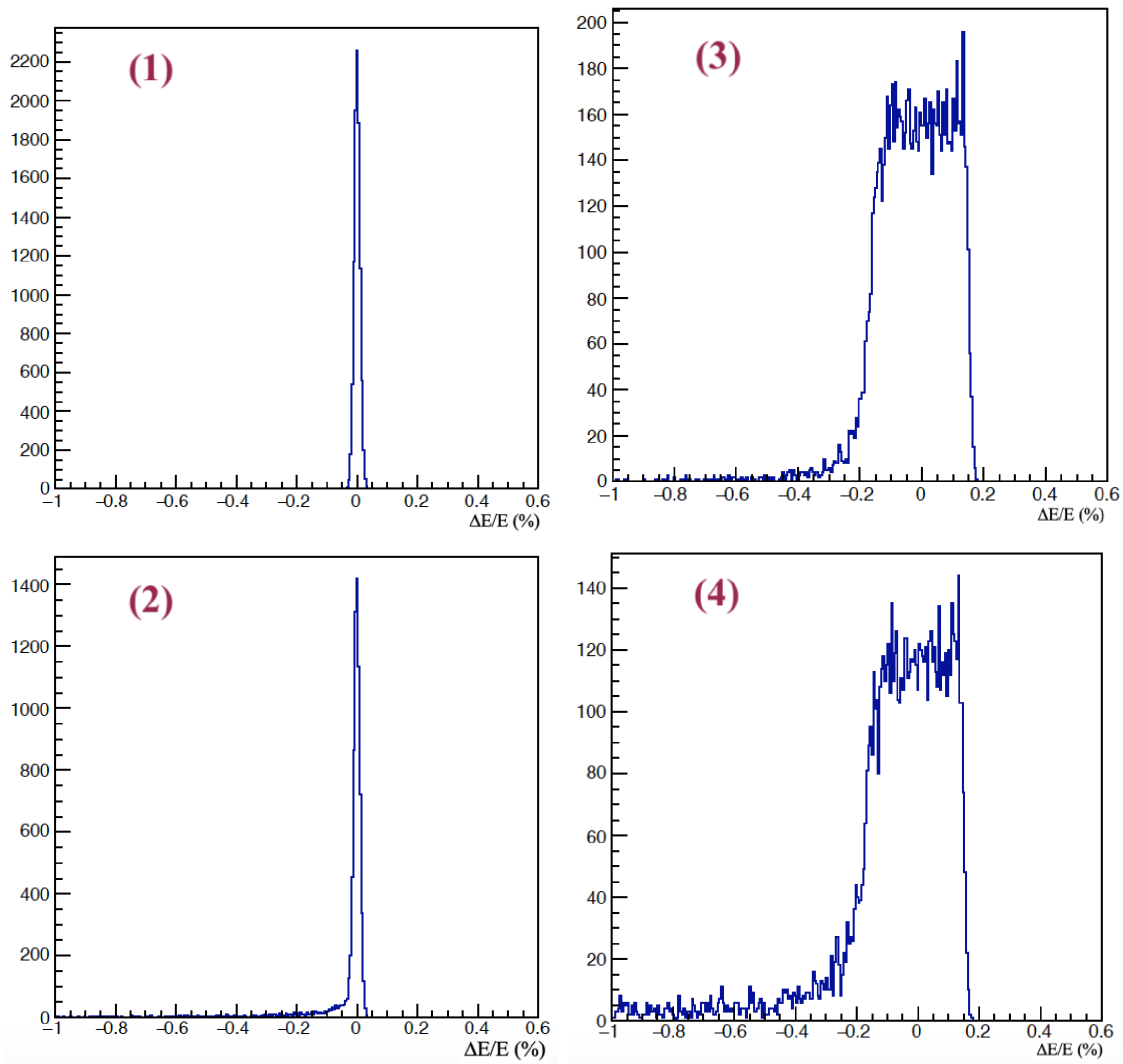

Figure 4.8: Incident energy distribution $\Delta E/E$ at the interaction vertex. 1- Uncorrected distribution. 2- After radiation energy loss correction. 3- After ionization loss correction. 4- With inclusion of both radiation and ionization energy loss corrections.

The evolution of the scattered electron energy distribution in the e-^{4}He scattering process

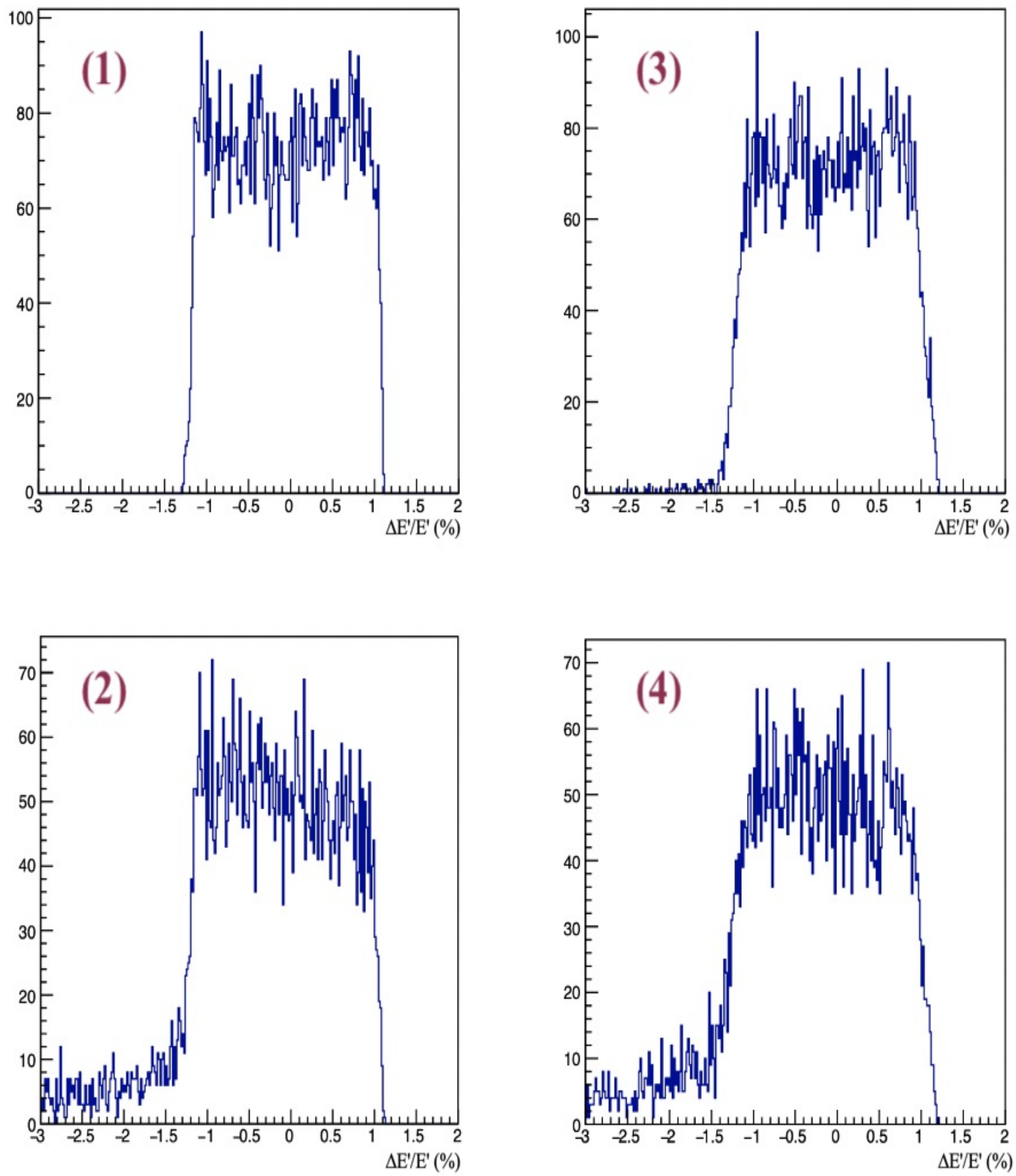

Figure 4.9: Scattered electrons energy distribution $\Delta E'/E'$ at the interaction vertex. 1- Uncorrected distribution. 2- After radiation energy loss correction. 3- After ionization loss correction. 4- With inclusion of both radiation and ionization energy loss corrections.

The evolution of the recoil nucleus energy distribution in the e-^{4}He scattering process

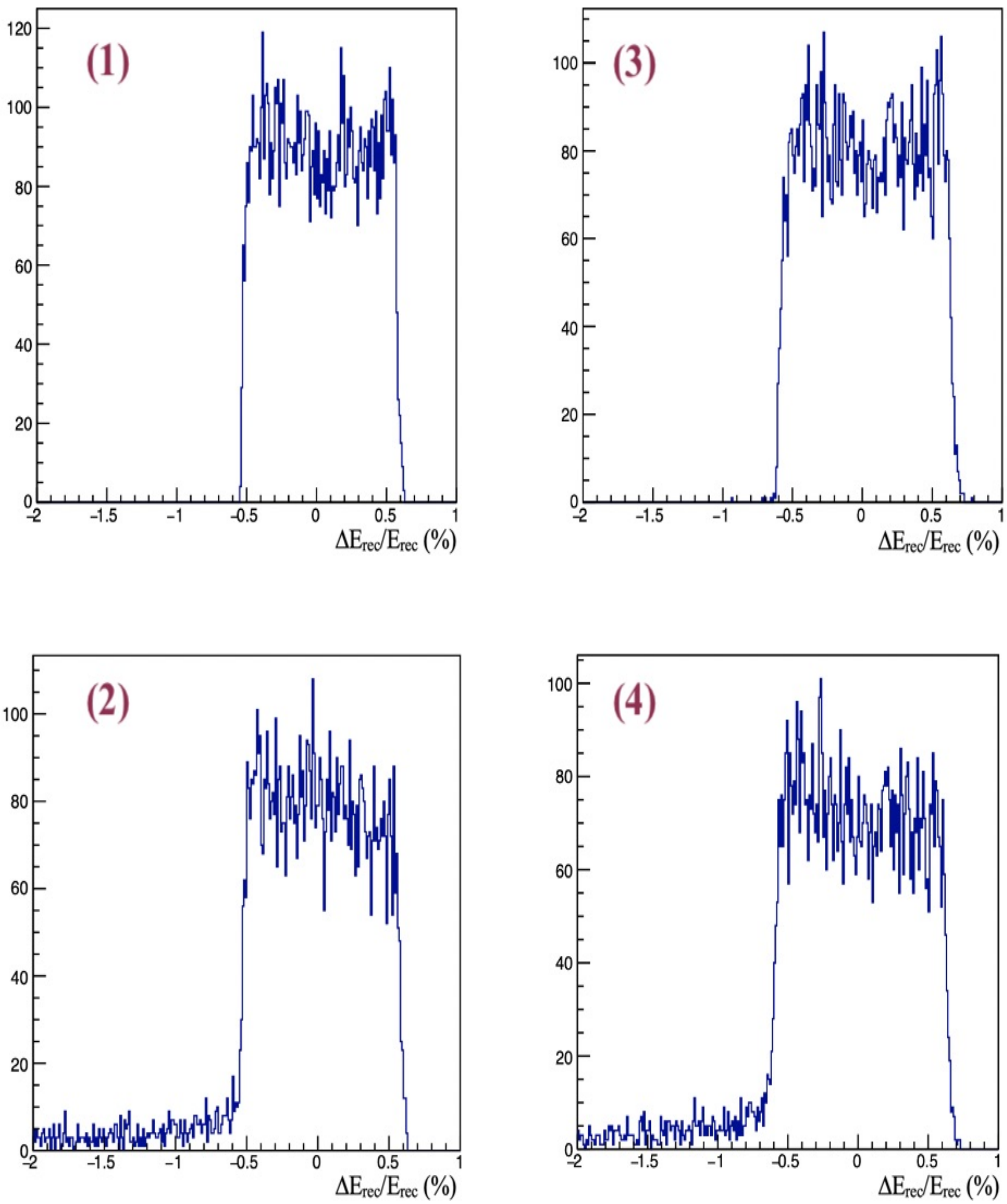

Figure 4.10: Recoil energy distribution $\Delta E_{rec}/E_{rec}$ at the interaction vertex. 1- Uncorrected distribution. 2- After electron radiation energy loss correction. 3- After ionization loss correction. 4- With inclusion of both radiation and ionization energy loss corrections.

The evolution of the scattered electron energy distribution in the e-^{3}He scattering process

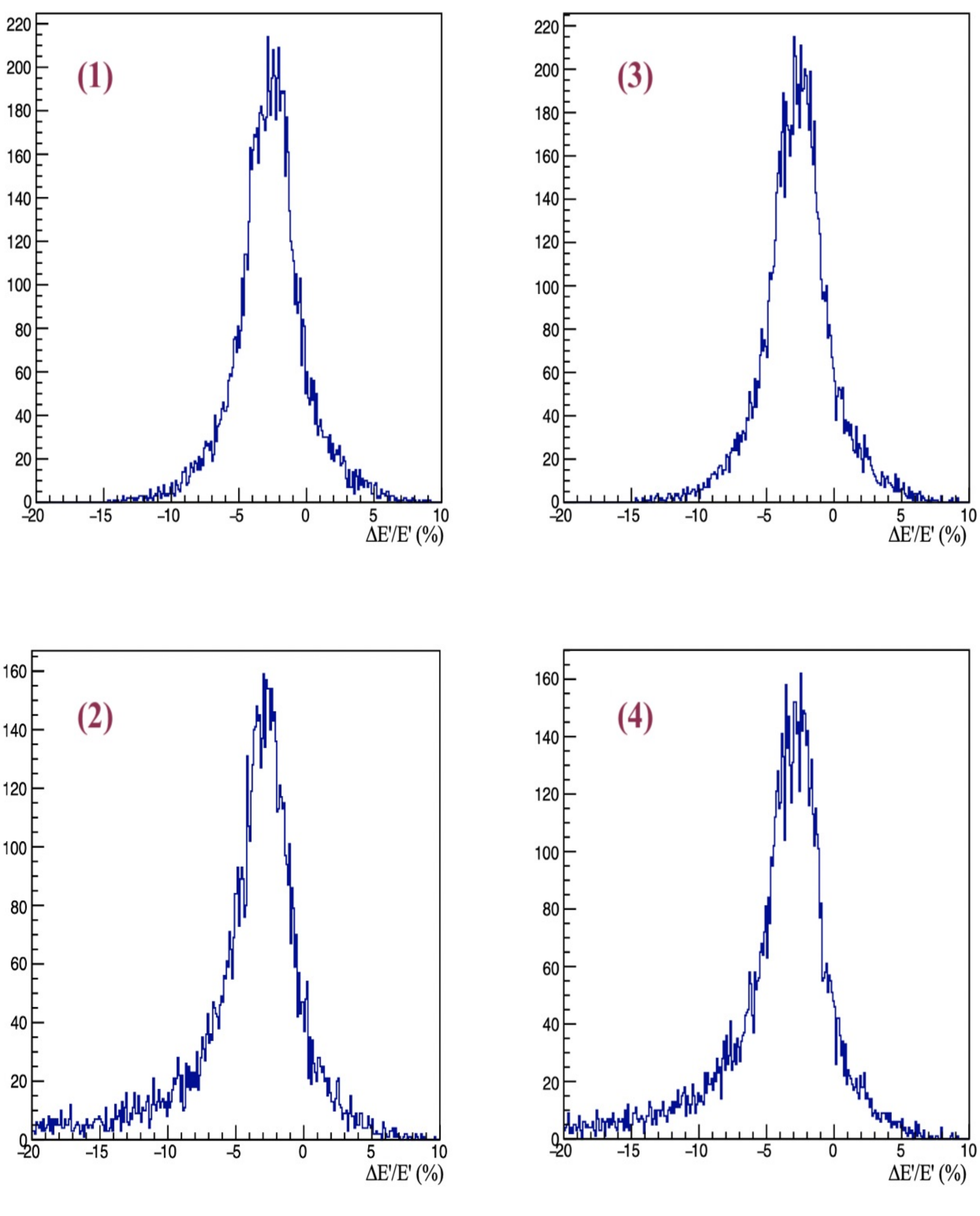

Figure 4.11: Scattered electrons energy distribution $\Delta E'/E'$ at the interaction vertex. 1- Uncorrected distribution. 2- After radiation energy loss correction. 3- After ionization loss correction. 4- With inclusion of both radiation and ionization energy loss corrections.

The evolution of the recoil nucleus energy distribution in the e-^{3}He scattering process

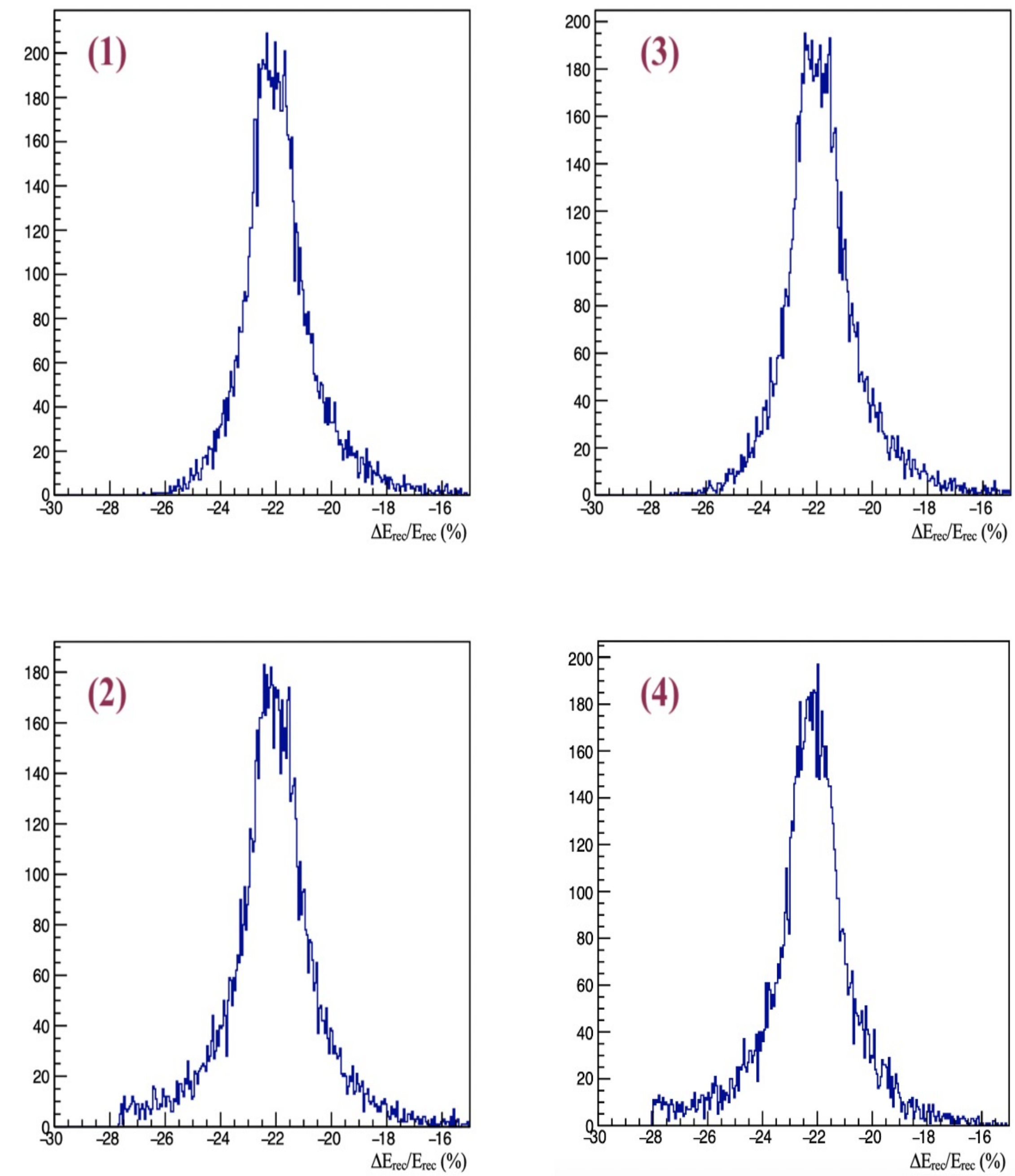

Figure 4.12: Recoil energy distribution $\Delta E_{rec}/E_{rec}$ at the interaction vertex. 1- Uncorrected distribution. 2- After electron radiation energy loss correction. 3- After ionization loss correction. 4- With inclusion of both radiation and ionization energy loss corrections.

4.7 Average Separation Energy

The average nucleon separation or removal energy, E_s, is the average amount of energy needed to remove a nucleon from a given nucleus. In the quasielastic scattering process in consideration in this work, the incident electron's energy at the interaction vertex must be reduced by E_s, the amount required to knock out a ^{3}He cluster from the ^{4}He nucleus, when interacting with the ^{3}He cluster in the ^{4}He nucleus. It is assumed that the energy to separate a single neutron is equivalent to the energy to separate a ^{3}He cluster in ^{4}He nucleus. This separation energy may depend on Q^2, as it has been suggested in Reference [96].

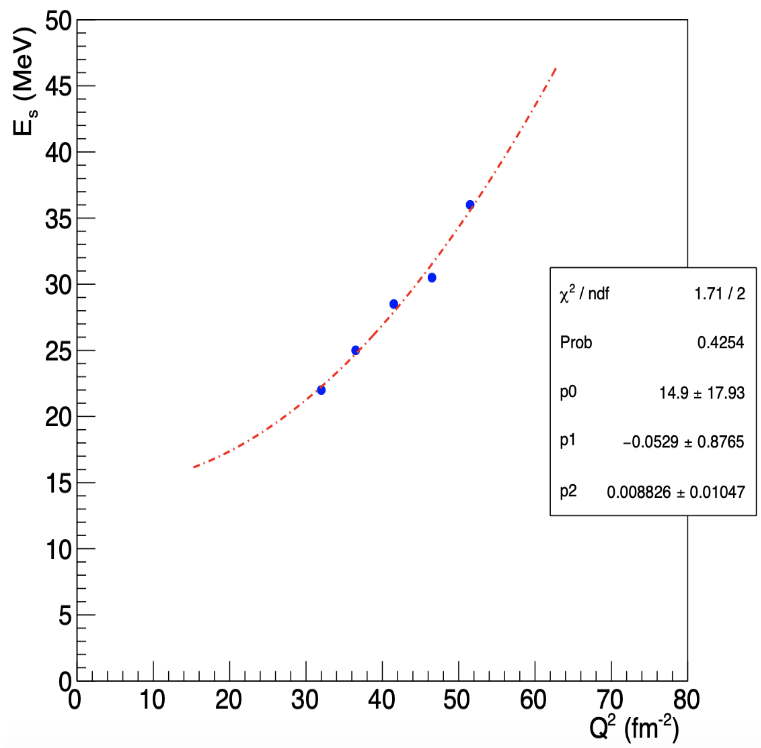

Figure 4.13: The separation energy of ^{3}He within ^{4}He. The blue circles represent the extracted average separation energy. The red line is the obtained fit.

In the MCSP, the average separation energy for each kinematic setting as function in Q^2, was extracted by comparing the simulation to experimental spectra. The separation energy was then fitted as seen in Figure 6.4 using the quadratic function:

$$E_s = p_0 + p_1 Q^2 + p_2 (Q^2)^2 \tag{4.35}$$

where p_0, p_1 and p_2 are free parameters determined by the fit.

In e-^{3}He quasielastic scattering process, after applying all the corrections to the incident electron beam E_{beam}, the new E' and Q^2 are calculated at the vertex. Using the fit function given by Equation (4.35), E_s can be estimated for all kinematic events. The direct subtraction method is used to determine the incident electron energy E_{qs} used in the quasielastic scattering kinematics before scattering, where we assume that the total incident electron beam E_{beam} is the sum of E_{qs} and separation energy as: $E_{qs} = E_{beam} - E_s$.

4.8 HRS Optics Transportation Model

In reality, not all particles that enter the spectrometers make it through them and get recorded by the detectors in their huts. In order to accurately determine the number and the coordinates of the events that make it to the VDCs and the other detectors, a ray-trace particle transportation model was developed for the two HRSs.

In this coincidence electron-nucleus scattering experiment under investigation, a scattered electron and a recoil particle travel through the magnet configuration of the HRSs (QQDQ, a dipole and 3 quadrupoles magnets) before they reach the Focal Plane in the detector package. The Monte Carlo simulation contains a realistic model of the two Hall A magnetic spectrometers. The particles can be transported through the spectrometers to the detectors by tracing each particle (ray) through a "ray-trace" model of the spectrometer system or using transport matrix elements directly. The transport matrix method will be discussed later in Section 4.9. The matrix method uses less computer time than an exact ray-tracing method. In the ray-tracing method, information about all spectrometer apertures needs to be supplied, such as the distance between them and their dimensions [61].

In the present Monte Carlo simulation, a combination of the ray-tracing and the transport matrix method was used to propagate the particles inside the spectrometers. After the events are generated at the target and applying all needed corrections, a forward transport matrix is used to transport the events to different locations in the spectrometer, where checks are made to ensure that the particles remain within the apertures of the magnets or the beam pipe elements. The provided forward matrices transport the particles from the target to five different locations to make the aperture checks:

- Target to the exit of the first quadrupole (Q1ex).
- Target to the Dipole entrance (Den).
- Target to the Dipole exit (Dex).
- Target to the third quadrupole entrance (Q3en).
- Target to the third quadrupole exit (Q3ex).

From there, the particles can be ray traced using either Backward (BW) or Forward (FW) drift routines as desired for more aperture checks. At the end of each step, the coordinate positions of the events with respect to the central ray are calculated and checked to see if they hit any apertures, which were assumed to be perfectly absorbing. Only the particles that pass through all the apertures are considered "good" events and transported to the FP. The location, distance, and size of each aperture are obtained from the engineering drawing and are listed in Table 4.3. The locations where apertures checks were made using the transport matrix are shown in Figure 4.14.

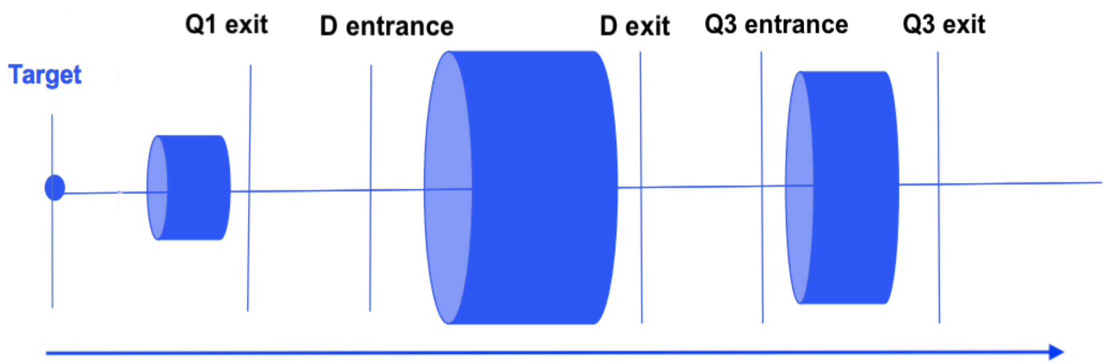

Figure 4.14: The location of the HRS apertures that are used in the transport matrix method to propagate the particles through the spectrometers.

A comparison between e-^{4}He and e-^{3}He events which make it through the apertures of Table 4.3 shows that about 60% of coincidence events from e-^{4}He scattering enter the Q1 entrance and only $\sim$ 10% of the events make it to the FP. However, the e-^{3}He coincidence events that make it to the FP was only $\sim$ 0.5%. This is because these events are close to the acceptance limits of the two spectrometers. Figures 4.15 to 4.18 show the coincidence events at different locations with the aperture cuts shapes as listed in Table 4.3.

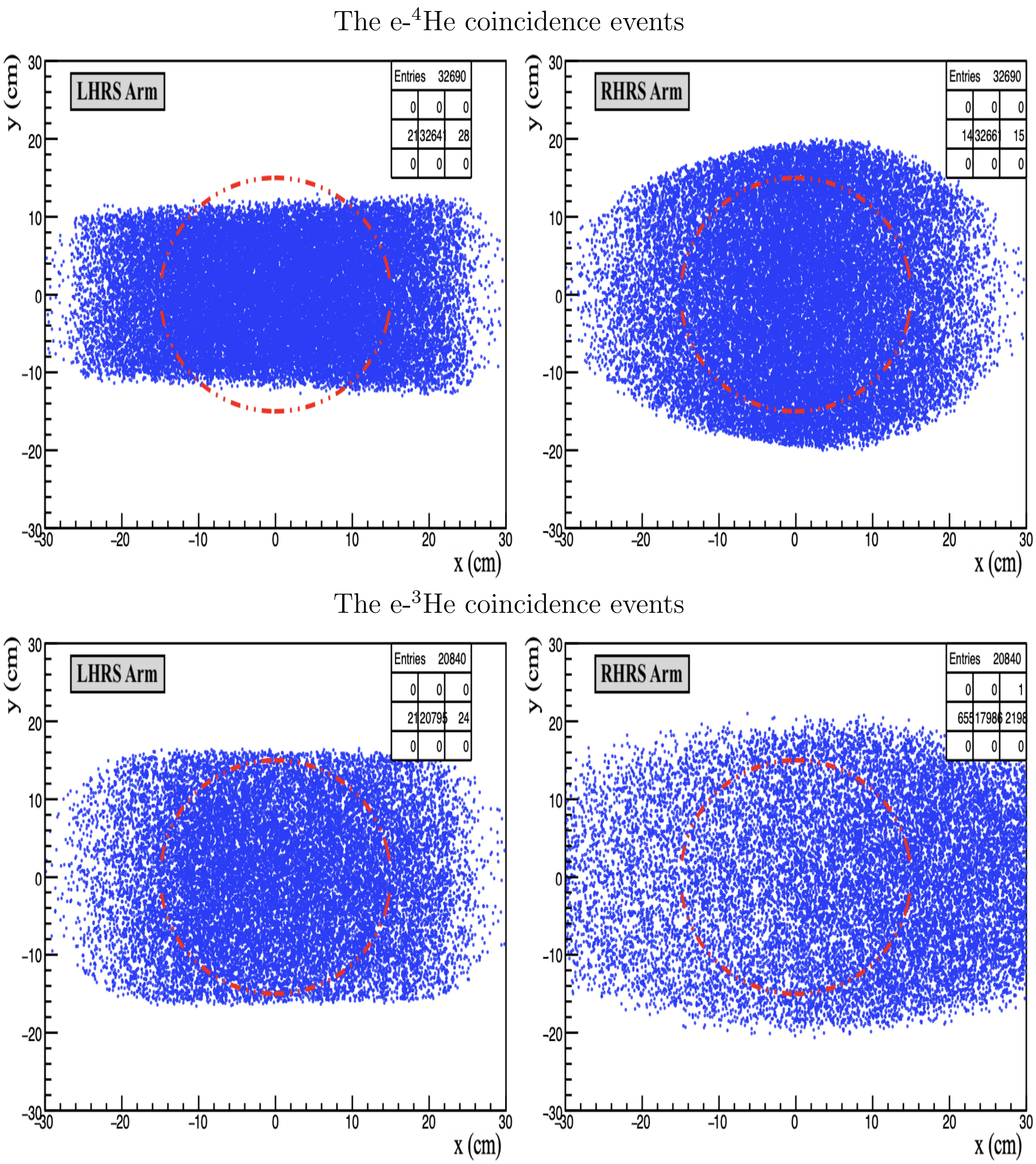

Figure 4.15: The position of Monte Carlo elastic e-^{4}He and quasielastic e-^{3}He events shown at the exit of quadrupole Q1 of the LHRS (electrons) and RHRS (recoils). The blue dot markers represent the events at the Q1 exit. The red dashed circle represents the applied cut (physical aperture of Q1).

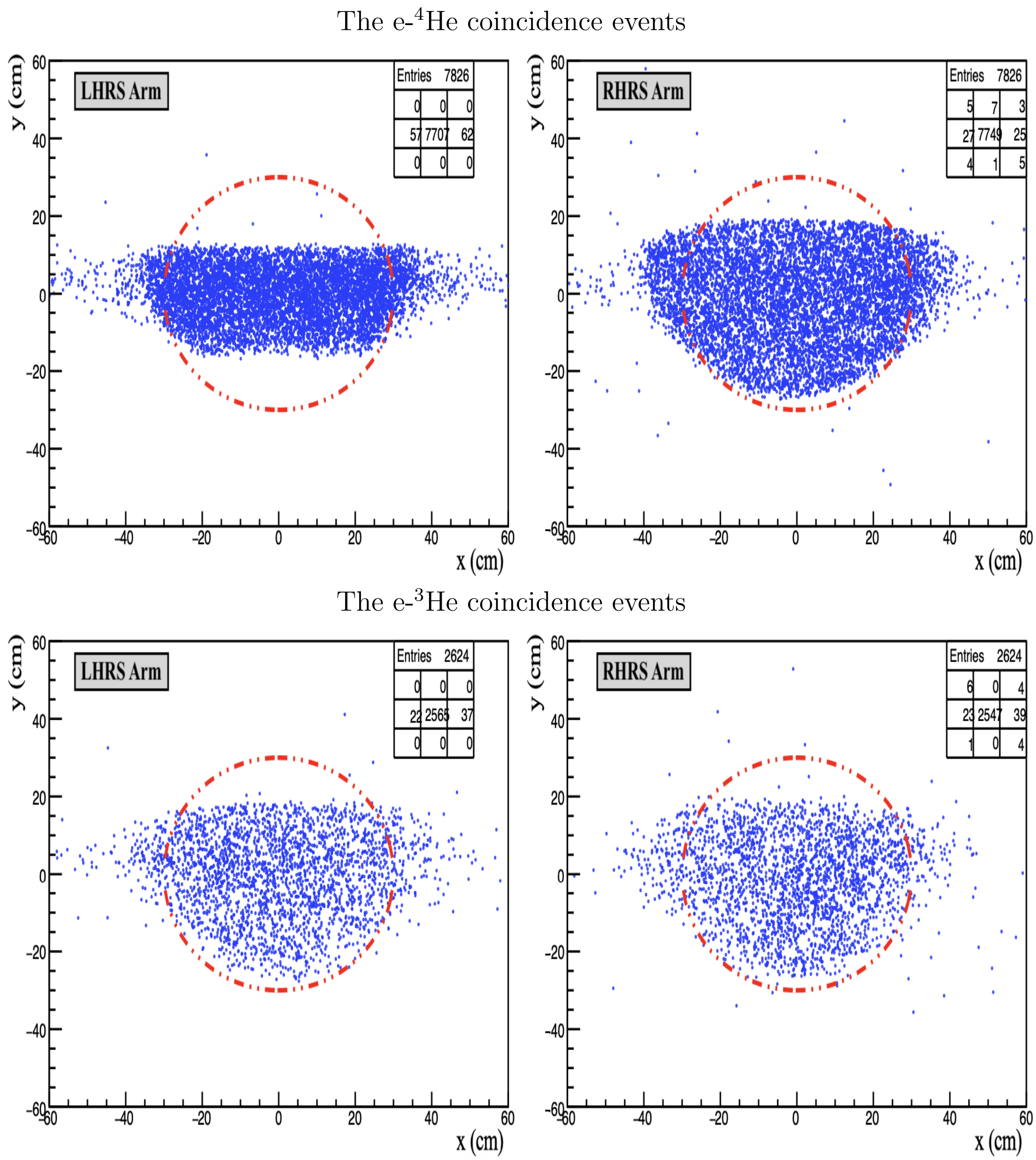

Figure 4.16: The position of Monte Carlo elastic e-^{4}He and quasielastic e-^{3}He events shown at the exit of quadrupole Q2 of the LHRS (electrons) and RHRS (recoils). The blue dot markers represent the events at the Q2 exit. The red dashed circle represents the applied cut (physical aperture of Q2).

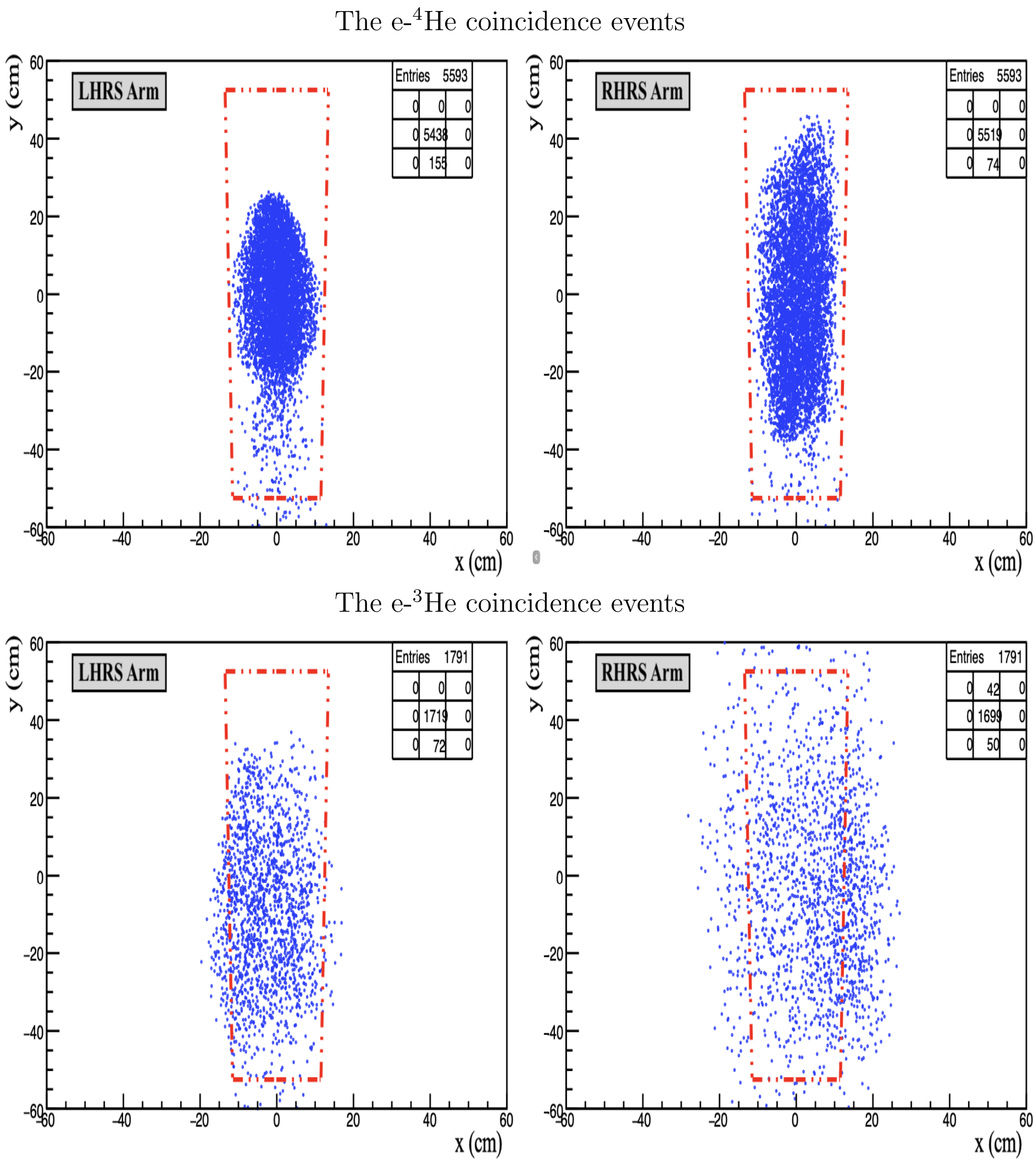

Figure 4.17: The position of Monte Carlo elastic e-^{4}He and quasielastic e-^{3}He events shown at the exit of dipole D of the LHRS (electrons) and RHRS (recoils). The blue dot markers represent the events at the D exit. The red dashed trapezoid line represents the applied cut (physical aperture of D).

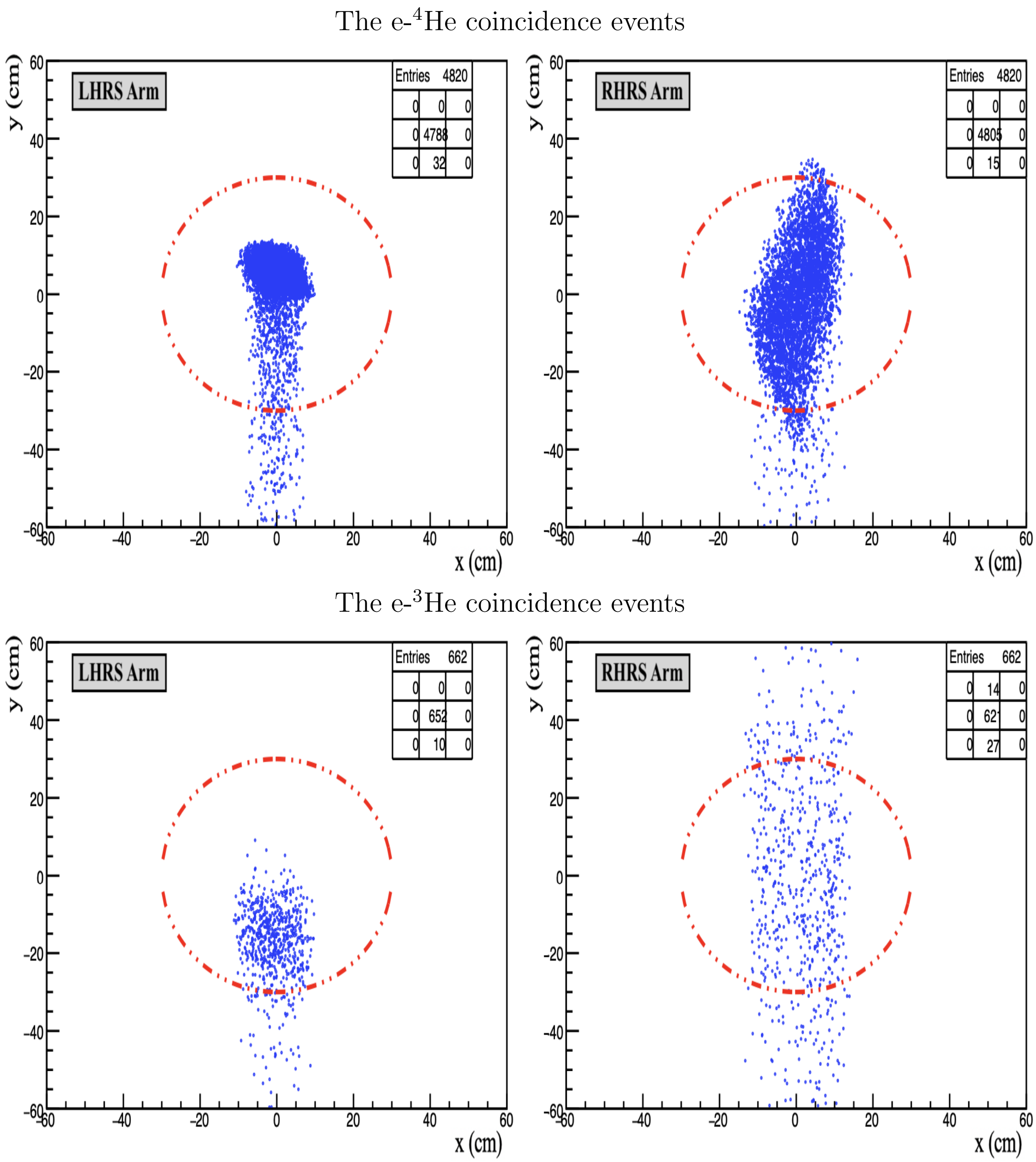

Figure 4.18: The position of Monte Carlo elastic e-^{4}He and quasielastic e-^{3}He events shown at the exit of quadrupole Q3 of the LHRS (electrons) and RHRS (recoils). The blue dot markers represent the events at the Q3 exit. The red dashed circle represents the applied cut (physical aperture of Q3).

Location	Method	Distance (cm)	Aperture Shape	Aperture Size (cm)
Q1 entrance (Q1en)	FW from target	159.0	Circle	$\sqrt{x^2+y^2} < 15.0$
Q1 exit (Q1ex)	Matrix	——	Circle	$\sqrt{x^2+y^2} < 15.0$
Q1 Vacuum Pipe (Q1VP)	FW from Q1ex	61.0(LHRS) 61.3(RHRS)	Circle	$\sqrt{x^2+y^2} < 15.0$
Q2 entrance (Q2en)	FW from Q1 VP	56.2(LHRS) 54.3(RHRS)	Circle	$\sqrt{x^2+y^2} < 30.0$
Dipole entrance (Den)	Matrix	——	Trapezoid	$\|x\| < 25 \times (1 + 0.00149y)$ $\|y\| < 52.5$
Q2 exit (Q2ex)	BW from Den	393.1(LHRS) 393.6(RHRS)	Circle	$\sqrt{x^2+y^2} < 30.0$
Q2 Vacuum Pipe (Q2VP)	FW from Q2ex	6.7	Circle	$\sqrt{x^2+y^2} < 30.0$
Bellows	FW from (Q2VP)	32.2	Rectangle	$\sqrt{x^2+y^2} < 31.8$
Vacuum Pipe before Den	BW from Den	——	Rectangle	$\|x\| < 15.0$ $\|y\| < 70.0$
Dipole exit (Dex)	Matrix	——	Trapezoid	$\|x\| < 25 \times (1 + 0.00149y)$ $\|y\| < 52.5$
Aperture	FW from Dex	39.3(LHRS) 39.9(RHRS)	Rectangle	$\|x\| < 15.0$ $\|y\| < 30.3$
Q3 entrance (Q3en)	Matrix	——	Circle	$\sqrt{x^2+y^2} < 30.0$
Aperture	BW from Q3en	69.9(LHRS) 69.2(RHRS)	Rectangle	$\|x\| < 15.0$ $\|y\| < 30.3$
Q3 exit (Q3ex)	Matrix	——	Circle	$\sqrt{x^2+y^2} < 30.0$
Comister	FW from Q3ex	57.5	Circle	$\sqrt{x^2+y^2} < 35.3$
Bellows	FW from Comister	25.2	Rectangle	$\|x\| < 17.15$ & $\|y\| < 35.6$
Window	FW from Bellows	247.1	Rectangle	$\|x\| < 17.14$ & $\|y\| < 99.8$

Table 4.3: The HRS apertures check list. FW and BW mean drifting particles Forward and Backward, respectively.

4.9 Momentum Acceptance

Since it is known that the HRS momentum acceptance limits are -0.05 (-5%) and $+0.05$ ($+5\%$) in relative momentum, in the Monte Carlo, events with relative momentum beyond these limits were not propagated through the spectrometers. The relative momentum of either the scattered or recoil particle is defined as:

$$\delta = \frac{P - P_o}{P_o} \tag{4.36}$$

where P is the momentum of that particle and P_o is the central momentum setting of the spectrometer.

In experiment E04-018, the central momentum of the electron HRS was lowered by 1.0% in order to get more of the radiative tail from e-^{4}He scattering process into the LHRS acceptance. For consistency and accuracy, the same was done in the simulation. This means that for the electron spectrometer, the events accepted were in the relative momentum range (-0.06, $+0.04$). For the recoil spectrometer, the events accepted were in the relative momentum range (-0.05, $+0.05$). Figures 4.19 to 4.22 show the δ distribution for the scattered electron and recoil events before, and after passing through the apertures cuts without applying the momentum acceptance cut.

4.10 Transport Matrix

Each spectrometer arm has unique optics matrices for its different magnetic elements. Up to 5th order forward matrices are used to transport particles from the target to different locations within the spectrometer and to the Focal Plane. The forward matrix code was generated by J. Lerose [55, 61] based on the SNAKE program in Fortran and has been adjusted to provide the correct measured optical properties.

The δ relative momentum distribution of the e-^{4}He elastic scattering process

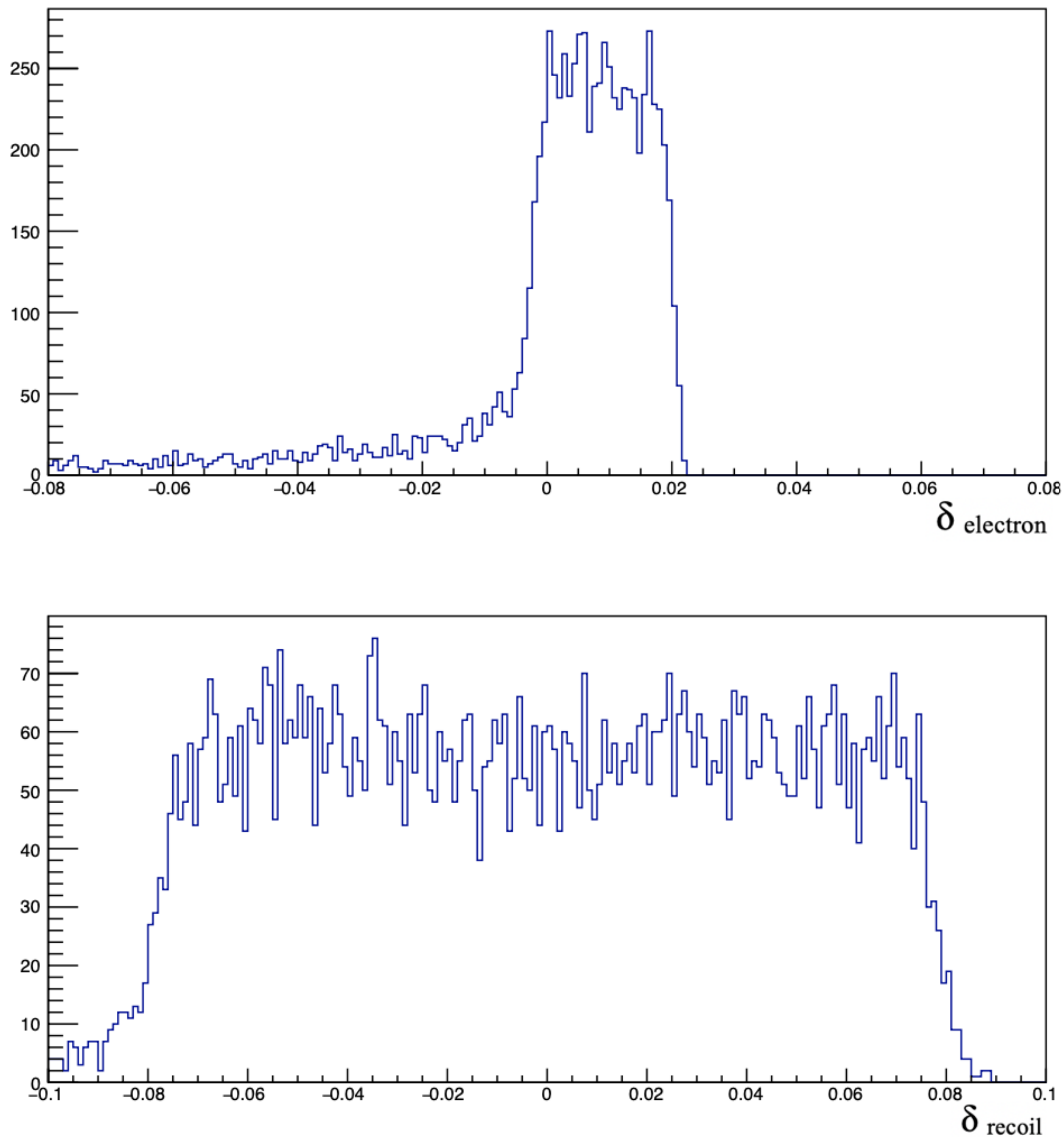

Figure 4.19: The relative momentum δ distribution for the LHRS (top plot) and RHRS (bottom plot) for kinematic Kin34. All corrections are applied but without any spectrometer aperture cuts.

The δ relative momentum distribution of the e-^{4}He elastic scattering process

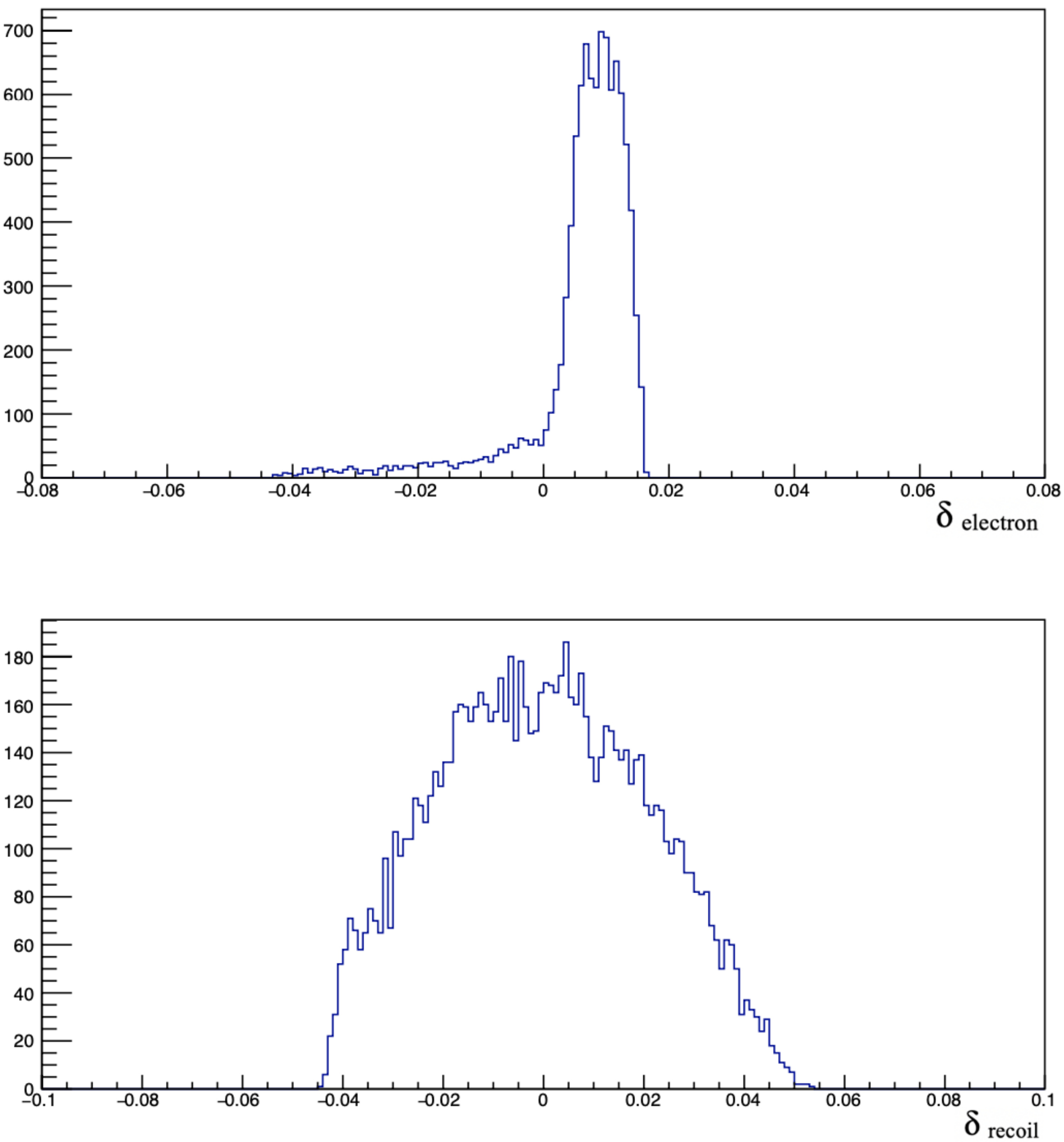

Figure 4.20: The relative momentum δ distribution for the LHRS (top plot) and RHRS (bottom plot) for kinematic Kin34. All corrections are applied with spectrometer aperture cuts.

The δ relative momentum distribution of the e-^{3}He quasielastic scattering process

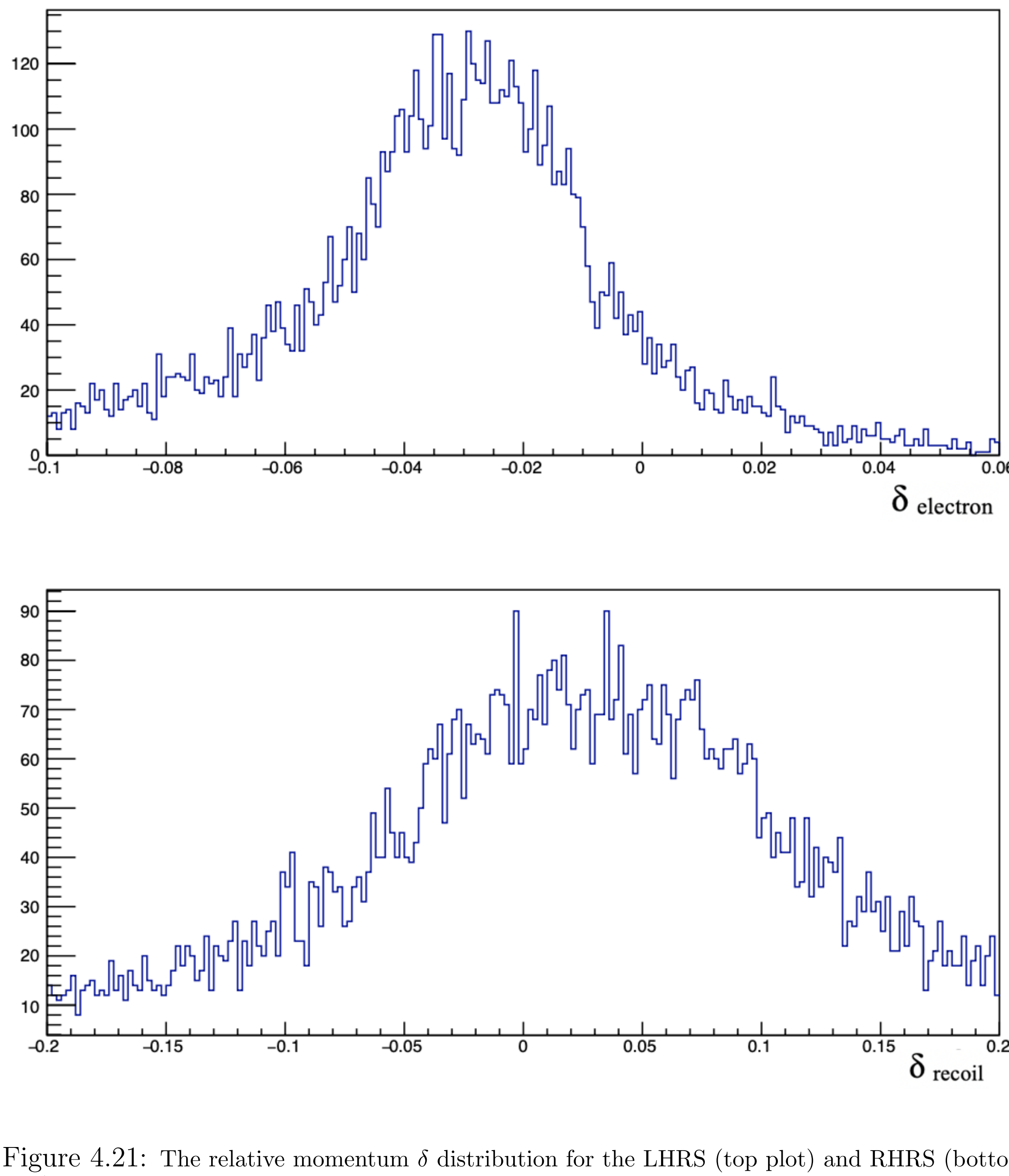

Figure 4.21: The relative momentum δ distribution for the LHRS (top plot) and RHRS (bottom plot) for kinematic Kin34. All corrections are applied but without any spectrometer aperture cuts.

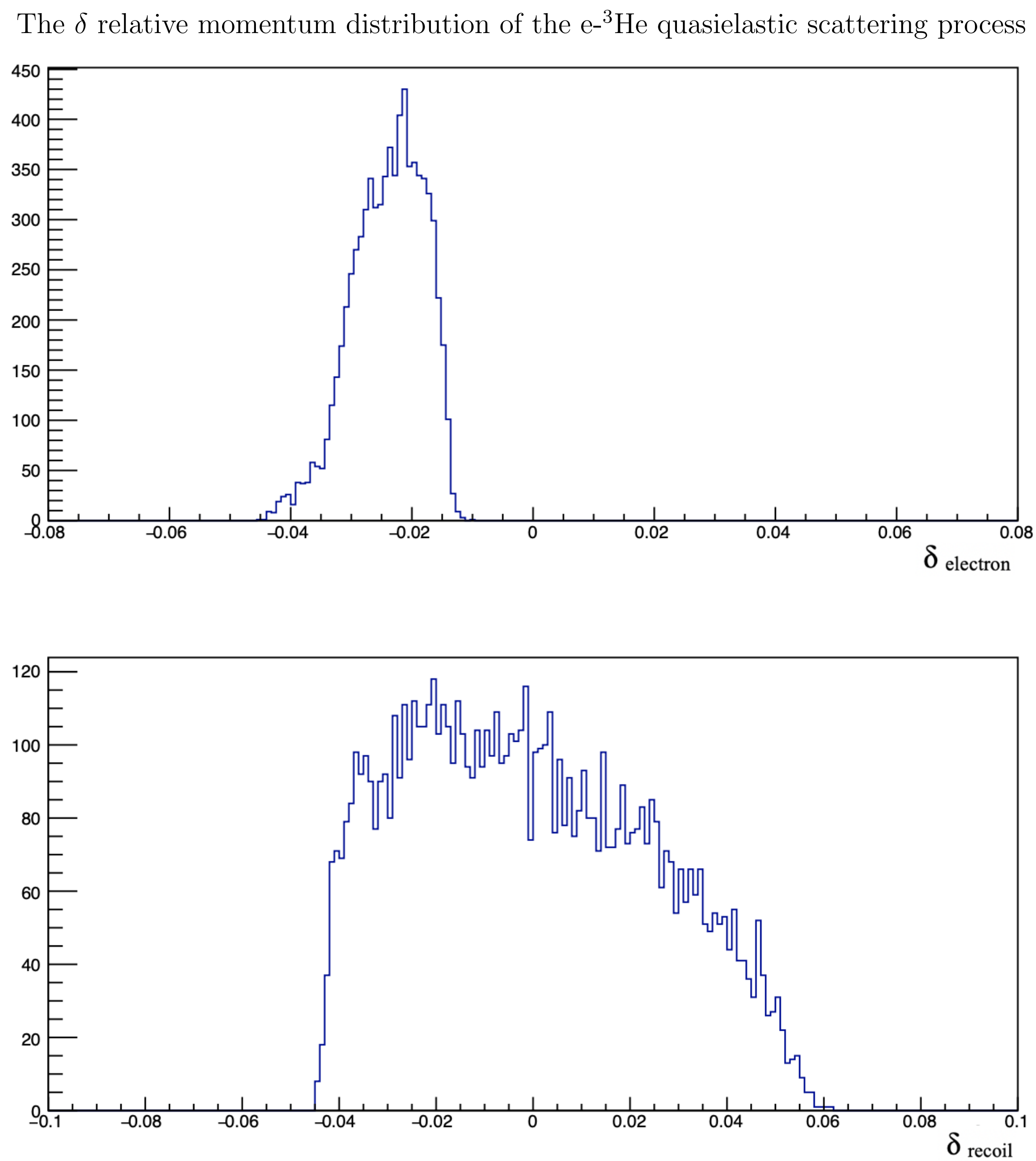

Figure 4.22: The relative momentum δ distribution for the LHRS (top plot) and RHRS (bottom plot) for kinematic Kin34. All corrections are applied with spectrometer aperture cuts.

The code was converted to C language before applying it into this simulation. The position and angles of the scattered and the recoil particles are calculated at the FP and in other locations by the provided matrix elements as functions of (x_{trg}, y_{trg}, θ_{trg}, ϕ_{trg}, δ). The coordinates y_{trg} and x_{trg} are the position of the particles in the dispersive and non-dispersive direction, respectively. The z axis is along the central ray of the spectrometer. The coordinates ϕ_{trg} and θ_{trg} are the slopes of the ray at the target dy_{trg}/dz and dx_{trg}/dz, respectively. The quantity δ, which has been defined earlier, is the fractional deviation of the particle's momentum from the central spectrometer momentum. The corresponding coordinates y, x, ϕ and θ at the FP or any desired longitudinal location along the spectrometer are given by a set of polynomials:

$$\begin{aligned} y &= \textstyle\sum_{i,j,k,l,m} \ Y_{ijklm} \ y^i_{trg}\phi^j_{trg}x^k_{trg}\theta^l_{trg}\delta^m \\ \phi &= \textstyle\sum_{i,j,k,l,m} \ P_{ijklm} \ y^i_{trg}\phi^j_{trg}x^k_{trg}\theta^l_{trg}\delta^m \\ x &= \textstyle\sum_{i,j,k,l,m} \ X_{ijklm} \ y^i_{trg}\phi^j_{trg}x^k_{trg}\theta^l_{trg}\delta^m \\ \theta &= \textstyle\sum_{i,j,k,l,m} \ T_{ijklm} \ y^i_{trg}\phi^j_{trg}x^k_{trg}\theta^l_{trg}\delta^m \end{aligned} \tag{4.37}$$

where the four sets of coefficients Y_{ijklm}, P_{ijklm}, X_{ijklm}, and T_{ijklm} arise from the optical properties of the spectrometer system, and are symbolically given by:

$$Y_{ijklm} = \ (y \ |y^i_{trg}\phi^j_{trg}x^k_{trg}\theta^l_{trg}\delta^m) \tag{4.38}$$

The summation over $i, \ j, \ k, l$ and m is up to order 5 ($i + j + k + l + m \leq 5$) which is the order of the transport matrix used by the MC program.

4.11 The Coincidence Time of Flight

The coincidence Time of Flight (TOF) was used to identify e-^{3}He quasielastic and e-^{4}He elastic events. A particle's time of flight is, in general, the time for it to travel a distance L between two points along its path such as two detectors. In the MCSP, we consider TOF, the time it takes for a particle to travel between the target and the FP. This time is given by:

$$t_{TOF} = \frac{L_o}{\upsilon} = \frac{L_o}{\beta c} \tag{4.39}$$

where L_o is the distance from the target to the FP, which is equal to 25.0 m [55], and υ is the speed of the particle (in units of c), which is equal to 1 for electrons and P/E for hadrons, where P and E are the hadron momentum and energy, respectively. The Time of Flight difference ΔTOF, which is the difference in time it takes for an electron and a hadron to travel over the corresponding distance in each HRS, is given by:

$$\Delta TOF = |t^e_{TOF} - t^h_{TOF}| \tag{4.40}$$

Using the above Equations, the ΔTOF was calculated for all the events that reached the two FPs. This calculation results in a narrow ΔTOF "peak" (stripe). Corrections to the coincidence ΔTOF must be done in the MC analysis to resemble the real process. These corrections which are related to the scintillator time resolution and to path lengths inside the spectrometers, are summarized in the following section.

The coincidence time spread is determined by the individual timing resolution of each HRS. These resolutions are determined by the timing resolution of the two scintillator planes which each particle goes through when it enters the detector package [55]. The time resolution is approximately $\sigma = 0.5$ ns. In addition, the path length correction is accounted for in the TOF through the spectrometer as the total path length is $L = L_o + \Delta L$. The path difference ΔL is the difference between the length of the central ray and the path length of a particular particle inside the spectrometer. ΔL(HSRE) for the electrons and ΔL(HSRH) for the hadrons are calculated by the forward matrix in terms of the target coordinates, y_{trg}, ϕ_{trg}, x_{trg}, θ_{trg}, and δ provided by the SNAKE algorithm as:

$$\Delta L = \sum_{i,j,k,l,m} L_{ijklm} \; y^i_{trg} \phi^j_{trg} x^k_{trg} \theta^l_{trg} \delta^m \tag{4.41}$$

where $i + j + k + l + m \le 5$ and L_{ijklm} expresses the optical properties of the spectrometer system. Figures 4.23 and 4.24 show the coincidence ΔTOF before and after applying the corrections.

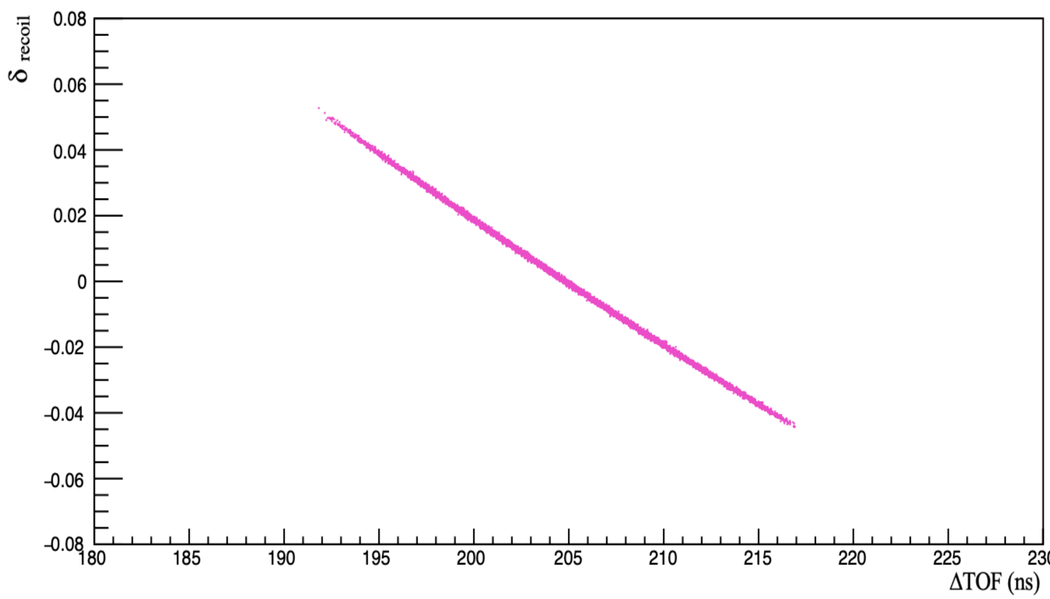

Figure 4.23: The δ_{recoil} relative momentum (RHRS) versus the coincidence ΔTOF. Only multiple scattering, ionization and radiation corrections are included.

4.12 Cross Section Model

In the simulation, the scattered electron and recoil nucleus are detected in coincidence, and all corrections (ionization loss, multiple scattering, and radiation loss) are applied to each trial event. The cross section model from Experiment E04-018 is used to add the weighting factor for each good event in the simulation before it can be compared to the experimental data. An event is considered a good event

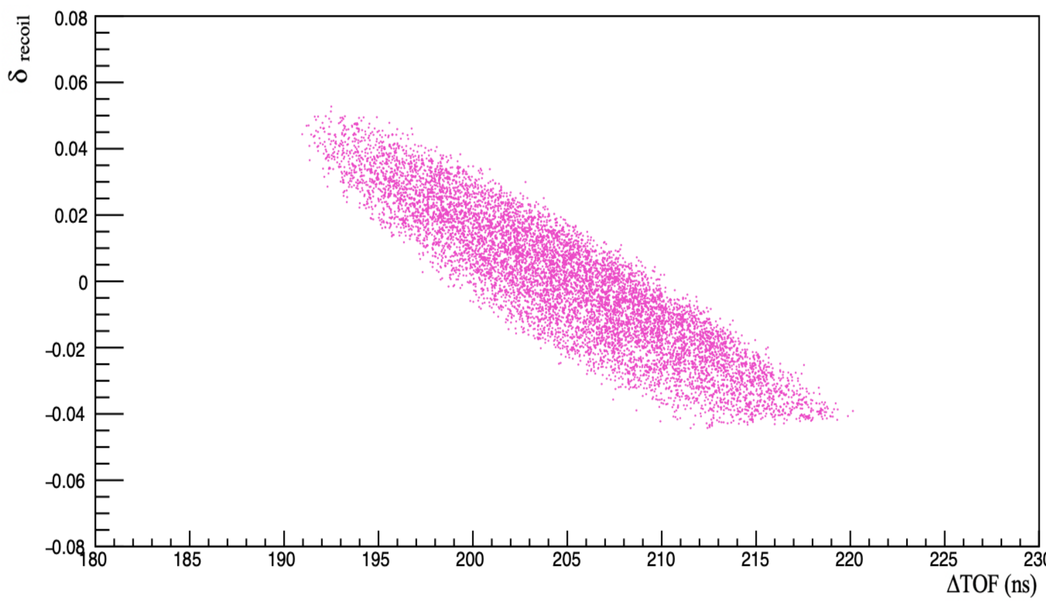

Figure 4.24: The δ_{recoil} relative momentum (RHRS) versus the coincidence ΔTOF. All corrections have been applied.

when both the scattered electron and the recoiling nucleus pass all the way through the modeled spectrometers to the detectors without being lost or absorbed by any limiting aperture or element.

The cross sections of e-^{3}He and e-^{4}He are calculated using Equation (1.13) and (1.16), respectively. The charge $F_C(Q^2)$ and magnetic $F_M(Q^2)$ form factors of ^{3}He and the charge form factor $F_C(Q^2)$ of ^{4}He are determined by fitting the data of References [11] and [10]. Different fits are applied for different kinematics due to the large variation in the form factors with Q^2 in this region. The sensitivity arises from the fact of the presence of an apparent second diffraction minimum. The second diffraction minimum of the ^{4}He charge form factor exists at Q^2= 51.7 fm^{-2} as shown in Figure 1.5. On the other hand, the second diffraction minima of the ^{3}He form factors are located at Q^2= 62.0 fm^{-2} for the F_C, and at Q^2= 49.3 fm^{-2} for the F_M, as can be seen in Figure 1.4. The form factors are fitted using a polynomial function:

$$F_{C,M}(Q^2) = \Sigma_0^n \; p_n (Q^2)^n \tag{4.42}$$

where p_n are the fit coefficient, and n is the order of the polynomial function. The fit functions in Figures 4.25 to 4.29 are used to estimate the form factors for the Q^2 of each good event, and then the corresponding cross section is calculated. In order to apply cross section weighting to the MC events, the maximum values of the cross section $(\frac{d\sigma}{d\Omega})_{max}$ are set above the cross section of ^{3}He for each kinematics, as listed in Table 4.4. Then, all the good events in the FP are weighted using the acceptance-rejection method [70].

Kinematic setting	$(\frac{d\sigma}{d\Omega})_{max}$ (cm^2/sr)
Kin34	3.5×10^{-36}
Kin39	1.5×10^{-36}
Kin45	3.0×10^{-36}
Kin50	1.0×10^{-36}
Kin55	2.5×10^{-37}

Table 4.4: The maximum values of the ^{3}He used for the cross section weighting in the simulation.

After all information is incorporated in the simulation and all corrections and cuts have been applied, we are ready to compare the experimental data and the simulation for all five kinematics, as will be presented in Chapter 6.

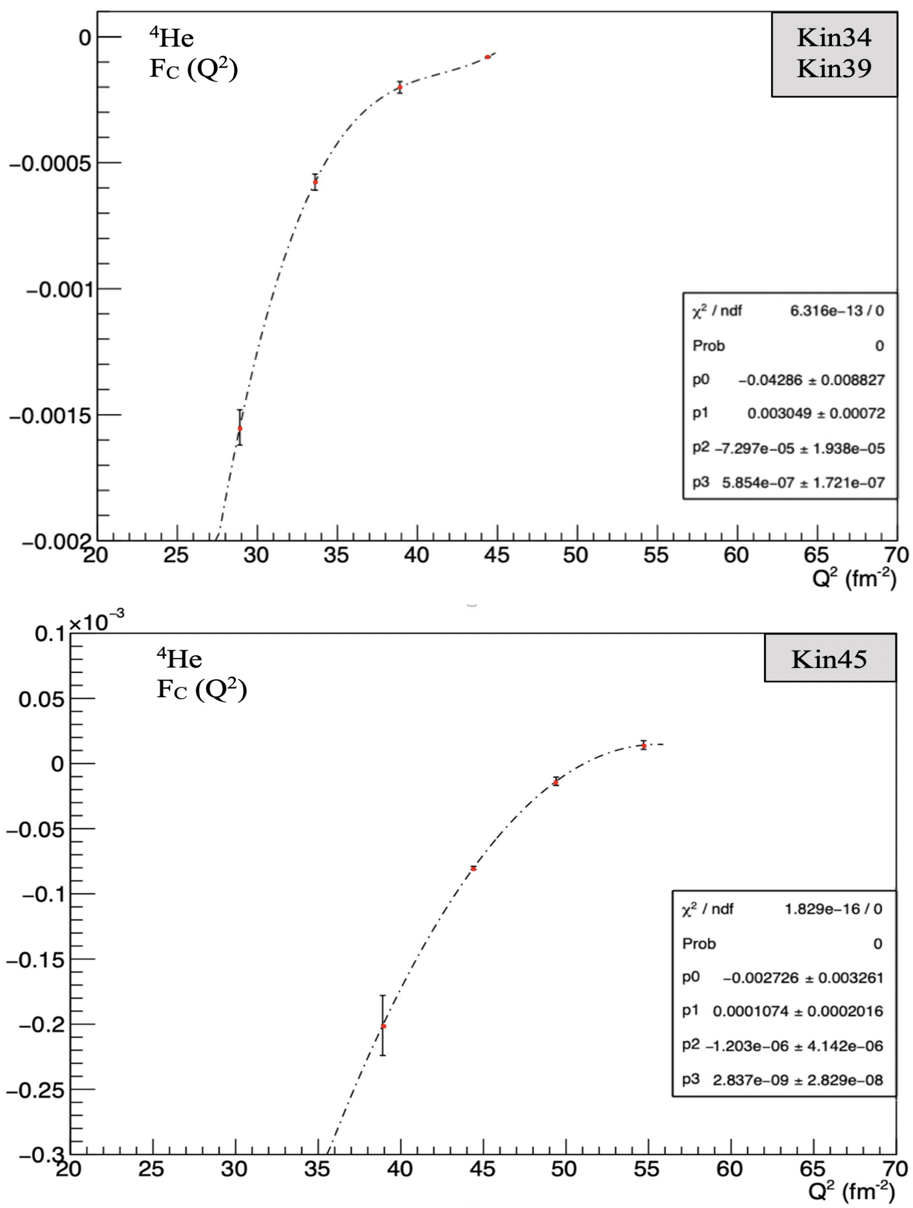

Figure 4.25: The colored circles represent the measured values of F_C versus Q^2 for ^{4}He from Reference [10]. The black dashed line represents the fit used in this work.

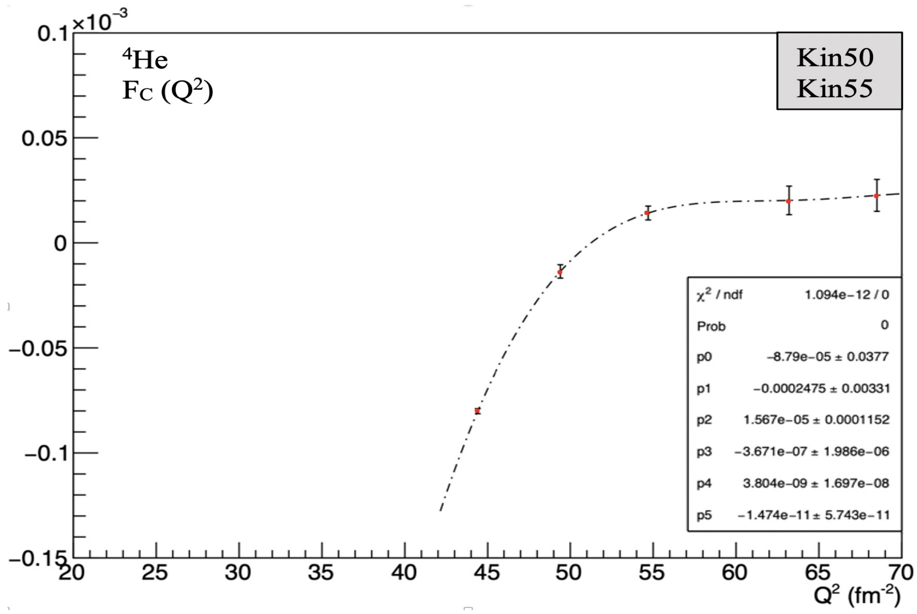

Figure 4.26: The colored circles represent the measured values of F_C versus Q^2 for ^{4}He from Reference [10]. The black dashed line represents the fit used in this work.

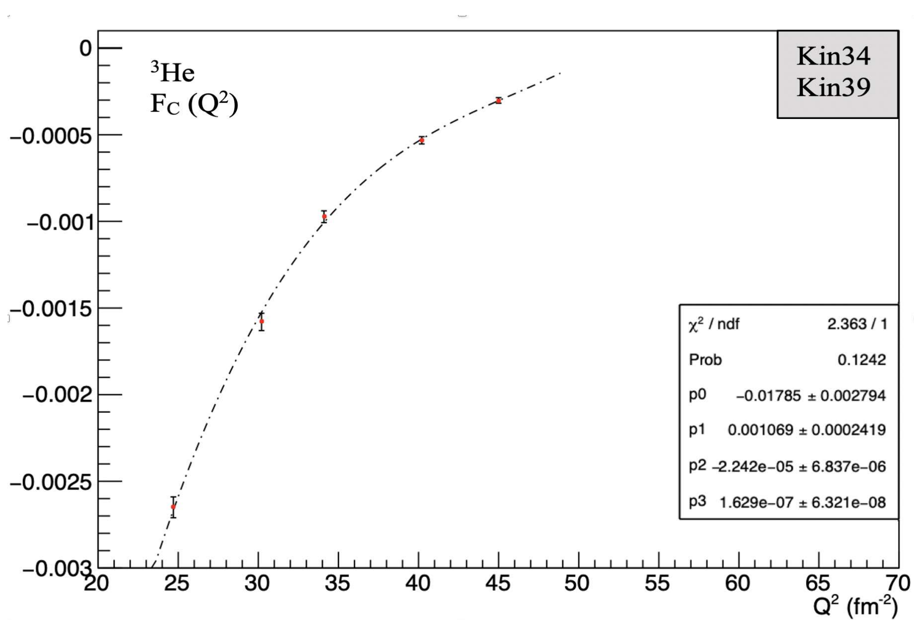

Figure 4.27: The colored circles represent the measured values of F_C versus Q^2 for ^{3}He from Reference [11]. The black dashed line represents the fit used in this work.

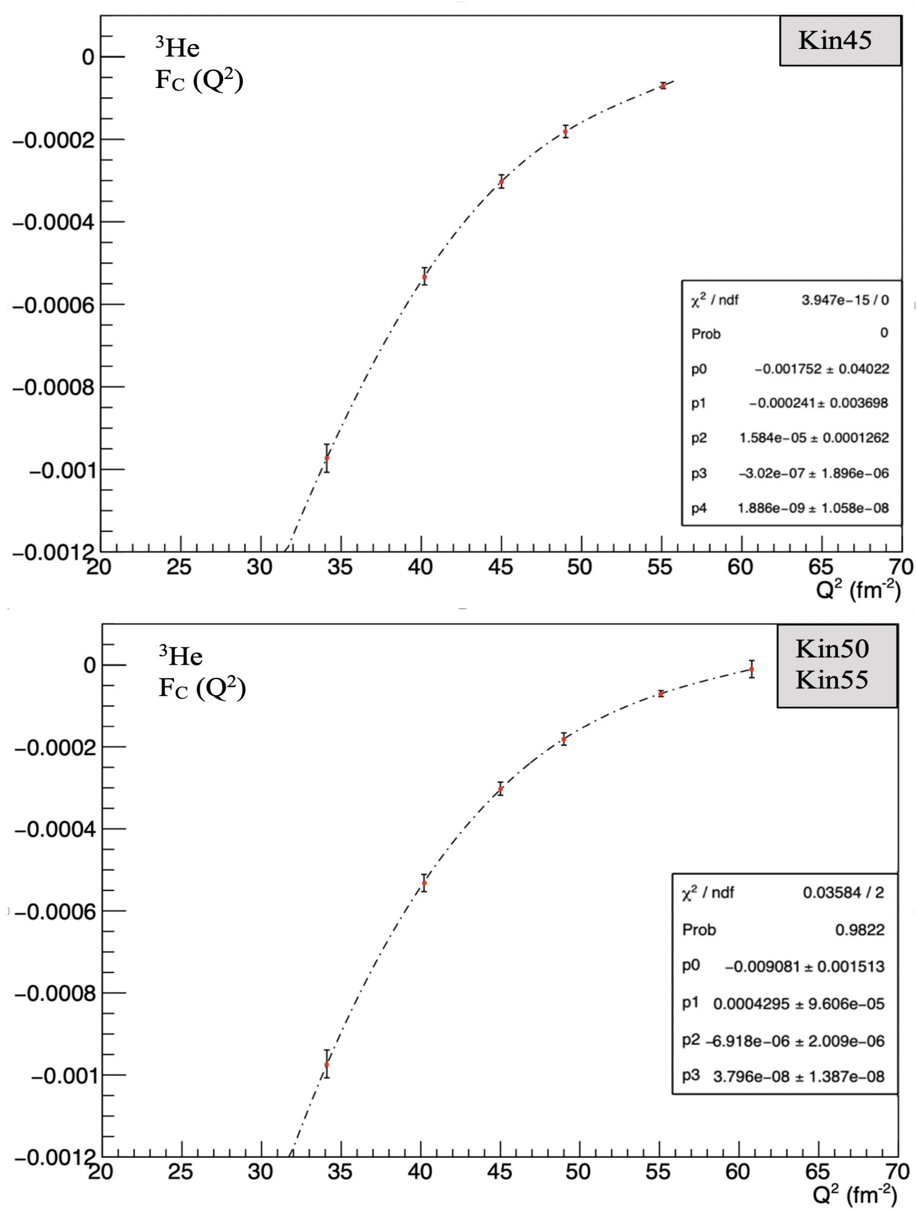

Figure 4.28: The colored circles represent the measured values of F_C versus Q^2 for ^{3}He from Reference [11]. The black dashed line represents the fit used in this work.

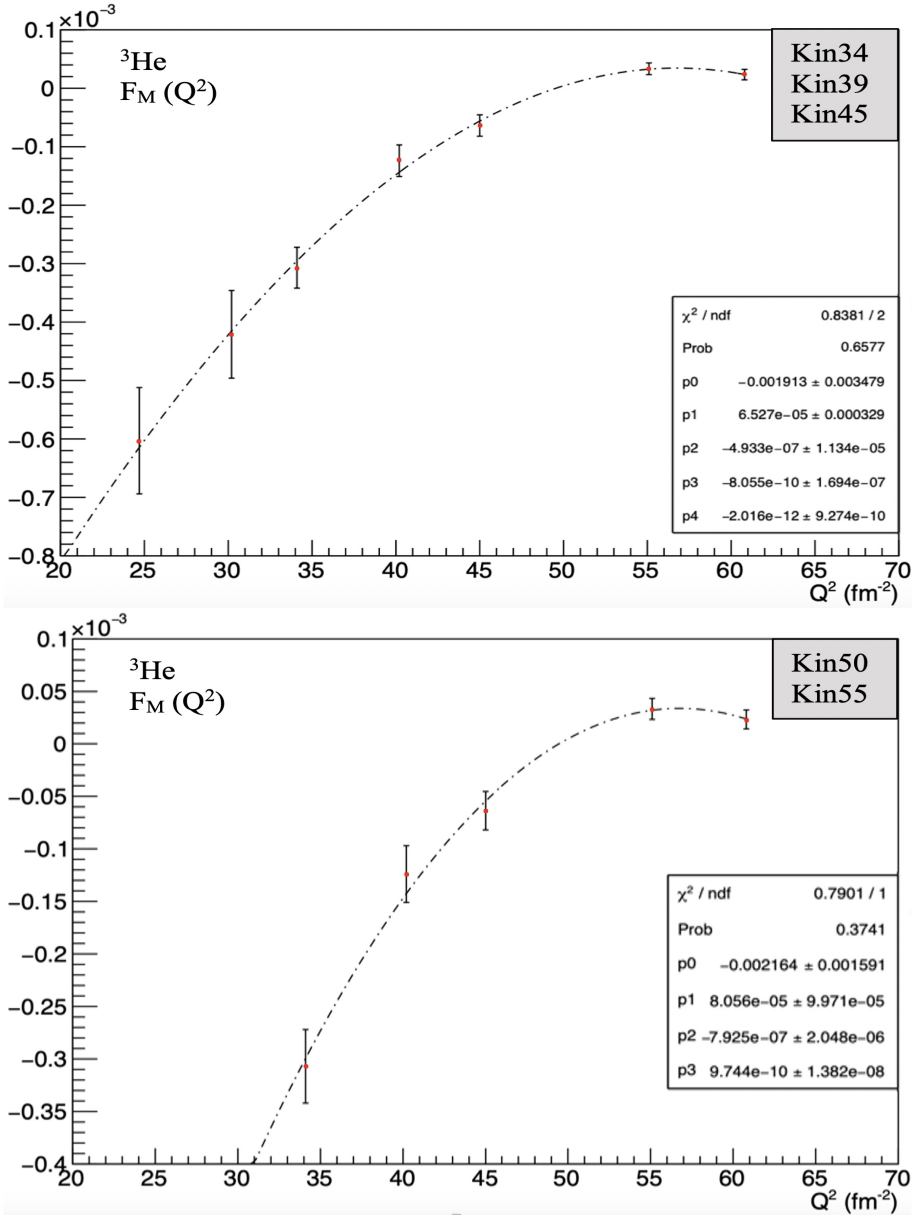

Figure 4.29: The colored circles represent the measured values of F_M versus Q^2 for ^{3}He from Reference [11]. The black dashed line represents the fit used in this work.

Chapter 5

Experimental Data Analysis

In scattering experiments, particles are identified by the unique signatures they leave in detector systems. Each component of the spectrometer detector package utilizes a specific set of particle properties. Therefore, the detector package components may vary in different experiments to accomplish the experiment's purpose. The main goal of this thesis analysis is to confirm the presence of ^{3}He clusters within α particles by identifying and separating ^{3}He quasielastic from ^{4}He elastic events and comparing the results with the Monte Carlo simulation. This chapter will outline the steps and procedures necessary to separate the two classes of events. This requires first the application of a set of appropriate cuts to select out the events we are interested in by using information from the data. While in principle this is straightforward, care must be taken when placing cuts to the data to reject background events, and study the overlapping of e-^{3}He and e-^{4}He events at high Q^2, which could appear to mimic each other.

In general, the analysis can be divided into three parts to achieve this goal, based on the cuts needed to be applied in order to select the desired events, as follows:

- Electron identification.
- ^{4}He recoil identification.
- ^{3}He recoil identification.

5.1 Experiment E04-018

As mentioned in Chapter 3, for this experiment, the Left High Resolution Spectrometer (LHRS) was used to detect scattered electrons and the Right High Resolution Spectrometer (RHRS) was used to detect recoil ^{4}He nuclei. The LHRS fractional central momentum setting was lowered by 1.0% in order to detect more electrons (and corresponding recoils) from the radiative "tail" into the spectrometer's acceptance. A very unique and unexpected class of data from this experiment appeared in the region of this radiative tail. A preliminary analysis pointed out to the assumption of ^{3}He clustering within ^{4}He [97]. This assumption was supported by the notion of existence of ^{3}He clusters in ^{4}He as presented in Chapter 2.

During the E04-018 experiment, the Hall A Data Acquisition system recorded raw data directly on hard disks files. The Hall A Analyzer software read the raw data for each run and produced summary files with all events that could correspond to a coincidence of an electron with a hadron originating from the target. As mentioned in Section 3.8, the dummy target was used to estimate the contribution from the target cell endcaps. During the use of the dummy target in this experiment, no coincidence electron-hadron events were observed that could be attributed to e-^{4}He or e-^{3}He scattering [10, 11].

The output data summary files of E04-018 contained all information for the events such as positions, momenta, and difference in coincidence Time of Flight (ΔTOF). These files were sorted for further analysis for extraction of the ^{4}He and ^{3}He elastic from factors [10, 11] and, in this thesis work, for a potential study of quasielastic electron scattering from ^{3}He clusters in ^{4}He.

5.2 Data Files

The analysis described in this thesis used the condensed summary data files for electron scattering using the ^{4}He target of experiment E04-018. Five different kinematics files provided all needed information for studying the elastic ^{4}He and quasielastic ^{3}He events. Each kinematics file contains the essential physics quantities for all the events. The large Q^2 kinematics Kin55 and Kin50 condensed files do not contain events with trigger T6 as it was concluded in the preliminary analysis that there were no elastic events which failed to fire the S2 scintillator plane of RHRS. In this case, the recoil nucleus gave a signal in both scintillator S1 and S2 planes (in coincidence with the electron trigger). The kinematics Kin34, Kin39, and Kin45 files contain a section with events produced by the T6 electronic trigger. Here, the electron triggered both scintillator planes, whereas the recoil in coincidence gave a signal only in the S1 plane. This is the case where recoil particles with lower energy did not make it to the S2 plane as they were absorbed totally in the S1 plane or in the air gap between S1 and S2 planes. All files contain the following quantities:

1. Event trigger number.
2. Electron and recoil relative momentum δ.
3. Electron and recoil angles at the target, ϕ_{trg} and θ_{trg}.
4. Electron and recoil angles at the Focal Plane (FP), ϕ_{fp} and θ_{fp}.
5. Electron and recoil positions at the FP, y_{fp} and x_{fp}.
6. The difference in coincidence Time of Flight (ΔTOF).
7. ADC signals for the recoil S1 and S2 scintillators (RHRS).
8. Electron Cherenkov sum ADC signal.
9. The ratio of the energy of the LHRS particle to the momentum of its track, E'/P.

Using this information, a combination of cuts was applied to these quantities to separate background events from the elastic e-^{4}He and quasielastic e-^{3}He events of interest.

5.3 Electron Identification (EID)

In order to separate good electron events from negatively charged pions and other background, appropriate cuts must be applied to the signals of the two electron identification detectors. In this experiment, the Cherenkov counter, which identifies electrons using the Cherenkov radiation emission effect, and the lead-glass calorimeter, which identifies electrons based upon the energy they deposit in it, are used in the LHRS to eliminate an underlying mostly pion background.

As discussed in Section 3.7.3, the Cherenkov detector is responsible for discriminating electrons from pions. The Cherenkov detector will generally only fire for electrons, while the vast majority of pions should not produce Cherenkov light. The electrons appear as a wide peak at ADC channels above 100. The spectrum of the sum of the 10 Cherenkov ADC signals is shown in Figure 5.1. In order to remove pion contamination, the cut was set to select the events above channel 200. By placing this cut, pions or other background are completely removed.

Although the expectation is that the Cherenkov cut will reject most of the pions, there are a small number of high momentum pions that are capable of emitting Cherenkov light or by knocking out electrons “knock-on electrons”, which in turn produce light. Consequently, the electromagnetic calorimeter was used as second detector to separate pions from electrons. The configuration and working principles of the calorimeter were described in Section 3.7.4. A calorimeter cut was defined which is the ratio of the energy the particle deposits in the calorimeter to the corresponding

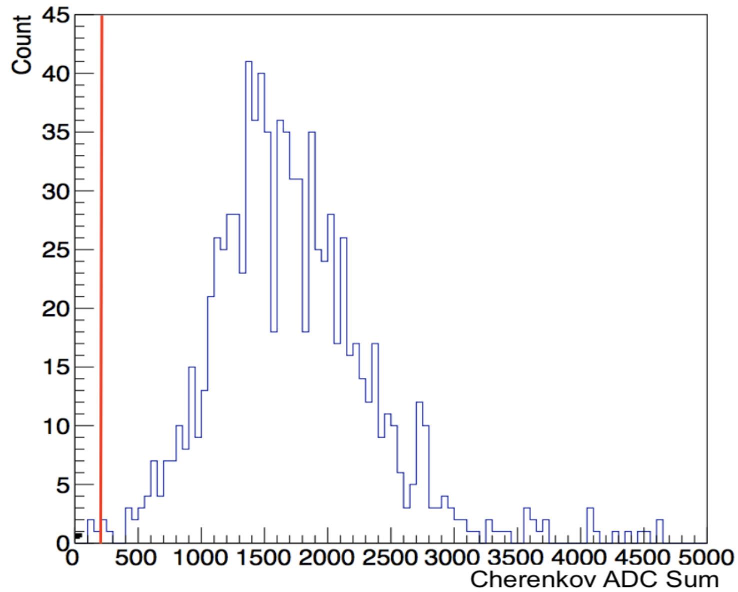

Figure 5.1: Cherenkov Sum ADC spectrum for the LHRS. The plot shows events from kinematics Kin50. The red line shows where the analysis cut is applied.

momentum from the VDC track, E'/P. As mentioned before, when electrons pass through the calorimeter, they deposit all of their energy and are completely absorbed. Other particles with a larger mass like pions produce significantly smaller signal in the calorimeter. For electrons, the E'/P ratio is expected to be approximately 1. Any particle of larger mass that passes through the calorimeter will have an E'/P value smaller than 1. To separate the electrons from pions, a cut on E'/P is placed at 0.7. Figure 5.2 shows the calorimeter E'/P spectrum, and the cut placed on the spectrum.

The combination of the Cherenkov and the calorimeter cuts are adequate to isolate electron events from background. This can be seen clearly by plotting the Cherenkov ADC sum and E'/P on a 2D histogram, as shown in Figure 5.3. The summary of the electron identification cuts used in this analysis is listed in Table 5.1.

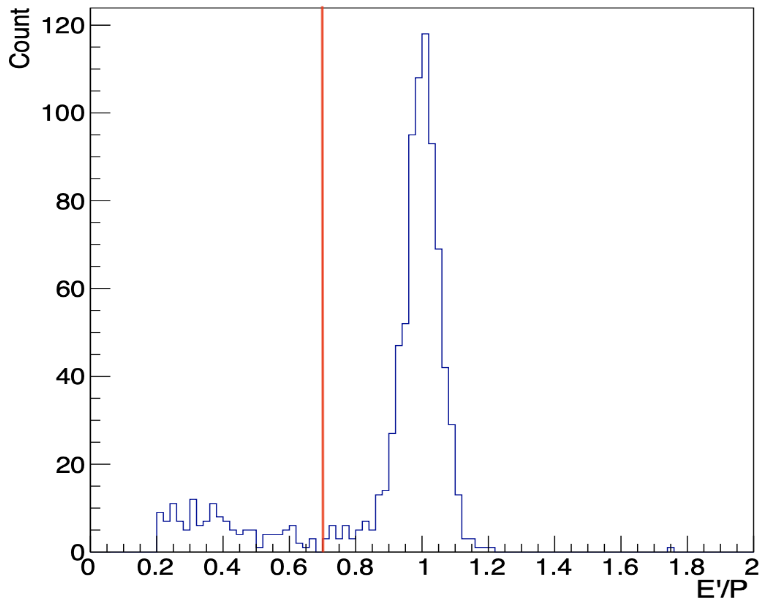

Figure 5.2: Calorimeter E'/P spectrum from the LHRS. This plot shows events from kinematics Kin50. The red line shows where the cut is applied.

Electron Identification	Cuts selected for this analysis
Cherenkov ADC sum	$>$ 200 channel
E'/P	>0.7

Table 5.1: List of the electron identification cuts used during the current analysis.

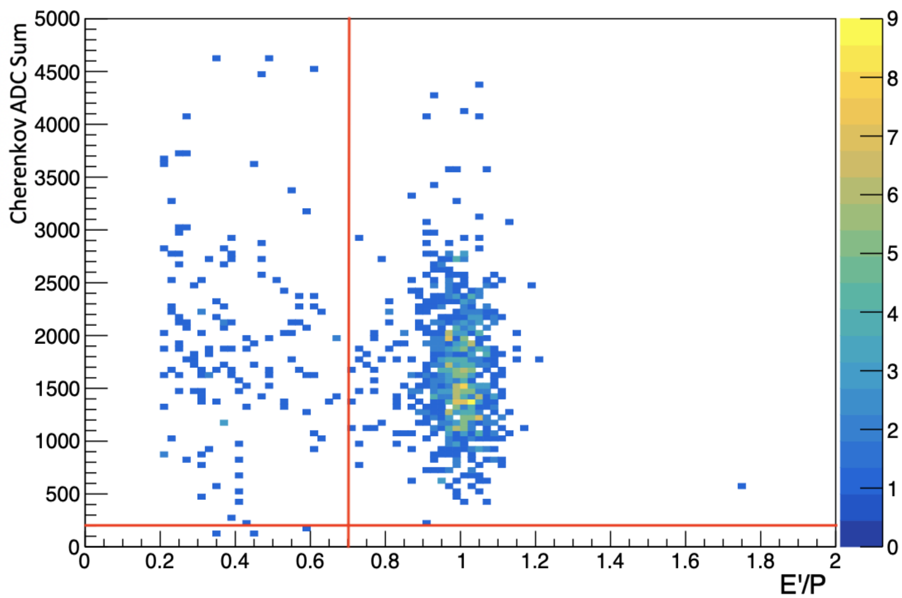

Figure 5.3: 2D Cherenkov ADC sum versus calorimeter E'/P spectrum for the LHRS. This plot shows events from kinematics Kin55. The red lines show where the cuts are applied. The events in the upper-right quadrant are considered to be good electrons.

5.4 ^{3}He and ^{4}He Identification

In order to achieve the main goal of the analysis, which was to identify elastic electron-^{4}He coincidence events and quasielastic electron-^{3}He coincidence events and to separate them from accidental background events such as electron-proton or electron-deuteron coincidence events, a set of cuts was needed to be applied on the particle's tracking and triggering quantities. Specifically, in addition to the Cherenkov and Calorimeter cuts, cuts were applied to particle coordinates as determined by the VDCs, recoil ADC signals for both scintillators, and to the ΔTOF.

As discussed in Section 3.7.2, the Scintillators provided the triggering information in the HRSs and the coincidence TOF. When charged particles pass through the scintillator paddles, they emit light that will be detected by both PMTs. The PMT signals are sent to TDCs. The coincidence timing information between the two scintillator planes in both spectrometers serve the purpose of distinguishing different particles, as heavier particles take a longer time to pass the distance between the two scintillators S1 and S2. For a ^{4}He particle, since it has a larger mass as compared to the ^{3}He one and to deuteron or proton background, the coincidence TOF is expected to be larger. The same type of cut is applied to discriminate ^{3}He particles from the background. The difference in the coincidence TOF provides a good separation between ^{3}He clusters and ^{4}He nuclei. Moreover, analyzing the ADC-integrated shape of the emitted light signal (pulse-shape discrimination technique) [77] in the S1 and S2 planes provides an unequivocal separation between ^{3}He and ^{4}He events.

The VDCs were responsible for the tracking information for the scattered electron and recoil particle at the Focal Planes of the two HRSs. Since the central momentum of the LHRS was lowered by 1.0%, the dispersive plane position in the FP $y_{electron}$ and

$\delta_{electron}$ for electron events was shifted. For a ^{4}He particle, most of these quantities are expected to be bigger than zero, except for the radiative tail events. The ^{3}He particles, which are expected to appear at the radiative tail of ^{4}He, have $y_{electron}$ and $\delta_{electron}$ smaller than zero.

Using the above information, we applied a combination of appropriate cuts to accurately select out the events we were interested in, which resulted in a clean sample of events with ample separation between ^{4}He events and ^{3}He clusters to be compared with simulation. These cuts include:

- **Scintillator cuts:** referred to these graphical cut as <u>S12</u> in the plots. These cuts involve two triggering related quantities: the sum of S1 and S2 ADC signals. The S1 versus S2 patterns are shown in the top plots of Figures 5.4 and 5.7 for Kin34 and Kin45, respectively. The blue and red rectangles in the bottom plots of Figures 5.4 and 5.7 represent ^{3}He and ^{4}He events, respectively, showing where the relevant cuts are placed.

- **Difference in the coincidence Time Of Flight cuts** (ΔTOF)**:** These cuts are referred to as <u>TOF</u> in the plots. The cut is applied on the quantities: y_{recoil} (dispersive position in the FP for the recoil events) and the ΔTOF. The y_{recoil} versus ΔTOF patterns are shown in the top plots of Figures 5.5 and 5.8 for Kin34 and Kin45, respectively. In the bottom plots, the enclosed events between the red lines are ^{4}He events, while the ones enclosed by the blue lines are ^{3}He events.

The above cuts vary with each kinematics. The different kinematics can be classified into two categories, depending on their beam energy. The first category includes Kin34 and Kin39 with beam energy 2.1 GeV. The other category include the kinematics with beam energy 4.1 GeV, which are Kin45, Kin50 and Kin55 (see Table

4.1).

5.4.1 Kinematics with Beam Energy of 2.1 GeV

As mentioned above, there were two kinematics with 2.1 GeV beam energy but with different scattering angles. For these two kinematics, the background events were fewer as compared to the kinematics with 4.1 GeV beam. As shown in the top plot in Figure 5.4, there are three different areas where the ADC signals from S1 and S2 are clustered. The three areas represented ^{4}He events, ^{3}He events, and background events proton/deuteron. The red and blue rectangles indicate the cuts applied to S1 and S2 ADC signals. Even though the S12 cut rejects most of the background, as seen in the bottom plot of Figure 5.5, it is still possible for some of it to exist within the cuts limit. Therefore, the TOF cut is needed to be applied in order to remove the remaining background events, as shown in the bottom plot of Figure 5.5. After applying these cuts, most of the unwanted background events is eliminated, and the separation between ^{4}He and ^{3}He events can be seen clearly in Figure 5.6. Since the clustered events in the top plots in Figures 5.4 and 5.5 are clearly observable, one can apply S12 cut then TOF cut, or vice versa. The plots in Figures 5.4 to 5.6 are for kinematics Kin34. The plots showing the effect of different cuts for kinematics Kin39 are listed in Appendix A.

Kin34 Analysis:

Recoil scintillator S1 ADC sum versus S2 ADC sum

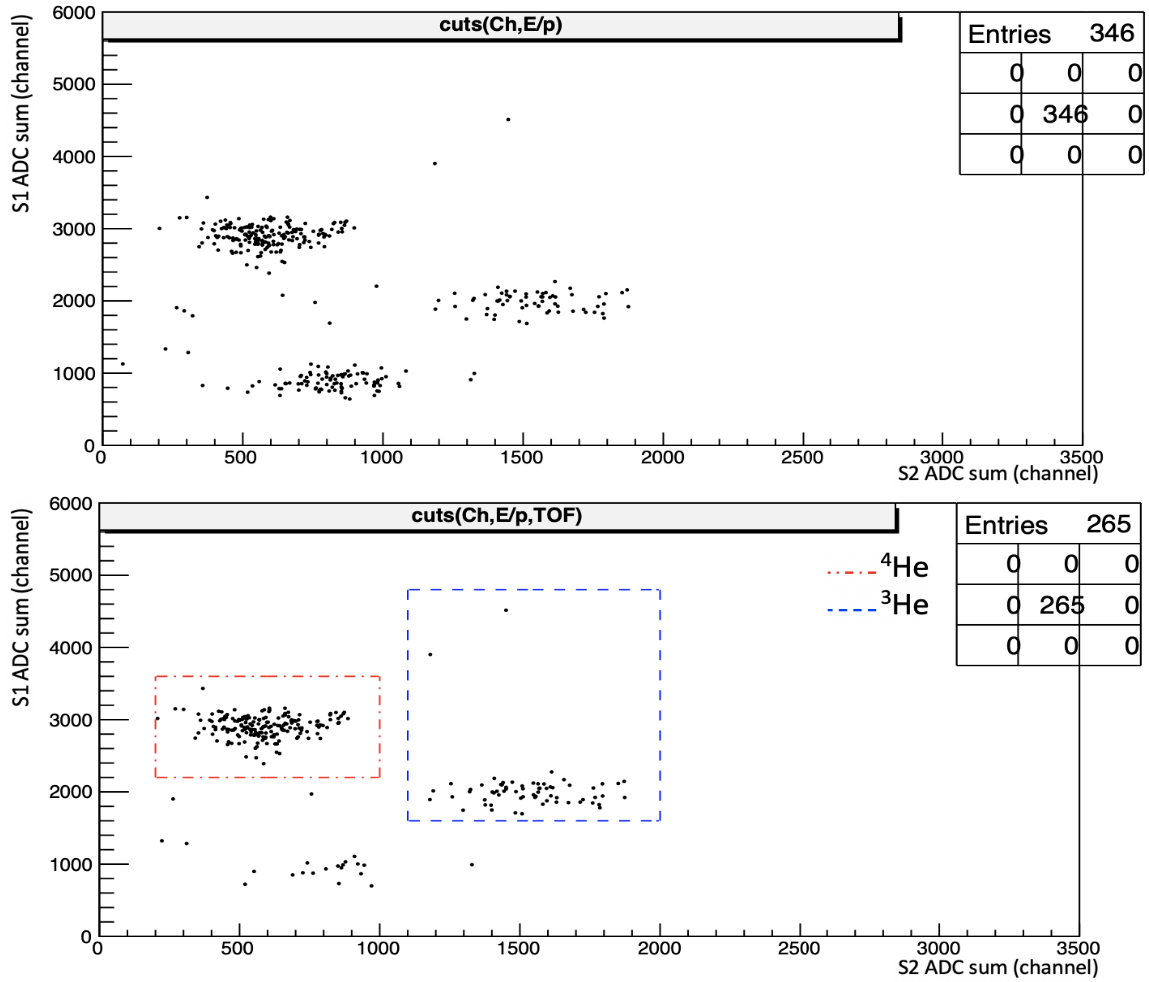

Figure 5.4: Recoil scintillator S1 ADC signal versus recoil scintillator S2 ADC signal. In the top plot, only the Cherenkov ADC sum and the E'/P cuts have been applied. In the bottom plot, all cuts including the TOF cut for both ^{3}He and ^{4}He have been applied. The red and blue rectangles show where the recoil scintillators ADCs cuts for either ^{3}He or ^{4}He selection have been applied.

Recoil Focal Plane y_{recoil} versus ΔTOF

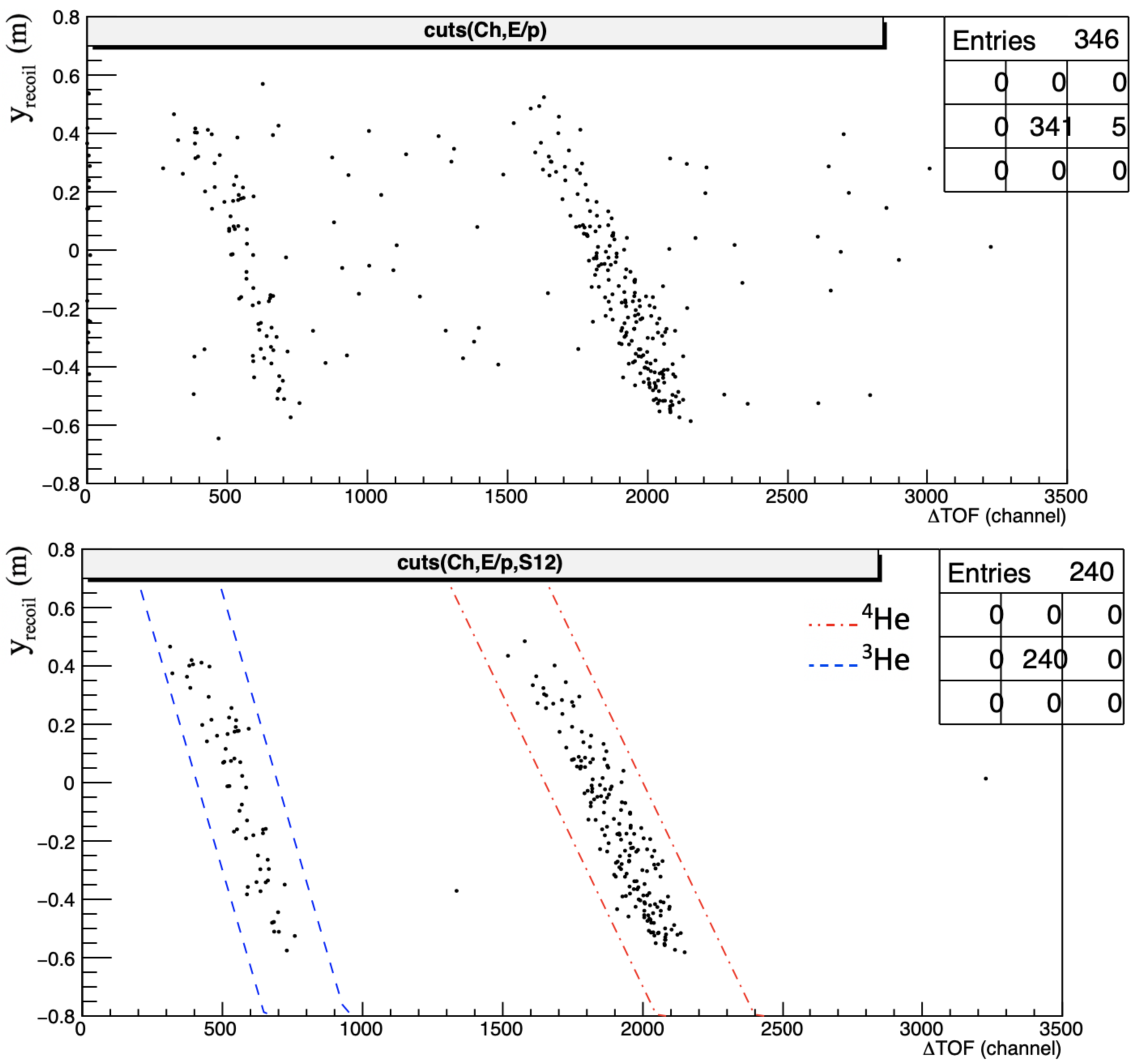

Figure 5.5: y_{recoil} in FP versus ΔTOF. In the top plot, only the Cherenkov ADC sum and the E'/P cuts have been applied. In the bottom plot, all cuts including the recoil scintillators ADCs cuts for both ^{3}He and ^{4}He have been applied. The red and blue lines show where the TOF cuts for either ^{3}He or ^{4}He selection have been applied.

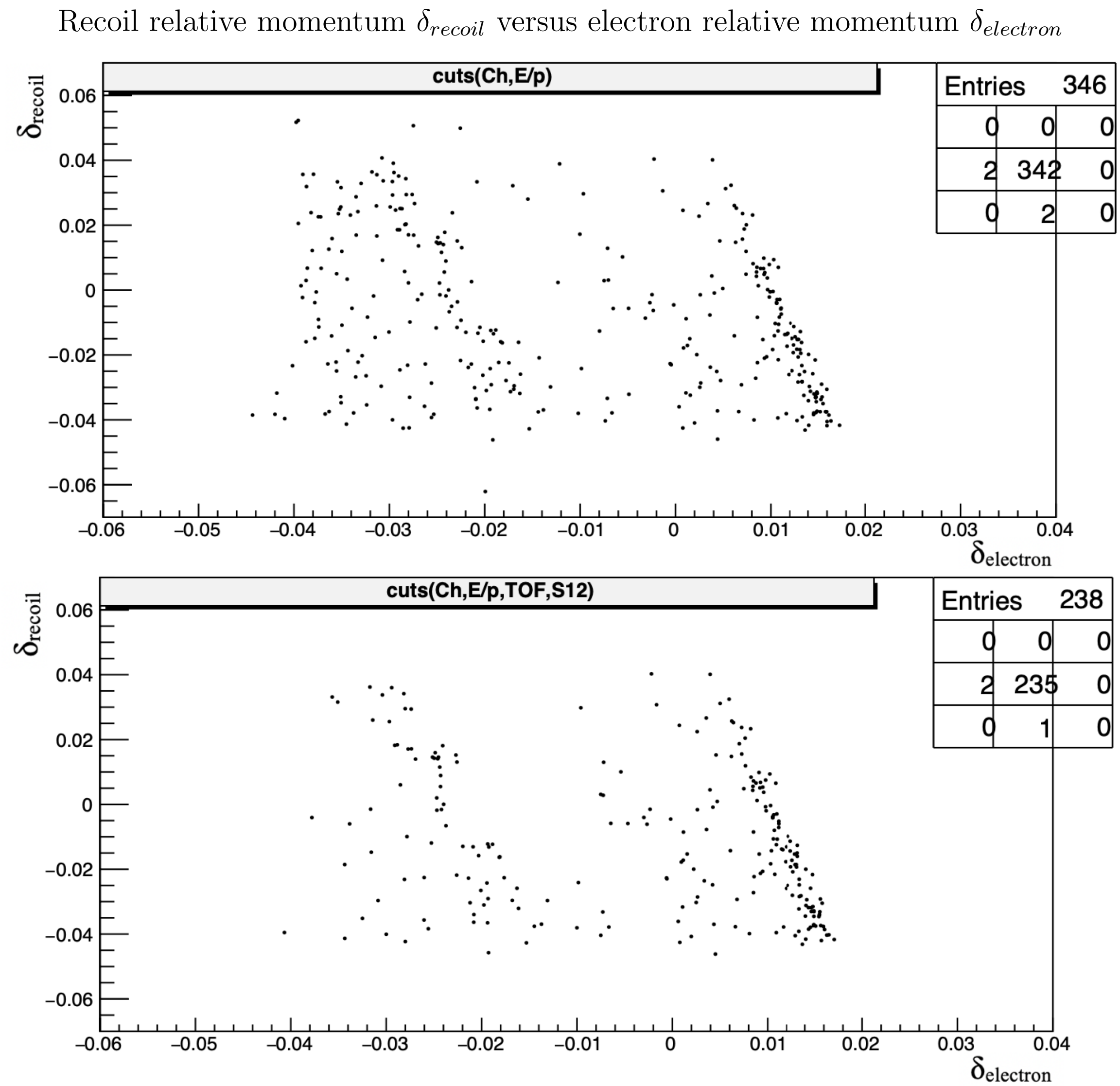

Figure 5.6: δ_{recoil} versus $\delta_{electron}$. In the top plot, only the Cherenkov ADC sum and the E'/P cuts have been applied. In the bottom plot, all cuts including recoil scintillators ADCs and TOF cuts for both ^{3}He and ^{4}He selection have been applied.

5.4.2 Kinematics with Beam Energy of 4.1 GeV

There were three kinematics with 4.1 GeV beam energy but with different angles: Kin45, Kin50, and Kin55. With the 4.1 GeV beam energy, the background events increased, the number of ^{4}He events were significantly reduced, and the sum of S1 and S2 signals became closer or even started to overlap. However, in Kin45, the three different areas, where the ADC signals from S1 and S2 are clustered, are still observable, as shown in the top plot of Figure 5.7. Therefore, the same type of cuts that are used in kinematics Kin34 are capable of eliminating background events. Unlike Kin34, the clustered events in the top plot of Figure 5.8 are not clear. As a result, the cuts need to be applied in the order, S12 cut then TOF cut. By applying these cuts, the separation between ^{4}He and ^{3}He events can be seen clearly in Figure 5.9.

In Kin50 and Kin55, the sum of S1 and S2 signals overlap, and only two areas can be observed, as shown in the top plot of Figures A.4 and A.7. One of the areas represents background events, while the other area represents ^{4}He and ^{3}He together. Therefore, a new cut, referred to as "4y", is applied to the $\delta_{electron}$ before using S12 and TOF cuts to specify ^{4}He events. The middle plots in Figures A.4, A.5, A.7, and A.8 show the effect of applying this cut. The 4y cut must be applied after the E'/P and Cherenkov cuts to ensure the accuracy in placing S12 and TOF cuts. The effect of applying different cuts to Kin50 and Kin55 are shown in plots of Appendix A.

Kin45 Analysis:

Recoil scintillator S1 ADC sum versus S2 ADC sum

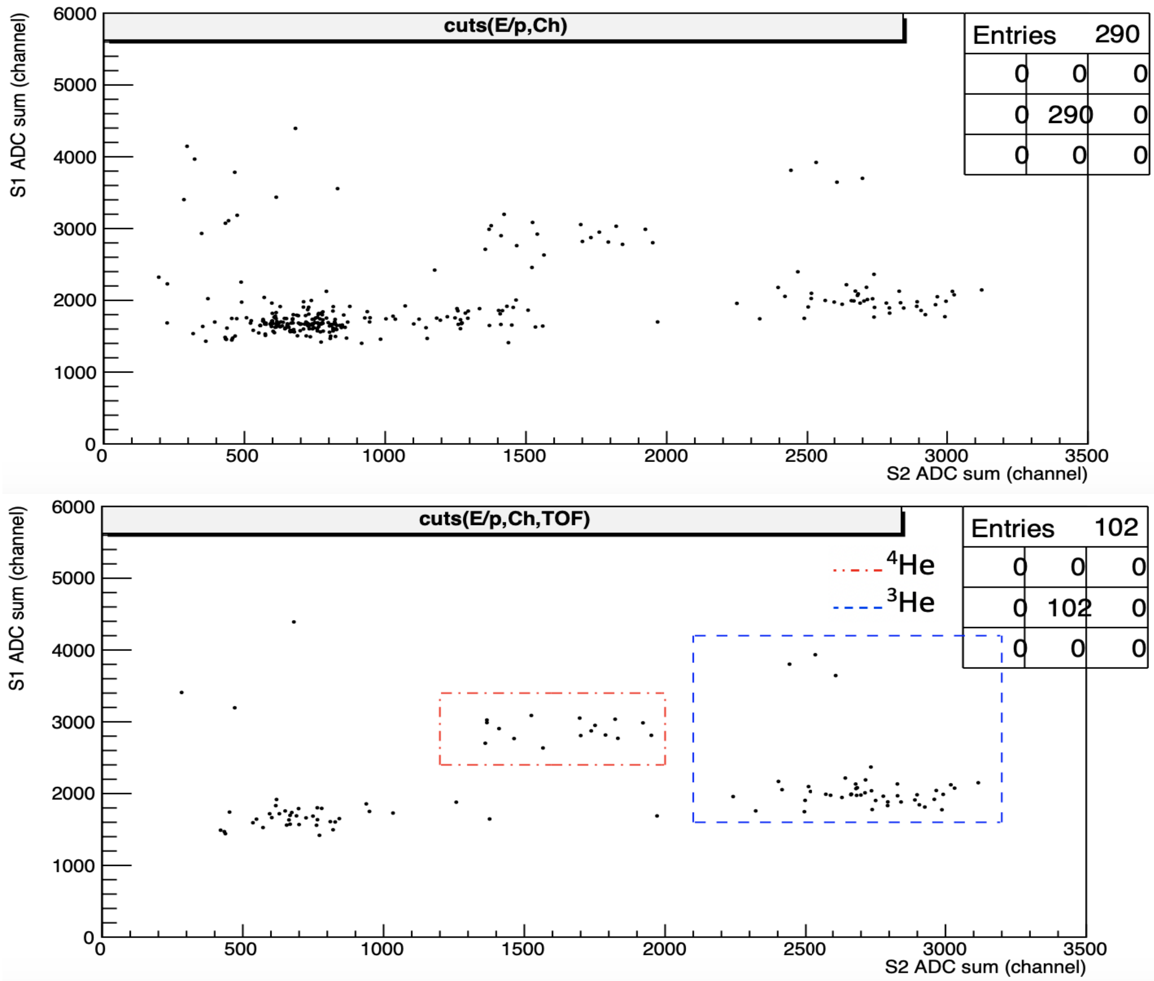

Figure 5.7: Recoil scintillator S1 ADC signal versus recoil scintillator S2 ADC signal. In the top plot, only the Cherenkov ADC sum and the E'/P cuts have been applied. In the bottom plot, all cuts including the TOF cut for both ^{3}He and ^{4}He have been applied. The red and blue rectangles show where the recoil scintillators ADCs cuts for either ^{3}He or ^{4}He selection have been applied.

Recoil Focal Plane y_{recoil} versus ΔTOF

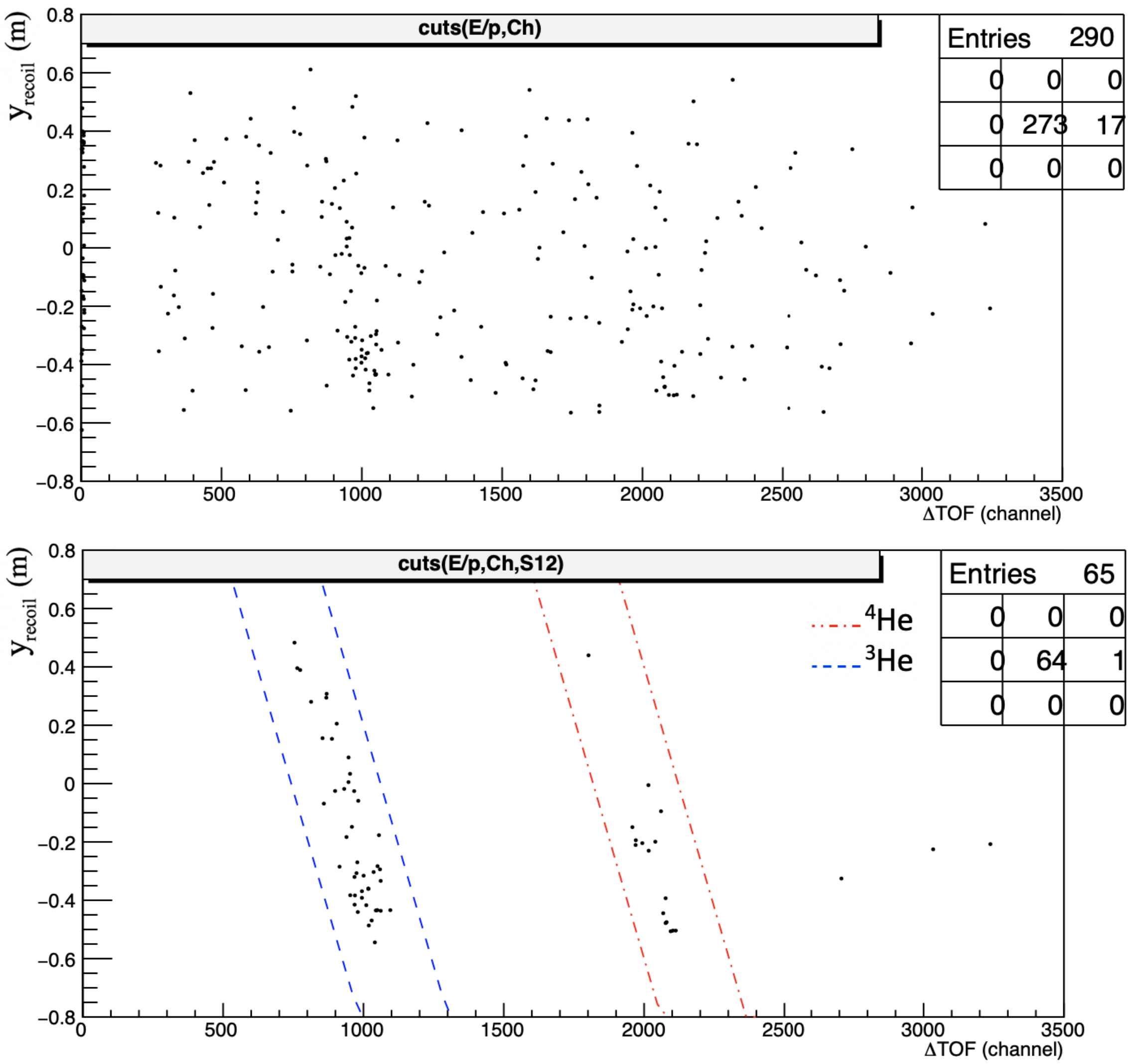

Figure 5.8: y_{recoil} in FP versus ΔTOF. In the top plot, only the Cherenkov ADC sum and the E'/P cuts have been applied. In the bottom plot, all cuts including the recoil scintillators ADCs cuts for both ^{3}He and ^{4}He have been applied. The red and blue lines show where the TOF cuts for either ^{3}He or ^{4}He selection have been applied.

Recoil relative momentum δ_{recoil} versus electron relative momentum $\delta_{electron}$

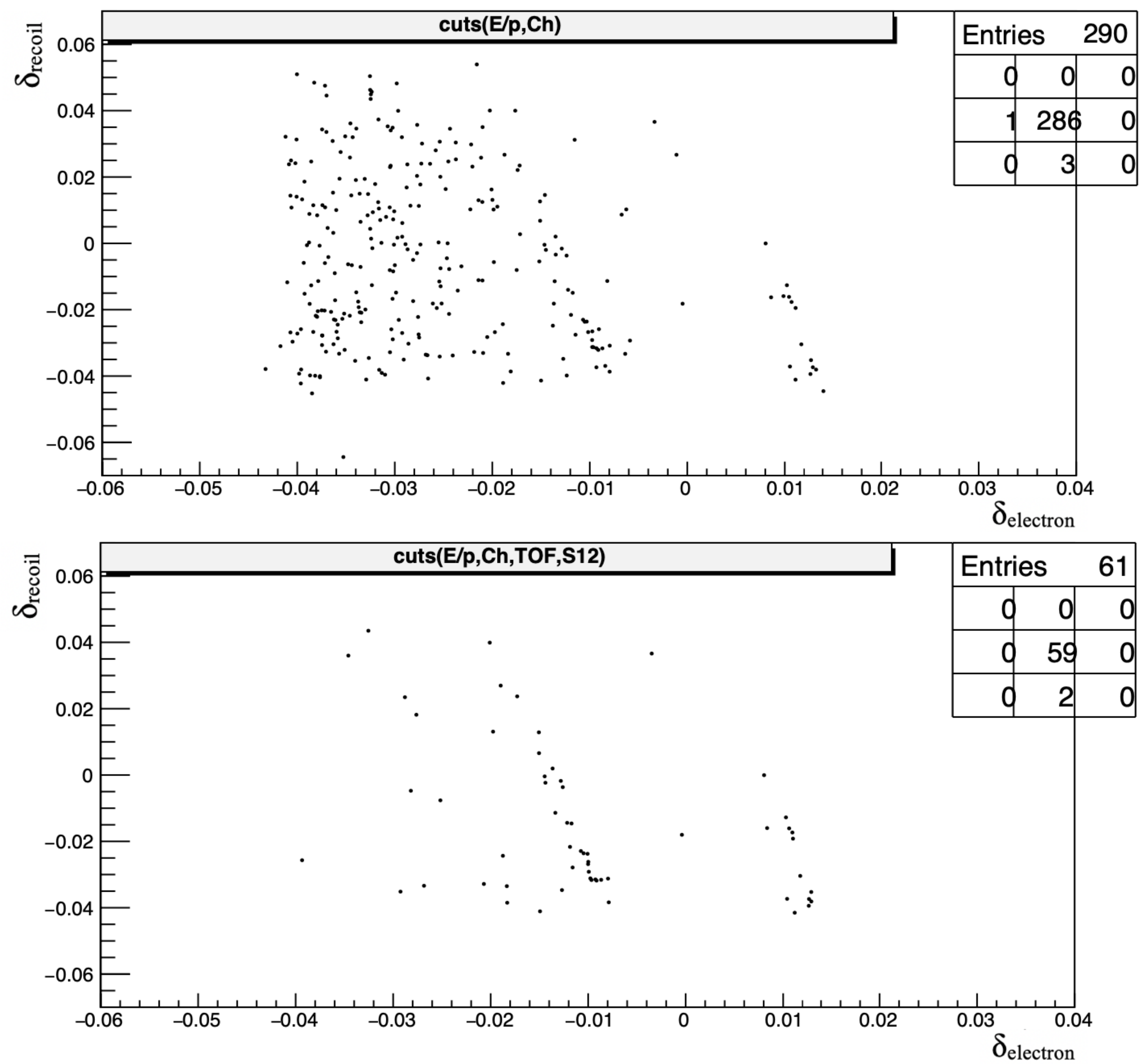

Figure 5.9: δ_{recoil} versus $\delta_{electron}$. In the top plot, only the Cherenkov ADC sum and the E'/P cuts have been applied. In the bottom plot, all cuts including recoil scintillators ADCs and TOF cuts for both ^{3}He and ^{4}He selection have been applied.

The list of all cuts are summarized here:

• Cherenkov cut (Ch): selects electrons where the ADC channel for the sum of the Cherenkov signals is greater than 200.

• Calorimeter cut ($\underline{E'/P}$): selects electron events where E'/P ratio is greater than 0.7.

• Difference in coincidence Time of Flight cut (TOF): selects only the events within a limited range, as shown in Tables 5.3 and 5.4.

• Scintillator cuts (S12): selects only events within a chosen graphical shape, as shown in Table 5.2.

• Relative momentum of electron cut (4y): selects only the events where $\delta_{electron}$ is greater than 0.0 (used in Kin50 and Kin55).

All of the above cuts can be applied separately to show the pattern of ^{3}He or ^{4}He events as needed for the comparison with Monte Carlo simulation. A summary of all cuts applied in the the analysis for all kinematics can be found in the following tables.

Kinematics	S12 cut for ^{4}He events	S12 cut for ^{3}He events
Kin34	$2200 < S1 < 3600$ $200 < S2 < 1000$	$1600 < S1 < 4800$ $1100 < S2 < 2000$
Kin39	$2000 < S1 < 4400$ $700 < S2 < 1500$	$1200 < S1 < 4000$ $1700 < S2 < 2700$
Kin45	$2400 < S1 < 3400$ $1300 < S2 < 2000$	$1600 < S1 < 4200$ $2100 < S2 < 3200$
Kin50	$2200 < S1 < 3200$ $1400 < S2 < 2500$	$1600 < S1 < 4200$ $1600 < S2 < 4000$
Kin55	$2200 < S1 < 2800$ $1800 < S2 < 2800$	$1400 < S1 < 3800$ $1600 < S2 < 4000$

Table 5.2: List of the ^{4}He and ^{3}He identification cuts applied to S1 and S2 ADC sum signals for the different kinematics of the experiment.

Kinematics	TOF cut for ^{4}He events
Kin34	$(y - 3.30)/(-0.002) < TOF < (y - 4.00)/(-0.002)$
Kin39	$(y - 3.30)/(-0.002) < TOF < (y - 4.00)/(-0.002)$
Kin45	$(y - 6.00)/(-0.002) < TOF < (y - 7.00)/(-0.002)$
Kin50	$(y - 5.4)/(-0.0032) < TOF < (y - 6.00)/(-0.0032)$
Kin55	$(y - 6.00)/(-0.0035) < TOF < (y - 7.00)/(-0.0035)$

Table 5.3: List of the ^{4}He identification linear cuts applied to y_{recoil} versus ΔTOF plots for the different kinematics of the experiment.

Kinematics	TOF cut for ^{3}He events
Kin34	$(y - 1.35)/(-0.0033) < TOF < (y - 2.30)/(-0.0033)$
Kin39	$(y - 1.70)/(-0.0033) < TOF < (y - 2.70)/(-0.0033)$
Kin45	$(y - 2.45)/(-0.0033) < TOF < (y - 3.50)/(-0.0033)$
Kin50	$(y - 2.45)/(-0.0033) < TOF < (y - 3.30)/(-0.0033)$
Kin55	$(y - 4.00)/(-0.0045) < TOF < (y - 5.00)/(-0.0045)$

Table 5.4: List of the ^{3}He identification linear cuts applied to y_{recoil} versus ΔTOF plots for the different kinematics of the experiment.

Chapter 6

Results and Discussion

In this chapter, the comparison between Focal Plane (FP) particle distributions for the experimental data from JLab experiment E04-018 and the present Monte Carlo simulation are presented for different kinematics. In addition, the number of ^{3}He cluster quasielastic events and the number of ^{4}He elastic events are extracted from the data. The ratios of the two types of events are calculated from the experimental data and the Monte Carlo simulation. Moreover, some characteristics of ^{3}He cluster events that make it to the FP are presented. The momentum distribution of the ^{3}He events, the separation energy, and angles are plotted after applying all corrections and cuts. Due to the absence of theoretical predictions for the existence of ^{3}He clusters within ^{4}He, our discussion is limited. The hope is that the results of this study will spur new theoretical and experimental investigations.

6.1 The ^{3}He Events at the Focal Plane

In the MC, the incident electron is assumed to interact with non-stationary ^{3}He clusters. The ^{3}He particles within the ^{4}He nuclei move with Fermi momentum P_t and with directional angles θ_t and ϕ_t. The momentum distribution of the ^{3}He clusters has been shown in Figure 4.6. The angles θ_t and ϕ_t are chosen to be uniformly distributed within the limits $\pm 180^o$ and $\pm 90^o$, respectively. After the scattering process and applying all the corrections, the events are transported through the spectrometer. Only events that passed the optics model apertures and all other applied cuts are recorded to have reached the FP. Figures 6.1, 6.2, and 6.3 show the momentum distribution and directional angles of the ^{3}He cluster events that have reached the FP for the lowest and highest kinematics, respectively.

Figure 6.1 implies that only ^{3}He clusters with low Fermi momentum of values around 100 MeV/c (see Figure 4.6 in Chapter 4) are of interest. The ^{3}He clusters with high momentum at the interaction vertex, before scattering occurs, have nearly zero probability to pass through the apertures of the spectrometer, after the scattering process, due to its finite angular and momentum acceptances. One can see from Figure 4.21 that although the range of the relative momentum distribution is very wide, most of the events are out the acceptance limits and do not reach the FP.

From Figure 6.1, one can see that the momentum distribution ^{3}He clusters within the target has roughly a Gaussian shape with a tail toward large momenta for both the lower and higher Q^2 kinematics (with incident beam energy 2.094 GeV and 4.051 GeV, respectively). Figure 6.2 shows the transverse angular distribution for the ^{3}He clusters events that made it to the FP. It is evident from Figure 6.2 that the contribution of the events from the backward transverse angles dominates in contrast to the forward transverse angles. At high kinematics, the contribution from the forward angles is almost nonexistent. However, the dispersive angles ϕ_t of ^{3}He events are distributed over the entire possible range limit, as seen in Figure 6.3, with smaller contribution for the angles that get closer to the vertical or horizontal planes, $\pm 90^o$ or 0^o, respectively.

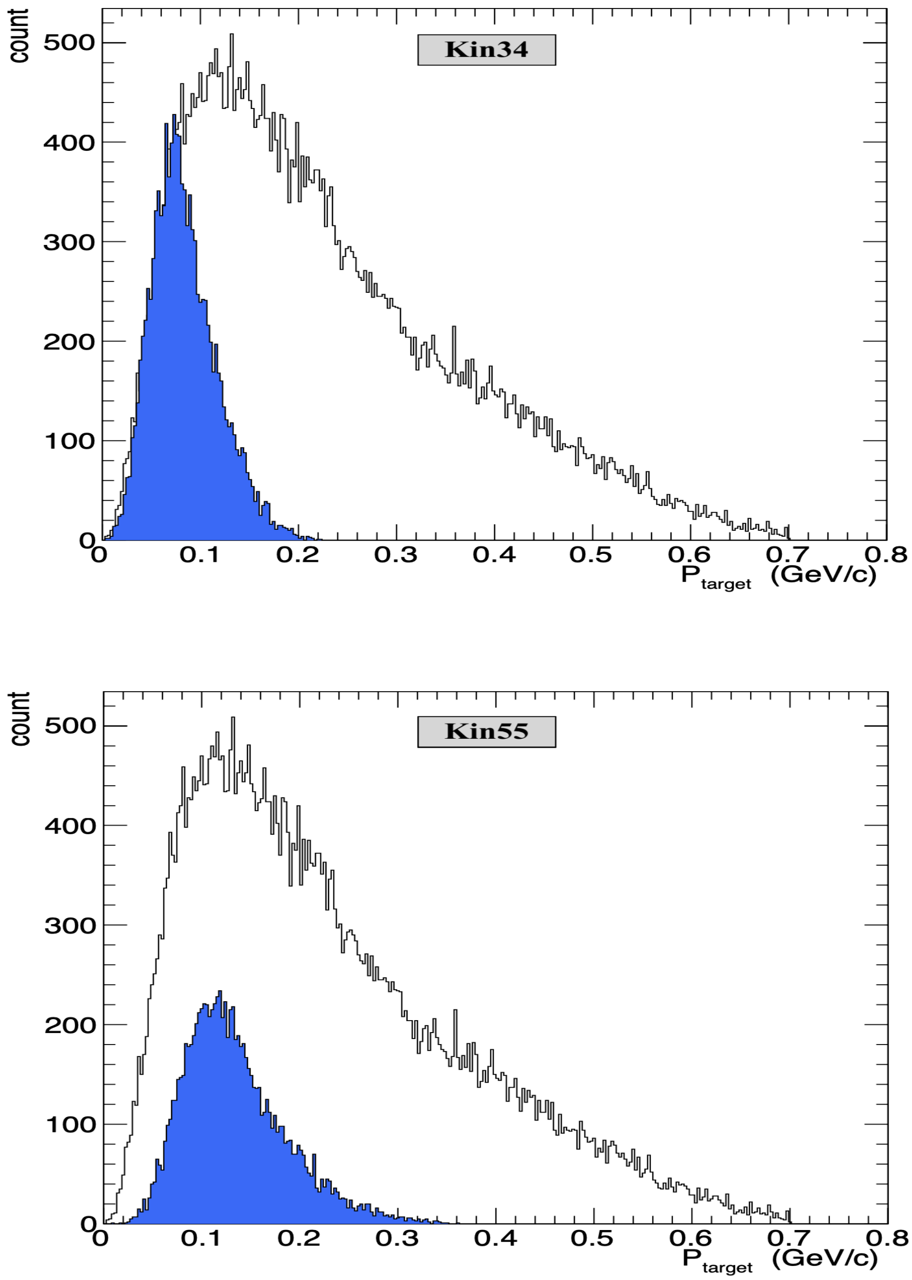

Figure 6.1: The area represents the momentum distribution of ^{3}He clusters in ^{4}He nuclei for successful coincidence events (for which both electrons and ^{3}He reach the detectors). The black line represents the initial distribution as appear in Figure 4.6 (the number of initial events was reduced for the comparison).

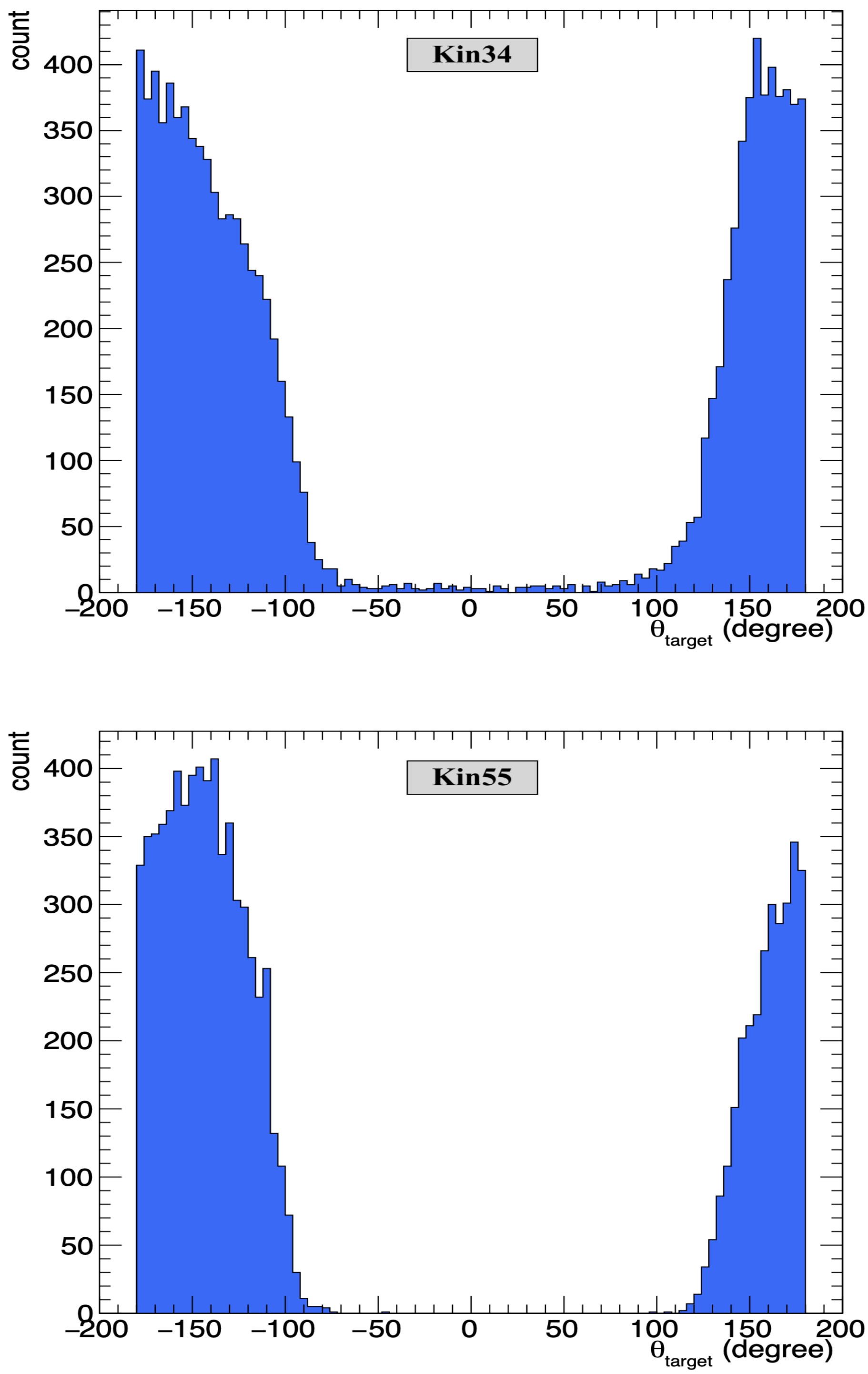

Figure 6.2: The transverse angle θ_t distribution of ^{3}He clusters in ^{4}He nuclei for successful coincidence events (for which both electrons and ^{3}He reach the detectors).

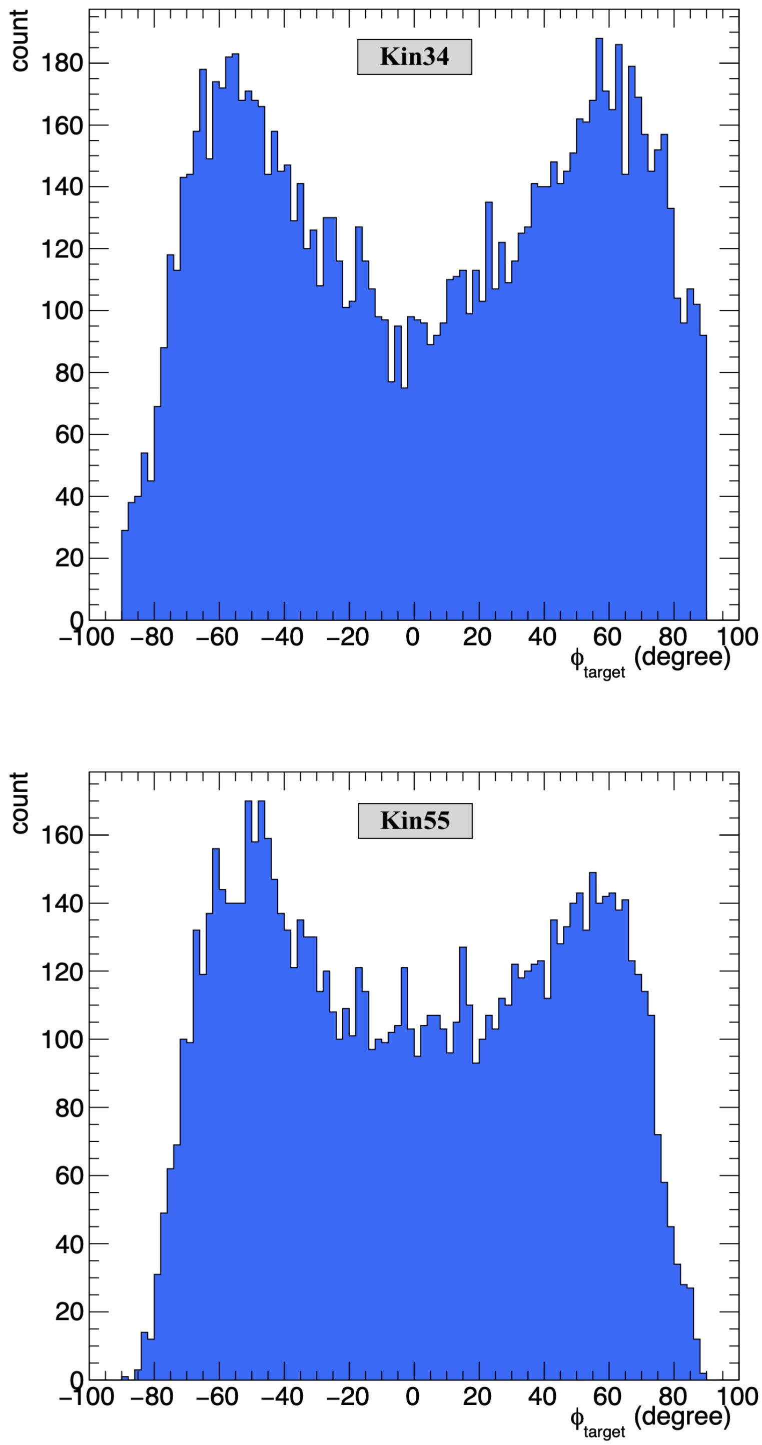

Figure 6.3: The dispersive angle ϕ_t distribution of ^{3}He clusters in ^{4}He nuclei for successful coincidence events (for which both electrons and ^{3}He reach the detectors).

6.2 Separation Energy

As mentioned in Section 4.6, the incident beam deposited a small amount of energy into the ^{4}He nuclei to separate the ^{3}He clusters during the scattering interaction. Use of a constant value for the separation energy for all kinematics could not describe well the observed quasielastic stripe of the relative momenta of the scattered electrons and recoil ^{3}He clusters. It was found empirically that, for good agreement between the MC simulation and the data, the separation energy had to increase quadratically with Q^2, as shown in Figure 6.4, for all ^{3}He events of the five kinematics. The different colors in the Figure correspond to the different kinematical settings.

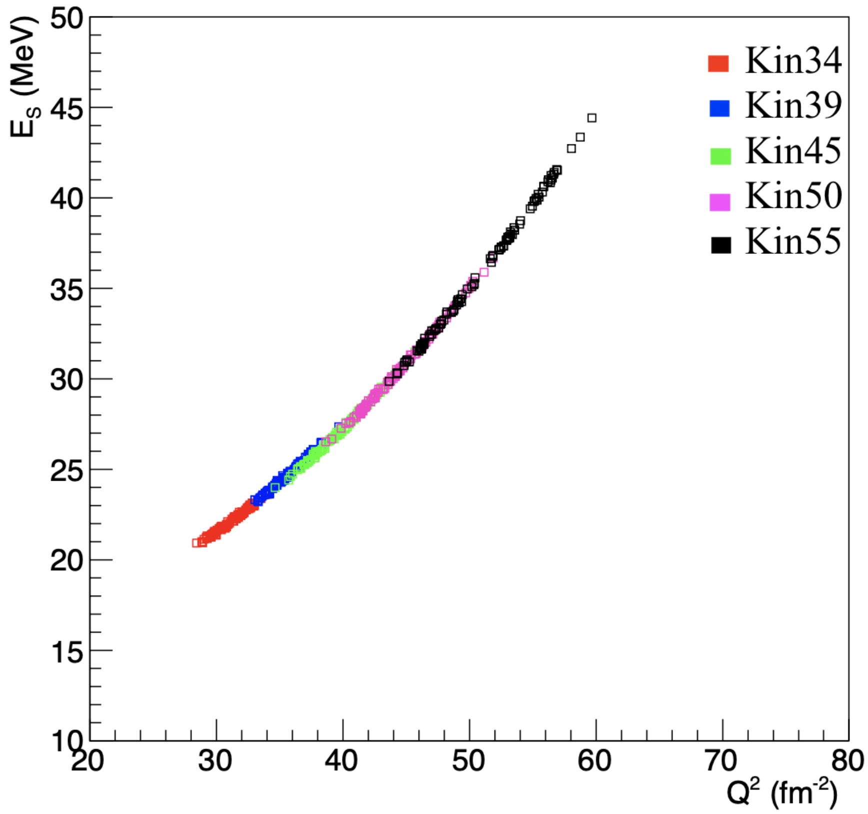

Figure 6.4: The separation energy E_s of all ^{3}He events versus Q^2 for the different kinematics. The values were determined empirically to match the experimental data.

6.3 Comparison Between Experimental Data and the MC Simulation

In order to have an accurate comparison between the data of experiment E04-018 and the results of the simulation, the MC was developed to mimic as close as possible the experiment setup and conditions. The multiple scattering, ionization, and radiative corrections were applied, where applicable, to the incident, scattered, and recoil events. Fifth order transport matrices were used to transport the events of interest from the target to the Focal Planes of the two spectrometers. A cross section model based on previous experimental results of E04-018 [10, 11] was used to weight trial events of the simulation before comparing with the data. The working principle of this simulation was presented in detail in Chapter 4. The experimental data were analyzed to clearly distinguish ^{4}He from ^{3}He events, as described in Chapter 5. After having carefully eliminated background events, the events of interest were unambiguously separated. The applied cuts for all kinematics can be seen in Tables 5.2, 5.3, and 5.4.

Figures 6.5 to 6.24 show various physical quantities for the scattered electrons and recoil nuclei at the FP position. The quantities are plotted for both the experimental data and the simulation results for all kinematics settings. The black circles and squares represent experimental data for ^{3}He clusters and ^{4}He nuclei, respectively. The blue circles represent ^{3}He simulation events, while the red squares represent ^{4}He simulation events.

The difference in the coincidence time-of-flight ΔTOF was calculated as described in Section 4.9. The positions and angles of the events at the FP were determined by using the fifth order transport matrix coefficients. The vertical positions for the recoil events y_{recoil} versus ΔTOF are plotted for all kinematics. It is evident from

Figures 6.5 to 6.9 that the correlated stripes of the data and the MC simulation are in excellent mutual agreement. This agreement implies that the experimental black circles ought to be ^{3}He events.

To emphasize this conclusion, more correlations with different quantities were considered in the comparison. The Hall A spectrometers have good particle identification in the vertical (dispersive) direction. The relative momenta, δ_{recoil} versus $\delta_{electron}$, and the vertical position, y_{recoil} versus $y_{electron}$, at the FP have been plotted for all kinematics. The experimental data are consistent with the simulation results even at low statistics kinematics. This significant result indicates that the black circles are indeed ^{3}He events which correspond to pre-existing clusters within ^{4}He nuclei.

In Figures 6.15 to 6.19, the top and the bottom plots present the ΔTOF versus the electron vertical position and the electron relative momentum, respectively. As it can be seen, there is a good separation between ^{4}He and ^{3}He events in both experimental and simulation data, which allows for the identification of the two classes of the particles clearly. The left side of Figures 6.20 through 6.24 show $\phi_{electron}$ versus $y_{electron}$, and the right side show ϕ_{recoil} versus $\phi_{electron}$. It is also clear from these Figures that there is excellent agreement everywhere among experimental data and simulation predictions even at low statistics kinematics where there is a small number of events. This agreement can be considered as additional clear, undisputed evidence of the presence of a ^{3}He cluster within the ^{4}He nucleus.

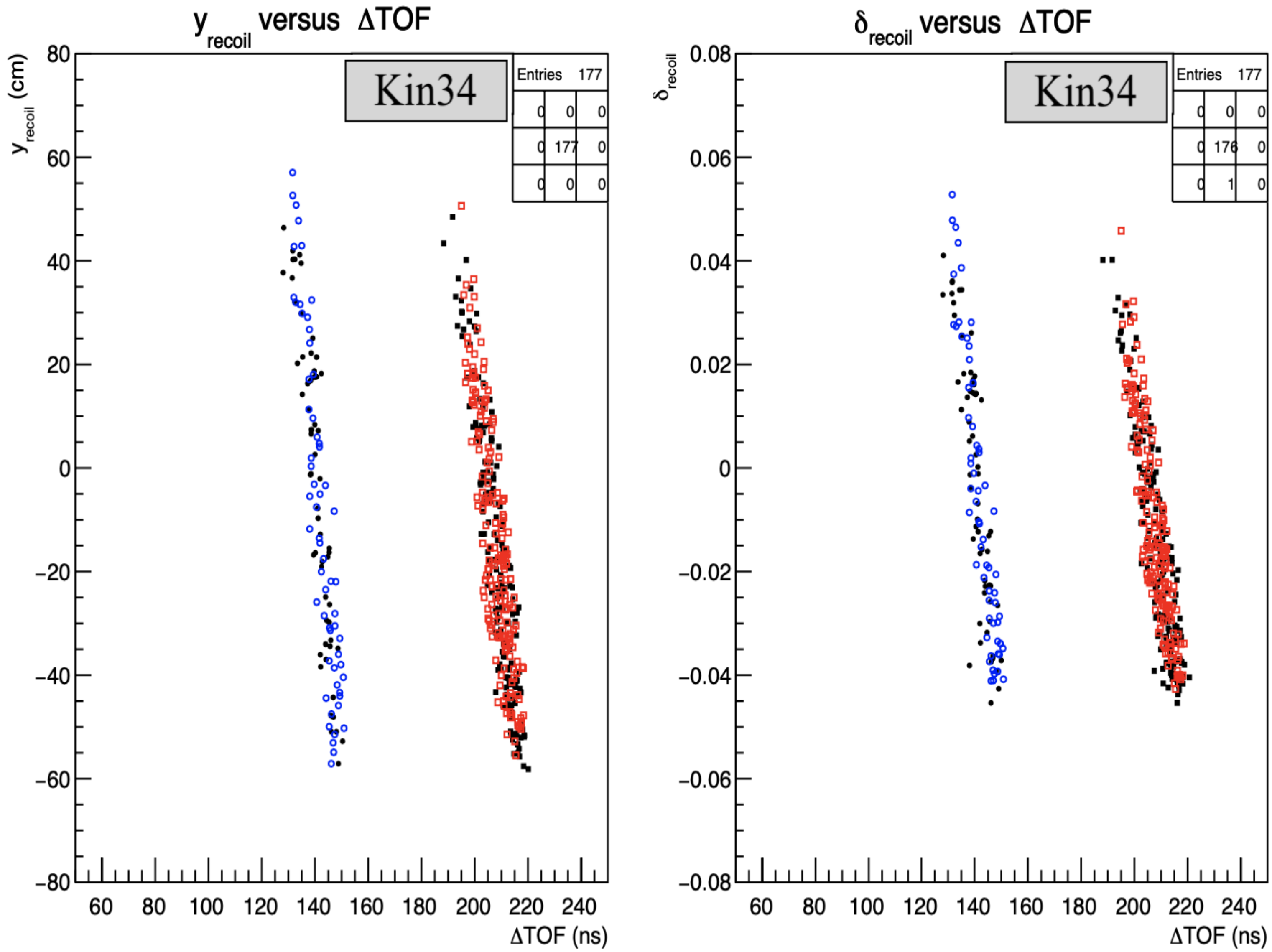

Figure 6.5: Kinematics Kin34: (Left) y_{recoil} versus ΔTOF and (Right) δ_{recoil} versus ΔTOF. The solid black circles and squares represent ^{3}He and ^{4}He experimental data, respectively. The open blue circles and red squares represent the corresponding Monte Carlo simulation for ^{3}He and ^{4}He, respectively. The statistics box shows the ^{4}He number of events. All cuts and corrections have been applied.

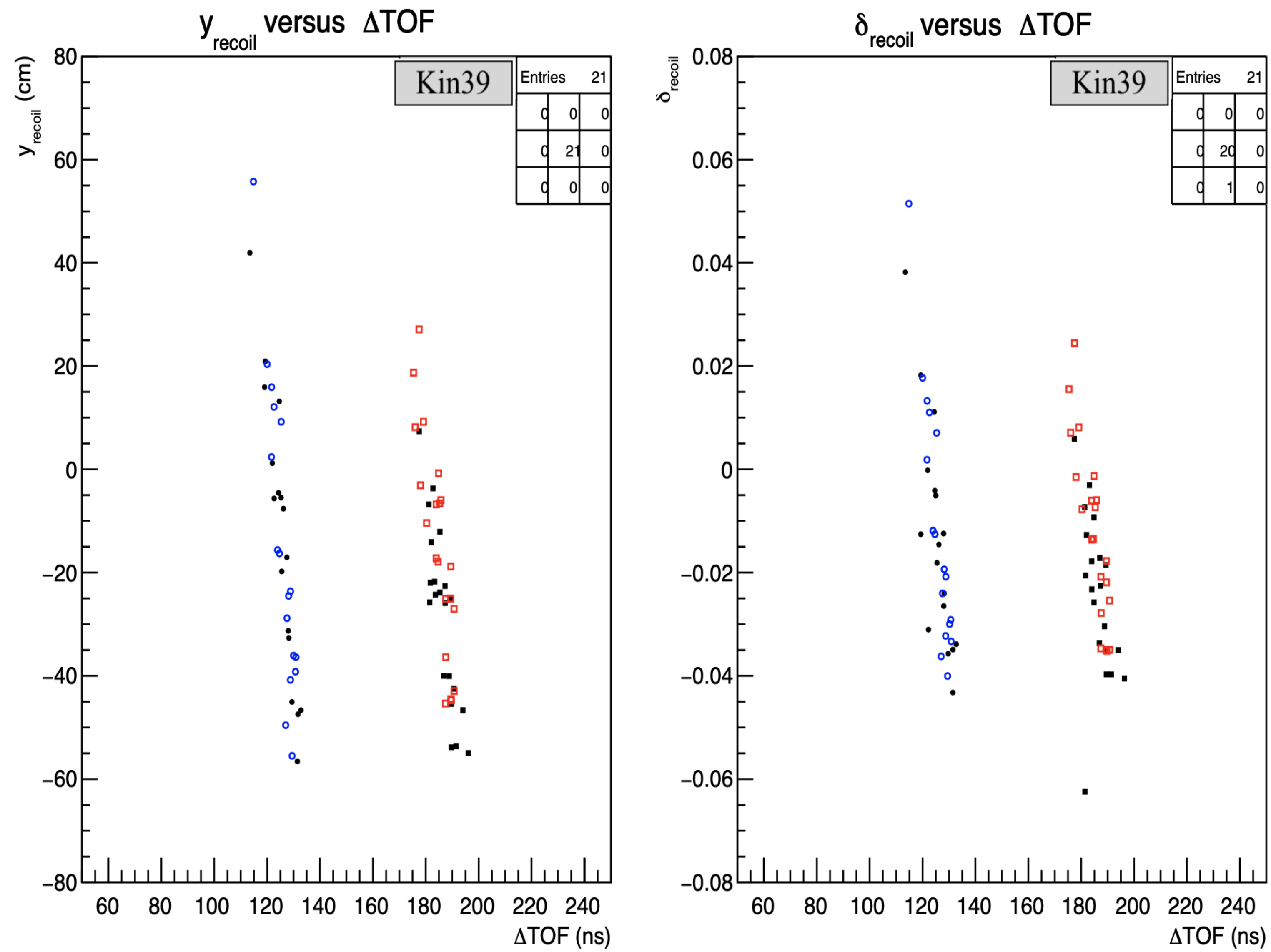

Figure 6.6: Kinematics Kin39: (Left) y_{recoil} versus ΔTOF and (Right) δ_{recoil} versus ΔTOF. The solid black circles and squares represent ^{3}He and ^{4}He experimental data, respectively. The open blue circles and red squares represent the corresponding Monte Carlo simulation for ^{3}He and ^{4}He, respectively. The statistics box shows the ^{4}He number of events. All cuts and corrections have been applied.

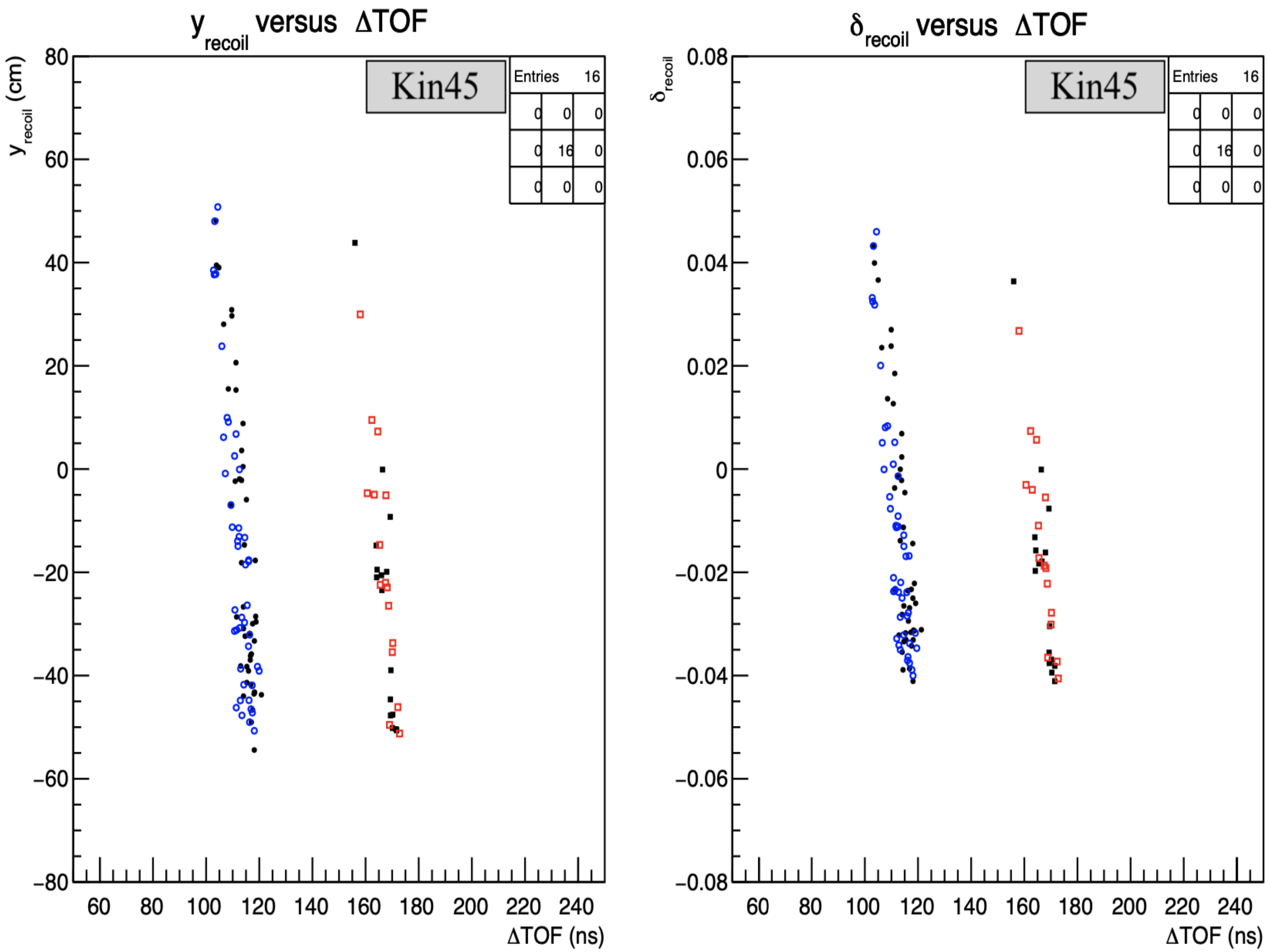

Figure 6.7: Kinematics Kin45: (Left) y_{recoil} versus ΔTOF and (Right) δ_{recoil} versus ΔTOF. The solid black circles and squares represent ^{3}He and ^{4}He experimental data, respectively. The open blue circles and red squares represent the corresponding Monte Carlo simulation for ^{3}He and ^{4}He, respectively. The statistics box shows the ^{4}He number of events. All cuts and corrections have been applied.

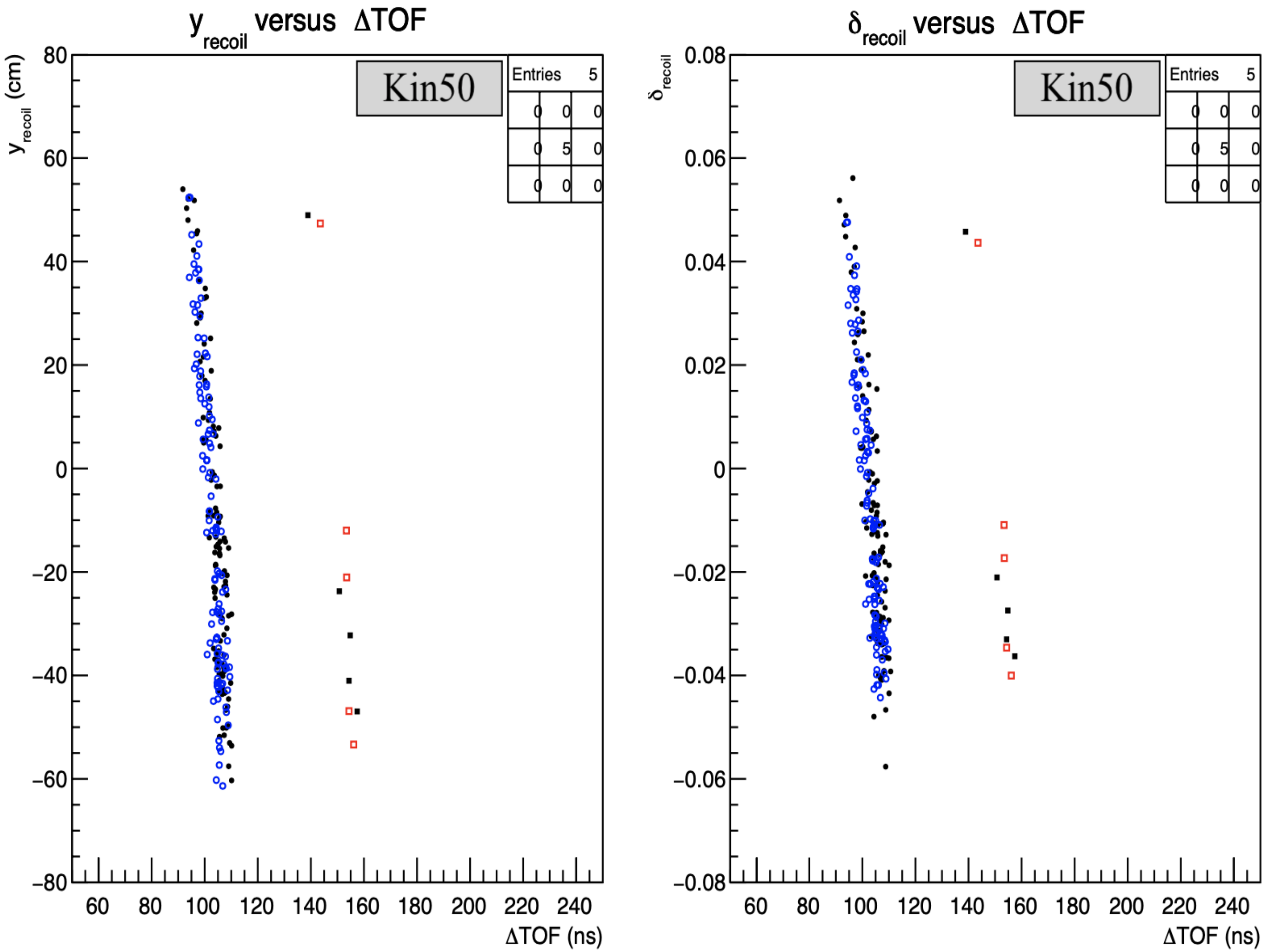

Figure 6.8: Kinematics Kin50: (Left) y_{recoil} versus ΔTOF and (Right) δ_{recoil} versus ΔTOF. The solid black circles and squares represent ^{3}He and ^{4}He experimental data, respectively. The open blue circles and red squares represent the corresponding Monte Carlo simulation for ^{3}He and ^{4}He, respectively. The statistics box shows the ^{4}He number of events. All cuts and corrections have been applied.

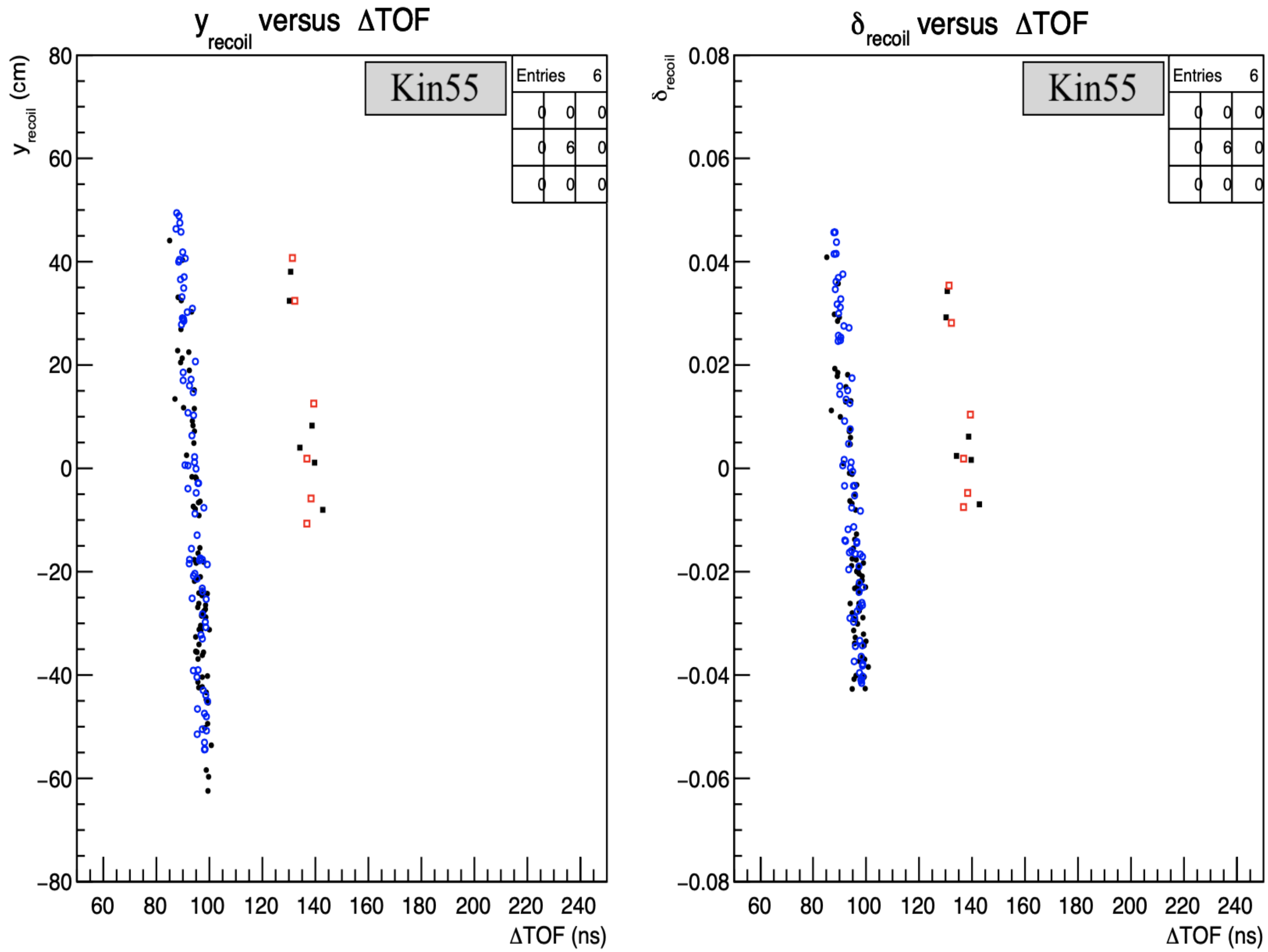

Figure 6.9: Kinematics Kin55: (Left) y_{recoil} versus ΔTOF and (Right) δ_{recoil} versus ΔTOF. The solid black circles and squares represent ^{3}He and ^{4}He experimental data, respectively. The open blue circles and red squares represent the corresponding Monte Carlo simulation for ^{3}He and ^{4}He, respectively. The statistics box shows the ^{4}He number of events. All cuts and corrections have been applied.

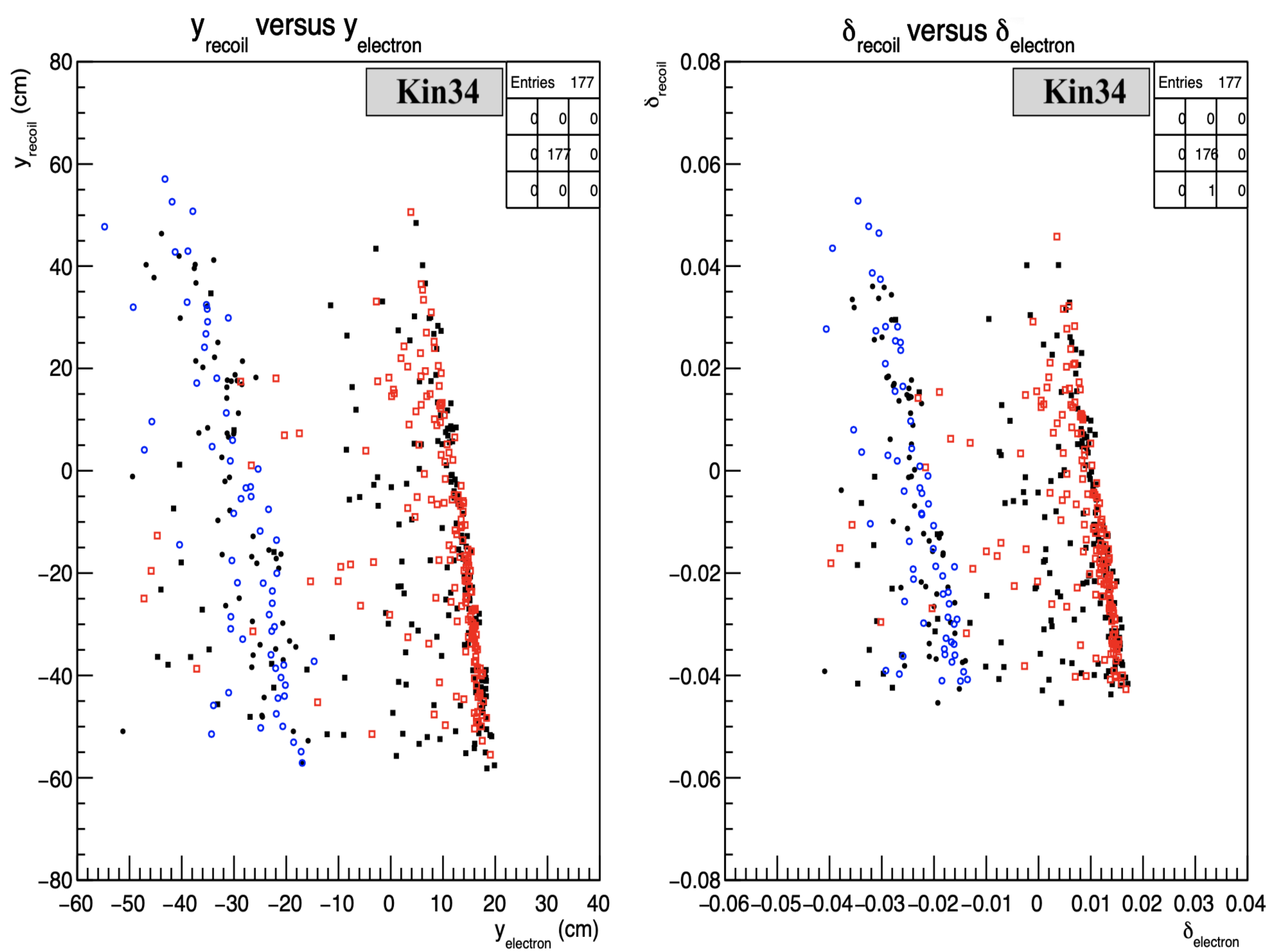

Figure 6.10: Kinematics Kin34: (Left) y_{recoil} versus $y_{electron}$ and (Right) δ_{recoil} versus δ_{recoil}. The solid black circles and squares represent ^{3}He and ^{4}He experimental data, respectively. The open blue circles and red squares represent the corresponding Monte Carlo simulation for ^{3}He and ^{4}He, respectively. The statistics box shows the ^{4}He number of events. All cuts and corrections have been applied.

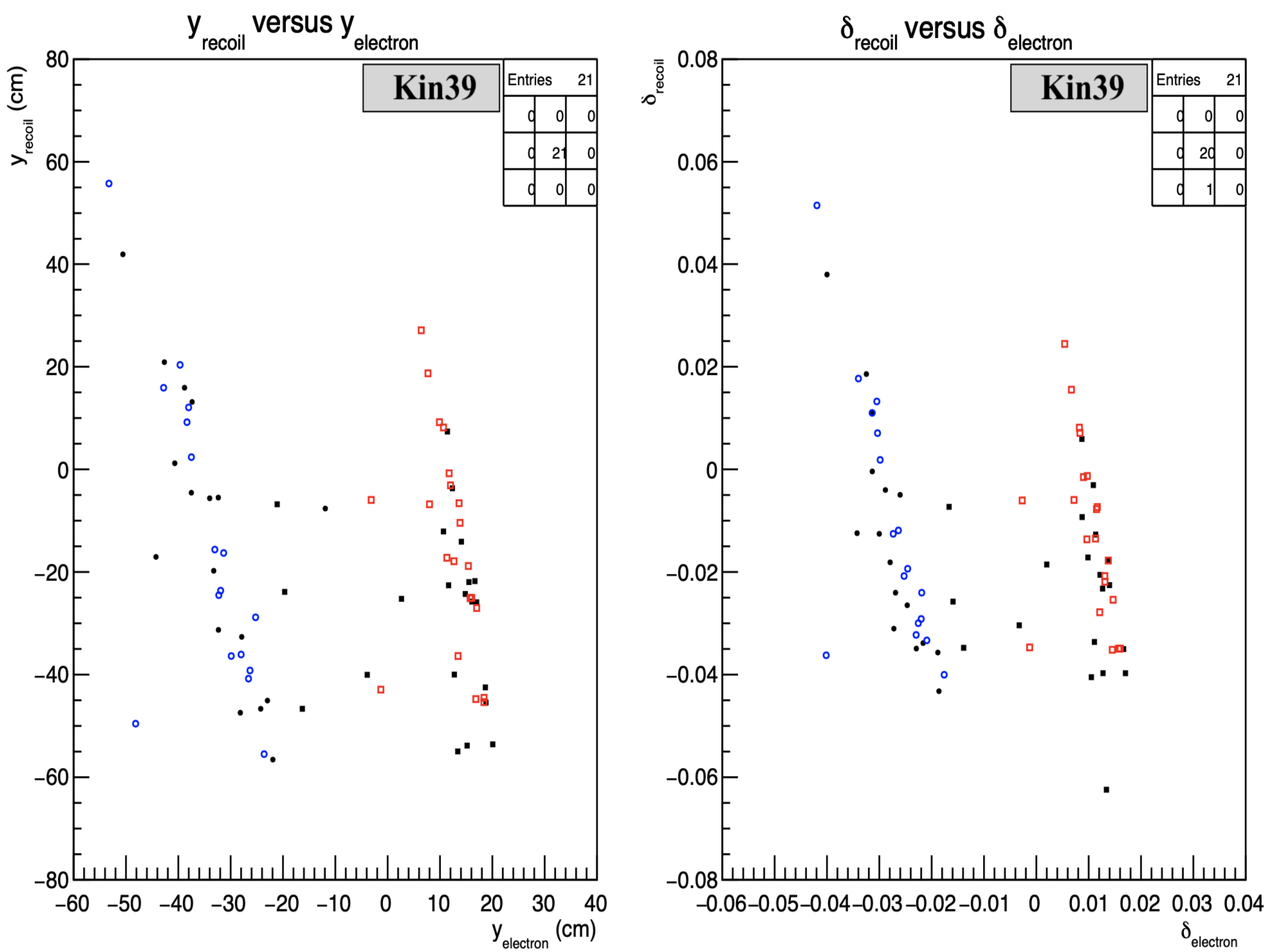

Figure 6.11: Kinematics Kin39: (Left) y_{recoil} versus $y_{electron}$ and (Right) δ_{recoil} versus δ_{recoil}. The solid black circles and squares represent ^{3}He and ^{4}He experimental data, respectively. The open blue circles and red squares represent the corresponding Monte Carlo simulation for ^{3}He and ^{4}He, respectively. The statistics box shows the ^{4}He number of events. All cuts and corrections have been applied.

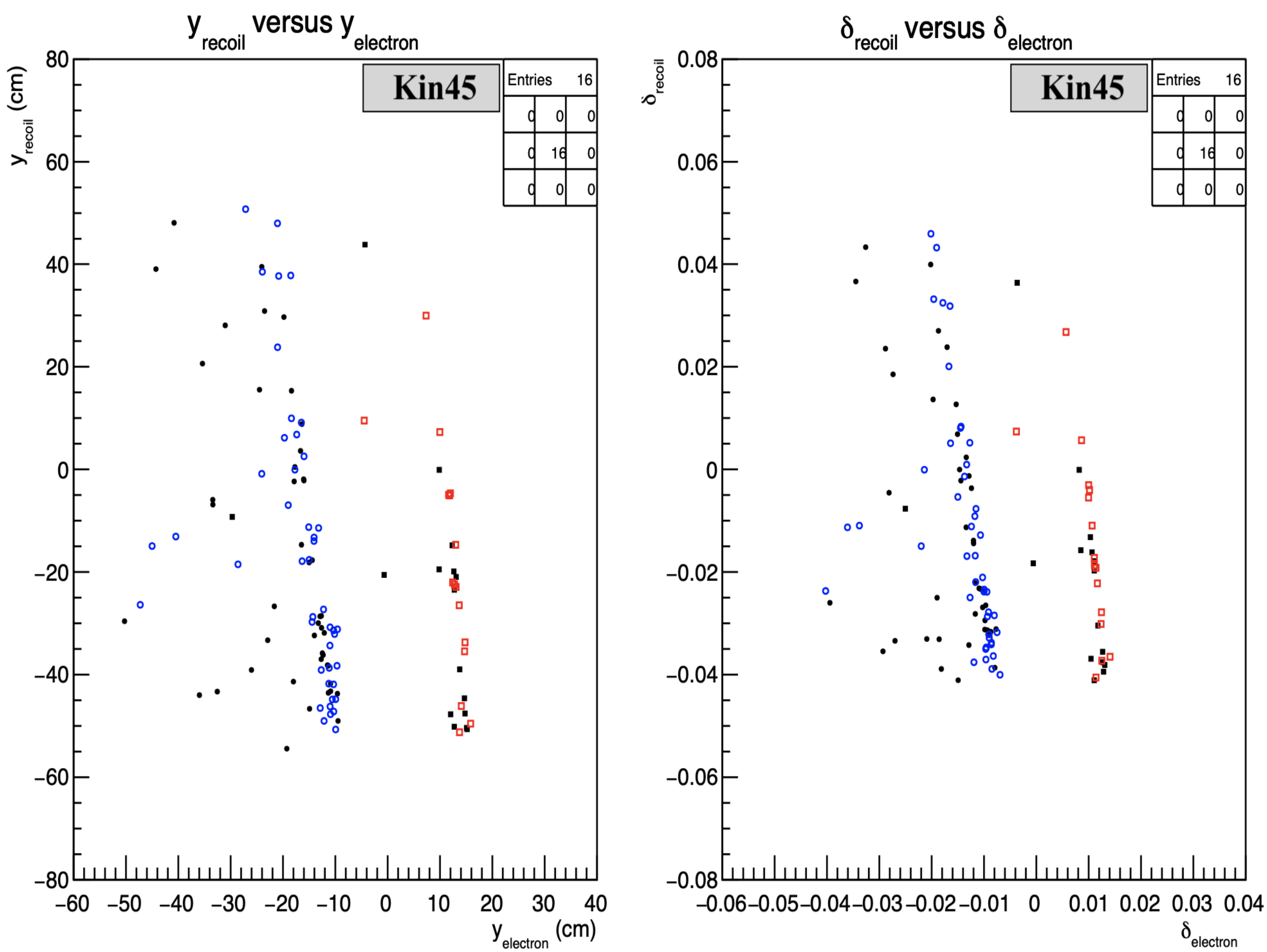

Figure 6.12: Kinematics Kin45: (Left) y_{recoil} versus $y_{electron}$ and (Right) δ_{recoil} versus δ_{recoil}. The solid black circles and squares represent ^{3}He and ^{4}He experimental data, respectively. The open blue circles and red squares represent the corresponding Monte Carlo simulation for ^{3}He and ^{4}He, respectively. The statistics box shows the ^{4}He number of events. All cuts and corrections have been applied..

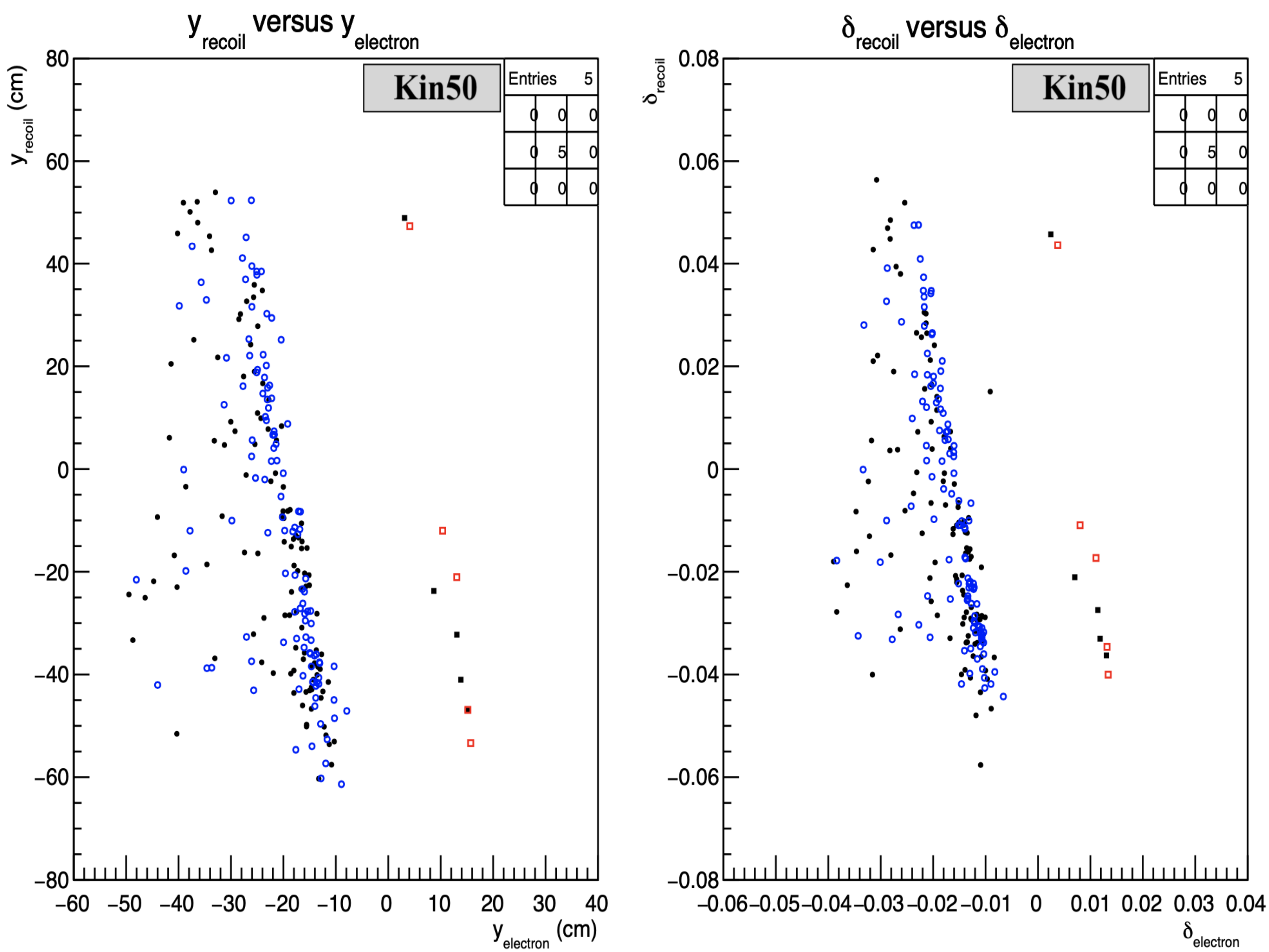

Figure 6.13: Kinematics Kin50: (Left) y_{recoil} versus $y_{electron}$ and (Right) δ_{recoil} versus δ_{recoil}. The solid black circles and squares represent ^{3}He and ^{4}He experimental data, respectively. The open blue circles and red squares represent the corresponding Monte Carlo simulation for ^{3}He and ^{4}He, respectively. The statistics box shows the ^{4}He number of events. All cuts and corrections have been applied.

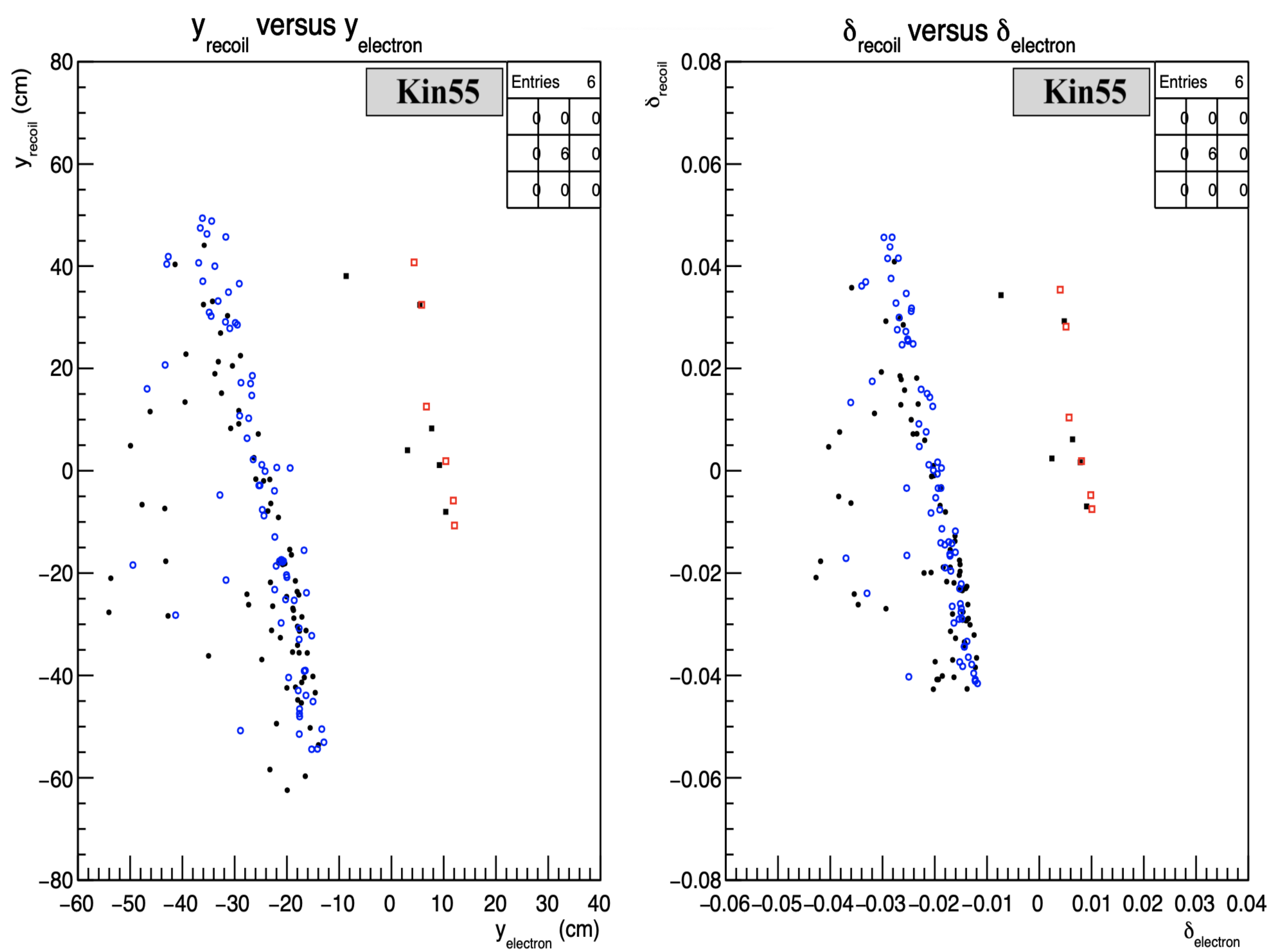

Figure 6.14: Kinematics Kin55: (Left) y_{recoil} versus $y_{electron}$ and (Right) δ_{recoil} versus δ_{recoil}. The solid black circles and squares represent ^{3}He and ^{4}He experimental data, respectively. The open blue circles and red squares represent the corresponding Monte Carlo simulation for ^{3}He and ^{4}He, respectively. The statistics box shows the ^{4}He number of events. All cuts and corrections have been applied.

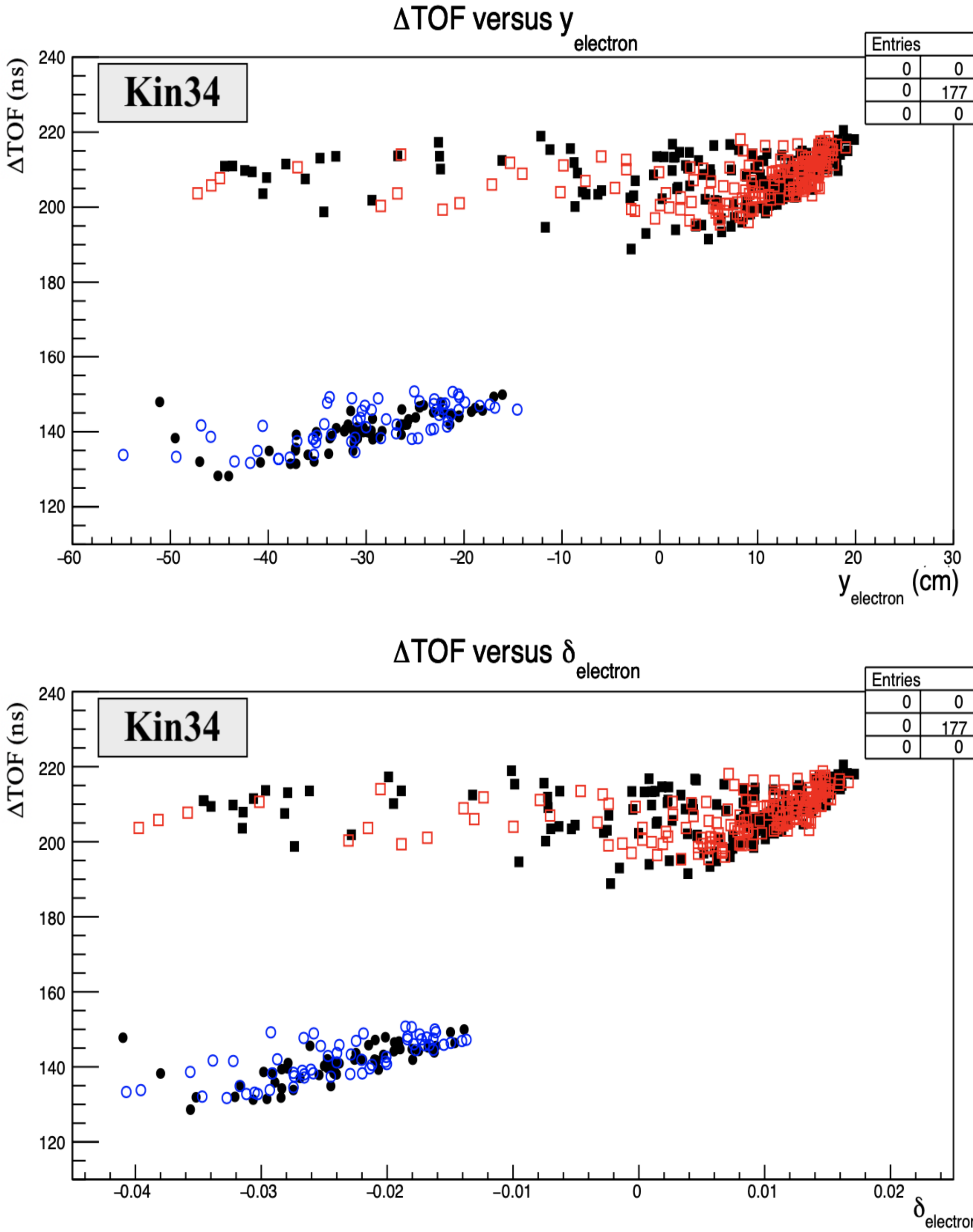

Figure 6.15: Kinematics Kin34: (Top) ΔTOF versus $y_{electron}$ and (Bottom) ΔTOF versus $\delta_{electron}$. The solid black circles and squares represent ^{3}He and ^{4}He experimental data, respectively. The open blue circles and red squares represent the corresponding Monte Carlo simulation for ^{3}He and ^{4}He, respectively. The statistics box shows the ^{4}He number of events. All cuts and corrections have been applied.

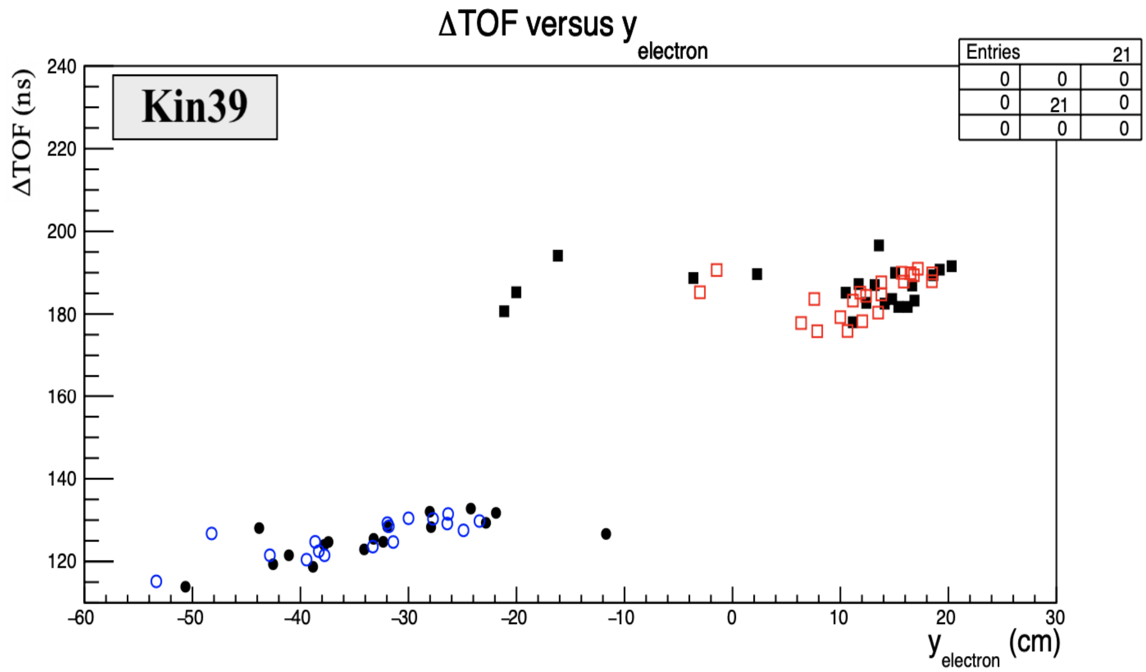

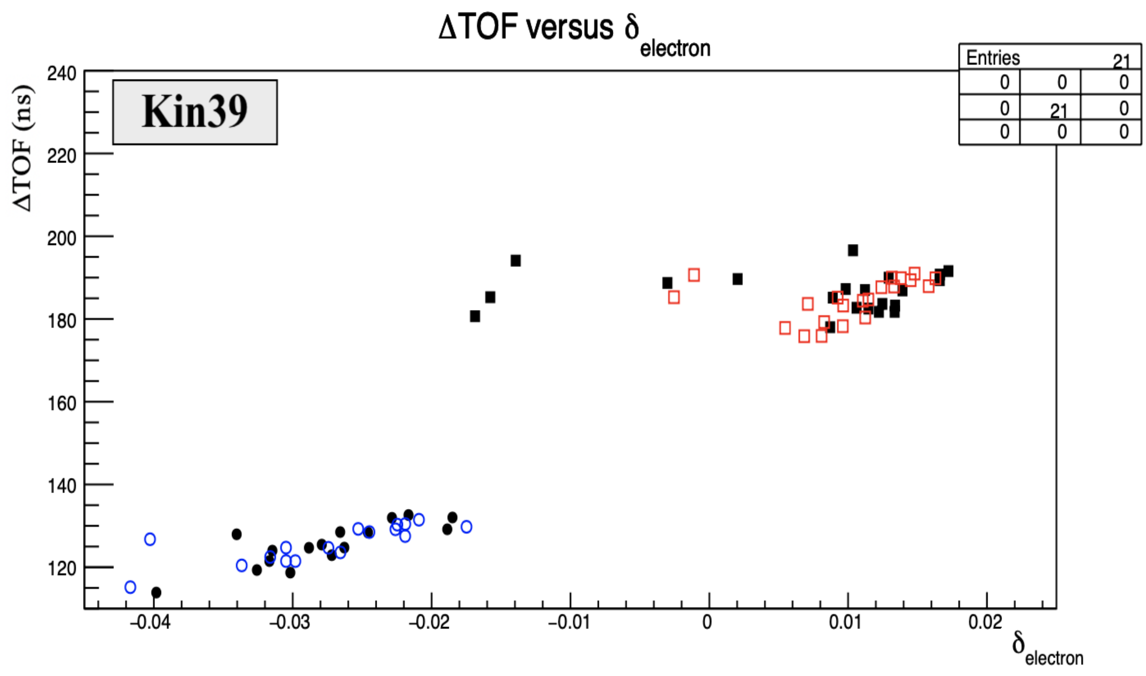

Figure 6.16: Kinematics Kin39: (Top) ΔTOF versus $y_{electron}$ and (Bottom) ΔTOF versus $\delta_{electron}$. The solid black circles and squares represent ^{3}He and ^{4}He experimental data, respectively. The open blue circles and red squares represent the corresponding Monte Carlo simulation for ^{3}He and ^{4}He, respectively. The statistics box shows the ^{4}He number of events. All cuts and corrections have been applied.

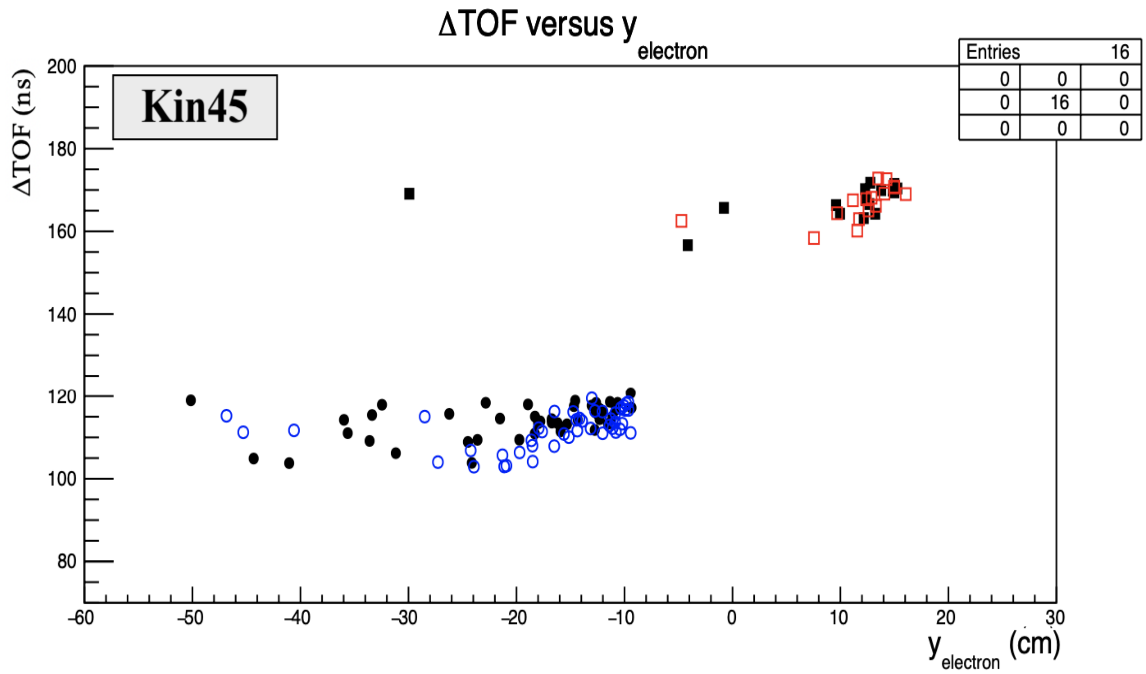

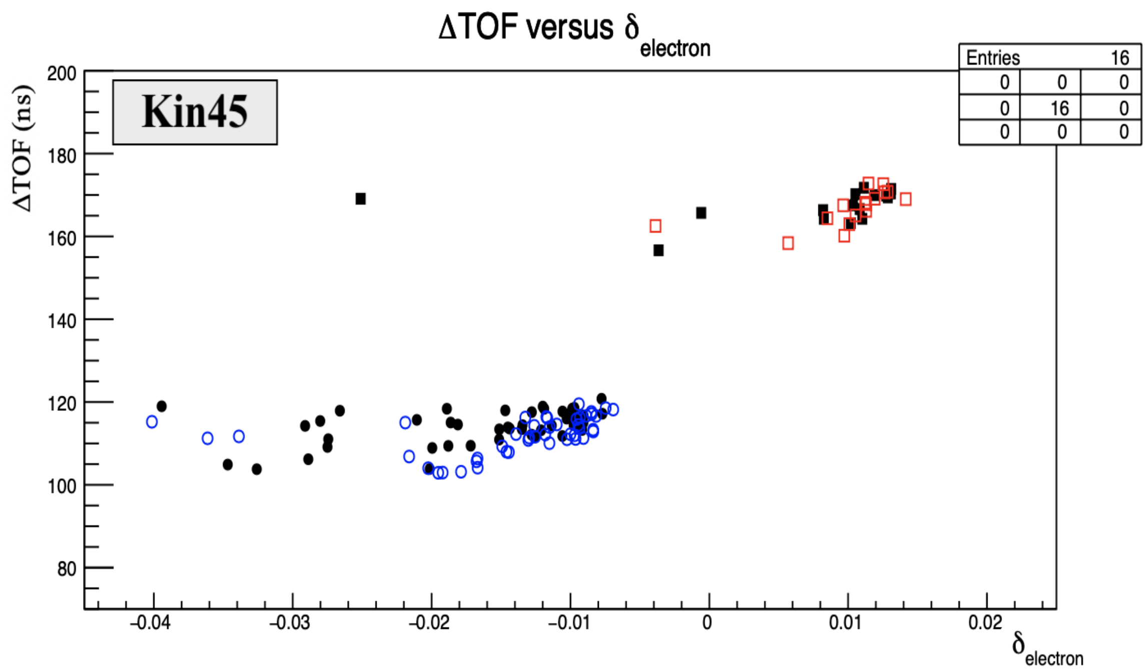

Figure 6.17: Kinematics Kin45: (Top) ΔTOF versus $y_{electron}$ and (Bottom) ΔTOF versus $\delta_{electron}$. The solid black circles and squares represent ^{3}He and ^{4}He experimental data, respectively. The open blue circles and red squares represent the corresponding Monte Carlo simulation for ^{3}He and ^{4}He, respectively. The statistics box shows the ^{4}He number of events. All cuts and corrections have been applied.

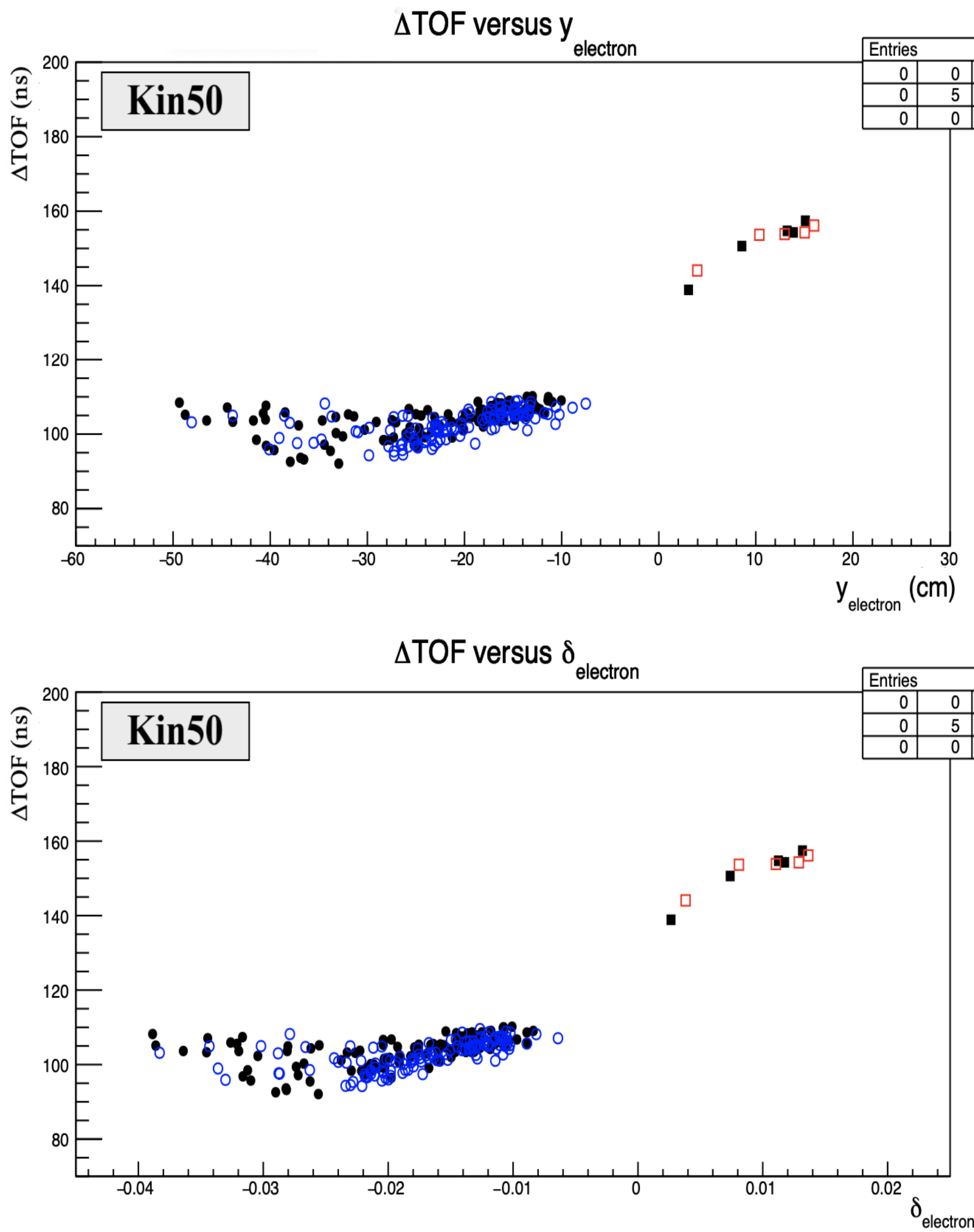

Figure 6.18: Kinematics Kin50: (Top) ΔTOF versus $y_{electron}$ and (Bottom) ΔTOF versus $\delta_{electron}$. The solid black circles and squares represent ^{3}He and ^{4}He experimental data, respectively. The open blue circles and red squares represent the corresponding Monte Carlo simulation for ^{3}He and ^{4}He, respectively. The statistics box shows the ^{4}He number of events. All cuts and corrections have been applied.

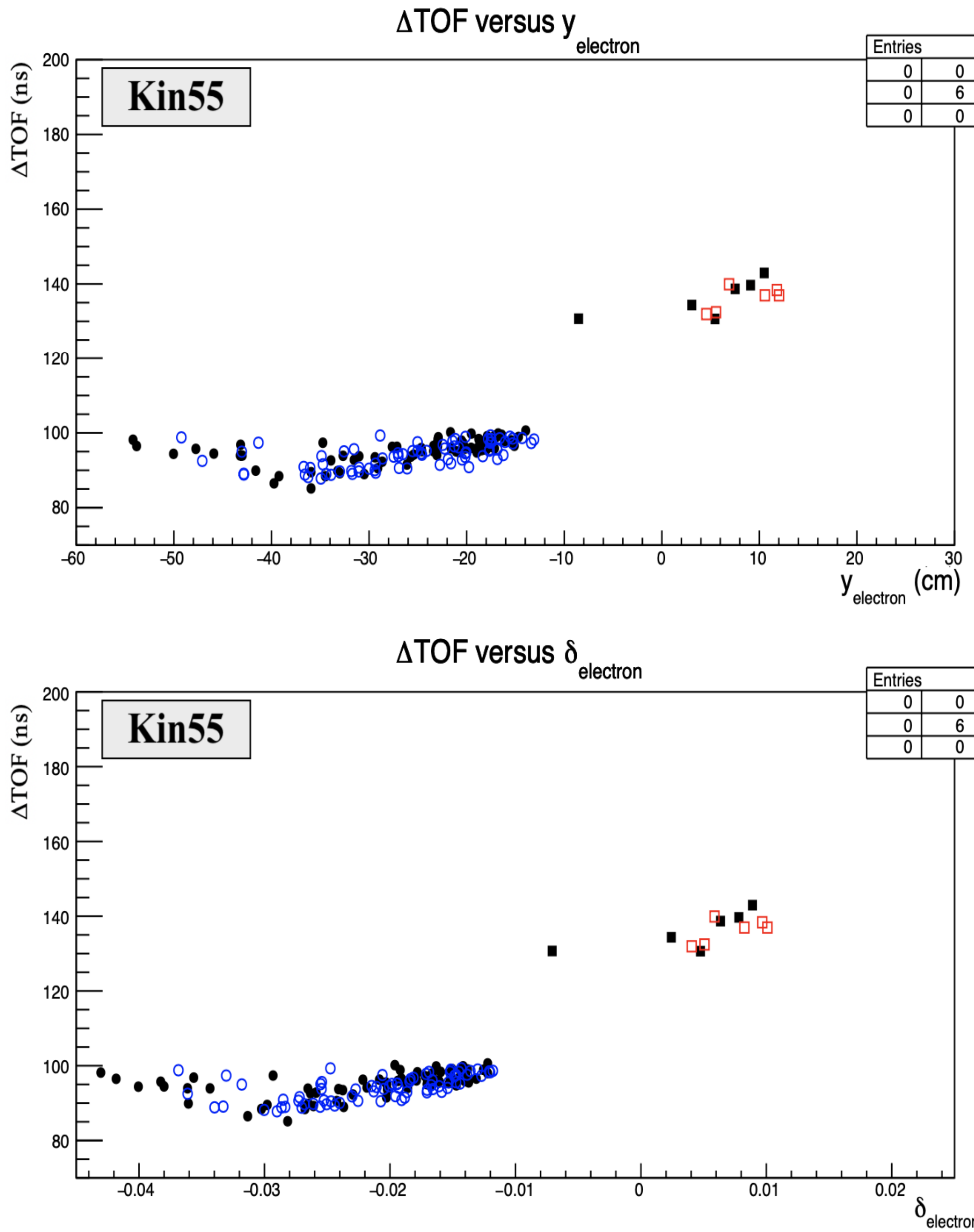

Figure 6.19: Kinematics Kin55: (Top) ΔTOF versus $y_{electron}$ and (Bottom) ΔTOF versus $\delta_{electron}$. The solid black circles and squares represent ^{3}He and ^{4}He experimental data, respectively. The open blue circles and red squares represent the corresponding Monte Carlo simulation for ^{3}He and ^{4}He, respectively. The statistics box shows the ^{4}He number of events. All cuts and corrections have been applied.

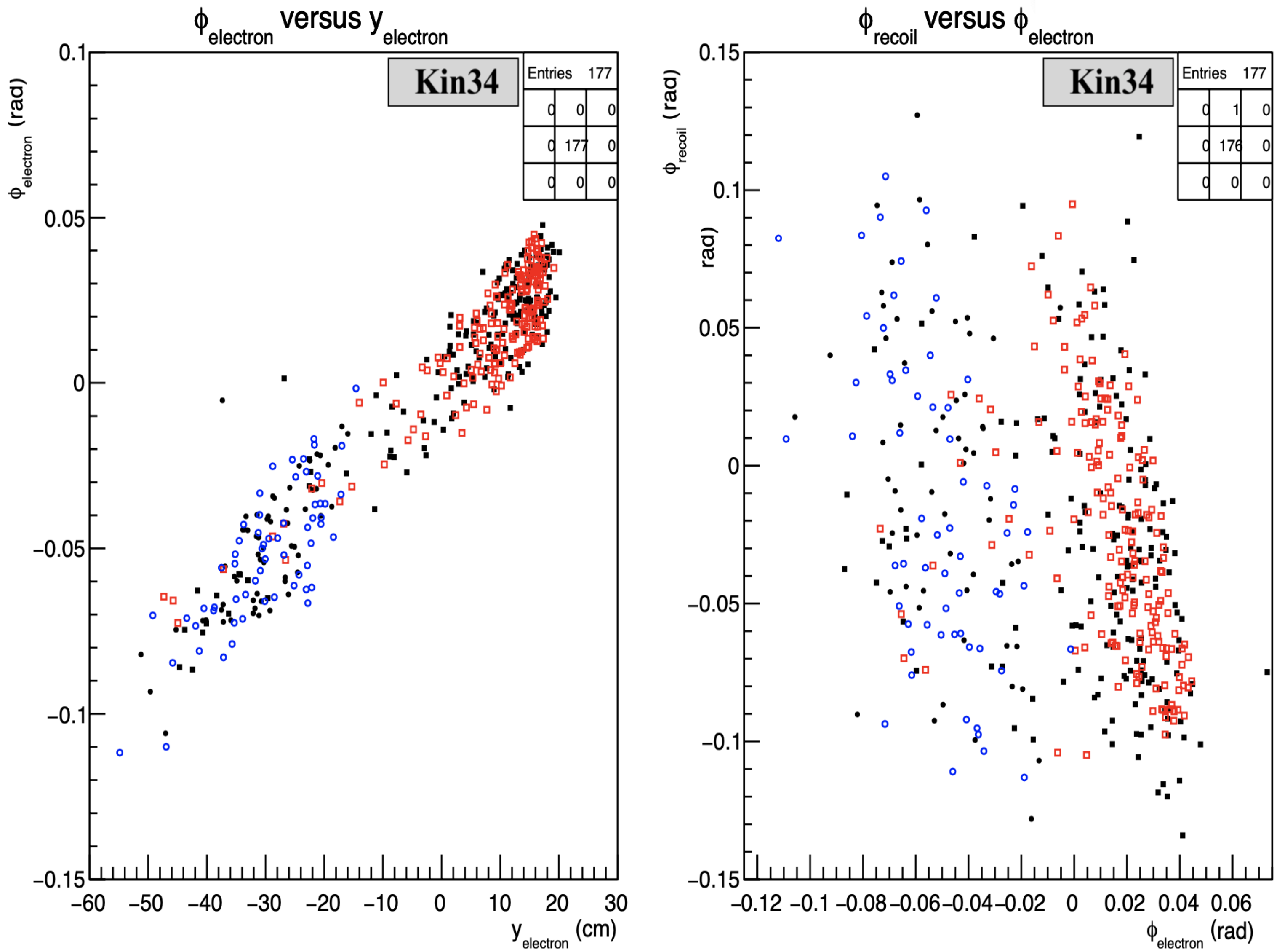

Figure 6.20: Kinematics Kin34: (Left) $\phi_{electron}$ versus $y_{electron}$ and (Right) ϕ_{recoil} versus $\phi_{electron}$. The solid black circles and squares represent ^{3}He and ^{4}He experimental data, respectively. The open blue circles and red squares represent the corresponding Monte Carlo simulation for ^{3}He and ^{4}He, respectively. The statistics box shows the ^{4}He number of events. All cuts and corrections have been applied.

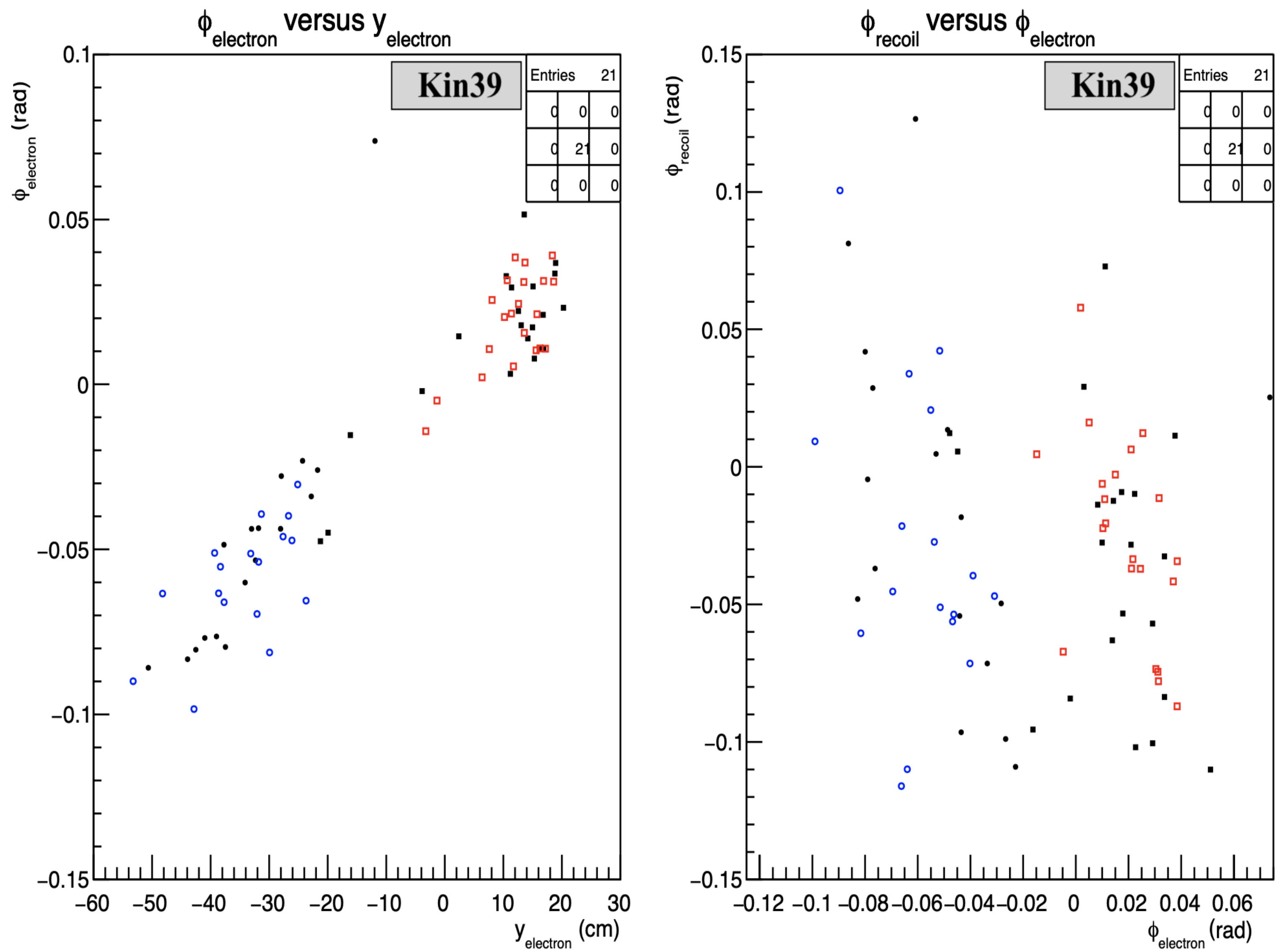

Figure 6.21: Kinematics Kin39: (Left) $\phi_{electron}$ versus $y_{electron}$ and (Right) ϕ_{recoil} versus $\phi_{electron}$. The solid black circles and squares represent ^{3}He and ^{4}He experimental data, respectively. The open blue circles and red squares represent the corresponding Monte Carlo simulation for ^{3}He and ^{4}He, respectively. The statistics box shows the ^{4}He number of events. All cuts and corrections have been applied.

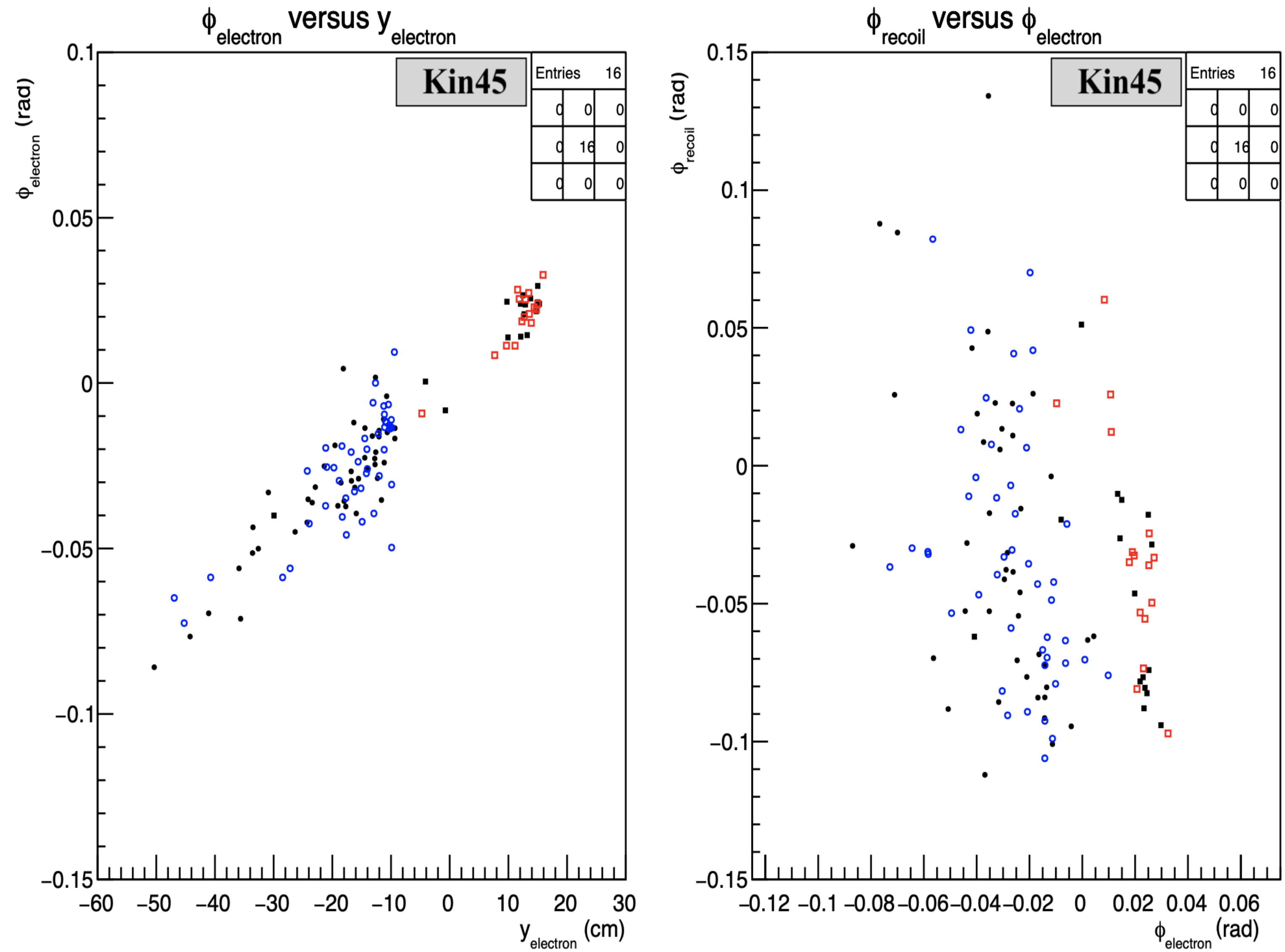

Figure 6.22: Kinematics Kin45: (Left) $\phi_{electron}$ versus $y_{electron}$ and (Right) ϕ_{recoil} versus $\phi_{electron}$. The solid black circles and squares represent ^{3}He and ^{4}He experimental data, respectively. The open blue circles and red squares represent the corresponding Monte Carlo simulation for ^{3}He and ^{4}He, respectively. The statistics box shows the ^{4}He number of events. All cuts and corrections have been applied.

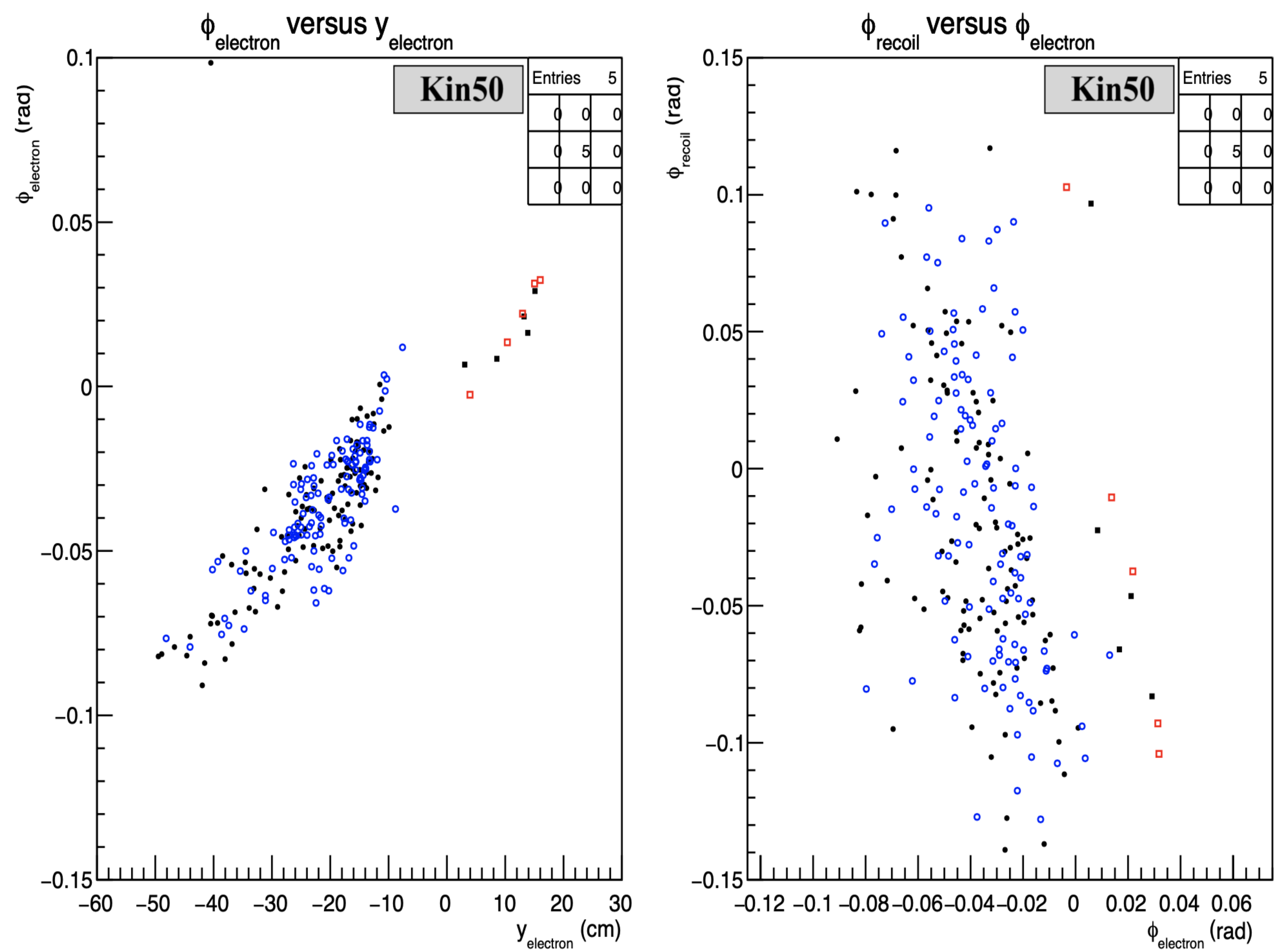

Figure 6.23: Kinematics Kin50: (Left) $\phi_{electron}$ versus $y_{electron}$ and (Right) ϕ_{recoil} versus $\phi_{electron}$. The solid black circles and squares represent ^{3}He and ^{4}He experimental data, respectively. The open blue circles and red squares represent the corresponding Monte Carlo simulation for ^{3}He and ^{4}He, respectively. The statistics box shows the ^{4}He number of events. All cuts and corrections have been applied.

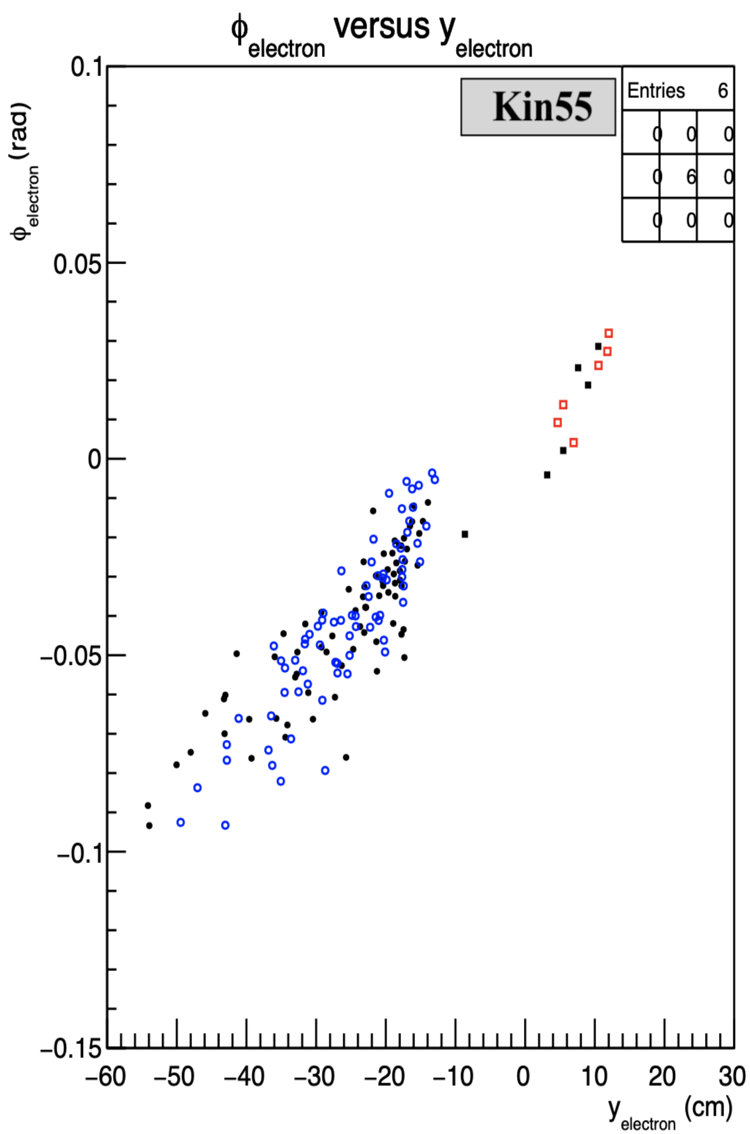

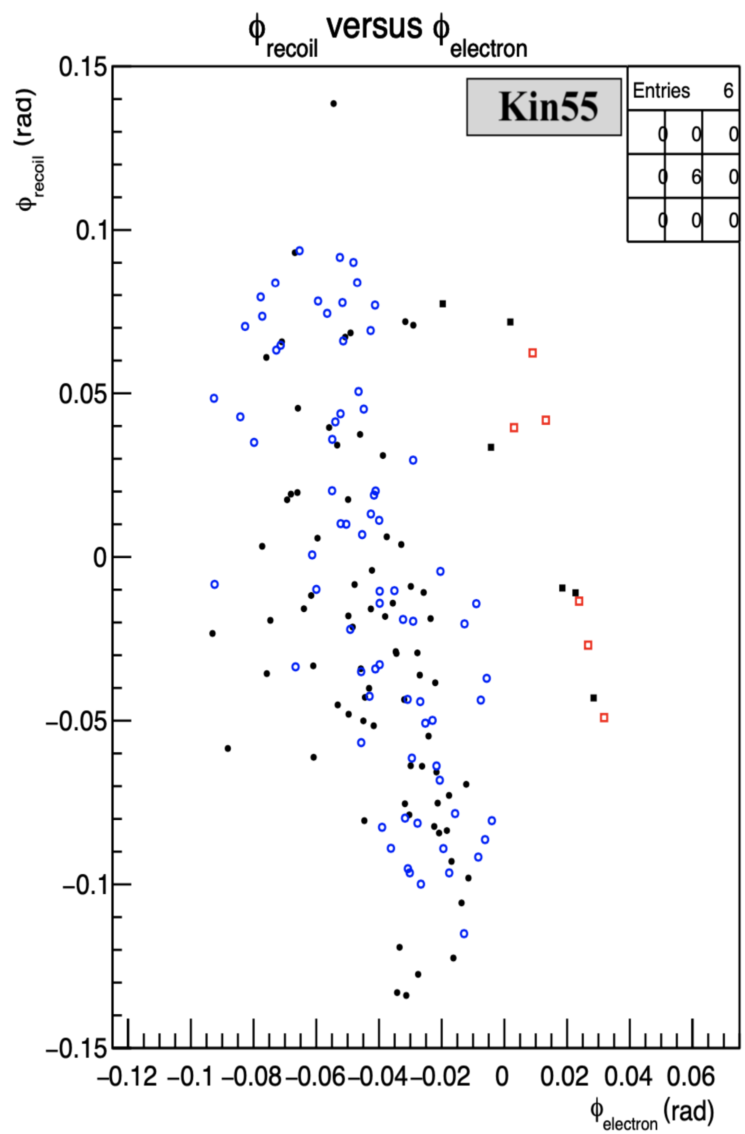

Figure 6.24: Kinematics Kin55: (Left) $\phi_{electron}$ versus $y_{electron}$ and (Right) ϕ_{recoil} versus $\phi_{electron}$. The solid black circles and squares represent ^{3}He and ^{4}He experimental data, respectively. The open blue circles and red squares represent the corresponding Monte Carlo simulation for ^{3}He and ^{4}He, respectively. The statistics box shows the ^{4}He number of events. All cuts and corrections have been applied.

6.4 Monte Carlo to Data Ratio Calculations

6.4.1 Experimental Data Ratio

As was discussed in Chapter 5, the Cherenkov and electromagnetic calorimeter detectors were employed to distinguish scattered electrons from background particles while the VDCs and the scintillator planes were used to distinguish between ^{3}He and ^{4}He events. After applying all needed cuts, the number of ^{3}He and ^{4}He coincidence events were extracted from the data in order to determine their ratio, R_{Data}, and its associated uncertainty. The R_{Data} ratio for each kinematics is simply calculated by:

$$R_{Data} = \frac{N_{^3\mathrm{He}}}{N_{^4\mathrm{He}}} \tag{6.1}$$

Here, $N_{^3\mathrm{He}}$ and $N_{^4\mathrm{He}}$ are the number of the coincidence e-^{3}He and e-^{4}He events that pass the cuts imposed on the experimental data. The uncertainty associated with the ratio, σ_{Data}, is given by:

$$\sigma_{Data} = R_{Data}\sqrt{\left(\frac{\sqrt{N_{^3\mathrm{He}}}}{N_{^3\mathrm{He}}}\right)^2 + \left(\frac{\sqrt{N_{^4\mathrm{He}}}}{N_{^4\mathrm{He}}}\right)^2} \tag{6.2}$$

6.4.2 Monte Carlo Simulation Ratio

In the same fashion, the ratio, R_{MC} and the associated uncertainty, σ_{MC}, for the simulation were calculated. Taking all the corrections and cuts into consideration and applying the cross section weighting, the number of ^{3}He and ^{4}He simulated events was adjusted to obtain, for plotting purposes, the same number of ^{4}He for a direct comparison to the experimental data. To calculate R_{MC}, the MC program was run at each kinematics so as to obtain 200 to 2000 e-^{4}He events in order to have a minimal error, much smaller than the associated experimental error.

6.4.3 Ratio of Experimental Data and Simulation Ratios

For each kinematics, the ratio, R_{MC}^{Data}, was calculated by dividing the two previous ratios:

$$R_{MC}^{Data} = \frac{R_{Data}}{R_{MC}} \tag{6.3}$$

with the corresponding uncertainties being given by:

$$\sigma_{MC}^{Data} = R_{MC}^{Data} \sqrt{\left(\frac{\sigma_{Data}}{R_{Data}}\right)^2 + \left(\frac{\sigma_{MC}}{R_{MC}}\right)^2} \tag{6.4}$$

The R_{MC}^{Data} for the five different kinematical settings are shown in Figure 6.25. The error bars in the Figure are due to the combined uncertainties of the experimental data and the simulation. The contribution to the errors from the simulation are minimized by increasing the number of trials thus, the experimental data errors dominate. The uncertainties at the large Q^2 kinematics Kin50 and Kin55, do not include contribution from the ^{3}He and ^{4}He elastic form factors large uncertainties. The large uncertainties of the form factors arise from statistics limitations and the existence of diffraction minima in this region, as mentioned in Section 4.10.

It can be seen from Figure 6.25 that the ratios, R_{MC}^{Data}, of Kin34, Kin39 and Kin45 give similar results within statistical uncertainties. Ultimately, the points of Kin50 and Kin55 are excluded due to the large form factor uncertainties. Then, the remaining three low Q^2 kinematics were combined through a weighted average by:

$$\overline{R} = \frac{\sum R_i w_i}{\sum w_i} \tag{6.5}$$

$$w_i = \frac{1}{\sigma_i^2} \tag{6.6}$$

where R_i and σ_i are the R_{MC}^{Data} and σ_{MC}^{Data} for each kinematics, respectively. The corresponding uncertainty is given by:

$$\sigma_{\overline{R}} = \sqrt{\frac{1}{\sum w_i}} \tag{6.7}$$

where w_i is the corresponding weight factor. The value of $\overline{R}$ for the three lowest Q^2 points is $\overline{R} = 1.73 \pm 0.22$, consistent with a value of 2.

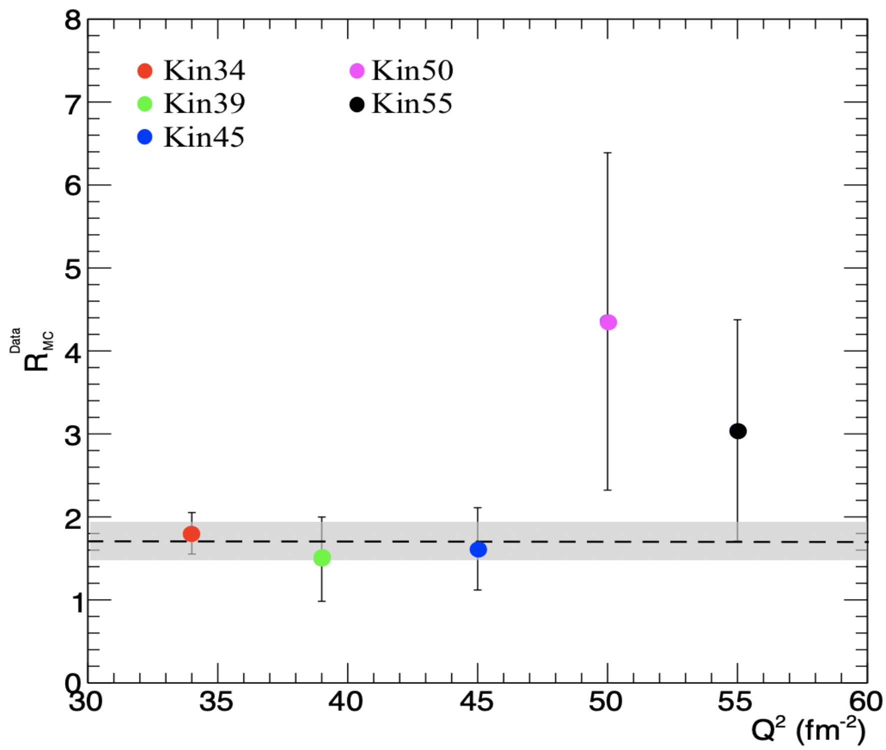

Figure 6.25: The color circles represent the R_{MC}^{Data} for the five different kinematics under consideration. The black dashed line is the weighted average, and the gray shaded area is the corresponding uncertainty with the last two points excluded.

The R_{MC}^{Data} and $\overline{R}$ results have very interesting implications. The ^{4}He nucleus has two protons and two neutrons. The ^{3}He cluster is comprised of the two protons and one of the two neutrons. The result can be understood in a simple way that, the ^{3}He cluster has two probabilities to form within ^{4}He. The incident electron can interact directly with ^{4}He nucleus or with one of the two possible ^{3}He clusters after giving up some energy to separate a neutron and leave a ^{3}He cluster. However, it is not clear yet what the actual circumstances and dynamics are related to e-^{3}He quasielastic scattering within ^{4}He.

Chapter 7

Summary and Conclusions

Experiment E04-018 was conducted in the Hall A Facility of the Thomas Jefferson National Accelerator Facility (JLab) in Virginia utilizing the two superconducting High-Resolution Spectrometers (HRSs) and the cryogenic target system of Hall A. The data were collected at different energies ranging between 2 GeV and 4 GeV, and five momentum transfer squared Q^2 values between 34 fm^{-2} and 55 fm^{-2}. The analysis of coincidence data from the experiment with the ^{4}He target was performed to achieve clear identification and to separate the ^{4}He nuclei from the ^{3}He clusters.

The Monte Carlo simulation program was developed in the C programming language. The program simulated both e-^{4}He elastic and e-^{3}He quasielastic scattering using the setup of E04-018. As described in Chapter 4, all the relevant physical effects in the scattering process were taken into account. Furthermore, the optical models for the two HRS magnetic systems were utilized in the simulation program and only events that passed through the spectrometer apertures were considered good events to be compared with the experimental data.

The current work has achieved its goal by comparing the experimental data from E04-018 with a simulation to identify a unique class of data from the experiment. The comparison between the experimental and simulation data indicate unequivocally pre-existing ^{3}He clusters in the ^{4}He target nuclei. These results can be considered as the first significant evidence to indicate that ^{4}He, the primary ingredient of clustering in medium and heavy nuclei, consists itself of a clustering structure of ^{3}He. However, the circumstances of the clustering mechanism and the actual underlying dynamics that leads to a knockout of a ^{3}He or ^{3}H cluster from e-^{4}He scattering process are not clear yet.

It is necessary to propose a future experiment at an electron beam laboratory with a ^{4}He target to measure simultaneously electron scattering from ^{3}He and ^{3}H clusters in ^{4}He using the coincidence method and the double arm TOF technique. This experiment should provide concrete information on the probability of $A = 3$ clustering in ^{4}He. Also, It is important that more theoretical work complements the results of the present JLab experiment.

Appendix A

Data Analysis Figures

Kin39 Analysis:

Recoil scintillator S1 ADC sum versus S2 ADC sum

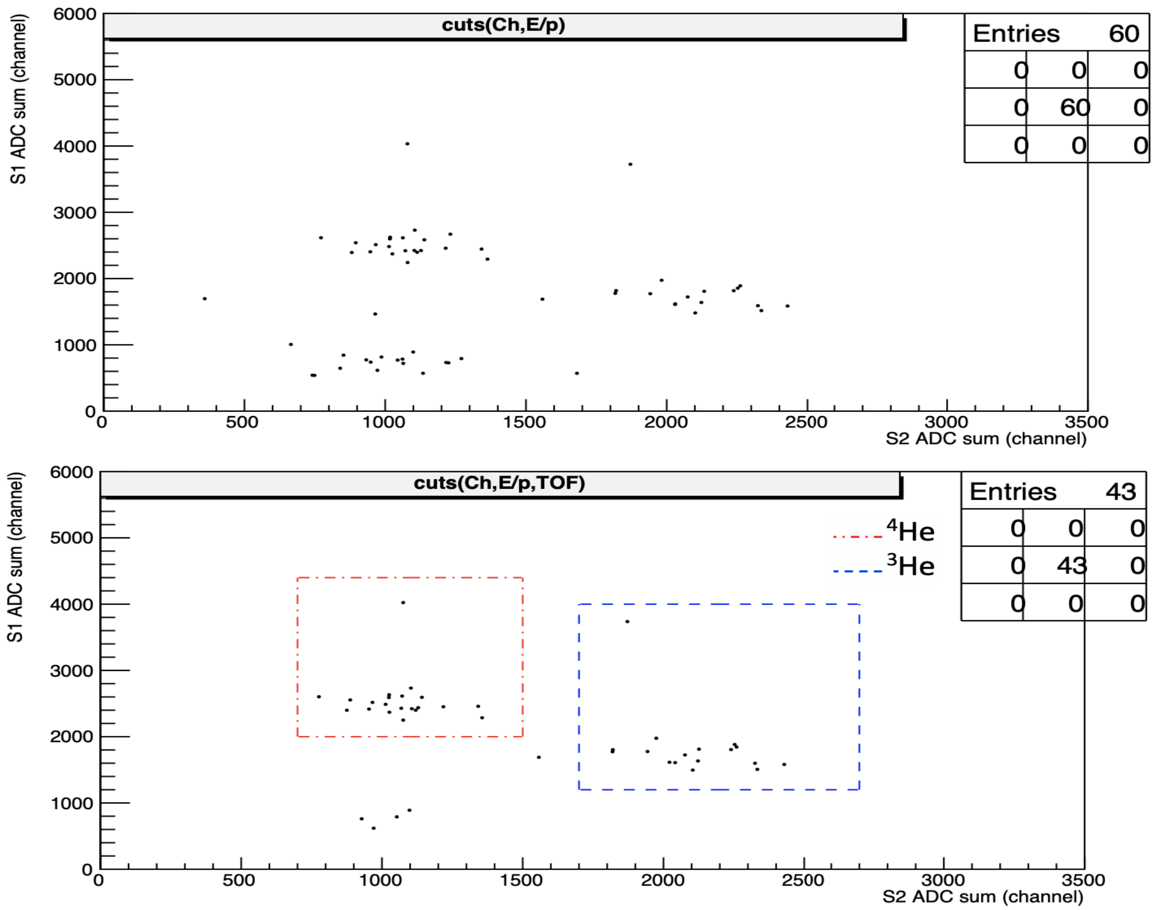

Figure A.1: Recoil scintillator S1 ADC signal versus recoil scintillator S2 ADC signal. In the top plot, only the Cherenkov ADC sum and the E'/P cuts have been applied. In the bottom plot, all cuts including the TOF cut for both ^{4}He and ^{3}He have been applied. The red and blue rectangles show where the recoil scintillators ADCs cuts for ^{3}He and ^{4}He selection have been applied.

Recoil Focal Plane y_{recoil} versus ΔTOF

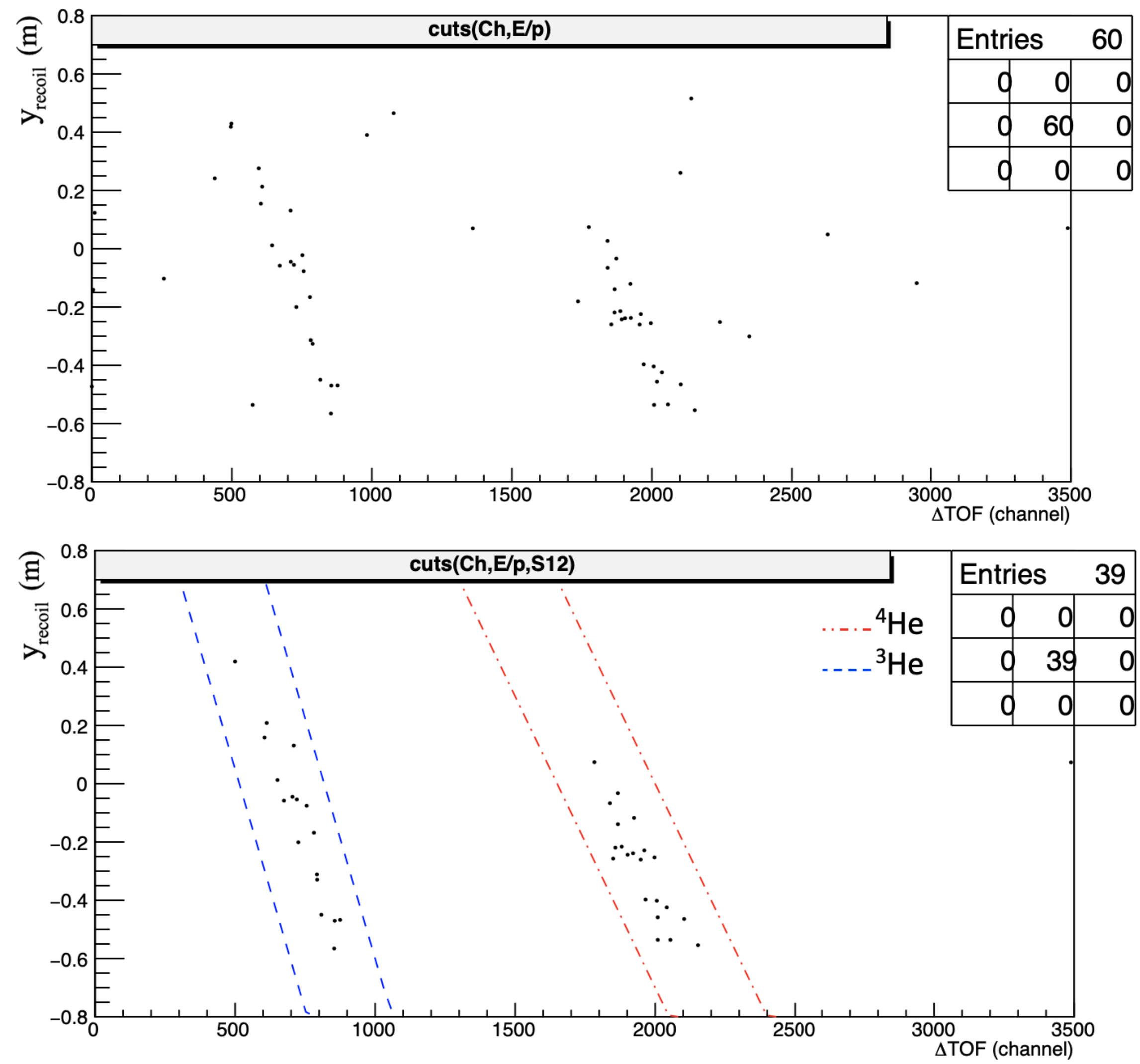

Figure A.2: y_{recoil} in FP versus ΔTOF. In the top plot, only the Cherenkov ADC sum and the E'/P cuts have been applied. In the bottom plot, all cuts including the recoil scintillators ADCs cuts for both ^{3}He and ^{4}He have been applied. The red and blue lines show where the TOF cuts for either ^{3}He or ^{4}He selection have been applied.

Recoil relative momentum δ_{recoil} versus electron relative momentum $\delta_{electron}$

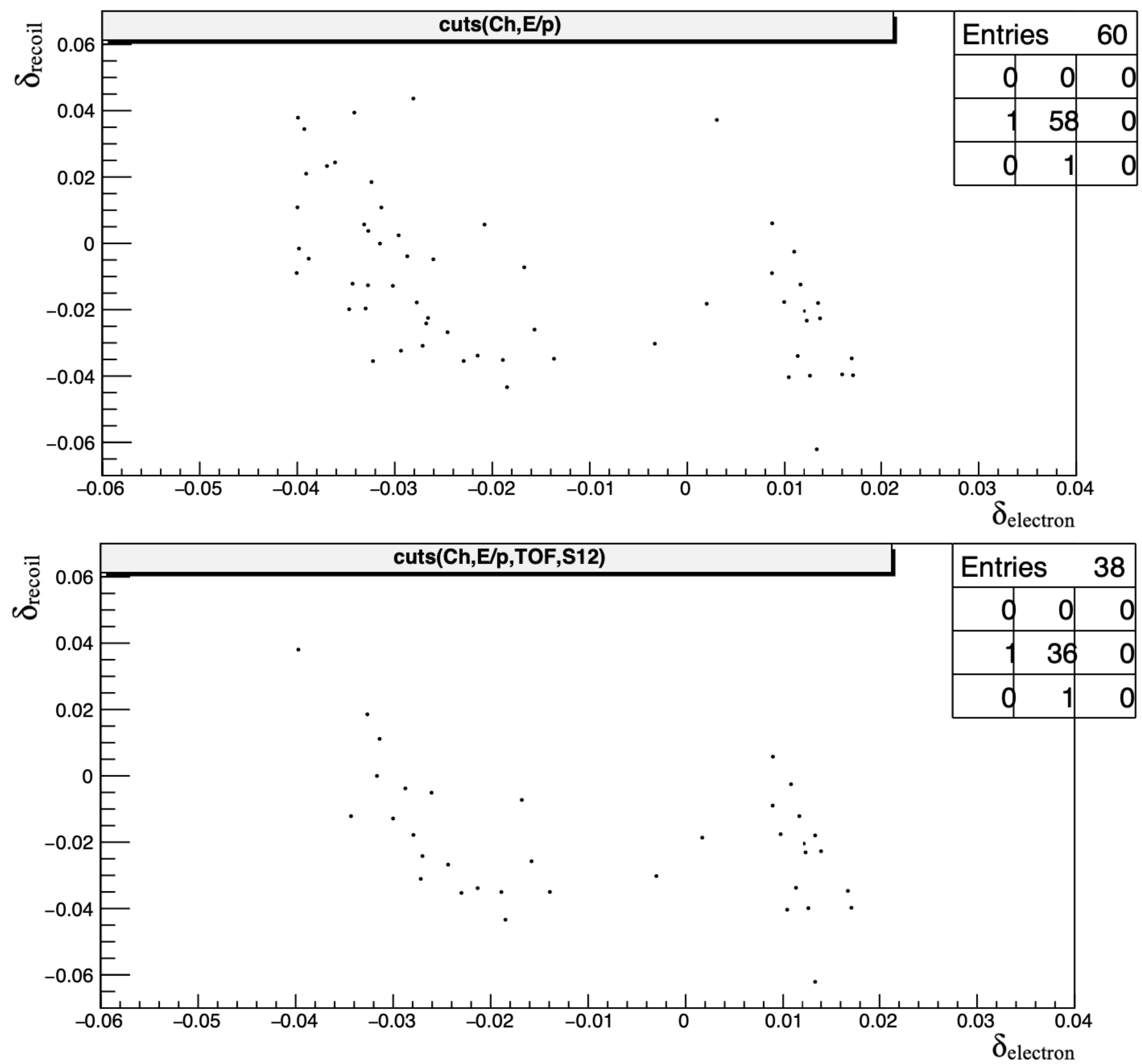

Figure A.3: δ_{recoil} versus $\delta_{electron}$. In the top plot, only the Cherenkov ADC sum and the E'/P cuts have been applied. In the bottom plot, all cuts including recoil scintillators ADCs and TOF cuts for both ^{3}He and ^{4}He selection have been applied.

Kin50 Analysis:

Recoil scintillator S1 ADC sum versus S2 ADC sum

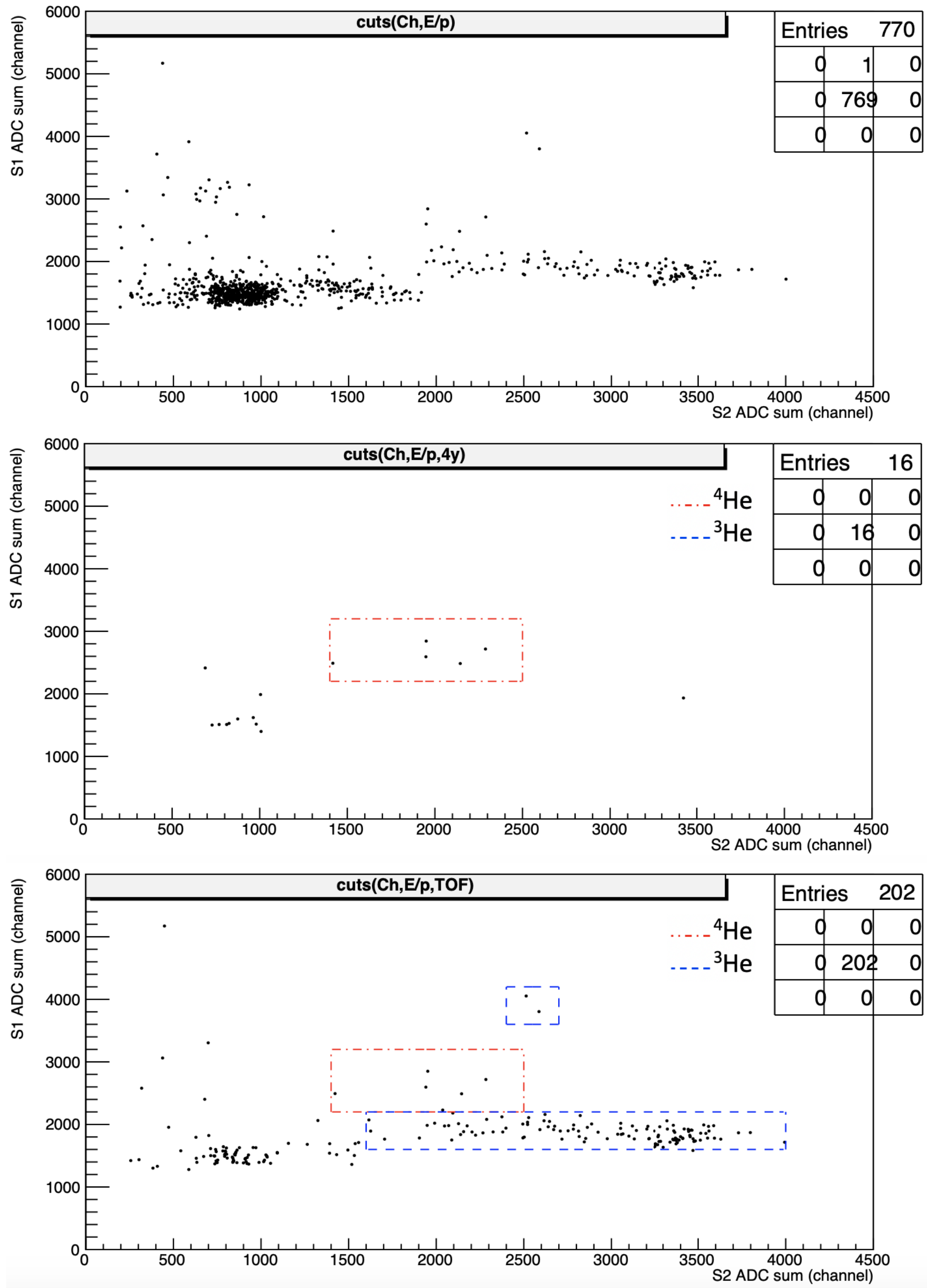

Figure A.4: Recoil scintillator S1 ADC signal versus recoil scintillator S2 ADC signal. In the top plot, only the Cherenkov ADC sum and the E'/P cuts have been applied. In the middle plot, the 4y cut has been applied beside of the previous two cuts. In the bottom plot, all cuts including the TOF cut for both ^{4}He and ^{3}He have been applied. The red and blue rectangles show where the recoil scintillators ADCs cuts for ^{3}He and ^{4}He selection have been applied.

Recoil Focal Plane y_{recoil} versus ΔTOF

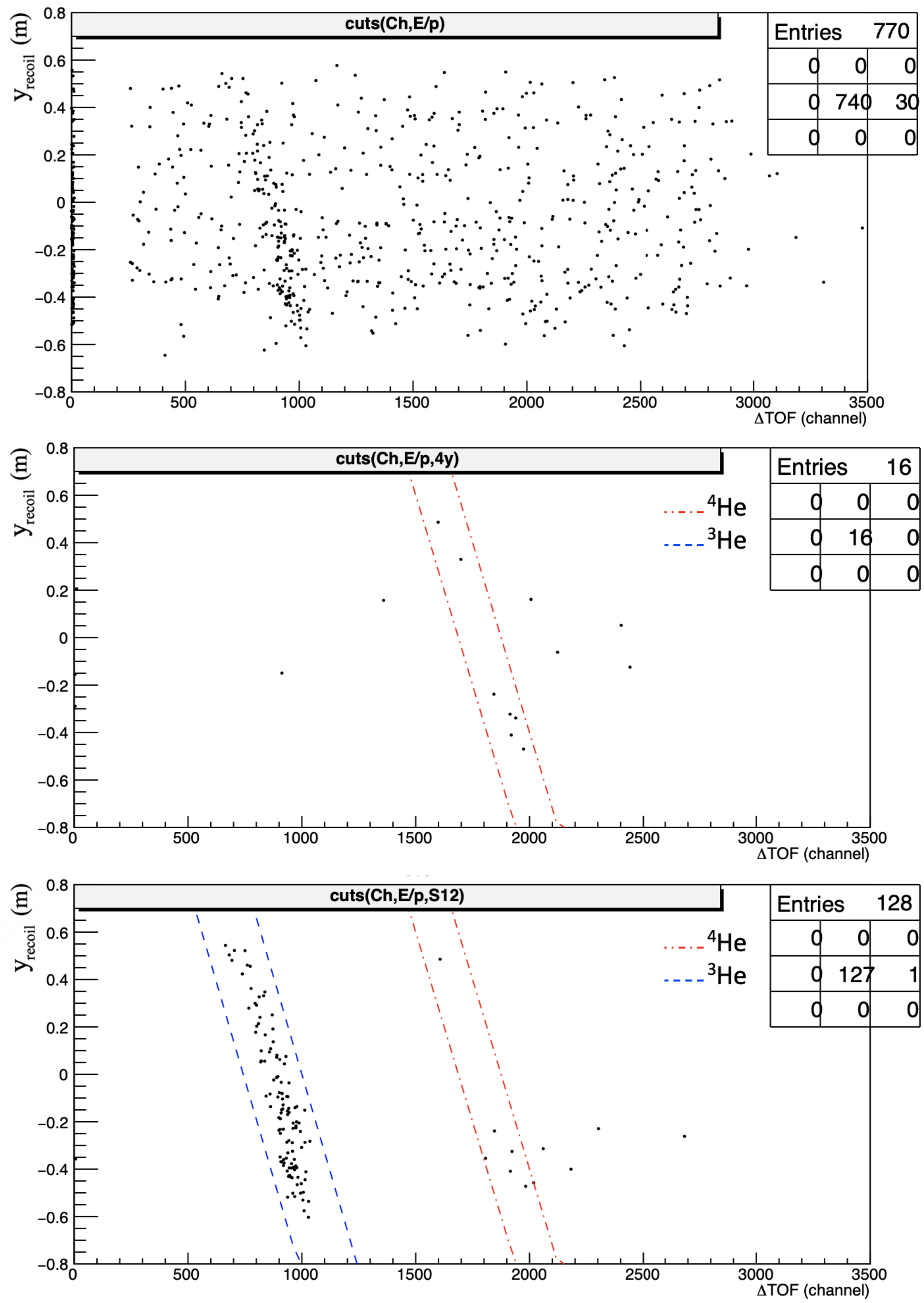

Figure A.5: y_{recoil} in FP versus ΔTOF. In the top plot, only the Cherenkov ADC sum and the E'/P cuts have been applied. In the middle plot, the 4y cut has been applied beside of the previous two cuts. In the bottom plot, all cuts including the recoil scintillators ADCs cuts for both ^{3}He and ^{4}He have been applied. The red and blue lines show where the TOF cuts for either ^{3}He or ^{4}He selection have been applied.

Recoil relative momentum δ_{recoil} versus electron relative momentum $\delta_{electron}$

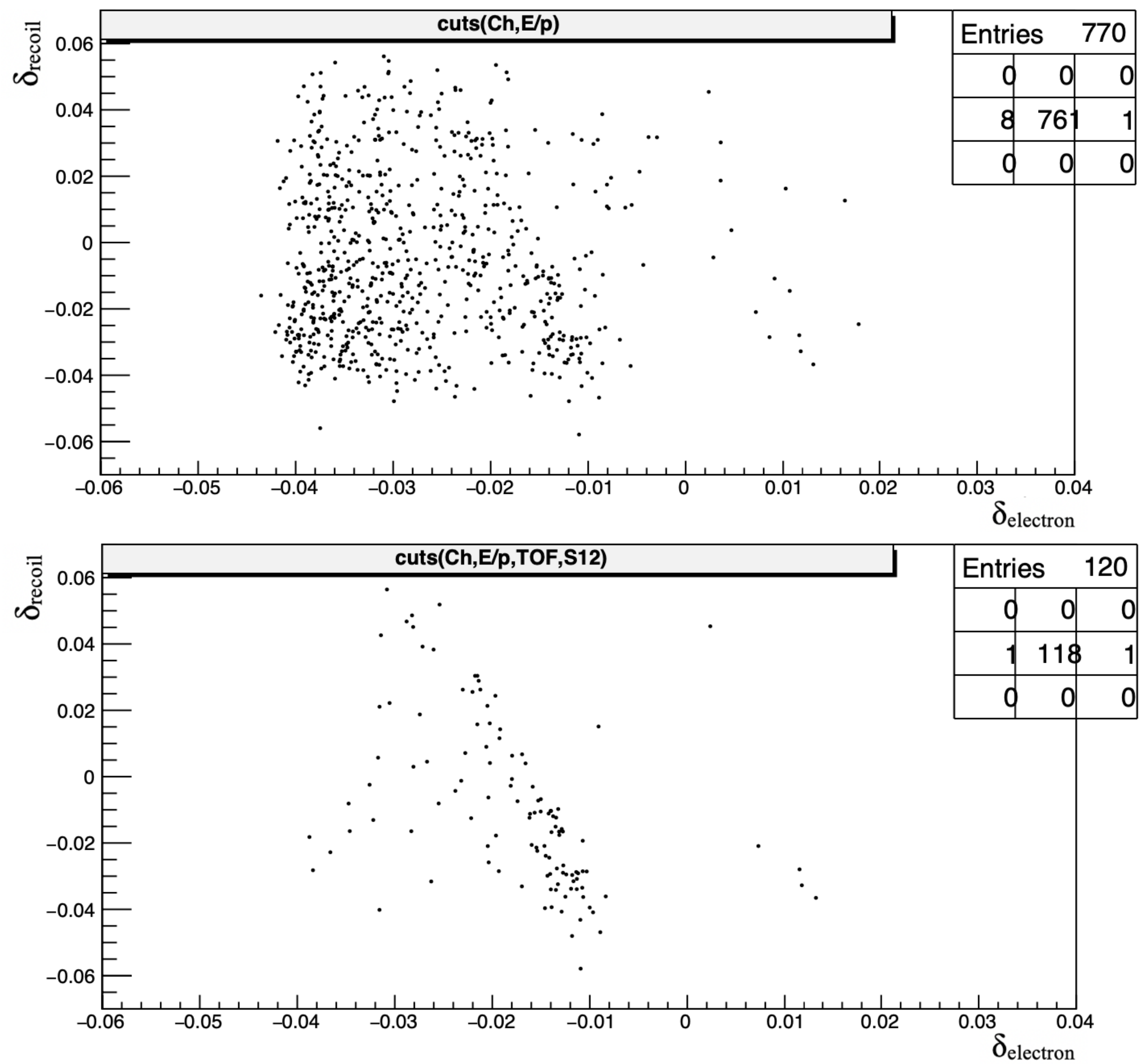

Figure A.6: δ_{recoil} versus $\delta_{electron}$. In the top plot, only the Cherenkov ADC sum and the E'/P cuts have been applied. In the bottom plot, all cuts including recoil scintillators ADCs and TOF cuts for both ^{3}He and ^{4}He selection have been applied.

Kin55 Analysis:

Recoil scintillator S1 ADC sum versus S2 ADC sum

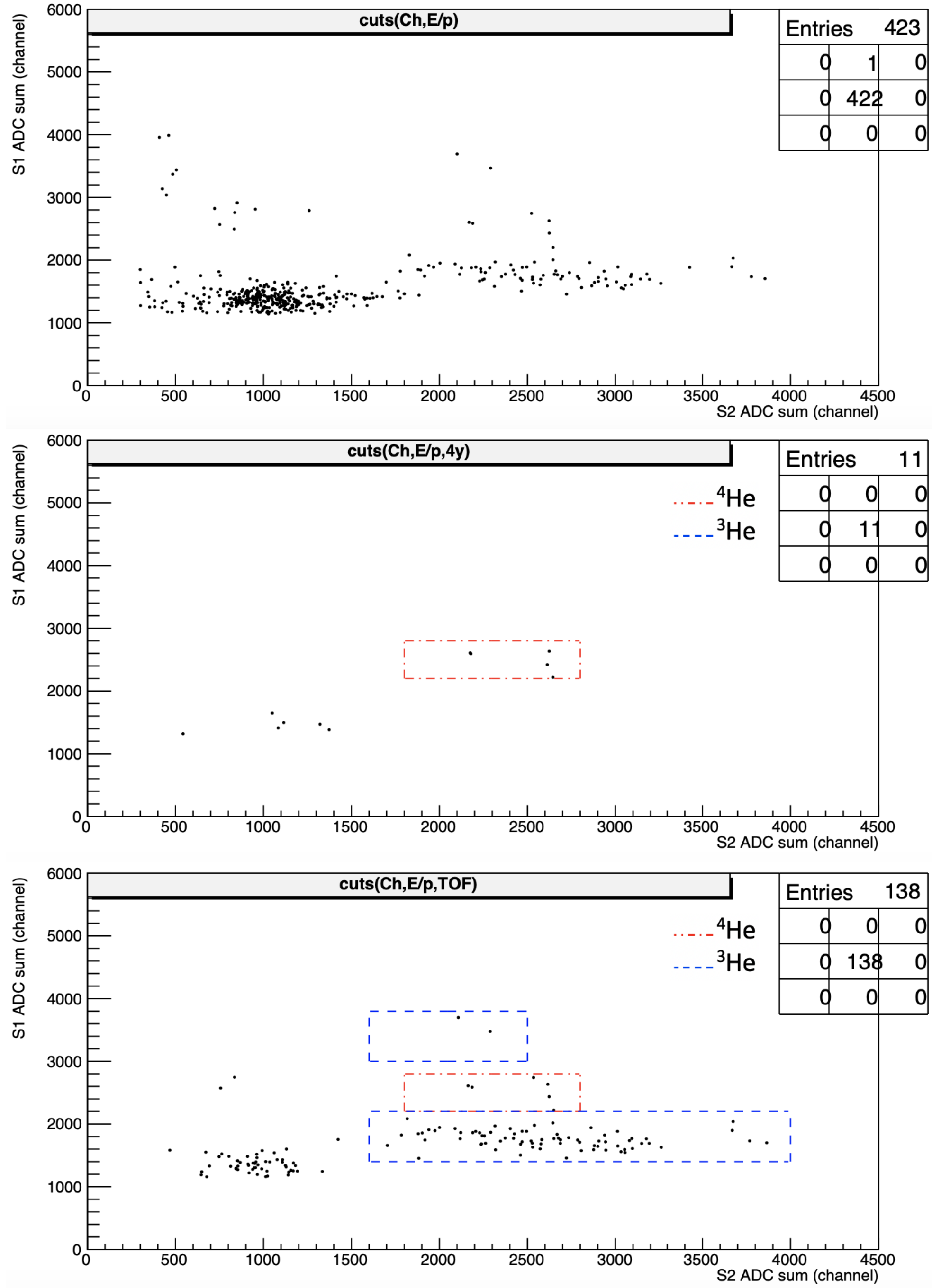

Figure A.7: Recoil scintillator S1 ADC signal versus recoil scintillator S2 ADC signal. In the top plot, only the Cherenkov ADC sum and the E'/P cuts have been applied. In the middle plot, the 4y cut has been applied beside of the previous two cuts. In the bottom plot, all cuts including the TOF cut for both ^{3}He and ^{3}He have been applied. The red and blue rectangles show where the recoil scintillators ADCs cuts for ^{3}He and ^{4}He selection have been applied.

Recoil Focal Plane y_{recoil} versus ΔTOF

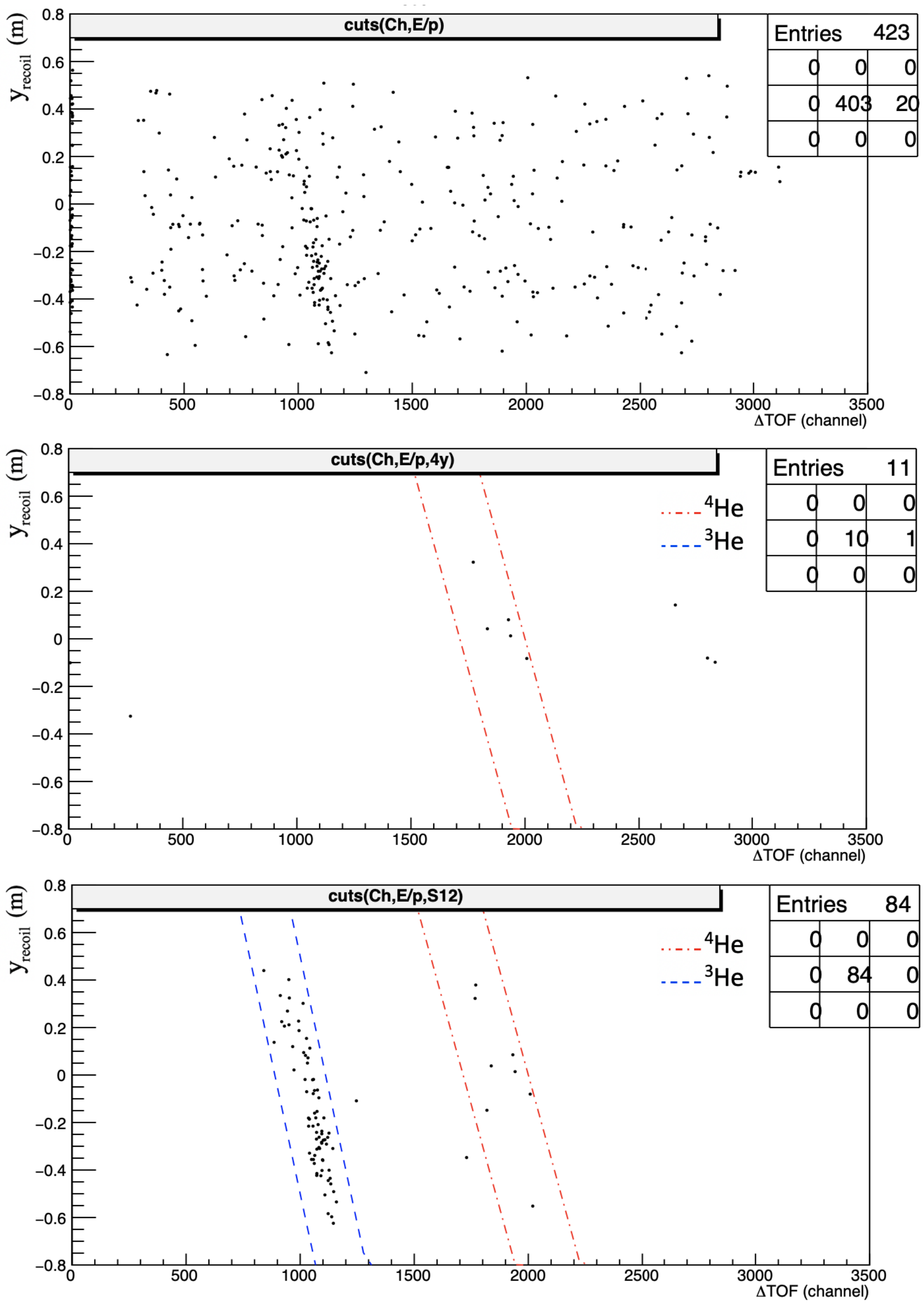

Figure A.8: y_{recoil} in FP versus ΔTOF. In the top plot, only the Cherenkov ADC sum and the E'/P cuts have been applied. In the middle plot, the 4y cut has been applied beside of the previous two cuts. In the bottom plot, all cuts including the recoil scintillators ADCs cuts for both ^{3}He and ^{4}He have been applied. The red and blue lines show where the TOF cuts for either ^{3}He or ^{4}He selection have been applied.

Recoil relative momentum δ_{recoil} versus electron relative momentum $\delta_{electron}$

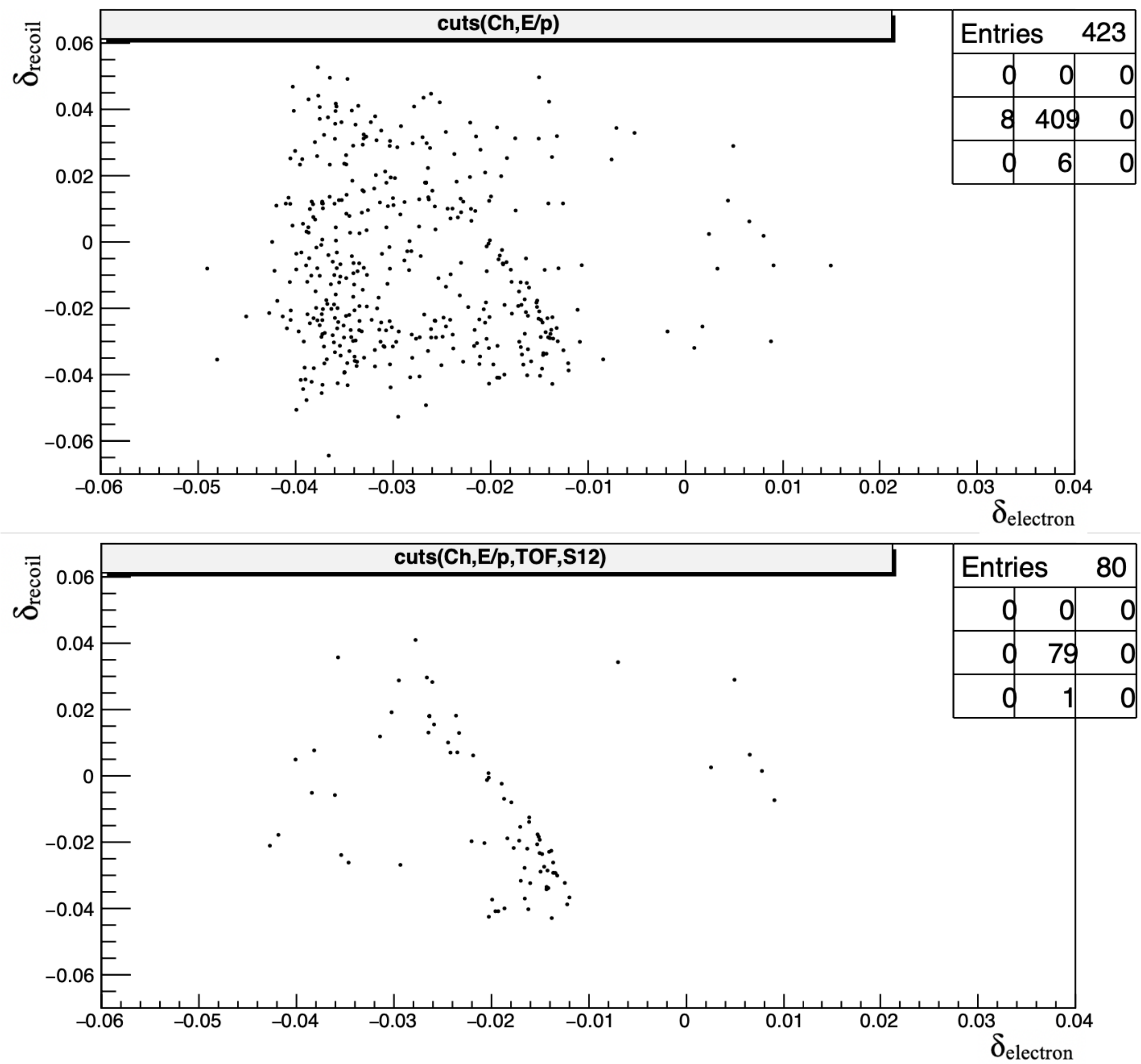

Figure A.9: δ_{recoil} versus $\delta_{electron}$. In the top plot, only the Cherenkov ADC sum and the E'/P cuts have been applied. In the bottom plot, all cuts including recoil scintillators ADCs and TOF cuts for both ^{3}He and ^{4}He selection have been applied.

References

[1] B. Povh, K. Rith, C. Scholz and F. Zetsche, *Particles and Nuclei: An Introduction to the Physical Concepts*, Springer-Verlag, 6th edition (2008).

[2] E. Rutherford, Phil. Mag. **21**, 669 (1911).

[3] J. J. Thomson, Proceedings of the Royal Institution of Great Britain **XV**, 4191795 (1897).

[4] R. Hofstadter, Rev. Mod. Phys. **28**, 214 (1956).

[5] R. E. Taylor, Rev. Mod. Phys. **63**, 573 (1991).

[6] M. Gell-Mann, Phys. Lett. **8**, 214 (1964).

[7] G. Zweig, *An SU_3 Model for Strong Interaction Symmetry and Its Breaking*, CERN Report No. TH 412 (Geneva, 1964); *Fractionally Charged Particles and SU_6*, in *Symmetry In Elementry Particle Physics*, p.192, Academic Press, New York (1965).

[8] F. Halzen, A. Martin, *Quarks and Leptons: An Introductory Course in Modern Particle Physics*, John Wiley & Sons (1984).

[9] W. E. Burcham and M. Jobes, *Nuclear and Particle Physics*, Longman Scientific & Technical (1995).

[10] A. Camsonne *et al.*, Phys. Rev. Lett. **112**, 132503 (2014).

[11] A. Camsonne *et al.*, Phys. Rev. Lett. **119**, 162501 (2017).

[12] B. Zhou and Z. Ren, Adv. Phys: X**2**, 359-372 (2017).

[13] A. Sandulescu, D. N. Poenaru, and W. Greiner, Sov. J. Part. Nucl. **11**, 528 (1980).

[14] D. N. Poenaru, R. A. Gherghescu and W. Greiner, Phys. Rev. **C83**, 014601 (2011).

[15] W. von Oertzen, M. Freer and Y. Kanada-En'yo, Phys. Rep. **432**, 43 (2006).

[16] G. Gamow, Proc. Roy. Soc. **A126**, 632 (1930).

[17] L. R. Hafstad and E. Teller, Phys. Rev. **54**, 681 (1938).

[18] D. M. Dennison, Phys. Rev. **57**, 454 (1954); Phys. Rev. **96**, 378 (1940).

[19] K. Ikeda, N. Tagikawa and H. Horiuchi, Prog. Theor. Phys. **464**, (Suppl.) (1968).

[20] S. Ali and A.R. Bodmer, Nucl. Phys. **80**, 99 (1966).

[21] D. M. Brink, J. Phys, Conf. Ser., **111**, 012001 (2008).

[22] J. A. Wheeler, Phys. Rev. **52**, 1083 (1937).

[23] M. Freer, *et al.*, Rev. Mod. Phys. **90**, 3 (2018).

[24] P. Schuck *et al.*, Phys. Scr. **91**, 123001 (2016).

[25] N. D. Cook, *Models of the Atomic Nucleus*, Springer Verlag, Berlin (2006).

[26] S. A. Abbas and S. Ahmad, Int. J. Mod. Phys. **E20**, 2101 (2011).

[27] M. H. Mac Gregor, Nuovo Cimento, **A364**, 113 (1976).

[28] O. Artun *et al.*, Phys. Rev. Lett. **35**, 773 (1975).

[29] A. M. Poskanzer *et al.*, Phys. Rev. Lett. **35**, 1701 (1975).

[30] H. Akimune *et al.*, Phys. Atom. Nuclei. **67**, 1721-1725 (2004).

[31] S. Ohkubo and Y. Hirabayashi, Phys. Rev. **C77**, 041303 (2008).

[32] J. P. Connelly *et al.*, Phys. Rev. **C57**, 1569 (1998).

[33] A. Cunsolo *et al.*, Phys. Rev. **C24**, 2127 (1981).

[34] T. W. Donnelly, J. A. Formaggio, B. R. Holstein, R. G. Milner, B. Surrow, *Foundations of Nuclear and Particle Physics*. Cambridge University Press (2017).

[35] A. Abbas, Mod. Phys. Lett. **A20**, 2443 (2005).

[36] C. W. Kim and H. Primakoff, Phys. Rev. **B566**, 140 (1965).

[37] J. G. Congleton and H. W. Fearing, Nucl. Phys. **A552**, 534(1993).

[38] A. A. Usmani *et al.*, Int. J. Mod. Phys. **E27**, 1850060 (2018).

[39] A. Abbas, Mod. Phys. Lett. **A19**, 2367 (2004).

[40] P. E. Hodgson, Contemp. Phys. **43**, 461 (2002).

[41] S. Hans Paetz gen, *Key Nuclear Reaction Experiments: Discoveries and Consequences*. p.4-15, IOP Publishing (2015).

[42] J. S. McCarthy, I. Sick and R. R. Whitney, Phys. Rev. **C15**, 1396 (1977).

[43] R. Hofstadter, Annu. Rev. Nucl. Sci. **7**, 231 (1957).

[44] A. Abbas, Mod. Phys. Lett. **A16**, 755 (2001).

[45] A. Abbas, Phys. Lett. **B167**, 150 (1986).

[46] H. Kanada, T. Kaneko, and Y. C. Tang, Phys. Rev. **C34**, 22 (1986).

[47] K. Langanke, *The third generation of nuclear physics with the microscopic cluster model, in Advances in Nuclear Physics*, ed. J. W. Vogt, p.85 (1994).

[48] H. Kanada, T. Kaneko and Y. C. Tang, Nuclear Physics, **A457**, 1 (1986).

[49] L. Pauling, Science, **150**, 297 (1965).

[50] L. Pauling, Nature **208**, 174 (1965).

[51] L. Pauling, Phys. Rev. Lett. **15**, 499 (1965); **15**, 868 (1969); **182**, 1357 (1969).

[52] L. Pauling, Phys. Rev. Lett. Lett. **36**, 162 (1976).

[53] S. G. Brush, Rev. Mod. Phys. **39**, 883 (1967).

[54] A. Camsonne, J. Gomez, A.T. Katramatou, G.G. Petratos: JLab experiment E04-018.

[55] J. Alcorn *et al.*, Nucl. Instrum. Meth. **A522**, 294 (2004).

[56] www.jlab.org/news/releases/jefferson-lab-completes-12-gev-upgrade.

[57] https://www.jlab.org/physics/GeV.

[58] https://hallaweb.jlab.org/equipment/beam/energy/arc_web.html.

[59] https://hallaweb.jlab.org/wiki/index.php/Raster.

[60] K. de Jager, Nucl. Phys. **A737**, 301 (2004).

[61] R. Suleiman, Kent State University, PhD Thesis (1999).

[62] Z.-J. Ding and R. Shimizu, Surf. Sci. **336**, 397 (1995).

[63] L. Cardman, R. Ent, N. Isgur, J.-M. Laget, C. Leemann, C. Meyer, Z.-E. Meziani (Jefferson Lab), *The Science Driving the 12 GeV Upgrade of CEBAF*, JLab Technical Report JLABR-2001-01 (2001).

[64] Hall A Rasters, https://hallaweb.jlab.org/wiki/index.php/Raster.

[65] P. Zhu *et al.*, Nucl. Inst. Meth. **A808**, 1 (2016).

[66] K. Fissum *et al.*, Nucl.Instrum.Meth. **A474**, 108 (2001).

[67] S. Tavernier, *Experimental Techniques in Nuclear and Particle Physics*, Springer, Berlin (2010).

[68] C. Grupen and B. Shwartz, *Particle Detectors*, Cambridge University Press, 2nd edition, (2008).

[69] N. Metropolis, *The Beginning. Los Alamos Science*, **15**, 125-130 (1987).

[70] L. R. Harrison, AIP conference proceedings, 1204, (2010).

[71] S. Tanny, Ph.D. Thesis, University of Toledo (2015).

[72] R. Shimizu and D. Ze-Jun, Rep. Prog. Phys. **55**, 487 (1992).

[73] https://root.cern.

[74] A. Bodek, M. E. Christy, B. Coopersmith, Nuclear and particle physics proceedings, **273**, 1705-1710 (2016).

[75] A. Bodek, M. E. Christy, B. Coopersmith, Eur. Phys. J. **C74**, 3091 (2014).

[76] W. Alahmade, M.S. Thesis, Kent State University (2015).

[77] W. R. Leo, *Techniques for Nuclear and Particle Physics Experiments*, Springer-Variag (1987).

[78] E. M. Henley and A. Garcia, *Subatomic Physics*, Ch 3, 2nd. Edition, Prentice-Hall (1991).

[79] H. A. Bethe, Phys. Rev. **89**, 1256 (1953).

[80] R. M. Sternheimer, *Methods of Experimental Physics*, edited by L. C. Yuan and C. S. Wu, Academic Press, NY (1961).

[81] G. R. Lynch and O. I. Dahl, Nucl. Instrum. Meth. **B58**, 6 (1991).

[82] R. M. Sternheimer, R. F. Peierls, Phys. Rev. **B3**, 3681(1971).

[83] R. M. Sternheimer, Phys. Rev. **88**, (1952).

[84] R. M. Sternheimer, M. J. Berger and S. M. Seltzer, Phys. Rev. **B27**, 6971 (1983).

[85] D. H. Beck et al., Phys. Rev. **C30**, 1403 (1984); Phys. Rev. Lett. **59**, 1537 (1987).

[86] A. Crispin and G. N. Fowler, Rev. Mod. Phys. **42**, 290 (1970).

[87] U. Fano, Annu. Rev. Nucl. Sci. **13**, 1 (1963).

[88] L. D. Landau, J. Phys. U.S.S.R, **8**, 201 (1944).

[89] T.Tabata and R. Ito, Nucl. Instrum. and Meth. **158**, 521,(1979).

[90] A. T. Katramatou, SLAC Report, SLAC-NPAS-TN-86-08 (1986); and references therein.

[91] G. Miller, SLAC Report SLAC-R-129 (1971).

[92] Y. S. Tsai, Radiative Corrections to Electron Scatterings, SLAC-PUB-848 (1971).

[93] L. W. Mo and Y. S. Tsai, Rev. Mod. Phys. **41**, 205 (1969).

[94] Y. S. Tsai, Phys. Rev. **122**, 1898 (1961).

[95] S. Stein et al., Phys. Rev. **D12**, 1884 (1975).

[96] E. J. Moniz, Phys. Rev. **184**, 1154 (1969).

[97] A. T. Katramatou and G.G. Petratos, private communication.